




University of
Stavanger

Faculty of Science and Technology

MASTER'S THESIS

Study program/Specialization: Petroleum Engineering / Drilling Technology	Spring semester, 2020 Open access
Writer: Lene Fattnes	 (Writer's signature)
Faculty supervisor: Mesfin Belayneh	
Thesis title: New Nanoparticle Based Drilling Fluid Formulation and Characterization: Experimental and Simulation Studies	
Credits (ECTS): 30	
Key words: <ul style="list-style-type: none">▪ Water-based drilling fluid▪ Flat rheology▪ Viscoelasticity▪ Nanoparticles▪ MWCNT-COOH▪ Silica▪ Aluminum oxide▪ Hydraulics performance simulations▪ T&D simulations	Pages: 189 + enclosure: 83 Stavanger, 15.07.2020

Abstract

Drilling fluids are an essential part of any drilling operation and it offers several functions of great importance, such as controlling the wellbore pressures and transporting cuttings to the surface. The design of a drilling fluid is greatly dependent on its performance, cost and environmental impact. To ensure a safe and successful drilling operation, the drilling fluid must be designed according to the expected wellbore conditions, such as the surrounding formation and thermodynamic state of the wellbore. Due to the global energy demands, the petroleum industry is expanding its exploration activities to depleted reservoirs, arctic, deepwater and geothermal wells, where a stable drilling fluid with enhanced properties is required.

The main issue with the use of bentonite fluids at higher temperatures is the flocculation of the bentonite platelets and the changes in the rheological properties it brings. The focus of this thesis is to design a thermally stable water-based drilling fluid containing both bentonite and various polymers. Thereafter, the impact of multi-walled carbon nanotube, silica and aluminum oxide nanoparticle suspensions on the flat rheology fluid is investigated. All fluids are characterized by their rheological, filtration, viscoelastic and frictional properties. Lastly, the performance of the flat rheology fluid and the optimum nanoparticle systems were investigated by performing hydraulics and T&D simulations.

Initially, a water-based drilling fluid containing soda ash, pac, polypac, bentonite and barite was formulated. This fluid was further modified with 0.016 wt% carbopol which provided the system with flat rheology characteristics. The thermal stability of the fluid was also verified by the hydraulics performance simulation where both the pump pressure and ECD are maintained at higher temperatures.

From the modification of the flat rheology fluid with the nanoparticle suspensions, it was found that the optimum concentrations were ~0.014 wt% MWCNT-COOH, ~0.025 wt% silica and ~0.014 wt% aluminum oxide. Results showed that these concentrations reduced the fluid loss of the flat rheology fluid with 23 %, 31 % and 32 %, respectively. Moreover, the lubricity was improved with 36.9 %, 23.1 % and 35.6 %, respectively. From the T&D simulations, it was observed that the increased lubricity reduced the torque and drag forces encountered in the wellbore significantly, which allows for longer drilling.

Acknowledgement

First and foremost, I would like to offer a special thanks to my supervisor Mesfin Belayneh for his never-ending guidance and motivational support. He has provided me with extensive knowledge throughout the entire process of this thesis work, as well as valuable and constructive suggestions. Mesfin, it has been wonderful to see your care for students and willingness to give of your time.

I would also like to thank my friends at the university for providing me with a great student experience, both socially and academically.

Finally, my sincerest gratitude goes to my parents for their support, patience and encouragement along the way in my studies and during the writing of this thesis.

Table of Content

Abstract	ii
Acknowledgement	iii
List of Figures	ix
List of Tables	xx
List of Symbols	xxii
List of Abbreviations	xxv
1 Introduction	1
1.1 Background	1
1.2 Problem Formulation	1
1.3 Objective	2
1.4 Research Methods	2
2 Theory	4
2.1 Drilling Fluid	4
2.1.1 Drilling Fluid Properties	4
2.1.2 Drilling Fluid Types	5
2.2 Rheology	7
2.2.1 Rheological Properties	8
2.2.2 Shear Stress and Shear Rate.....	9
2.2.3 Rotational Tests.....	10
2.3 Rheological Models	12
2.3.1 Newtonian Fluids.....	12
2.3.2 Non-Newtonian Fluids.....	13
2.4 Flat Rheology – Temperature Stable System	20
2.5 Clay Particle Associations	22
2.5.1 Flocculated System.....	23
2.5.2 Deflocculated System	23
2.5.3 Aggregated System.....	23

2.5.4	Dispersed System	23
2.6	Viscoelasticity	24
2.6.1	Oscillatory Tests	24
2.6.2	Approaches to Measuring Viscoelastic Behavior	25
2.7	Tribology and Friction.....	31
2.7.1	Definition of the Coulomb Model and the Coefficient of Friction	32
2.7.2	Application of Friction and Lubrication in the Industry	33
2.8	Torque and Drag Modelling	34
2.8.1	Drag	35
2.8.2	Torque	38
2.8.3	Tensile and Torsional Limit.....	39
2.9	Hydraulics Model	41
2.9.1	ECD	44
2.9.2	Pump Pressure.....	44
3	Literature Study	47
3.1	Nanotechnology.....	47
3.2	Nanoparticle Drilling Fluids.....	47
3.3	Literature Study: Application of Nanoparticles in Drilling Fluids	48
4	Experimental Work Study	54
4.1	Description of Drilling Fluid Additives	54
4.1.1	Bentonite	54
4.1.2	Soda Ash	55
4.1.3	Barite	56
4.1.4	Polymer Additives.....	56
4.1.5	Nanoparticle Additives	59
4.2	Experimental Equipment and Methodology	62
4.2.1	Hamilton Beach Mixer	62
4.2.2	OFITE Viscometer and Rheology Measurements.....	63
4.2.3	Anton Paar Rheometer	63
4.2.4	API Static Filter Press and Fluid Loss Measurement Procedure.....	65
4.2.5	Baroid Mud Balance and Density Measurement Procedure	66
4.2.6	pH-meter	66
4.2.7	Tribometer and Frictional Measurement.....	67

4.2.8	Scanning Electron Microscope	68
4.3	Drilling Fluid Formulation with Flat Rheology	69
4.4	Modification of Flat Rheology Drilling Fluid with Nanoparticles	73
5	Results.....	76
5.1	Effect of Hydrated versus Anhydrous Soda Ash on Rheological Parameters.....	76
5.2	Effect of Carbopol’s Method of Application on Rheological Parameters	78
5.3	Effect of Carbopol.....	80
5.4	Flat Rheology Drilling Fluid Formulation.....	82
5.4.1	Increasing the Viscosity of the Reference Fluid	82
5.4.2	Effect of Lignosulfonate and Temperature on Rheological Parameters.....	82
5.4.3	Effect of Lignosulfonate on Viscoelastic Properties.....	85
5.4.4	Effect of Carbopol and Temperature on Rheological Parameters	88
5.4.5	Effect of Carbopol on Viscoelastic Properties	92
5.5	Best Performing Flat Rheology Drilling Fluid System	95
5.5.1	Effect of Static Aging at Room Temperature on Rheological and Filtration Properties ..	95
5.5.2	Effect of Static Aging at Room Temperature on pH and Density.....	97
5.5.3	Effect of Static Aging at Room Temperature on Viscoelastic Properties.....	98
5.5.4	Effect of Static Aging at 62°C on Rheological Properties	99
5.6	MWCNT-COOH Nanoparticle Based Drilling Fluid	101
5.6.1	Effect of MWCNT-COOH on Rheological Properties	101
5.6.2	Effect of MWCNT-COOH on Fluid Loss.....	103
5.6.3	SEM Pictures and Element Analysis of Filter Cakes.....	104
5.7	SiO₂ Nanoparticle Based Drilling Fluid	108
5.7.1	Effect of SiO ₂ on Rheological Properties.....	108
5.7.2	Effect of SiO ₂ on Fluid Loss	109
5.8	Al₂O₃ Nanoparticle Based Drilling Fluid	110
5.8.1	Effect of Al ₂ O ₃ on Rheological Properties	110
5.8.2	Effect of Al ₂ O ₃ on Fluid Loss.....	111
5.9	Effect of Nanoparticle Suspensions on Viscoelastic Properties	112
5.10	Effect of Nanoparticle Suspensions on Frictional Properties.....	113
6	Modeling and Simulation Study	117
6.1	Rheological Modeling	117
6.1.1	Best-Fit Rheological Model.....	118

6.1.2	Effect of Temperature on Rheological Parameters.....	120
6.2	Hydraulics Performance Simulation	123
6.2.1	Simulation Arrangement	123
6.2.2	Pump Pressure Simulation Evaluation	125
6.2.3	ECD Simulation Evaluation	130
6.3	Torque and Drag Simulation	134
6.3.1	Simulation Arrangement	135
6.3.2	Simulation Evaluation.....	135
7	Summary and Discussion.....	137
7.1	Characterization of Drilling Fluid	137
7.1.1	Flat Rheology System	137
7.1.2	Nanoparticle Modified System.....	139
7.2	Carbopol’s Method of Application	143
7.3	Effect of Aging.....	145
7.4	Performance Evaluation	147
7.5	Rheological Model and Bingham Yield Stress.....	147
7.6	Limitations and Uncertainties	148
8	Conclusion	151
9	References.....	153
APPENDICES	163	
APPENDIX A – ROTATIONAL TEMPERATURE SWEEPS.....	163	
APPENDIX B – EFFECT OF MWCNT-COOH ON VISCOELASTIC PROPERTIES	164	
APPENDIX C – EFFECT OF SILICA ON VISCOELASTIC PROPERTIES.....	166	
APPENDIX D – EFFECT OF ALUMINUM OXIDE ON VISCOELASTIC PROPERTIES	167	
APPENDIX E – RHEOLOGICAL MODELLING DIAGRAMS	168	
Newtonian Model.....	168	
Bingham Plastic Model	169	
Power Law Model.....	170	
Herschel-Bulkley Model.....	172	
Unified Model.....	173	
Robertson-Stiff Model	174	
APPENDIX F – HYDRAULICS PERFORMANCE SIMULATIONS	176	

Pump Pressure Plots - Reference Fluid Containing Multi-Walled Carbon Nanotube	177
Pump Pressure Plots - Reference Fluid Containing Silica	177
Pump Pressure Plots - Reference Fluid Containing Aluminum Oxide	178
ECD Plots - Reference Fluid Containing Multi-Walled Carbon Nanotube	178
ECD Plots - Reference Fluid Containing Silica	179
ECD Plots - Reference Fluid Containing Aluminum Oxide	179
ECD Simulation - The Percentage Change from the Initial Mud Weight for Reference Fluid.....	180
ECD Simulation - The Percentage Change from the Initial Mud Weight for Nanoparticle Fluids	180
APPENDIX G – TORQUE AND DRAG SIMULATIONS.....	183
T & D Plots - Reference Fluid System (Short-Time).....	185
T & D Plots - Reference Fluid System (Long-Time).....	187
T & D Plots - Reference Fluid Containing 0.07 g MWCNT-COOH (Short-Time).....	189
T & D Plots - Reference Fluid Containing 0.13 g MWCNT-COOH (Long-Time).....	191
T & D Plots - Reference Fluid Containing 0.13 g SiO ₂	193
T & D Plots - Reference Fluid Containing 0.07 g Al ₂ O ₃	195
APPENDIX H – SEM PICTURES OF FILTER CAKES	197
Reference Fluid (Short-Time Aging)	197
Reference Fluid (Long-Time Aging)	198
Reference Fluid Containing 0.07 g Multi-Walled Carbon Nanotube (Short-Time Aging)	200
Reference Fluid Containing 0.07 g Multi-Walled Carbon Nanotube (Long-Time Aging)	201
APPENDIX I – SEM ELEMENT ANALYSIS OF FILTER CAKE SURFACE AREA	203
Reference Fluid (Short-Time Aging)	203
Reference Fluid (Long-Time Aging)	206
Reference Fluid Containing 0.07 g Multi-Walled Carbon Nanotube (Short-Time Aging)	210
Reference Fluid Containing 0.07 g Multi-Walled Carbon Nanotube (Long-Time Aging)	213
APPENDIX J – SEM ELEMENT ANALYSIS OF SELECTED AREAS OF THE FILTER CAKE.....	217
Reference Fluid (Short-Time Aging)	217
Reference Fluid (Long-Time Aging)	223
Reference Fluid Containing 0.07 g Multi-Walled Carbon Nanotube (Short-Time Aging)	231
Reference Fluid Containing 0.07 g Multi-Walled Carbon Nanotube (Long-Time Aging)	238

List of Figures

Figure 1.1: Summary of the research activities in this thesis	3
Figure 2.1: Illustration of a water-in-oil emulsion, [17].....	7
Figure 2.2: A material's structure in solid (left) and fluid state (right), [20].....	8
Figure 2.3: Two-plate model utilized to calculate shear rate and shear stress of a fluid, [20]...	9
Figure 2.4: Illustration of "cup and bob" setup, [17].....	11
Figure 2.5: Shear stress- shear rate relation of the Newtonian Model, [32].....	13
Figure 2.6: Shear stress-shear rate relation of the Bingham Plastic model, [32]	14
Figure 2.7: Shear stress-shear rate relation of the Power Law model, [32]	16
Figure 2.8: Shear stress-shear rate relation of the Herschel-Bulkley model, [32]	17
Figure 2.9: Example of log-log plot used to obtain A and B parameters for the R-S model, [38]	20
Figure 2.10: Typical rheological behavior of conventional and flat rheology drilling fluids, [43]	21
Figure 2.11: Forces acting on clay particles suspended in a liquid, [17]	22
Figure 2.12: Arrangement of clay particles in drilling fluids, [8]	22
Figure 2.13: Illustration of the two-plates model for an oscillatory test, [28]	24
Figure 2.14: Plot of the preset shear strain, γ , and resulting shear stress, τ , curves versus time, [47]	27
Figure 2.15: The preset of an amplitude sweep with five steps of increasing the amplitude, [20]	28
Figure 2.16: Illustration of the result from a strain amplitude sweep test, [28]	29
Figure 2.17: Illustration of a strain amplitude sweep result showing a G'' -peak, [28].....	30
Figure 2.18: Amplitude sweep result presented with shear stress plotted on the x-axis, [28].	30
Figure 2.19: Typical behavior of static and kinetic friction as a function of time, [51]	33
Figure 2.20: Illustration of a curved drill string divided into segments and the load distribution of each segment, [62]	36
Figure 2.21: Example of effective tension plot where no loads exceed the tensile limit (REF + 0.08 g CP system).....	40
Figure 2.22: Example of torque plot where no loads exceed the torsional limit (REF + 0.08 g CP system).....	40
Figure 2.23: Illustration of a typical circulation system, [29]	45
Figure 2.24: Frictional pressure losses in a circulation system,[77]	46

Figure 3.1: Illustration of the increase in the surface area to volume ratio with nanoparticles, [82]	48
Figure 4.1: Illustration of the basic structure of montmorillonite, [25]	55
Figure 4.2: Molecular structure of anhydrous sodium carbonate, [97]	56
Figure 4.3: Chemical structure of pac, [99].....	57
Figure 4.4: Typical chemical structure of carbopol polymers, [104]	58
Figure 4.5: Chemical structure of lignosulfonate, [8]	58
Figure 4.6: Chemical structure of MWCNT-COOH, [107]	59
Figure 4.7: MWCNT-COOH solution dispersed in water, immediately (left) and after 24 hours (right).....	60
Figure 4.8: Silica solution dispersed in water, immediately (left) and after 24 hours (right) ..	61
Figure 4.9: Aluminum oxide solution dispersed in water, immediately (left) and after 24 hours (right).....	62
Figure 4.10: Hamilton Beach Mixer (with mixing cup).....	62
Figure 4.11: OFITE Model 800 8-Speed viscometer	63
Figure 4.12: Anton Paar MCR 302 rheometer with parallel plate setup	64
Figure 4.13: "Cup and bob" (left) and parallel plate (right) setup with test sample	64
Figure 4.14: API static filter press setup and elements, [8]	65
Figure 4.15: Baroid mud balance, [8].....	66
Figure 4.16: Mettler Toledo FiveEasy™ pH meter	67
Figure 4.17: Illustration of ball-on-disc tribometer, [119]	67
Figure 4.18: CSM tribometer with test fluid (lift position).....	68
Figure 5.1: Viscometer data at 22°C for fluids with hydrated and anhydrous soda ash	76
Figure 5.2: pH data at 22°C of fluids with hydrated and anhydrous soda ash	77
Figure 5.3: Viscometer data at 50°C of fluids with hydrated and anhydrous soda ash.....	77
Figure 5.4: Viscometer data at 80°C for fluids with hydrated and anhydrous soda ash	78
Figure 5.5: Viscometer data at 50°C to compare ex-situ and in-situ application of carbopol (1)	79
Figure 5.6: Bingham yield stress to compare ex-situ and in-situ application of carbopol	79
Figure 5.7: Viscometer data at 50°C to compare ex-situ and in-situ application of carbopol (2)	80
Figure 5.8: Bingham yield stress to investigate the effect of carbopol alone	80
Figure 5.9: Free fluid accumulating at the surface after ~1 hour	81

Figure 5.10: Free fluid accumulated at surface after ~1 day	81
Figure 5.11: Viscometer data at 50°C for reference fluid containing 0.5 g carbopol	82
Figure 5.12: Viscometer data at 50°C for lignosulfonate fluids (0.6-0.9 g).....	83
Figure 5.13: Bingham yield stress of lignosulfonate fluids (0.6-0.9 g) at varied temperatures	83
Figure 5.14: Viscometer data at 50°C for lignosulfonate fluids (1.0-1.5 g).....	84
Figure 5.15: Bingham yield stress of lignosulfonate fluids (1.0-1.5 g).....	84
Figure 5.16: Amplitude sweep results for lignosulfonate fluids (0.6-0.9 g)	85
Figure 5.17: Amplitude sweep results for lignosulfonate fluids (1.0-1.5 g)	86
Figure 5.18: Phase shift angle vs. shear stress for lignosulfonate fluids.....	87
Figure 5.19: Viscometer data at 50°C for carbopol fluids (0.1-0.5 g)	88
Figure 5.20: Bingham yield stress of carbopol fluids (0.1-0.5 g)	89
Figure 5.21: Viscometer data at 50°C for carbopol fluids (0.05-0.1 g)	89
Figure 5.22: Bingham yield stress of carbopol fluids (0.05-0.1 g)	90
Figure 5.23: Temperature sweep results for some carbopol fluids	91
Figure 5.24: Amplitude sweep results for carbopol fluids (0.1-0.5 g).....	92
Figure 5.25: Amplitude sweep results for carbopol fluids (0.05-0.1 g).....	93
Figure 5.26: Phase shift angle vs. shear stress for carbopol fluids.....	94
Figure 5.27: Viscometer data at 50°C for best performing flat rheology fluid	96
Figure 5.28: Bingham yield stress of best performing flat rheology fluid.....	96
Figure 5.29: Fluid loss measurement of the best performing flat rheology fluid (in ml).....	97
Figure 5.30: pH measurement of the best performing flat rheology fluid	97
Figure 5.31: Amplitude sweep result for best performing flat rheology fluid	98
Figure 5.32: Phase shift angle vs. shear stress for best performing flat rheology fluid	99
Figure 5.33: Viscometer data at 50°C for best performing flat rheology fluid after aging at 62°C	100
Figure 5.34: Bingham yield stress of best performing flat rheology fluid after aging at 62°C	100
Figure 5.35: Viscometer data at 50°C for multi-walled carbon nanotube fluids (long-time aging)	101
Figure 5.36: Bingham yield stress of multi-walled carbon nanotube fluids (long-time aging)	102
Figure 5.37: Viscometer data at 22°C for multi-walled carbon nanotube fluids (short-time vs. long-time aging)	103

Figure 5.38: Fluid loss measurement of multi-walled carbon nanotube fluids (in ml)	103
Figure 5.39: Fluid loss measurement of multi-walled carbon nanotube fluid after 4 days (in ml)	104
Figure 5.40: SEM pictures at 20 μm magnification of reference fluid after short- (left) and long- time aging (right).....	105
Figure 5.41: SEM pictures at 20 μm magnification of 0.07 g MW system after short- (left) and long-time aging (right)	105
Figure 5.42: SEM picture at 10 μm magnification and element analysis for REF (short-time)	106
Figure 5.43: SEM picture at 10 μm magnification and element analysis for REF (long-time)	106
Figure 5.44: SEM picture at 10 μm magnification and element analysis for REF + 0.07 g MW (short-time).....	107
Figure 5.45: SEM picture at 10 μm magnification and element analysis for REF + 0.07 g MW (long-time).....	107
Figure 5.46: Viscometer data at 50°C for silica fluids	108
Figure 5.47: Bingham yield stress of silica fluids	109
Figure 5.48: Fluid loss measurement of silica fluids (in ml).....	109
Figure 5.49: Viscometer data at 50°C for aluminum oxide fluids	110
Figure 5.50: Bingham yield stress of aluminum oxide fluids	111
Figure 5.51: Fluid loss measurement of aluminum oxide fluids (in ml).....	111
Figure 5.52: Tribometer results for multi-walled carbon nanotube fluids	114
Figure 5.53: Tribometer results for silica fluids.....	114
Figure 5.54: Tribometer results for aluminum oxide fluids	115
Figure 5.55: Tribometer results for multi-walled carbon nanotube fluid (short-time storing)	116
Figure 6.1: % Deviation between measurement and model for best performing flat rheology system.....	118
Figure 6.2: Well setup for the hydraulics performance simulation	124
Figure 6.3: Pump pressures of flat rheology systems at 22°C, 50°C and 80°C	126
Figure 6.4: Pump pressure of 0.13 g MWCNT-COOH fluid at 22°C, 50°C and 80°C	127
Figure 6.5: Pump pressure of 0.13 g silica fluid at 22°C, 50°C and 80°C	127
Figure 6.6: Pump pressure of 0.07 g aluminum oxide fluid at 22°C, 50°C and 80°C	128
Figure 6.7: %Change in pump pressure for 0.13 g MW fluid at 22°C, 50°C and 80°C	128

Figure 6.8: % Change in pump pressure for 0.13 g Si fluid at 22°C, 50°C and 80°C	129
Figure 6.9: %Change in pump pressure for 0.07 g Al fluid at 22°C, 50°C and 80°C.....	129
Figure 6.10: ECD plot for the flat rheology fluid.....	130
Figure 6.11: ECD plot for 0.13 g MWCNT-COOH fluid at 22°C, 50°C and 80°C.....	131
Figure 6.12: ECD plot for 0.13 g silica fluid at 22°C, 50°C and 80°C	132
Figure 6.13: ECD plot for 0.07 g aluminum oxide fluid at 22°C, 50°C and 80°C	132
Figure 6.14: % Change of ECD from the REF + 0.08 g CP system for 0.13 g MW fluid.....	133
Figure 6.15: % Change of ECD from REF + 0.08 g CP system for 0.13 g silica fluid	133
Figure 6.16: % Change of ECD from REF + 0.08 g CP system for 0.07 g Al fluid	134
Figure 6.17: Maximum drilling depths from the T&D simulation.....	136
Figure 7.1: Bingham yield stress of lignosulfonate fluids (0.6-0.9 g) at 50°C and 80°C	138
Figure 7.2: Bingham yield stress of carbopol fluids (0.05-0.5 g) at 50°C and 80°C	138
Figure 7.3: Bingham yield stress of MW (left) and silica fluids (right) at 50°C and 80°C ...	140
Figure 7.4: Bingham yield stress of aluminum oxide fluids at 50°C and 80°C	141
Figure 7.5: Tribometer results for reference fluid after short- and long-time storing	146
Figure A. 1: The dried-out sample at measurement (left) and lift position (right) after completing the temperature sweep	163
Figure A. 2: Sample at measurement (left) and lift position (right) after completing the temperature sweep (“cup and bob”)	163
Figure B. 1: Amplitude sweep result for multi-walled carbon nanotube fluids	164
Figure B. 2: Phase shift angle vs. shear stress for multi-walled carbon nanotube fluids	164
Figure B. 3: Amplitude sweep result for multi-walled carbon nanotube fluids (short-time vs. long-time aging)	165
Figure B. 4: Phase shift angle vs. shear stress for multi-walled carbon nanotube fluids (short- time vs. long-time aging).....	165
Figure C. 1: Amplitude sweep result for silica fluids.....	166
Figure C. 2: Phase shift angle vs. shear stress for silica fluids.....	166
Figure D. 1: Amplitude sweep result for aluminum oxide fluids.....	167
Figure D. 2: Phase shift angle vs. shear stress for aluminum oxide fluids.....	167

Figure E. 1: Newtonian model versus flat rheology fluid at 22°C	168
Figure E. 2: Newtonian model versus flat rheology fluid at 50°C	168
Figure E. 3: Newtonian model versus flat rheology fluid at 80°C	169
Figure E. 4: Bingham Plastic model versus flat rheology fluid at 22°C	169
Figure E. 5: Bingham Plastic model versus flat rheology fluid at 50°C	170
Figure E. 6: Bingham Plastic model versus flat rheology fluid at 80°C	170
Figure E. 7: Power law model versus flat rheology fluid at 22°C.....	171
Figure E. 8: Power law model versus flat rheology fluid at 50°C.....	171
Figure E. 9: Power law model versus flat rheology fluid at 80°C.....	171
Figure E. 10: Herschel-Bulkley model versus flat rheology fluid at 22°C	172
Figure E. 11: Herschel-Bulkley model versus flat rheology fluid at 50°C	172
Figure E. 12: Herschel-Bulkley model versus flat rheology fluid at 80°C	173
Figure E. 13: Unified model versus flat rheology fluid at 22°C	173
Figure E. 14: Unified model versus flat rheology fluid at 50°C	174
Figure E. 15: Unified model versus flat rheology fluid at 80°C	174
Figure E. 16: Robertson-Stiff model versus flat rheology fluid at 22°C.....	175
Figure E. 17: Robertson-Stiff model versus flat rheology fluid at 50°C.....	175
Figure E. 18: Robertson-Stiff model versus flat rheology fluid at 80°C.....	175
Figure F. 1: Pump pressure of MWCNT-COOH fluids at 22°C, 50°C and 80°C.....	177
Figure F. 2: Pump pressure of silica fluids at 22°C, 50°C and 80°C	177
Figure F. 3: Pump pressure of aluminum oxide fluids at 22°C, 50°C and 80°C.....	178
Figure F. 4: ECD of MWCNT-COOH fluids at 22°C, 50°C and 80°C	178
Figure F. 5: ECD of silica fluids at 22°C, 50°C and 80°C.....	179
Figure F. 6: ECD of aluminum oxide fluids at 22°C, 50°C and 80°C	179
Figure F. 7: ECD simulation: % Change from initial mud weight (REF + 0.08 g CP system)	180
Figure G. 1: Illustration of the simulation well at the maximum depth for the reference fluid system.....	183
Figure G. 2: Stress trip out plot for reference fluid system (short-time).....	185
Figure G. 3: Stress trip in plot for reference fluid system (short-time).....	185

Figure G. 4: Torque plot for the reference fluid system (short-time).....	186
Figure G. 5: Effective tension plot for reference fluid system (short-time).....	186
Figure G. 6: Stress trip in plot for reference fluid system (long-time).....	187
Figure G. 7: Stress trip in plot for reference fluid system (long-time).....	187
Figure G. 8: Torque plot for reference fluid system (long-time)	188
Figure G. 9: Effective tension plot for reference fluid system (long-time).....	188
Figure G. 10: Stress trip out plot for REF + 0.07 g MW (short-time)	189
Figure G. 11: Stress trip in plot for REF + 0.07 g MW (short-time)	189
Figure G. 12: Torque plot for REF + 0.07 g MW (short-time)	190
Figure G. 13: Effective tension plot for REF + 0.07 g MW (short-time)	190
Figure G. 14: Stress trip out plot for REF + 0.13 g MW (long-time)	191
Figure G. 15: Stress trip in plot for REF + 0.13 g MW (long-time)	191
Figure G. 16: Torque plot for REF + 0.13 g MW (long-time).....	192
Figure G. 17: Effective tension plot for REF + 0.13 g MW (long-time)	192
Figure G. 18: Stress trip out plot for REF + 0.13 g Si	193
Figure G. 19: Stress trip in plot for REF + 0.13 g Si	193
Figure G. 20: Torque plot for REF + 0.13 g Si	194
Figure G. 21: Effective tension plot for REF + 0.13 g Si	194
Figure G. 22: Stress trip out plot for REF + 0.07 g Al.....	195
Figure G. 23: Stress trip in plot for REF + 0.07 g Al.....	195
Figure G. 24: Torque plot for REF + 0.07 g Al	196
Figure G. 25: Effective tension plot for REF + 0.07 g Al.....	196
Figure H. 1: SEM picture at 20 μm magnification of filter cake (REF system, short-time)..	197
Figure H. 2: SEM picture at 10 μm (left) and 2 μm (right) magnification of location 1 (REF system, short-time)	197
Figure H. 3: SEM picture at 10 μm (left) and 2 μm (right) magnification of location 2 (REF system, short-time)	198
Figure H. 4: SEM picture at 1 μm magnification of location 2 (REF system, short-time)	198
Figure H. 5: SEM picture at 200 μm (left) and 10 μm (right) magnification of the edge of the filter cake (REF system, long-time)	198
Figure H. 6: SEM picture at 10 μm magnification of location 1, Mag = 2.50 K X (left) and Mag = 5.00 K X (right) (REF system, long-time).....	199

Figure H. 7: SEM picture at 2 μm magnification of location 1, Mag = 10.00 K X (left) and Mag = 25.00 K X (right), (REF system, long-time) 199

Figure H. 8: SEM picture at 2 μm magnification of location 2 (REF system, long-time) 200

Figure H. 9: SEM picture at 20 μm magnification of filter cake, Mag = 1.00 K X (left) and Mag = 2.50 K X (right), (REF+0.07 g MW system, short-time)..... 200

Figure H. 10: SEM picture at 10 μm (left) and 2 μm (right) magnification of location 1 (REF+0.07 g MW system, short-time)..... 200

Figure H. 11: SEM picture at 1 μm magnification of location 1 (REF+0.07 g MW system, short-time)..... 201

Figure H. 12: SEM picture at 2 μm magnification of location 2 (REF+0.07 g MW system, short-time)..... 201

Figure H. 13: SEM picture at 20 μm magnification of filter cake, Mag = 1.00 K X (left) and Mag = 2.50 K X (right), (REF+0.07 g MW system, long-time) 201

Figure H. 14: SEM picture at 10 μm magnification of location 1 (REF+0.07 g MW system, long-time) 202

Figure H. 15: SEM picture at 2 μm magnification of location 1, Mag = 10.00 K X (left) and Mag = 10.00 K X (right), (REF+0.07 g MW system, long-time) 202

Figure I. 1: SEM picture and element analysis of surface at 10 μm magnification (REF system, short-time) 203

Figure I. 2: Element analysis: Sum spectrum (REF system, short-time) 203

Figure I. 3: Element analysis: SiK/O K/SrL/AIK/BaL/S K phase (REF system, short-time) 204

Figure I. 4: Element analysis: Unallocated phase (REF system, short-time)..... 205

Figure I. 5: Element analysis: O K/S K/BaL phase (REF system, short-time) 206

Figure I. 6: SEM picture and element analysis of surface at 10 μm (REF system, long-time) 206

Figure I. 7: Element analysis: Sum spectrum (REF system, long-time) 207

Figure I. 8: Element analysis: S K/BaL/SiK/O K phase (REF system, long-time)..... 208

Figure I. 9: Element analysis: O K/S K/SiK/BaL/FeK phase (REF system, long-time)..... 209

Figure I. 10: Element analysis: Unallocated phase (REF system, long-time)..... 210

Figure I. 11: SEM picture and element analysis of surface at 10 μm (REF + 0.07 g MW system, short-time) 210

Figure I. 12: Element analysis: Sum spectrum (REF + 0.07 g MW system, short-time)..... 211

Figure I. 13: Element analysis: Unallocated phase (REF + 0.07 g MW system, short-time) 212

Figure I. 14: Element analysis: O K/S K/BaL/SiK phase (REF + 0.07 g MW system, short-time) 213

Figure I. 15: SEM picture and element analysis of surface at 10 μm (REF + 0.07 g MW system, long-time) 213

Figure I. 16: Element analysis: Sum spectrum (REF + 0.07 g MW system, long-time) 214

Figure I. 17: Element analysis: O K/S K/BaL/SiK/AIK phase (REF + 0.07 g MW system, long-time)..... 215

Figure I. 18: Element analysis: Unallocated phase (REF + 0.07 g MW system, long-time). 216

Figure J. 1: SEM picture at 20 μm magnification of filter cake (REF system, long-time) 199

Figure J. 2: Area 1 - SEM picture and element analysis of surface at 100 μm (REF system, short-time) 217

Figure J. 3: Area 1 - Element analysis of selected area 1 (REF system, short-time) 217

Figure J. 4: Area 2 - SEM picture and element analysis of surface at 20 μm (REF system, short-time)..... 218

Figure J. 5: Area 2 - Element analysis of EDS spot 1 (REF system, short-time) 218

Figure J. 6: Area 2 - Element analysis of spot 2 (REF system, short-time) 219

Figure J. 7: Area 2 - Element analysis of spot 3 (REF system, short-time) 219

Figure J. 8: Area 2 - Element analysis of spot 4 (REF system, short-time) 220

Figure J. 9: Area 2 - Element analysis of spot 5 (REF system, short-time) 220

Figure J. 10: Area 2 - Element analysis of spot 6 (REF system, short-time) 221

Figure J. 11: Area 2 - Element analysis of spot 7 (REF system, short-time) 221

Figure J. 12: Area 2 - Element analysis of spot 8 (REF system, short-time) 222

Figure J. 13: Area 2 - Element analysis of selected area 1 (REF system, short-time) 222

Figure J. 14: Area 1 - SEM picture and element analysis of surface at 100 μm (REF system, long-time) 223

Figure J. 15: Area 1 - Element analysis of selected area 1 (REF system, long-time) 223

Figure J. 16: Area 2 - SEM picture and element analysis of surface at 20 μm (REF system, long-time)..... 224

Figure J. 17: Area 2 - Element analysis of spot 1 (REF system, long-time) 224

Figure J. 18: Area 2 - Element analysis of spot 2 (REF system, long-time) 225

Figure J. 19: Area 2 - Element analysis of spot 3 (REF system, long-time) 225

Figure J. 20: Area 2 - Element analysis of spot 4 (REF system, long-time) 226

Figure J. 21: Area 2 - Element analysis of spot 5 (REF system, long-time) 226

Figure J. 22: Area 2 - Element analysis of spot 6 (REF system, long-time) 227

Figure J. 23: Area 2 - Element analysis of spot 7 (REF system, long-time) 227

Figure J. 24: Area 2 - Element analysis of spot 8 (REF system, long-time) 228

Figure J. 25: Area 2 - Element analysis of spot 9 (REF system, long-time) 228

Figure J. 26: Area 2 - Element analysis of selected area 1 (REF system, long-time) 229

Figure J. 27: Filter paper - SEM picture and element analysis of surface at 20 μm (REF system, long-time) 229

Figure J. 28: Filter paper - Element analysis of spot 1 (REF system, long-time) 230

Figure J. 29: Filter paper - Element analysis of spot 2 (REF system, long-time) 230

Figure J. 30: Filter paper - Element analysis of spot 3 (REF system, long-time) 231

Figure J. 31: Area 1 - SEM picture and element analysis of surface at 100 μm (REF+ 0.07 g MW system, short-time) 231

Figure J. 32: Area 1 - Element analysis of selected area 1 (REF+ 0.07 g MW system, short-time) 232

Figure J. 33: Area 2 - SEM picture and element analysis of surface at 20 μm (REF+ 0.07 g MW system, short-time) 232

Figure J. 34: Area 2 - Element analysis of spot 1 (REF+ 0.07 g MW system, short-time) ... 233

Figure J. 35: Area 2 - Element analysis of spot 2 (REF+ 0.07 g MW system, short-time) ... 233

Figure J. 36: Area 3 - Element analysis of spot 2 (REF+ 0.07 g MW system, short-time) ... 234

Figure J. 37: Area 2 - Element analysis of spot 4 (REF+ 0.07 g MW system, short-time) ... 234

Figure J. 38: Area 2 - Element analysis of spot 5 (REF+ 0.07 g MW system, short-time) ... 235

Figure J. 39: Area 2 - Element analysis of spot 6 (REF+ 0.07 g MW system, short-time) ... 235

Figure J. 40: Area 2 - Element analysis of spot 7 (REF+ 0.07 g MW system, short-time) ... 236

Figure J. 41: Area 2 - Element analysis of spot 8 (REF+ 0.07 g MW system, short-time) ... 236

Figure J. 42: Area 2 - Element analysis of spot 9 (REF+ 0.07 g MW system, short-time) ... 237

Figure J. 43: Area 2 - Element analysis of spot 10 (REF+ 0.07 g MW system, short-time) . 237

Figure J. 44: Area 2 - Element analysis of selected area 1 (REF+ 0.07 g MW system, short-time) 238

Figure J. 45: Area 1 - SEM picture and element analysis of surface at 100 μm (REF+ 0.07 g MW system, long-time) 238

Figure J. 46: Area 1 - Element analysis of selected area 1 (REF+ 0.07 g MW system, long-time) 239

Figure J. 47: Area 2 - SEM picture and element analysis of surface at 20 μm (REF+ 0.07 g MW system, long-time) 239

Figure J. 48: Area 2 - Element analysis of spot 1 (REF+ 0.07 g MW system, long-time) 240

Figure J. 49: Area 2 - Element analysis of spot 2 (REF+ 0.07 g MW system, long-time) 240

Figure J. 50: Area 2 - Element analysis of spot 3 (REF+ 0.07 g MW system, long-time) 241

Figure J. 51: Area 2 - Element analysis of spot 4 (REF+ 0.07 g MW system, long-time) 241

Figure J. 52: Area 2 - Element analysis of spot 5 (REF+ 0.07 g MW system, long-time) 242

Figure J. 53: Area 2 - Element analysis of spot 6 (REF+ 0.07 g MW system, long-time) 242

Figure J. 54: Area 2 - Element analysis of spot 7 (REF+ 0.07 g MW system, long-time) 243

Figure J. 55: Area 2 - Element analysis of spot 8 (REF+ 0.07 g MW system, long-time) 243

Figure J. 56: Area 2 - Element analysis of spot 9 (REF+ 0.07 g MW system, long-time) 244

Figure J. 57: Area 2 - Element analysis of spot 10 (REF+ 0.07 g MW system, long-time) .. 244

Figure J. 58: Area 2 - Element analysis of selected area 1 (REF+ 0.07 g MW system, long-time)
..... 245

List of Tables

Table 2.1: Relationship between material behavior and phase shift angle, δ , [28].....	31
Table 2.2: Summary of parameters and equations applied in the Unified hydraulic model, [55]	43
Table 4.1: Chemical composition of bentonite, [95].....	54
Table 4.2: Mixing order and times for the reference formulation.....	69
Table 4.3: Recipe for WBM systems containing 0.5 g carbopol and various amounts of lignosulfonate.....	70
Table 4.4: Recipe for WBM systems with 0.5 g carbopol added ex-situ and in-situ.....	70
Table 4.5: Mixing order and times for lignosulfonate and carbopol (in-situ).....	71
Table 4.6: Recipe for WBM systems with 0.5 g carbopol and various amounts of lignosulfonate (1.0-1.5 g).....	71
Table 4.7: Recipe for WBM systems with various amounts of carbopol (ex-situ).....	72
Table 4.8: Recipe for WBM systems with varied amounts of soda ash anhydride and carbopol	72
Table 4.9: Mixing order and times for nanoparticle and carbopol (ex-situ).....	73
Table 4.10: Recipe for reference system with varied amounts of multi-walled carbon nanotube	74
Table 4.11: Recipe for reference system with varied amounts of silica.....	74
Table 4.12: Recipe for reference system with varied amounts of aluminum oxide.....	74
Table 5.1: Summary of important parameters obtained from the amplitude sweeps of lignosulfonate fluids.....	88
Table 5.2: Summary of important parameters obtained from the amplitude sweeps of carbopol fluids.....	95
Table 5.3: Summary of important parameters obtained from the amplitude sweeps of flat rheology fluid.....	99
Table 5.4: Summary of important parameters obtained from the amplitude sweeps of MW fluids	113
Table 5.5: Summary of important parameters obtained from the amplitude sweeps of silica fluids.....	113

Table 5.6: Summary of important parameters obtained from the amplitude sweeps of aluminum oxide fluids	113
Table 6.1: Viscometer dial readings of best performing flat rheology fluid	118
Table 6.2: Model parameters for best performing flat rheology system at 22°C.....	119
Table 6.3: Model parameters for best performing flat rheology system at 50°C.....	119
Table 6.4: Model parameters for best performing flat rheology system at 80°C.....	120
Table 6.5: Summary of all rheological parameters for the best performing flat rheology fluid	122
Table 6.6: Summary of viscometer dial readings applied in the hydraulics simulation (flat rheology system)	124
Table 6.7: Summary of viscometer dial readings applied in the hydraulics simulation (nanoparticle fluids)	125
Table 7.1: Fluid loss results of best performing fluid loss control quantities	142
Table 7.2: Tribometer results of best performing lubricant quantities.....	143
Table 7.3: Viscometer dial readings at 50°C comparing ex-situ and in-situ application of carbopol.....	144
Table 7.4: Bingham yield stresses comparing ex-situ and in-situ application of carbopol....	144
Table F. 1: Summary of viscometer dial readings applied in the hydraulics simulation (MW fluids).....	176
Table F. 2: Summary of viscometer dial readings applied in the hydraulics simulation (silica fluids).....	176
Table F. 3: Summary of viscometer dial readings applied in the hydraulics simulation (Al fluids)	176
Table F. 4: ECD simulation: % Change from initial mud weight (MWCNT-COOH fluids)	181
Table F. 5: ECD simulation: % Change from initial mud weight (silica fluids).....	181
Table F. 6: ECD simulation: % Change from initial mud weight (aluminum oxide fluids) ..	182
Table G. 1: Summary of the maximum depths obtained from the T&D simulation.....	184
Table G. 2: Summary of the factors limiting the maximum drilling depth of each fluid system	184

List of Symbols

A	Constant in Robertson-Stiff model similar to k, []
A	Surface area exposed to shear, [m ²]
A _i	Internal area of pipe, [m ²]
A _o	External area of pipe, [m ²]
B	Constant in Robertson-Stiff model similar to n, []
C	Constant in Robertson-Stiff model, correction factor, [1/s]
d	Diameter of the pipe, [m]
D	Hydraulic flow size, [m]
dr	Distance from pipe wall, [m]
dv	Fluid velocity, [m/s]
f	Friction factor, []
F	Applied force, [N]
F	Applied force, [N]
F	Tangential force, [N]
F _i	Frictional force, [N]
F _i	Weight on bit, [N]
G'	Storage modulus, [Pa]
G''	Loss modulus, [Pa]
k	Consistency index, [lbs/100ft ² /s]
L	Length of the flow line, [m]
M	Torque, [mNm]
n	Flow behavior index, []
N	Normal force, [N]
N _i	Contact force per unit length, [N/m]
P _p	Pump pressure, [Pa]
Q	Friction force, [N]
r	Radius of tube, [m]
r	Outer radius of pipe, [m]
S	Length of segment, [m]
S _i	Length of drill string segment, [m]
t	Time, [s]

$\tan \delta$	Damping factor, []
T_i	Torque at bottom, [$N \cdot m$]
T_{i+1}	Torque at top, [$N \cdot m$]
V	Volume, [ml]
v_a	Axial speed, [m/s]
w	Weight per unit length, [N/m]
w_i	Weight of drill string, [N/m]
β	Buoyancy factor, []
γ	Shear strain, [%]
γ^*	Geometric mean of shear rate, [1/s]
$\dot{\gamma}$	Shear rate, [1/s]
γ_a	Shear rate amplitude, []
γ_L	Yield point, [%]
ΔP_{pump}	Pump pressure, [bar]
ΔP_b	Pressure loss in nozzles of the drill bit, [bar]
ΔP_{tot}	Total frictional pressure loss, [bar]
ΔP_{fadc}	Pressure loss in the annular space between the wellbore and drill collar, [bar]
ΔP_{fadp}	Pressure loss in the annular space between the wellbore and the drill pipe, [bar]
ΔP_{fdc}	Pressure loss in drill collar, [Pa]
ΔP_{fdp}	Pressure loss in drill pipe, [bar]
ΔP_{fs}	Pressure loss in surface flow lines, [bar]
$\Delta P_{\text{annulus}}$	Pressure drop in annulus, [bar]
ΔS	Incremental pipe length, [m]
ΔT	Incremental torque, [$N \cdot m$]
δ	Phase shift angle, [°]
θ_x	Viscometer dial reading at x RPM, [°]
θ	Inclination of plane, [°]
θ	Inclination, [°]
θ_i	Inclination, [°]
μ	Viscosity, [cP]
μ	Coefficient of friction, []
μ_i	Coefficient of friction, []
μ_0	Coefficient of friction, []
μ_p	Plastic viscosity, [cP]

μ_a	Axial coefficient of friction, []
μ_t	Tangential coefficient of friction, []
ρ	Density of fluid, [kg/m ³]
ρ_o	Density of fluid in annulus, [kg/m ³]
ρ_i	Density of fluid in pipe, [kg/m ³]
ρ_{pipe}	Density of fluid, [kg/m ³]
τ	Shear stress, [lbf/100 ft ²]
τ^*	Geometric mean of shear stress, [lbf/100 ft ²]
τ_{yL}	Lower shear yield point, [lbf/100 ft ²]
τ_o	Yield point, [lbf/100 ft ²]
τ_a	Shear stress amplitude, [Pa]
τ_y	Yield stress, [Pa]
τ_f	Flow point, [Pa]
ϕ	Deflection angle, [mrad]
ϕ	Azimuth, [°]
ω	Angular frequency, [rad/s]

List of Abbreviations

Al	Aluminum oxide
BF	Base Fluid
CNT	Carbon nanotube
CoF	Coefficient of friction
CP	Carbopol
cP	Centipoise
ECD	Equivalent circulating density
FRDF	Flat rheology drilling fluid
GBs	Glass beads
GEL	Gel strength
GO	Graphene oxide
gpm	Gallons per minute
H-B	Herschel-Bulkley
HPHT	High pressure and high temperature
ID	Inside diameter
LS	Lignosulfonate
LSYS	Lower shear yield stress
LVE	Linear viscoelastic
MD	Measured depth
MW	Mud weight
MW	Multi-walled carbon nanotube
MWCNT	Multi-walled carbon nanotube
MWCNT-COOH	Multi-walled carbon nanotube (modified with a carboxyl group)
NP	Nanoparticle
OBM	Oil-based mud
OD	Outside diameter
Pac	Polyanionic cellulose
POOH	Pull out of hole
ppb	Pounds per barrel
ppg	Pounds per gallon
PV	Plastic viscosity
R-S	Robertson-Stiff
Ref	Reference fluid (with hydrous soda ash)
REF	Reference fluid (with anhydrous soda ash)

RIH	Run into hole
ROP	Rate of penetration
RPM	Rotation per minute
SA	Soda ash
SBM	Synthetic-based mud
SEM	Scanning electron microscope
SG	Specific gravity
Si	Silica
SWCNT	Single-walled carbon nanotube
T&D	Torque and drag
TOB	Torque on bit
TVD	True vertical depth
UiS	University of Stavanger
WBM	Water-based mud
WOB	Weight on bit
YP	Yield point
YS	Yield stress

1 Introduction

1.1 Background

One of the most important elements of a drilling operation is the drilling fluid. To ensure a safe and successful operation, it must be properly designed according to the expected wellbore conditions, as well as being maintained while drilling. As the petroleum industry has begun to explore deepwater, arctic, geothermal and extended-reach reservoirs, there is an increasing demand for drilling fluids with enhanced properties and thermal stability. This is related to the more extreme conditions and narrow operational window typically encountered in these drilling operations. Currently, oil-based drilling fluids (OBM) are more commonly applied when drilling such challenging wells because of their many favorable properties, such as increased lubricity, temperature tolerance and shale inhibition. Though, these fluids are associated with high costs and environmental concerns. Thus, increasing interest have been directed towards the development of water-based drilling fluids with the performance of OBMs [1, 2]. Previous studies have proven that the addition of certain polymers and nanoparticles could provide water-based drilling fluids with enhanced frictional, filtration and rheological properties, as well as flat rheology characteristics. The latter is an important property of bentonite fluids to prevent the flocculation of the bentonite platelets typically occurring at higher temperatures.

1.2 Problem Formulation

Water-based drilling fluids (WBM) are environmentally friendly and less expensive compared to oil-based mud. Though, its properties are known to be affected by high temperatures as bentonite flocculate and polymers degrade. Thus, the following issues will be addressed to design a drilling fluid for a cost effective, environmentally friendly and efficient drilling operation:

- Thermal stability of a bentonite/polymer hybrid water-based fluid
- Performance of nanoparticle suspensions on thermally stable fluid

1.3 Objective

The primary focus of this thesis work is to investigate the issues addressed in the problem formulation, presented in section 1.2. Both experimental work and simulation studies will be conducted with focus on the following activities:

- Formulation of bentonite/polymer hybrid fluid and rheological characterization at three temperatures (22°C, 50°C and 80°C) until flat rheology characteristics are obtained
- Modification and characterization of the flat rheology fluid with multiple nanoparticle suspensions (MWCNT-COOH, silica and aluminum oxide)
- Characterization of viscoelastic, frictional and filtration properties
- Modelling of rheological parameters
- Simulation of the hydraulics and T&D performance

1.4 Research Methods

The scope of this research work is illustrated in figure 1.1. As seen, the study is categorized into three main parts, namely; literature study, experimental work and performance study. The first part presents theory about the function of drilling fluids, rheology, viscoelasticity and tribology, as well as T&D and hydraulics. This part also deals with the description of chemicals and experimental equipment to be applied in this thesis work. This information will be applied in the analysis of the drilling fluid properties in the experimental work and simulation study. The second part of the study deals with the experimental work, which is conducted to design and characterize the flat rheology drilling fluid and nanoparticle systems. Lastly, the rheological parameters of the drilling fluid are modelled and the fluid performance is investigated through hydraulics and T&D simulations.

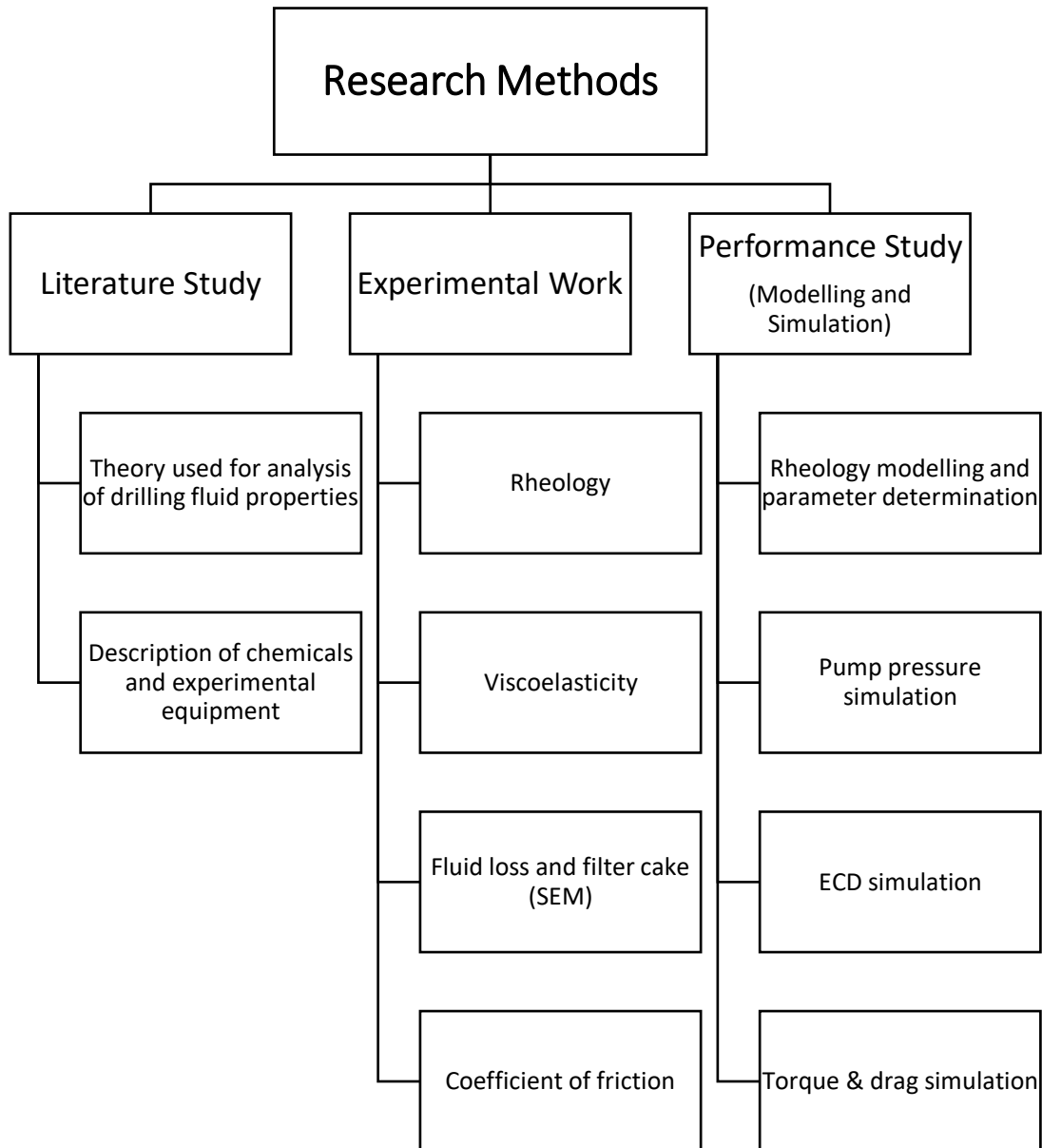


Figure 1.1: Summary of the research activities in this thesis

2 Theory

This section will describe the fundamental theory in which the experimental work, modelling and simulation study is based on. Theory regarding drilling fluids and its rheological, viscoelastic and frictional properties will be used in the characterization process, whereas knowledge about hydraulics and T&D will be needed in the simulation study.

2.1 Drilling Fluid

According to Schlumberger Oilfield Glossary [3], drilling fluids are any type of liquid or gaseous fluid, as well as mixtures of solids and liquids, that are used in drilling operations. It is often referred to as mud and serves several important functions such as: [3, 4]

- Maintaining wellbore stability and well control
- Cuttings removal
- Sealing permeable formations
- Cooling and lubricating the drill bit
- Providing information about the wellbore

In general, the drilling fluid accounts for approximately 10 % of the total tangible costs of any well construction. Having a properly designed and maintained drilling fluid can limit the cost by providing enhanced rates of penetration (ROP) and wellbore stabilization, as well as minimizing the potential for lost circulation. [5]

2.1.1 Drilling Fluid Properties

For a drilling fluid to perform said functions, it must be properly designed according to the wellbore conditions and maintained during the drilling operation [5]. Viscosity, mud weight and fluid loss are some of the most important drilling fluid properties to consider in order to ensure a safe and successful operation. Mud weight and fluid loss are described in the following subsections, whereas the rheological property known as viscosity is described in section 2.2.1.

2.1.1.1 Mud Weight

Mud weight, also known as the density of a mud, is defined as the mass per unit volume of a drilling fluid. It is an extremely important property as it controls the hydrostatic pressure exerted by the mud and thus, can prevent unwanted flow into the wellbore and collapse of the open hole or casing. The density of the mud should be selected such that the wellbore pressures are kept above and below the pore- and fracture pressure, respectively. This range is often referred to as the safe operational window and should not be exceeded in order to avoid the occurrence of lost circulation and flow of formation fluid into the wellbore. [6]

2.1.1.2 Fluid Loss

Fluid loss, also known as filtrate loss, is defined as the leakage of a drilling fluid's liquid phase into a permeable formation. Because of filtrate loss, the solid particles of a drilling fluid will accumulate on the wellbore wall, forming a solid matter known as the filter cake [7]. Whilst the thickness of the filter cake is dependent on the number of particles in the drilling fluid and the amount of fluid loss, the latter is dependent on the following: [8]

- Differential pressure between the wellbore and formation
- Porosity and permeability of the formation
- Ability of the drilling fluid to form a dense filter cake

For a water-based drilling fluid, a significant amount of fluid loss can lead to irreversible changes in its properties, such as density and rheology [9]. Moreover, the filter cake can cause differential sticking, as well as higher torque and drag during the drilling operation. Thus, fluid loss control is necessary in order to minimize the thickness and permeability of the filter cake, consequently reducing the amount of filtrate lost to the formation [8]. Fluid loss additives are typically applied for this purpose. [7]

2.1.2 Drilling Fluid Types

Due to great dependency between the drilling fluid and the success of the drilling operation, it is important to consider the type of drilling fluid that is to be used, as well as its composition, carefully. The fluid is selected based on the anticipated well conditions as well as the specific interval of the well being drilled. In addition to the technical performance, the fluids cost and its environmental impact are key factors that influence the decision. Usually, it is distinguished

between water-based mud, oil-based mud, synthetic-based mud (SBM) and pneumatic drilling fluids. [5, 10]

2.1.2.1 Water-Based Mud

Water-based mud is used in around 80 % of all the drilling operations, making it the type of drilling fluid most frequently used. Schlumberger Oilfield Glossary [11] defines water-based mud as “*a drilling fluid (mud) in which water or saltwater is the major liquid phase as well as the wetting (external) phase*”. Thus, liquids such as freshwater, seawater, brine, saturated brine or formate brine can be used as the base fluid. [5, 11]

Typically, water-based mud is divided into dispersed and non-dispersed fluids. A dispersed mud is designed such that a clay will be allowed to hydrate or expand, i.e. disperse, if present in the system. In a non-dispersed mud, however, the hydration and dispersion of the clay will be minimized. This is most commonly achieved by encapsulating the clay with a polymer to limit the amount of water available for the clay to react with. The clay can also be managed through dilution and/or flocculation. [5, 12, 13]

Compared to oil-based and synthetic-based drilling fluids, water-based mud is in general less expensive, explaining why it is so widely used. However, when drilling more demanding wells, such as HPHT, directional and horizontal wells, oil-based fluids have several favorable properties that make it the better option. Due to its environmental impact, however, oil-based drilling fluids are now being replaced by synthetic muds and WBM enhanced with nanoparticles. [5, 14, 15]

2.1.2.2 Oil-Based and Synthetic-Based Mud

Both oil-based and synthetic-based muds, also known as invert-emulsion systems, are defined as a drilling fluid where the external phase is an oil or a synthetic fluid, respectively, and the internal phase is brine. Water is typically added to improve the rheological properties of the systems, though it is not a requirement. Even though invert-emulsion muds usually have a higher unit cost, these systems are preferred to water-based muds when increased lubricity and/or reliable shale inhibition is a necessity due to the wellbore conditions. This is because of the many favorable properties they provide, such as better shale inhibition, lubrication, ROP and HPHT tolerance. [5, 16]

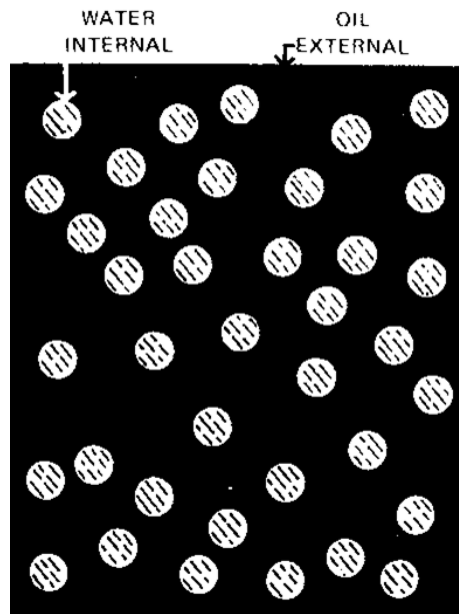


Figure 2.1: Illustration of a water-in-oil emulsion, [17]

2.1.2.3 Pneumatic Drilling Fluid

A pneumatic drilling fluid is not actually a fluid, but the application of compressed air, mist, foam or gas as a drilling fluid. Such systems are most commonly applied in situations where the formation pressures are relatively low, while the risk of formation damage and lost circulation is relatively high. In said situations, pneumatic systems are beneficial for several reasons, such as higher ROP and prevention of lost circulation and formation damage. In addition, it allows for rapid evaluation of cuttings for the presence of hydrocarbons. [5]

2.2 Rheology

Rheology is commonly defined as the science of deformation and flow of any substance, such as a solid, liquid or gas [17]. In the petroleum industry, the term primarily focuses on the flow characteristics of the fluid applied in a well, like drilling, completion and workover fluids. When considering the rheological properties of a drilling fluid, the relation between the flow rate and flow pressure is of particular interest. This is because of its influence on the fluid flow characteristics, which affects the cuttings transport efficiency as well as the circulation pressure. [5, 13, 18]

2.2.1 Rheological Properties

The flow characteristics of a fluid is typically described using certain parameters. Viscosity, μ , is perhaps the most common and is defined as a fluid's resistance to flow. Plastic viscosity, yield point and gel strength are other rheological parameters typically used to describe a fluid. These are further elaborated on in the following subsections. [19]

2.2.1.1 Plastic Viscosity

Plastic viscosity, PV, is defined as the flow resistance generated by mechanical friction within the fluid, which is induced by particle to particle, particle to fluid and fluid to fluid interactions. The unit of measurement is centipoise, cP, and its value is determined by the viscosity and particle content of the fluid. [8, 19]

2.2.1.2 Yield Point

The yield point, YP, is defined as the lowermost shear stress value required to make a sample flow. The parameter, also known as yield stress, is generated due to electrostatic attractive forces between the particles in a fluid, which cause the particles to form a stable, three-dimensional network when the fluid is at rest. As illustrated in figure 2.2, this structure begins to break down at shear stress values beyond the yield point and the material starts to flow. Thus, the yield point represents the shear stress value at which a material stops acting as a solid matter and begin to behave like a fluid [8, 20].

In the petroleum industry, the parameter is useful in order to evaluate a fluid's ability to lift cuttings out of the annulus [21]. Furthermore, yield point is dependent on the shear rate and its value typically decreases with increasing shear rate [8].

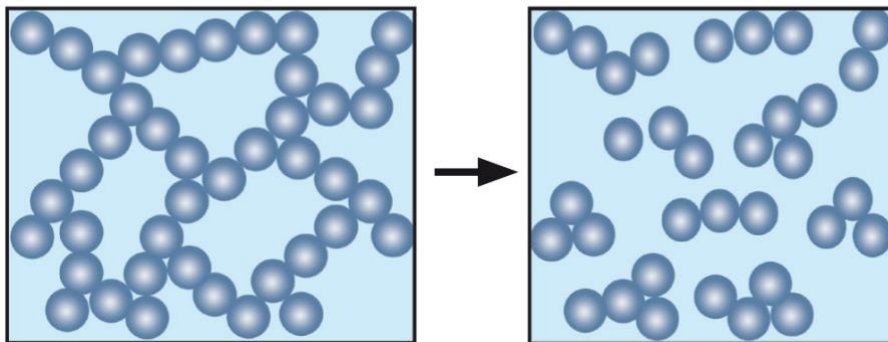


Figure 2.2: A material's structure in solid (left) and fluid state (right), [20]

2.2.1.3 Gel Strength

Gel strength is the ability of a fluid to form a gel like structure over time when kept at rest and then liquefy again when exposed to shearing. The time dependent property is also known as thixotropy and is, to some extent, a desirable characteristic of drilling fluids. This is related to the fact that a fluid's ability to provide efficient cuttings transport during drilling and support of weight material when at rest is reliant on this property. Like the yield point, gel strength is also related to the electrostatic attractive forces between particles within a static drilling fluid. The parameter is commonly denoted as GEL and is given in lb/100 ft². [8, 22]

2.2.2 Shear Stress and Shear Rate

The two concepts known as shear stress and shear rate are widely used in the petroleum industry. This is because their measurement enables mathematical description of fluid flow, making them important terms to further elaborate upon [17]. In the following subsections, the rheological parameters are defined using the two-plate model presented in figure 2.3. It is an idealized illustration showing two individual planar fluid layers of a sample. Both layers are moving in the same direction, but are displaced relative to one another as their velocity differs. [8, 20]

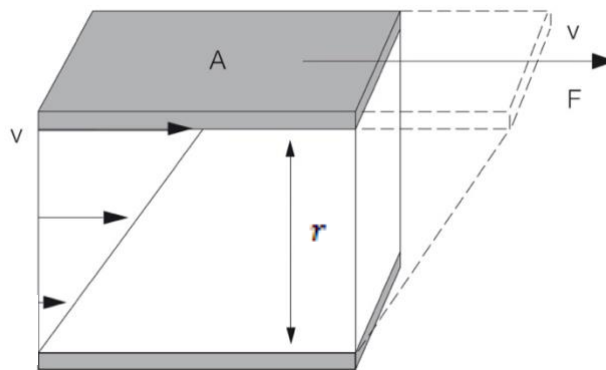


Figure 2.3: Two-plate model utilized to calculate shear rate and shear stress of a fluid, [20]

2.2.2.1 Shear Stress

Shear stress is defined as the force required to maintain a constant rate of fluid flow and corresponds to the pump pressure in the petroleum industry. The parameter describes the frictional resistance occurring between the displaced fluid layers within a fluid and can be thought of as a fluid's resistance to the applied shear rate or force. Mathematically, shear stress can be expressed as follows: [17, 19, 23]

$$\tau = \frac{F}{A} \quad (2.1)$$

Where:

- τ = Shear stress, [Pa]
- F = Applied force, [N]
- A = Surface area exposed to shear, [m²]

2.2.2.2 Shear Rate

Shear rate is defined as the velocity gradient exhibited across the diameter of fluid flow through a particular geometrical configuration, such as a pipe or annulus. In other terms, the parameter is the ratio of the velocity and distance from a tube wall, which decreases from the center line to the wall. It is expressed mathematically as shown in equation 2.2. [17, 24]

$$\dot{\gamma} = \frac{dv}{dr} \quad (2.2)$$

Where:

- $\dot{\gamma}$ = Shear rate, [1/s]
- dv = Fluid velocity, [m/s]
- dr = Distance from pipe wall, [m]

Considering fluid flow through a pipe, the shear rate is equal to zero in the middle of the pipe and increases to its maximum value at the wall. As seen in figure 2.3, this is the opposite of how the fluid velocity behaves [25]. The magnitude of shear rate is dependent on the geometrical structure, viscous properties and overall velocity of the fluid flow. [17]

2.2.3 Rotational Tests

Rotational tests are conducted to characterize the viscous behavior of a fluid and is one of the most important methods of investigating the quality of a drilling fluid. This is related to the great impact viscosity has in nearly all production stages, such as pumping mud through a pipe and the mixing process. Rotational viscometers are well suited to measure the viscosity of fluids and is perhaps the apparatus most commonly applied for this purpose. There are several

viscometers to choose between, but an OFITE Model 800 viscometer is utilized later in this thesis. In addition, an Anton Paar rheometer with a “cup and bob” setup is used to obtain the viscous behavior of certain fluids over a range of temperatures. [26]

2.2.3.1 “Cup and Bob” Setup

As mentioned, viscosity is commonly obtained using concentric cylindrical viscometers, whose “cup and bob” setup is illustrated in figure 2.4. This setup follows the Couette principle, which means that the rotor is turned at constant speed whilst measuring the angular deflection of the bob. Said angle is the viscometer dial reading and is caused by the fluid’s resistance to flow. Equipment having this set up usually have a separate cup in which the fluid is poured and then, both rotor and bob is lowered into this cup. The OFITE Model 800 viscometer is based on this principle, whereas the Anton Paar rheometer follows the Searle principle. An apparatus based on this measuring principle will have a fixed cup, in which the fluid is poured, and a rotating measuring bob. The bob is lowered into the fluid and rotates with a preset velocity whilst measuring the torque required for it to be turning against the viscous fluid. Furthermore, rotational instruments can differ in the way the torque is measured. The instruments can have either a spring or a servo motor, but this will not be further discussed in this thesis. [17, 27]

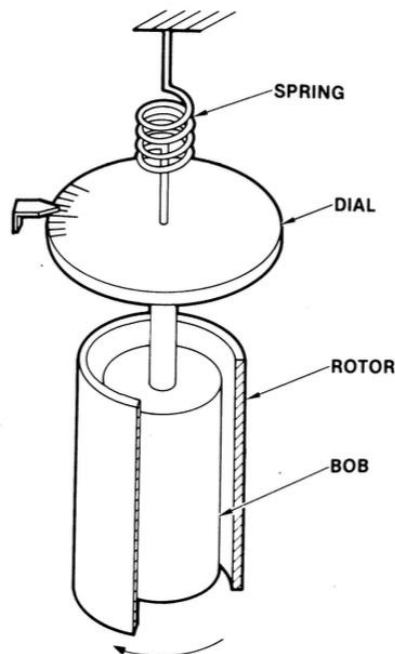


Figure 2.4: Illustration of "cup and bob" setup, [17]

2.2.3.2 Rotational Temperature Sweep

A temperature sweep is a rotational test that can be conducted using an Anton Paar MCR 302 rheometer. When performing temperature sweeps on a sample, the temperature is increased in steps, whilst the amplitude and frequency is kept constant. Hence, temperature is the only variable and its influence on the viscosity can be examined. Usually, the viscosity of a fluid decreases when exposed to heat, though for clay fluids, the viscosity typically increases with temperature [28]. The temperature in a wellbore increases with depth and is known to alter the viscosity of the applied fluid. Since both the cuttings transport and circulation pressure is dependent on the rheological properties of the fluid, evaluating the effect of temperature is extremely important in order to achieve a successful and safe drilling operation.

2.3 Rheological Models

Over the years, several mathematical models have been developed in order to describe fluids. These are called rheological models and are used to predict a drilling fluid's flow behavior. Even though the experimentally obtained data of most drilling fluids do not match these models accurately over all ranges of shear rates, one or more of the models typically provide an estimate with sufficient accuracy. [5, 29, 30]

To attain an adequate description of fluid behavior, the applied rheological model should correlate well with the observed rheological data of the drilling fluid. The accuracy of the rheological model to be applied is dependent on the fluid type of the investigated mud. Primarily, it is distinguished between two types of fluids when considering the shear stress-shear rate relation. These are known as Newtonian and non-Newtonian fluids and are further described in the following subsections [17, 30].

2.3.1 Newtonian Fluids

A fluid is described as Newtonian if its viscosity is independent of shear rate, which means that the fluid viscosity only varies with temperature or pressure. Newtonian fluids are quite simple and clean fluids which do not contain any particles larger than molecules. Water, brine, oil and gases are examples of fluids who exhibit a Newtonian behavior and obey the straight-line relationship given by the Newtonian model shown in equation 2.3. [5, 17, 31]

$$\mu = \frac{\tau}{\dot{\gamma}} \quad (2.3)$$

Where:

$\dot{\gamma}$ = Shear rate, [1/s]

τ = Shear stress, [Pa]

μ = Viscosity, [cP]

Figure 2.5 illustrates the relationship between shear stress and shear rate of Newtonian fluids. As seen, the flow resistance increases linearly with flow deformation, resulting in a straight line that runs through the origin of the diagram [29].

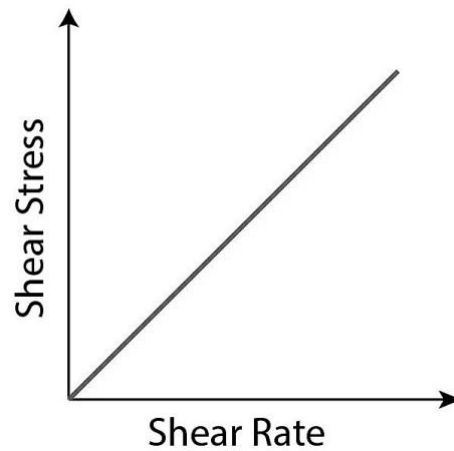


Figure 2.5: Shear stress- shear rate relation of the Newtonian Model, [32]

2.3.2 Non-Newtonian Fluids

All fluids that cannot be described by the Newtonian model are referred to as non-Newtonian. Unlike Newtonian fluids, which display liquid behavior, non-Newtonian fluids can behave both as a solid and a liquid. Most drilling fluids are non-Newtonian and exhibit a non-linear relationship between shear stress and shear rate [33]. The Newtonian model does not fit well with the typical behavior exhibited by drilling fluids and thus, non-Newtonian models must be applied. There are several rheological models which are developed to describe the flow behavior of non-Newtonian fluids. In this thesis the Bingham Plastic, Power Law, Herschel-Bulkley, Unified and Robertson-Stiff models are used to determine rheological parameters of the formulated drilling fluids. These models are further described in the following subsections.

2.3.2.1 Bingham Plastic Model

The Bingham Plastic model is widely used in the petroleum industry to describe the flow of drilling fluids. It is a two-parameter model which is characterized using the rheological parameters known as yield stress and plastic viscosity. Like the Newtonian model, Bingham Plastic fluids exhibit a linear shear stress-shear rate relationship after reaching a threshold shear stress called the yield stress. [34]

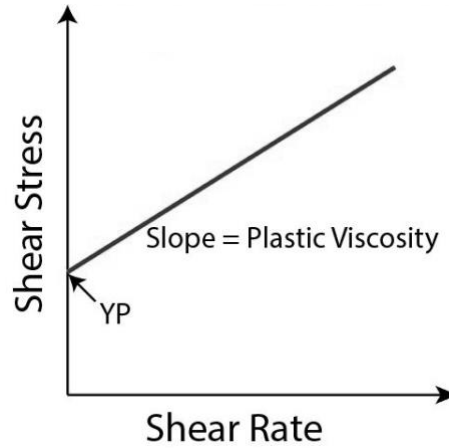


Figure 2.6: Shear stress-shear rate relation of the Bingham Plastic model, [32]

Figure 2.6 illustrates the shear stress-shear rate relationship of the model, whereas equation 2.4 presents the model mathematically using PV and YS (also known as YP). These parameters are determined from the viscometer dial readings as shown in equation 2.5 and 2.6, respectively.

$$\tau = YS + PV \cdot \dot{\gamma} \quad (2.4)$$

$$PV [cP] = \theta_{600} - \theta_{300} \quad (2.5)$$

$$YS \left[\frac{lbf}{100ft^2} \right] = \theta_{300} - PV = 2 \cdot \theta_{300} - \theta_{600} \quad (2.6)$$

Where:

- τ = Shear stress, [lbf/100 ft²]
- YS = Yield stress, [lbf/100 ft²]
- PV = Plastic viscosity, [cP]
- $\dot{\gamma}$ = Shear rate, [1/s]
- θ_{600} = Viscometer dial reading at 600 RPM, [°]
- θ_{300} = Viscometer dial reading at 300 RPM, [°]

2.3.2.2 Power Law Model

Application of the Bingham Plastic model is extremely limited by the small range of shear rates, 300-600 RPM, where it is able to describe the flow characteristics of a suited fluid precisely. Furthermore, the model assumes a linear relationship between shear stress and shear rate, which means that a fluid is assumed to exhibit constant viscosity at any shear rate. This does not reflect reality, where the viscosity tends to increase non-linearly with shear rate. The Power Law model is another rheological model which is known to provide a better description of a drilling fluid's flow characteristics. The model describes the flow characteristics of the following fluids: [25, 35]

- **n < 1:** Pseudoplastic fluids, where the viscosity declines with increasing shear rate (shear thinning)
- **n = 1:** Newtonian fluids, where the viscosity is independent of the shear rate
- **n > 1:** Dilatant fluids, where the apparent viscosity increases with shear rate (shear thickening)

The Power Law model is a two-parameter model which utilizes the parameters referred to as the consistency index, k , and flow behavior index, n . Mathematically, k and n are calculated from the viscometer dial readings as shown in equation 2.8 and 2.9, respectively, and the Power Law model is calculated as presented in equation 2.7 [35]. From the formula, it is seen that the model assumes zero yield stress.

$$\tau = k \cdot \dot{\gamma}^n \quad (2.7)$$

$$k = \frac{\theta_{300}}{511^n} = \frac{\theta_{600}}{1022^n} \quad (2.8)$$

$$n = 3.32 \log \left(\frac{\theta_{600}}{\theta_{300}} \right) \quad (2.9)$$

Where:

- τ = Shear stress, [lbf/100 ft²]
- k = Consistency index, [lbs/100 ft²/s]

- $\dot{\gamma}$ = Shear rate, [1/s]
 n = Flow behavior index, []
 θ_{600} = Viscometer dial reading at 600 RPM, [°]
 θ_{300} = Viscometer dial reading at 300 RPM, [°]

It is to be noted that drilling fluids seldom acts as dilatant fluids [25]. Hence, the shear stress-shear rate relation of the model for shear thinning fluids is shown in figure 2.7.

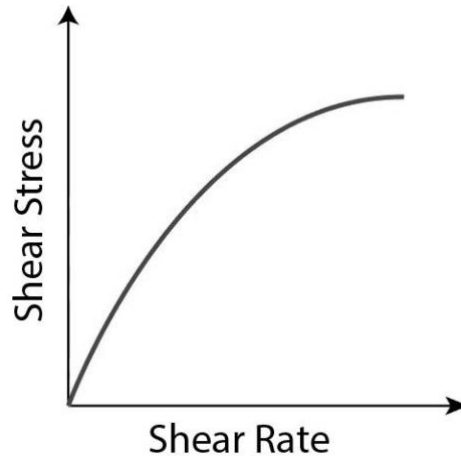


Figure 2.7: Shear stress-shear rate relation of the Power Law model, [32]

2.3.2.3 Herschel-Bulkley Model

The Herschel-Bulkley model is a yield modified Power Law model, which means that it considers the yield stress usually exhibited by drilling fluids. Since the model considers the force required to initiate flow and describes the shear thinning properties of a fluid, the model is more realistic and provide a better description of a drilling fluid's rheological properties. Hence, the model is preferred to the Bingham Plastic and Power Law models. As seen in figure 2.8, the shear stress-shear rate relation is similar to that of the Power Law model, whilst the inclusion of the yield stress is analogous to the Bingham Plastic model. [35, 36]

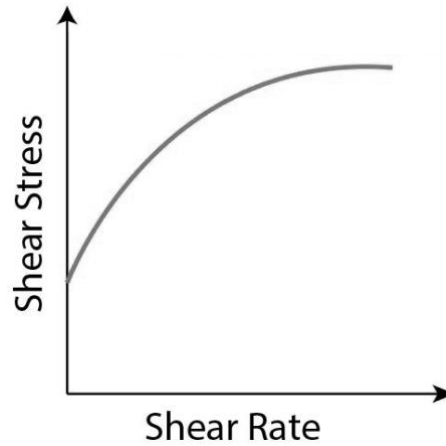


Figure 2.8: Shear stress-shear rate relation of the Herschel-Bulkley model, [32]

Equation 2.10 presents the H-B model mathematically, where it is seen that the three parameters yield stress, k and n are used to describe the flow characteristics of a fluid. Both the consistency- and flow behavior index are determined graphically using curve fitting between the measured data and the model. The yield stress, τ_y , and the geometric mean of shear rate, $\dot{\gamma}^*$, are calculated as shown in equation 2.11 and 2.12, respectively. The τ^* parameter is determined with interpolation using the shear stress values corresponding to the $\dot{\gamma}^*$ parameter. The latter will be equal to ~ 72.25 1/s when the lowest and highest measuring speeds are 3 RPM and 600 RPM. [35]

$$\tau = \tau_y + k \cdot \dot{\gamma}^n \quad (2.10)$$

$$\tau_y = \frac{\tau^{*2} - \tau_{min} \cdot \tau_{max}}{2\tau^* - \tau_{min} - \tau_{max}} \quad (2.11)$$

$$\dot{\gamma}^* = \sqrt{\dot{\gamma}_{min} \cdot \dot{\gamma}_{max}} = \sqrt{5.11 \cdot 1021.38} \approx 72.25 \text{ s}^{-1} \quad (2.12)$$

Where:

- τ = Shear stress, [lbf/100 ft²]
- k = Consistency index, [lbs/100 ft²/s]
- $\dot{\gamma}$ = Shear rate, [1/s]
- n = Flow behavior index, []
- τ_y = Yield stress, [lbf/100 ft²]

2.3.2.4 Unified Model

Like the H-B model, the Unified model is also a modified Power Law model. Both describe fluid flow with the same three-parameter equation, which is shown in equation 2.10. In fact, the Unified model is a simplification of the more complex H-B model and was developed with the intent of providing front-line drilling and mud engineers with a practical, yet accurate, model for field use. The main difference between the two models is in the estimation of the three parameters yield stress, consistency index and flow behavior index. [37]

Firstly, the Unified model estimates the yield stress by using the lower shear stress dial readings as shown in equation 2.14. This parameter is referred to as the lower shear yield point, τ_{yL} , and replace the yield stress value, τ_y , previously applied in the H-B model. The modified equation is presented in equation 2.13. Furthermore, the k and n parameters are determined using equations for either pipe or annular flow, which are shown in equations 2.15-2.18. The letters “a” and “p” are used to denote whether the equation is applied for annular or pipe flow, respectively. [38]

$$\tau = \tau_{yL} + k \cdot \dot{\gamma}^n \quad (2.13)$$

$$\tau_{yL} = (2 \cdot \theta_3 - \theta_6) \cdot 1.066 \quad (2.14)$$

Calculation of consistency index and flow behavior index for annular flow:

$$n_a = 3.32 \cdot \log \left(\frac{2 \cdot \mu_p + \tau_y - \tau_{yL}}{\mu_p + \tau_y - \tau_{yL}} \right) \quad (2.15)$$

$$k_a = 1.066 \cdot \frac{\mu_p + \tau_y - \tau_{yL}}{511^n} \quad (2.16)$$

For pipe flow:

$$n_p = 3.32 \cdot \log \left(\frac{2 \cdot \mu_p + \tau_y}{\mu_p + \tau_y} \right) \quad (2.17)$$

$$k_p = 1.066 \cdot \frac{\mu_p + \tau_y}{511^n} \quad (2.18)$$

Where:

- τ = Shear stress, [lbf/100 ft²]
- τ_{yL} = Lower shear yield point, [lbf/100 ft²]
- k = Consistency index, [lbs/100 ft²/s]
- $\dot{\gamma}$ = Shear rate, [1/s]
- n = Flow behavior index, []
- θ_6 = Viscometer dial reading at 6 RPM, [°]
- θ_3 = Viscometer dial reading at 3 RPM, [°]
- μ_p = Bingham plastic viscosity (PV), [cP]
- τ_y = Bingham yield point (YP), [lbf/100 ft²]

2.3.2.5 Robertson-Stiff Model

In 1976, Robertson and Stiff published an SPE journal paper proposing an improved mathematical model describing the shear stress-shear rate relation of drilling fluids and cement slurries [39]. This rheological model is known as the Robertson-Stiff model and has a more general approach of describing a fluid's rheological behavior. The basic equation of the model is given as follows: [38]

$$\tau = A(\dot{\gamma} + C)^B \quad (2.19)$$

The R-S parameters denoted as A and B resembles the k and n parameters of the Power Law model, while C is a correction factor to the shear rate. The term $(\dot{\gamma}+C)$ can be thought of as the effective shear rate, where C can be calculated as shown in equation 2.20. The geometric average of the shear stress, τ^* , is determined using equation 2.21 and thereafter, the corresponding shear rate, $\dot{\gamma}^*$, is obtained using interpolation [38]. The yield stress, τ_0 , of the R-S model is obtained by setting the shear rate equal to zero and is given in equation 2.22. [35]

$$C = \frac{\dot{\gamma}_{min} \cdot \dot{\gamma}_{max} - (\dot{\gamma}^*)^2}{2 \cdot \dot{\gamma}^* - \dot{\gamma}_{min} - \dot{\gamma}_{max}} \quad (2.20)$$

$$\tau^* = \sqrt{\tau_{min} \cdot \tau_{max}} \quad (2.21)$$

$$\tau_0 = AC^B \quad (2.22)$$

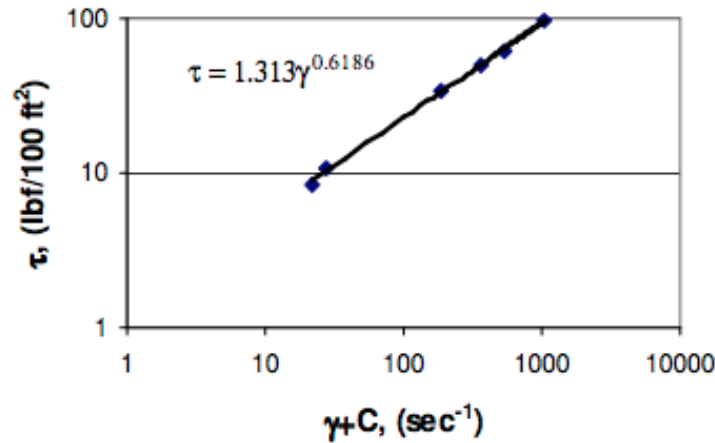


Figure 2.9: Example of log-log plot used to obtain A and B parameters for the R-S model, [38]

Both A and B can be obtained from a log-log diagram displaying the logarithmic form of equation 2.19, which is given in equation 2.23. As seen in figure 2.9, the logarithmic form of the model will plot a straight line in a log-log diagram. When plotting the shear stress, τ , versus the effective shear rate, $(\gamma+C)$, B and A are obtained as the slope and the intersection at which $(\gamma+C)$ is equal to one, respectively. The paper published by Robertson and Stiff in 1976 also presents equations which can be applied to obtain the A and B parameters without plotting. Though, these are not further elaborated on in this thesis. [39]

$$\log \tau = \log A + B \log(\dot{\gamma} + C) \quad (2.23)$$

2.4 Flat Rheology – Temperature Stable System

It is well known that temperature and pressure increases with varying gradients towards the center of the Earth. Hence, the temperature and pressure in a wellbore are also changing with depth, influencing the performance of equipment and fluids applied in any operation conducted below the surface. In this thesis, however, the focus is put on drilling fluids and the effect of temperature on its rheological properties.

The rheological properties of drilling fluids are crucial parameters to consider during an operation, especially when drilling deepwater, HPHT and extended-reach wells. This is due to the more extreme conditions and the narrow safe operational window typically encountered in

such wells. Oil-based drilling fluids are almost exclusively applied in said drilling operations due to providing improved temperature stability, as well as having the ability to be applied in wellbores with a narrow operational window. Companies performing complex drilling operations, especially those with high temperature bottom-hole conditions, have expressed a desire for the development of drilling fluids with minimal temperature sensitivity of the flow properties [40, 41]. This have brought forth the concept known as flat rheology, which is used to describe fluids having thermally independent rheological properties. [42]

Flat rheology drilling fluids (FRDF) have been used for years and has shown high performance in many application areas such as arctic drilling and high angle wells, in addition to those already mentioned. The FRDFs provide efficient hole cleaning and high rates of penetration, in addition to the temperature stable rheological profile. Moreover, the stable fluids have aided in efficient control of the ECD and thus, reduced loss of drilling fluids due to exceeding the fracture gradient. However, some aspects are still limiting the application of the fluids and the flat rheology properties can still be influenced by uncontrollable parameters and phenomena in the wellbore. This could be salinity effects, changes in the rheological modifier concentration and interaction between the rheological modifier additives and cuttings, to mention a few. [42-44]

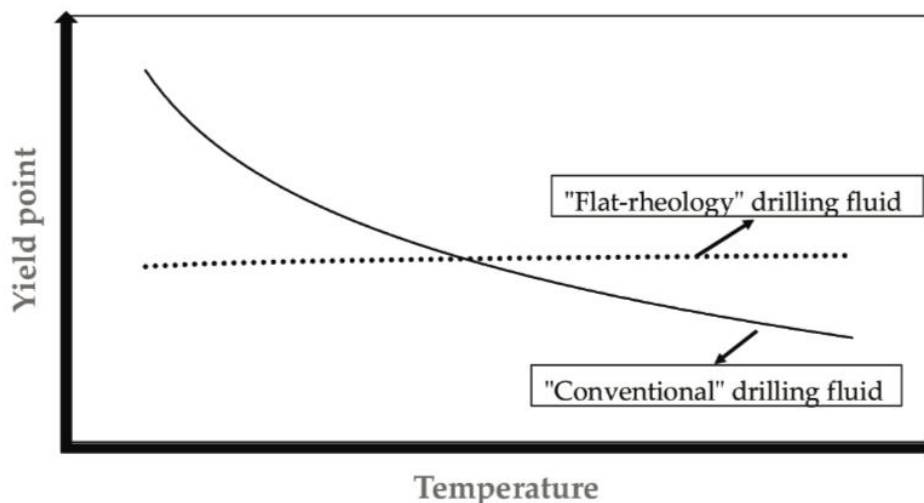


Figure 2.10: Typical rheological behavior of conventional and flat rheology drilling fluids, [43]

Figure 2.10 display the yield stress as a function of temperature for both a conventional and a flat rheology drilling fluid. The yield stress, 6 RPM and 3 RPM viscometer dial readings are typically considered in relation to temperature stability since they are influenced by both physical and chemical interactions [42]. Later in this thesis, the temperature stability of the formulated drilling fluids is investigated by considering the Bingham yield stress, which is calculated from the viscometer dial readings obtained at 22°C, 50°C and 80°C.

2.5 Clay Particle Associations

Clays are usually added to water-based drilling fluids to increase its viscosity, gel strength and yield point, as well as decreasing the fluid loss. There are several types of clay, but montmorillonite, which is applied in this thesis, is the most commonly used due to its ability to form a more homogeneous mixture with water. Montmorillonite, usually referred to as bentonite, is highly reactive and when suspended in liquids the particles are subjected to repulsive and attractive forces. Figure 2.11 illustrates how these forces act on the planar surfaces and edges of the clay particles. The drilling fluid properties will depend strongly on how these forces are distributed in the mixture, whilst the distribution of the forces is determined by the type of electrolytes present and the pH. Thus, the properties of a drilling fluid can be controlled with additives, such as soda ash, lignosulfonate and carbopol. [17]

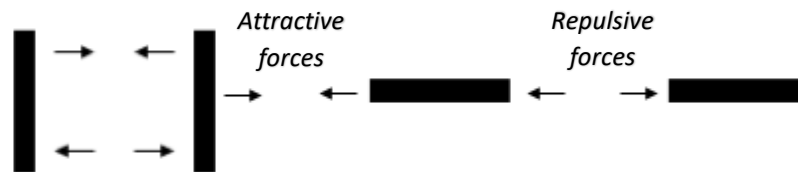


Figure 2.11: Forces acting on clay particles suspended in a liquid, [17]

There are four possible equilibrium states that can exist when clay particles are mixed with fluid systems. As mentioned, the particle association will depend on the chemical environment, i.e. the type, concentration and surface chemistry of the additives. The particle associations are illustrated in figure 2.12 and will be further described in subsections 2.5.1-2.5.4. [8, 17]

	Flocculated	Deflocculated
Aggregated		
Dispersed		

Figure 2.12: Arrangement of clay particles in drilling fluids, [8]

2.5.1 Flocculated System

A fluid system is considered to be flocculated when weak mechanical forces create clusters of particles as illustrated to the left in figure 2.12. Accumulation of clay particles is due to a net electrostatic attractive force between the particles causing either end-to-end, surface-to-surface or end-to-surface bonds. In terms of fluid properties, flocculation will provide higher viscosity, yield stress and fluid loss. [8]

2.5.2 Deflocculated System

Deflocculation is caused by a net electrostatic repulsive force between the particles in a fluid system. As shown to the right in figure 2.12, the clay particles repel each other due to having the same electric charge. According to Strand [8], a completely deflocculated system can only be obtained by adding chemicals which will neutralize the positive charges of the particles. Later in this thesis, lignosulfonate will be used to deflocculate a drilling fluid system to reduce the yield strength of the solution. Both fluid loss and yield stress values will be low in deflocculated systems. [8]

2.5.3 Aggregated System

A fluid is aggregated when several single particles binds together to form aggregates as seen in the top half of figure 2.12. Aggregates can essentially be thought of as a deck of cards since their crystal structure consists of several flakes stacked together. The number of particles and thus also the particle surface, is reduced when a drilling fluid is in an aggregated state. Typically, the apparent and plastic viscosities of aggregated fluids will be low, while the fluid loss values will be higher. [8]

2.5.4 Dispersed System

As seen in the lower half of figure 2.12, a system is dispersed when there are no aggregates present. Both flocculated and deflocculated systems can be dispersed by splitting the aggregates into single clay particles, which is achieved by generating repulsive forces between them. This means that clay particles may have both negative and positive charges depending on the pH of the system. Typically, a bentonite system which is both dispersed and deflocculated will be favorable. [8]

2.6 Viscoelasticity

Viscoelasticity is described as a property of materials who exhibit both viscous and elastic behavior when subjected to shear forces. As mentioned, viscosity is defined as a fluid's resistance to flow when put into motion and is induced due to internal friction between molecules and particles flowing within the fluid [20]. Elasticity, however, is a solid material's ability to return to its original shape and size when the forces causing deformation are removed [45]. The viscous and elastic portion is known to behave according to Newton's and Hooke's law respectively, which means that a viscoelastic material can act both as a fluid and as a solid depending on their physical behavior. [20, 28]

In regard to drilling fluids, viscoelasticity is a desired property because it provides the formation of a gel structure when a fluid is at rest or experience shear flow. During static conditions, the gel structure prevents solid particles from settling, while at dynamic conditions, it will enhance a fluid's capacity to transport cuttings and reduce dynamic sag. Furthermore, the gel structure formation is helpful towards keeping the drilling fluid from flowing into the formation. Thus, information about a drilling fluid's viscoelastic properties is of importance to evaluate its gel structure and strength, barite sag, hydraulic modelling and suspension of solids. [46]

2.6.1 Oscillatory Tests

Viscoelastic properties of a material can be investigated by performing oscillatory tests. In this thesis, such experiments will be conducted using an Anton Paar MCR 302 rheometer with rotational oscillation. Figure 2.13 illustrates the two-plates model, which is commonly used to describe oscillatory shear tests [20]. The model is valid under the assumption that the sample has contact with both plates without experiencing any wall-slip effects, as well as being deformed homogeneously. [28]

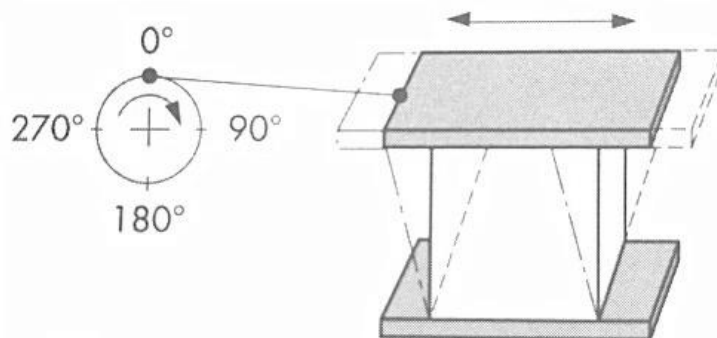


Figure 2.13: Illustration of the two-plates model for an oscillatory test, [28]

In the two-plates model, a sample is placed between two plates where one is movable and the other remains stationary. Typically, the lower plate remains in place and the upper plate moves. As illustrated to the left in figure 2.13, the movement of the upper plate is due to rotation of the drive wheel and causes the sample to be sheared. During the shearing process, the deflection of the sample is measured and evaluated as shear strain, while the counterforce required to keep the lower plate stationary is measured and evaluated as shear stress. As seen in figure 2.14, this results in two time-dependent sine curves, one for the preset shear strain and another for the resulting shear stress. However, if the preset shear strain a sample is exposed to is too large, the resulting shear stress curve would not be sinusoidal due to destroying the inner structure of the sample. [20]

2.6.2 Approaches to Measuring Viscoelastic Behavior

There are four different oscillatory tests which are commonly conducted to measure the viscoelastic behavior of a sample. The four tests are as follows: [28]

- Amplitude sweep
- Frequency sweep
- Time sweep
- Temperature sweep

In this thesis, oscillatory amplitude sweeps are performed and therefore, only this test will be further described in the following subsection.

2.6.2.1 Viscoelastic Parameters of Amplitude Sweeps

Shear Stress and Shear Strain

Shear stress and shear strain are denoted as τ and γ , respectively. Oscillatory tests results in two sinusoidal curves known as the preset shear strain and resulting shear stress curves. These are described by equation 2.24 and 2.25, respectively. [46]

$$\gamma(t) = \gamma_a \cdot \sin(\omega t) \quad (2.24)$$

$$\tau(t) = \tau_a \cdot \sin(\omega t + \delta) \quad (2.25)$$

Where:

- γ_a = Shear rate amplitude, []
- τ_a = Shear stress amplitude, [Pa]
- t = Time, [s]
- ω = Angular frequency, [rad/s]
- δ = Phase shift angle, [°]

Furthermore, the equations above can be expanded and collected such that shear stress is expressed in terms of shear strain. At first, equation 2.25 is expanded using the sum formula for sine, resulting in equation 2.26. This equation is further multiplied with γ_a/γ_a to obtain equation 2.27. Finally, equation 2.28 is constructed by applying the expressions for storage and loss modulus. [46]

$$\tau(t) = \tau_a[\sin(\omega t) \cos \delta + \cos(\omega t) \sin(\delta)] \quad (2.26)$$

$$\tau(t) = \gamma_a \left[\left(\frac{\tau_a}{\gamma_a} \cos \delta \right) \sin(\omega t) + \left(\frac{\tau_a}{\gamma_a} \sin \delta \right) \cos(\omega t) \right] \quad (2.27)$$

$$\tau(t) = [G' \sin(\omega t) + G'' \cos(\omega t)] \quad (2.28)$$

The Phase Shift Angle

The phase shift angle, sometimes referred to as the loss angle, is defined as the offset between the preset shear strain and resulting shear stress curves plotted versus time. When performing an oscillatory test, the curves are sinusoidal and when testing a viscoelastic material, the resulting strain curve will always have some delay compared to the preset stress curve. This is illustrated in figure 2.14, where the red curve is the preset shear strain and the blue curve is the resulting shear stress. As seen, the phase shift angle is denoted as δ and is always between 0° and 90° . [20, 28]

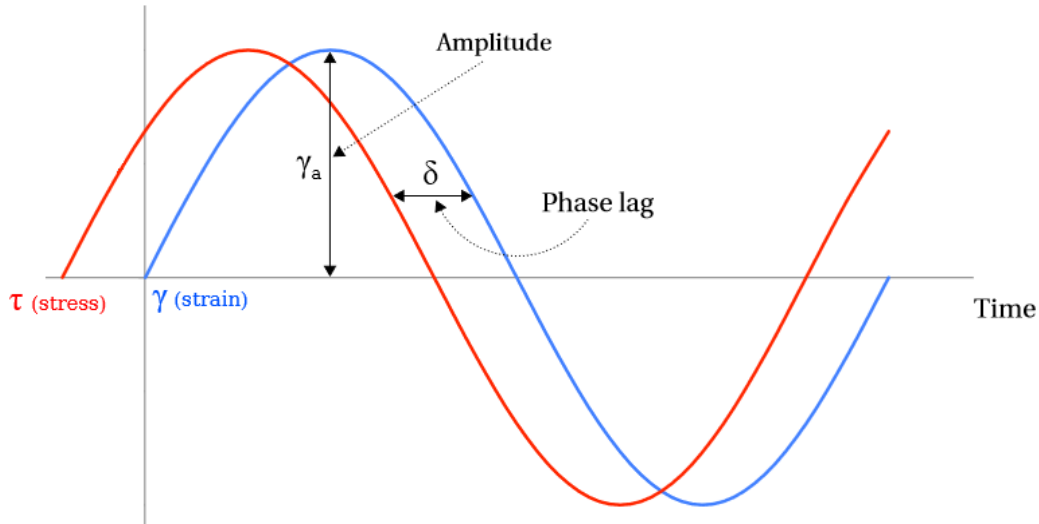


Figure 2.14: Plot of the preset shear strain, γ , and resulting shear stress, τ , curves versus time, [47]

The Storage Modulus

Storage modulus is usually denoted as G' and is given in pascal. The parameter represents the elastic portion of viscoelastic behavior and is a measure of the energy stored in a deformed material, i.e. a material experiencing shear. The unused deformation energy stored in the material is what drives it to return to its original size and shape upon release of the load causing the deformation [20]. The storage modulus can be expressed in terms of cosine as follows: [28]

$$G' = \frac{\tau_a}{\gamma_a} \cos \delta \quad (2.29)$$

The Loss Modulus

Similar to the storage modulus, pascal is also the unit of loss modulus. The parameter is denoted as G'' and represents the viscous portion of viscoelastic behavior. Loss modulus is a measure of the deformation energy being used by a deformed material and upon release of the load causing deformation, this energy is lost [28]. It has been used to change the material's structure and is completely spent by the internal friction developed when flowing [20]. The loss modulus can be expressed in terms of sine as follows: [28]

$$G'' = \frac{\tau_a}{\gamma_a} \sin \delta \quad (2.30)$$

The Loss Factor

The loss factor, also known as the damping factor, is given by equation 2.31. As seen, the parameter is calculated as the ratio between loss modulus and storage modulus, i.e. the viscous and elastic portion of viscoelastic behavior. Like the phase shift angle, the damping factor can also be used to describe the behavior of a deformed material. A material behaves ideally elastic and ideally viscous when $\tan \delta$ is zero and infinitely large, respectively. At a damping factor equal to one, the viscous and elastic portions of the viscoelastic behavior are exactly balanced. This is also presented in table 2.1. [28]

$$\tan \delta = \frac{G''}{G'} \quad (2.31)$$

2.6.2.2 Amplitude Sweep

Amplitude sweeps are oscillatory tests which are performed at various amplitudes while keeping the frequency, ω , and temperature constant. As illustrated in figure 2.15, the amplitude is increased in steps and kept constant for a certain period of time at each step [20]. In general, amplitude sweep tests are conducted to determine the upper limit of the linear viscoelastic range, also referred to as the LVE range [28]. Furthermore, the test can be used to determine the gel strength, dynamic yield point and the structural stability of a sample. [46]

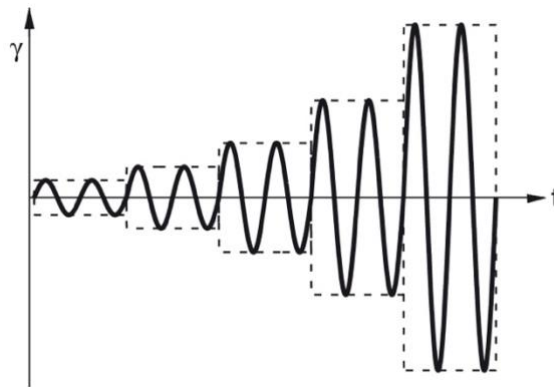


Figure 2.15: The preset of an amplitude sweep with five steps of increasing the amplitude, [20]

Viscoelastic materials are time-dependent and therefore, the particular response of a sample will depend on how fast or slow an experiment is conducted compared to the natural time of the material. Typically, a sample will appear as viscous rather than elastic when an experiment is relatively slow, while it appears as elastic rather than viscous when the experiment is relatively fast [46].

Figure 2.16 illustrates a typical measuring result of an amplitude sweep test. Initially, it is seen that the sample, whose internal structure is not yet broken, is exposed to small strains such that its deformation is linear viscoelastic. Thereafter, the strain is increased until the sample's deformation is irreversible. At this point, a critical strain has been reached and the deformation will go from being linear to non-linear viscoelastic [46]. At strains above the limiting value, which is denoted as γ_L , the storage and loss modulus curves will begin to deviate from the constant plateau they have shown up until this point and consequently, the LVE range is exceeded. Depending on the structural character of the sample, the storage modulus could be greater than the loss modulus and vice versa. Furthermore, it would also determine whether the two curves will have a crossover point or not. Below, the amplitude sweep of a sample showing a gel or solid like character is illustrated to the left, while that of a liquid is illustrated to the right. [28]

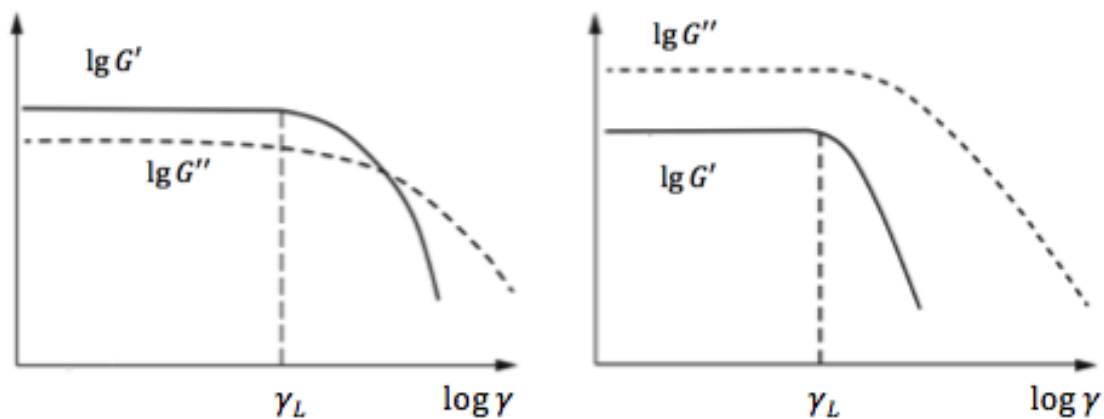


Figure 2.16: Illustration of the result from a strain amplitude sweep test, [28]

However, the storage and loss modulus curves will not always slope downwards with increasing deformation as seen in figure 2.16. In some cases, the loss modulus shows a peak after reaching the upper limit of the LVE range as illustrated in figure 2.17. The increasing loss modulus indicates that only parts of the internal structure of a sample is irreversibly deformed at first. This is because the deformation energy being used up by the sample before breaking its internal structure is indeed increasing [28]. At first, micro cracks will appear within the sample as the loss modulus increases. Thereafter, when exceeding the maximum peak of the curve, a macro crack develops and at the crossover point, the entire sample ruptures. At that time, the viscous portion of the viscoelastic behavior overcomes the elastic one [48]. The occurrence of a G'' -peak might be due to the following: [28]

- Relative motion between molecules
- Side chains or end-pieces of chains are flexible
- Long network bridges
- Single particles which are mobile
- Unlinked or otherwise unfixed agglomerates or superstructures in the network

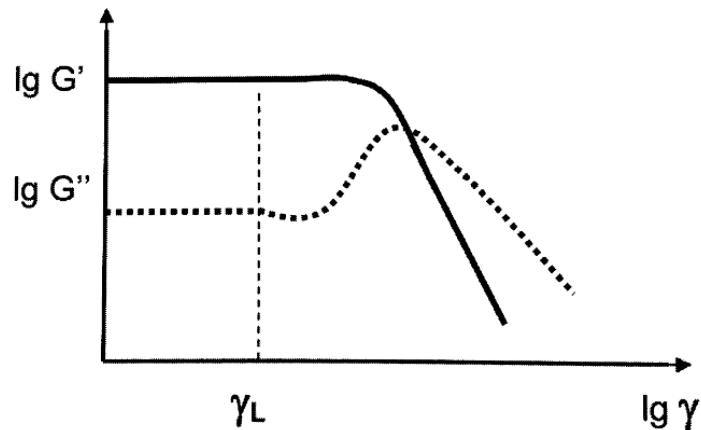


Figure 2.17: Illustration of a strain amplitude sweep result showing a G'' -peak, [28]

Amplitude sweeps are typically used to define the LVE range, as well as evaluating the storage and loss modulus curves. However, the measuring results can also be used to determine the yield point and flow point of a sample. Regardless of whether the amplitude sweep is strain controlled or stress controlled, these values are obtained using a diagram with shear stress plotted on the x-axis. As illustrated in figure 2.18, the yield point defines the upper limit of the LVE range and the flow point is obtained at the crossover point between the storage and loss modulus curves. The yield point and flow point are denoted as τ_y and τ_f , respectively. [48]

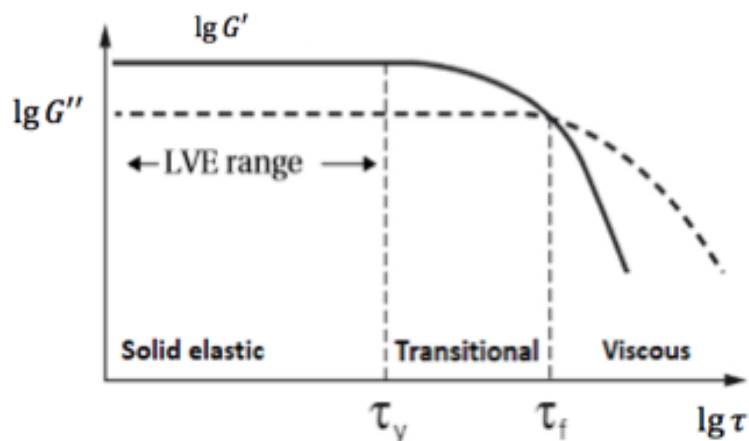


Figure 2.18: Amplitude sweep result presented with shear stress plotted on the x-axis, [28]

In figure 2.16, the sample exhibit viscoelastic gel or solid behavior when the storage modulus is greater than the loss modulus, i.e. when the elastic behavior dominates the viscous one. At the flow point, G' and G'' are balanced and the sample shows a behavior which is in the borderline between liquid and gel-like. Furthermore, the sample exhibit viscoelastic liquid behavior when the viscous portion is greater than the elastic portion, i.e. G'' is greater than G' . [28]

As seen in table 2.1, a material experiences viscoelastic behavior when in the transition zone between being ideally viscous and ideally elastic. It is observed that a material is perfectly elastic and perfectly viscous when the phase shift angle, δ , is equal to 0° and 90° , respectively. At an angle of 45° , also called the flow point, the material has equal portions of viscous and elastic properties. [28]

Table 2.1: Relationship between material behavior and phase shift angle, δ , [28]

Ideally viscous flow behavior	Viscoelastic liquid behavior	50/50 ratio between viscous and elastic portions	Viscoelastic gel or solid behavior	Ideally elastic behavior
$\delta = 90^\circ$	$90^\circ > \delta > 45^\circ$	$\delta = 45^\circ$	$45^\circ > \delta > 0^\circ$	$\delta = 0^\circ$
$\tan \delta \rightarrow \infty$	$\tan \delta > 1$	$\tan \delta = 1$	$\tan \delta < 1$	$\tan \delta \rightarrow 0$
$G' \rightarrow 0$	$G'' > G'$	$G' = G''$	$G' > G''$	$G'' \rightarrow 0$

2.7 Tribology and Friction

Tribology is commonly defined as the science of interactive surfaces in relative motion and includes the study of friction, wear and lubrication [49]. The force limiting the sliding or rolling of one surface over another is known as friction, whereas the removal of material from the surface of one object by a contacting body is known as wear. Lubrication, on the other hand, is the action of reducing the friction and wear between sliding surfaces. This is achieved by applying lubricants into the interface of the moving surfaces. [50]

2.7.1 Definition of the Coulomb Model and the Coefficient of Friction

The two first laws of friction were established by Guillaume Amontons in 1699, while Charles Augustin de Coulomb derived the third one after studying static and kinetic friction. The three laws of friction are as follows: [51]

1. The force of friction is directly proportional to the applied load.
2. The force of friction is independent of the apparent area of contact.
3. Kinetic friction is independent of the velocity.

To introduce Amontons work to mechanics, Antoine Parent defined the relation shown in equation 2.32. The inclination of the plane, tangential- and normal force are denoted as θ , F and N , respectively. [51]

$$\tan \theta = \frac{F}{N} \quad (2.32)$$

Euler later proved that the coefficient of friction, μ , could be defined using the following relation: [51]

$$\mu = \tan \theta \quad (2.33)$$

The combination of equation 2.32 and 2.33 leads to the definition commonly used to determine the coefficient of friction today, i.e. as a ratio between a friction force and normal force applied to the interactive surfaces. The relation is shown in equation 2.34, where “i” will denote whether the friction is static or kinetic, and F_i is the frictional force. [51]

$$\mu_i = \frac{F_i}{N} \quad (2.34)$$

As seen, friction can be characterized as either static or kinetic. When the two surfaces are not moving relative to each other, the resistance force is known as static friction. In contrast, the kinetic friction is the force limiting the sliding or rolling of two surfaces. Figure 2.19 illustrates how the static and kinetic friction typically behaves as a function of time. [51]

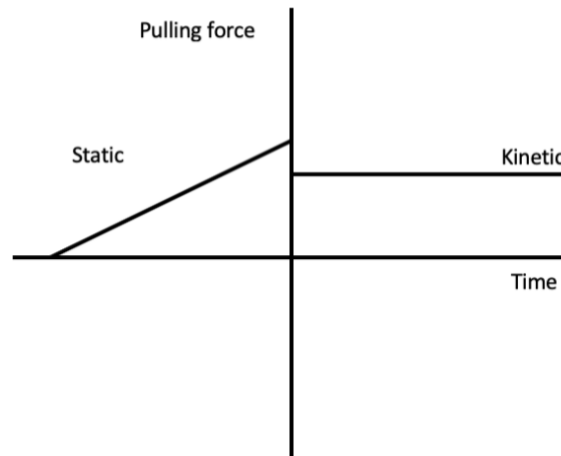


Figure 2.19: Typical behavior of static and kinetic friction as a function of time, [51]

In the petroleum industry, the well friction is typically analyzed using the Coulomb friction model. This is a simple one-parameter model which neglects the impact of temperature. By rearranging the parameters of equation 2.34, the model can be written as shown in equation 2.35, where the friction force is denoted as Q . [51]

$$Q = \mu \cdot N \quad (2.35)$$

Even though the simple one-parameter model is applied, the environment of which the coefficient of friction is obtained should be included when presenting its values as it can be influenced by many factors. Some examples of factors contributing to altered values are surface roughness, applied load, humidity, temperature, viscosity and speed. [51]

2.7.2 Application of Friction and Lubrication in the Industry

Lubricants are given much attention regarding development and testing to achieve further improvement of the substance [50]. This is related to the fact that many industries, amongst those the petroleum industry, benefit from the considerable savings in energy gained by reducing the friction and wear. During an operation, the presence of excessive friction can damage the materials directly or indirectly due to generation of heat. Moreover, the lifetime of the applied components is greatly dependent on their resistance to wear. Tribology studies are therefore of importance as the main outcomes of such measurement are the coefficient of friction and wear rate [52].

Friction plays a central role in the petroleum industry and the ability to predict the frictional loads in the wellbore is beneficial in regard to phases such as well planning [51, 53]. As drilling operations are becoming more complex with extended-reach drilling and deeper targets, increasing friction have become a major limiting factor concerning further development. By reducing wellbore friction, higher rates of penetrations can be applied since the effect of mechanical wear and drag forces are reduced [2, 51, 54]. Increasing the duration of which the applied components can be utilized and improving drilling performance can ultimately lead to reduced costs, making the coefficient of friction a vital parameter [55]. Later in this thesis, the coefficients of friction of the nanoparticle fluids are measured using a CSM tribometer.

2.8 Torque and Drag Modelling

Prediction of frictional resistance in the wellbore is primarily beneficial in the planning phase of a well. First off, deep and highly deviated wells can be planned in such a manner that torque and drag is minimized. Thereafter, the most suitable well path can be selected using torque and drag as criteria. In addition, improved drill string techniques and components, which takes the additional forces into account, can be applied if needed. Thus, knowledge about friction is highly valuable to ensure a successful drilling operation and reaching target depth. [53]

Torque and drag is present to some extent in all drilling operations and their magnitudes are normally related as both occur due to interaction between pipe and formation. Consequently, excessive torque and high drag forces typically occur simultaneously. The parameters tend to be more problematic in extended-reach drilling where very deep and highly deviated wells are designed. In directional wells, sliding friction is considered the main source of torque and drag, although there are several reasons to why the parameters can be excessive. These are listed below and are primarily associated with troublesome conditions in the wellbore. [53, 56]

- Sliding friction
- Key seats
- Sloughing hole
- Differential sticking
- Poor hole cleaning
- Tight-hole conditions
- Dogleg severity

- Hole instabilities [57]

A torque and drag model, that is perhaps the only “standard” model in use today, was first introduced by Johancsik et al in 1984, though Sheppard et al put the model in a more mathematical and standard form in 1987. Since then, the model has been used extensively in the field and for well planning due to its simplicity and general availability. In fact, it is the model in which most of the commercial simulation software’s are based on. Amongst those are the Halliburton Landmark’s WellPlan™ software, which is used to perform torque and drag simulations later in this thesis. However, the model neglects the bending stiffness and is therefore a so called “soft-string” model. Even though the model is thought to only approximate real drill string behavior, experience have shown that it usually works well in the field. [58-60]

2.8.1 Drag

Drag is an additional force occurring mainly due to the frictional resistance generated by interaction between the drill string and the wellbore. The force is experienced in addition to the weight of the freely rotating drill string when tripping in or out of the hole.

It is desirable to attain a smooth well path during drilling and this is particularly important in order to successfully complete long-reach wells. However, this is seldom the reality as both inclination and azimuth often change continuously during drilling [61]. A curved drill string and a free body diagram of its segments is presented in figure 2.20. This figure shows that the change in length of a pipe segment can be caused by thermal, hydrostatic and fluid flow shear forces, in addition to the tensile (+) or compressive (-) load applied at the top and bottom. By balancing the vector sum of the axial weight, net force and friction force, a first order differential force can be presented as shown in equation 2.36. [62]

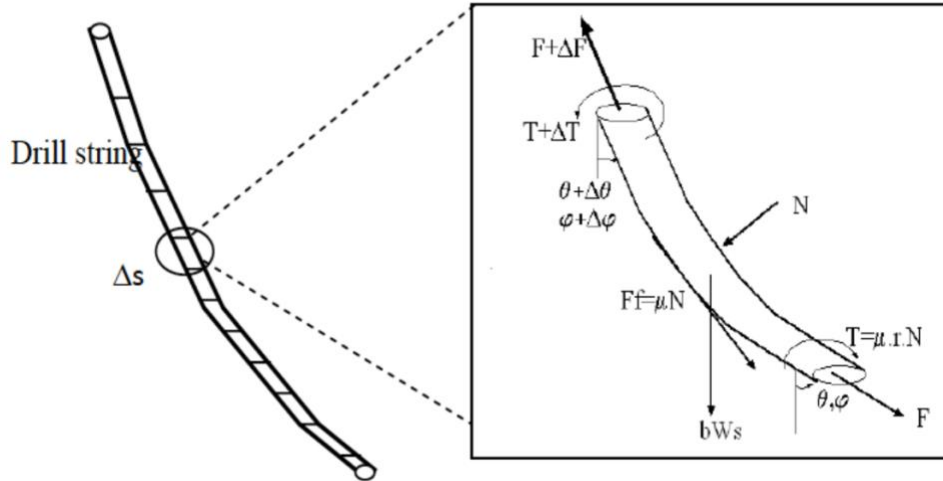


Figure 2.20: Illustration of a curved drill string divided into segments and the load distribution of each segment, [62]

$$\frac{dF}{ds} = \pm\mu \left(\sqrt{\left(\beta \cdot w_s \cdot \sin \theta + F \cdot \frac{d\theta}{ds} \right)^2 + \left(F \cdot \sin \theta \cdot \frac{d\varphi}{ds} \right)^2} \right) + \beta \cdot w_s \cdot \cos \theta \quad (2.36)$$

$$N_i = \sqrt{\left(\left(\beta \cdot w_i \cdot \sin \left(\frac{\theta_{i+1} + \theta_i}{2} \right) + F_i \cdot \left(\frac{\theta_{i+1} - \theta_i}{S_{i+1} - S_i} \right) \right)^2 + \left(F_i \cdot \sin \left(\frac{\theta_{i+1} + \theta_i}{2} \right) \cdot \frac{\varphi_{i+1} - \varphi_i}{S_{i+1} - S_i} \right)^2 \right)} \quad (2.37)$$

Where:

- μ = Coefficient of friction, []
- β = Buoyancy factor, []
- w = Weight per unit length, [N/m]
- θ = Inclination, [°]
- S = Length of segment, [m]
- φ = Azimuth, [°]
- N_i = Contact force per unit length, [N/m]

In equation 2.36, the normal force per unit length for a curved well can be observed as the square root term. Further, the normal force for each drill string segment can be obtained as shown in equation 2.37.

The buoyancy factor is presented in equation 2.38. As seen, it is given terms of the density of the fluid in the annulus, ρ_o , and in the pipe, ρ_i , as well as the density of the pipe, ρ_{pipe} .

$$\beta = 1 - \frac{\rho_o A_o - \rho_i A_i}{\rho_{pipe} (A_o - A_i)} \quad (2.38)$$

Where:

- A_o = External area of pipe, [m²]
 A_i = Internal area of pipe, [m²]

As seen in equation 2.39, a plus-minus sign takes the movement of the pipe into account when determining the drag force. When tripping out of the well, the friction will add to the axial load of the pipe, whereas the opposite is the case when tripping in. The non-linear first order differential equation shown below is the one implemented in Halliburton Landmark's WellPlant™ simulator. [62]

$$F_{i+1} = F_i + \sum_{i=1}^n \left[\left(\beta \cdot w_i \cos \frac{\theta_{i+1} + \theta_i}{2} \right) \pm \mu_t \cdot N_i \right] (S_{i+1} - S_i) \quad (2.39)$$

Where:

- F_i = Weight on bit, [N]
 β = Buoyancy factor, []
 w_i = Weight of drill string, [N/m]
 θ_i = Inclination, [°]
 μ_i = Coefficient of friction, []
 N_i = Contact force per unit length, [N/m]
 S_i = Length of drill string segment, [m]

The axial coefficient of friction, μ_a , is written in terms of the axial speed, v_a , and rotational speed, $\omega \cdot r$, as:

$$\mu_a = \mu_o \cdot \frac{v_a}{\sqrt{(\omega \cdot r)^2 + v_a^2}} \quad (2.40)$$

Where:

$$\begin{aligned}\mu_0 &= \text{Coefficient of friction, []} \\ v_a &= \text{Axial speed, [m/s]} \\ \omega &= \frac{2\pi N}{60}, \text{ N= rotation per minute, [RPM]} \\ r &= \text{Radius of tube, [m]}\end{aligned}$$

2.8.2 Torque

Torque is defined as the force generating the rotation of an object around its axis and thus, it is also known as the moment of a force [63]. In general, torque is obtained as the product of the force and the length from the object's axis to which the force is applied. Considering a drilling operation, torque is described as the moment required to rotate the drill string. To do so, the moment must overcome the rotational friction resistance produced in the wellbore and at the bit due to pipe and bit interaction with the formation. [62]

During drilling, torque is applied to the upper part of the drill string. For deviated wells, the available torque at the bit can differ significantly from that applied at the surface, while the torque is identical at the surface and at the bit in ideal vertical wells when neglecting the minor loss present due to the viscous force exerted by the mud. Torque is a consequence of friction in the wellbore and is especially significant in long, complex and extended-reach wells. This is because the pipe is more susceptible to contact with the formation under these conditions, generating increased frictional forces. In extended-reach drilling, excessive torque and drag are major limiting factors regarding the horizontal displacement and thus, improvement of drilling fluids as lubricants is of importance [61, 62].

As mentioned, torque is dependent on the radius of rotation, although it is also affected by other factors such as the coefficient of friction and normal force of the pipe. Equation 2.41 shows the formula for calculating increment torque, while equation 2.42 defines the torque loss per unit length for both a buckled and non-buckled string. [62]

$$\Delta T = \mu_t \cdot N_i \cdot r \cdot \Delta S \quad (2.41)$$

$$T_{i+1} = T_i + \sum_{i=1}^n \mu_t \cdot r_i \cdot N_i \cdot (S_{i+1} - S_i) \quad (2.42)$$

Where:

- ΔT = Incremental torque, [$N \cdot m$]
- μ_t = Tangential coefficient of friction, []
- N_i = Contact force per unit length, [N/m]
- r = Outer radius of pipe, [m]
- ΔS = Incremental pipe length, [m]
- T_{i+1} = Torque at top, [$N \cdot m$]
- T_i = Torque at bottom, [$N \cdot m$]
- S_i = Length of drill string segment, [m]

The tangential coefficient of friction, μ_t , is written in terms of the axial speed and rotational speed as:

$$\mu_t = \mu_o \cdot \frac{\omega r}{\sqrt{(\omega r)^2 + v_a^2}} \quad (2.43)$$

Where:

- μ_o = Coefficient of friction, []
- v_a = Axial speed, [m/s]
- ω = $\frac{2\pi N}{60}$, N= rotation per minute, [RPM]
- r = Radius of tube, [m]

2.8.3 Tensile and Torsional Limit

To ensure a safe drilling operation, it is critical that the drill string can withstand the loads it will be exposed to in the wellbore. By generating a drill string mechanics program during the planning phase of the well, a safe operational window can be defined. This window is bounded by the tensile and torsional limits [62]. Figure 2.21 and 2.22 illustrates the effective tension and torsion plots obtained when performing simulations using the WellPlan™ software. Both are examples of an operation where all loads are within the safe operational window.

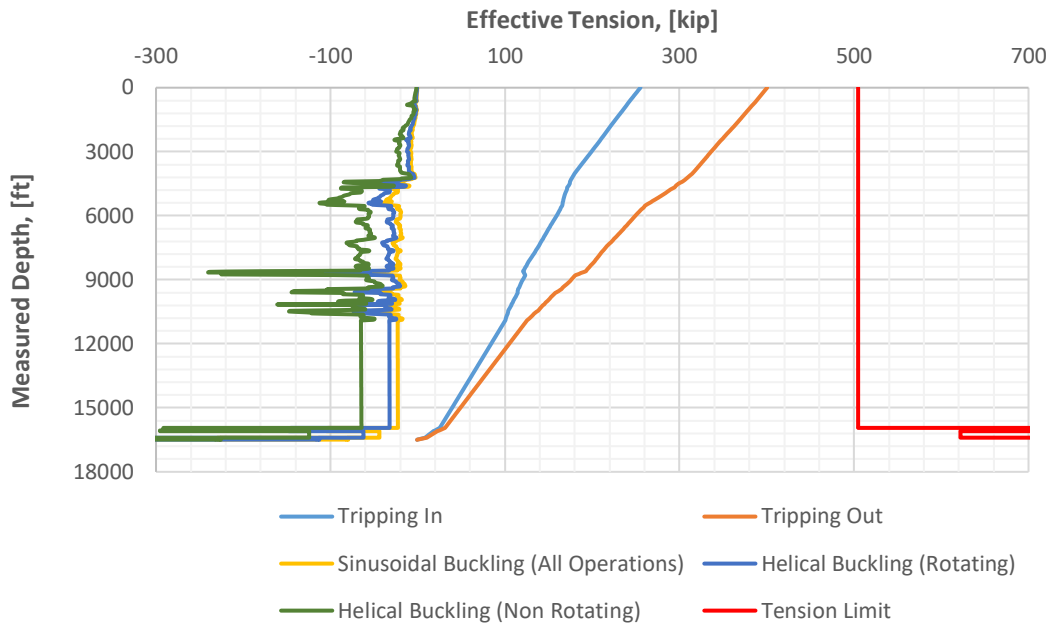


Figure 2.21: Example of effective tension plot where no loads exceed the tensile limit (REF + 0.08 g CP system)

Tensile failure occurs when the tensile load applied in an operation exceeds the yield strength of the weakest component of the drill string, while torsional failure occurs when the compressive load exceeds the critical buckling load of the string [59, 64]. Exceeding the tensile and torsional limits typically results in failure in the pipe body and tool joints, respectively. To avoid this, the total stresses of the drill string, which are induced by combined bending, torsion and tensile stresses, should be considered [65]. In this thesis, Halliburton Landmark’s WellPlan™ software is used to obtain maximum drilling depth when applying the different nanoparticle fluid systems by considering the safe operational window.

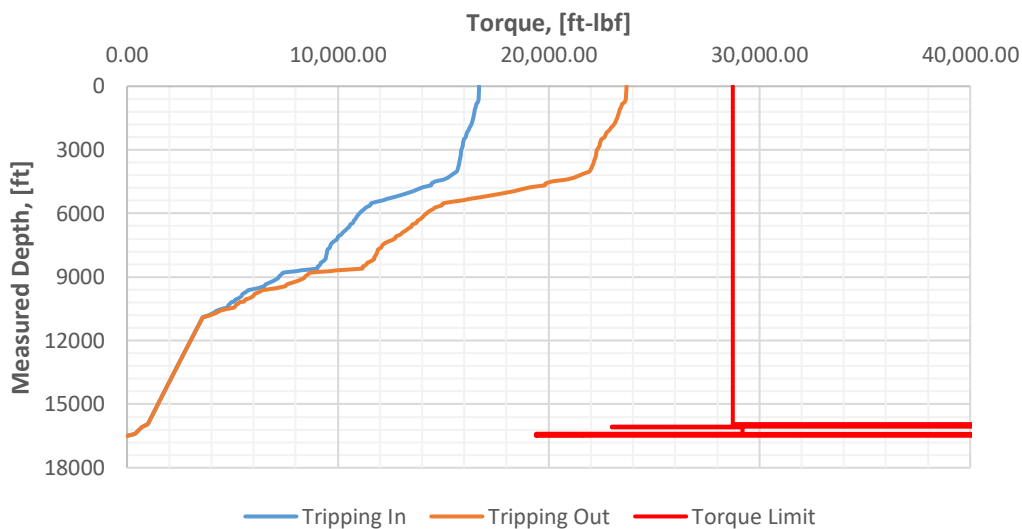


Figure 2.22: Example of torque plot where no loads exceed the torsional limit (REF + 0.08 g CP system)

As the torsional and tensile limits constricts the torque and drag in the wellbore, friction becomes a vital parameter. This is related to the fact that its presence will initiate pipe buckling and failure at lower compressive and tensile loads, respectively. Exceeding the critical buckling load of the pipe will at first cause sinusoidal buckling, while increasing the load further results in helical buckling and in worst case lock-up. The latter situation is when the string cannot be moved farther into the wellbore as a consequence of the frictional resistance encountered. Furthermore, high compressive forces restrict the application of higher weight on bit (WOB) if conditions indicate that higher ROP and torque on bit (TOB) is necessary. Higher tensile loads, on the other hand, can cause permanent deformation or alter the stability of a material. Exceeding the yield strength of the string ultimately results in material failure and parting of the pipe. [59, 62, 66]

2.9 Hydraulics Model

Hydraulics is the study of fluids, primarily liquids, in motion and addresses subjects such as flow in pipes and tanks. It is closely related to fluid mechanics, the science of a fluid's response to an applied force, which provides most of its theoretical foundation [67, 68]. Moreover, the drilling performance of mud is vastly affected by fluid hydraulics, making it an important factor to consider in order to drill a well safely and successfully [29, 69]. A drilling hydraulics analysis is typically applied for this purpose. The objective of such an analysis is to address the following concerns: [29]

- The selected pump can deliver the required pump pressure.
- The downhole ECD does not exceed the pore- and fracture gradient (to prevent loss of circulation and kicks from occurring).
- The cuttings are controlled.
- The flow rate is maximizing either the bit hydraulic horsepower or jet impact force to meet other requirements.

Cuttings transport, prevention of fluid influx and maintenance of wellbore stability depend on the flow of the applied drilling fluid, as well as the pressures associated with that flow. Keeping the downhole pressures under control is extremely important in order to avoid the occurrence of a kick and a potential blowout. Thus, accurate prediction of pressures and flow of fluids in the wellbore is vital to design a proper drilling fluid system [70]. Prediction of the flow

performance is typically performed using mathematical models known as hydraulics models. These can be applied to compute the pressure profiles along the entire wellbore and in the annulus, as well as to describe the flow behavior of drilling fluids. Hence, the relation between flow rate and pressure drop for any given geometry of a flow conduit, flow regime and fluid properties can be defined by the application of hydraulics models [29, 71]. As for rheology models, there are several distinctive hydraulics models to be applied. The models consider different types of fluids and thus, differ in their calculations. [29]

A previous study performed by Jeyhun Sadigov in 2013 investigated the rheology and hydraulics models of drilling fluids. The predictive power of different models was compared and the Unified hydraulics model was found to correlate better with the measured data [72]. Consequently, it was decided to apply the Unified model when conducting the hydraulics simulations later in this thesis. Table 2.2 presents a summary of the most important parameters, equations and relations in the Unified hydraulics model.

Table 2.2: Summary of parameters and equations applied in the Unified hydraulic model, [55]

Unified Hydraulic Model	
Pipe Flow	Annular Flow
$\mu_p = R_{600} - R_{300}$	$\tau_y = R_{300} - \mu_p$
$\tau_0 = 1.066(2R_3 - R_6)$	
$n_p = 3.32 \log \left(\frac{2\mu_p + \tau_y}{\mu_p + \tau_y} \right)$	$n_p = 3.32 \log \left(\frac{2\mu_p + \tau_y - \tau_y}{\mu_p + \tau_y - \tau_y} \right)$
$k_p = 1.066 \left(\frac{\mu_p + \tau_y}{511} \right)$	$k_p = 1.066 \left(\frac{\mu_p + \tau_y - \tau_0}{511} \right)$
$G = \left(\frac{(3 - \alpha)n + 1}{(4 - \alpha)n} \right) \left(1 + \frac{\alpha}{2} \right)$	
$\alpha = 0$ for pipe	$\alpha = 1$ for annuli
$v_p = \frac{24.51 q}{D_p^2} \text{ [ft/min]}$	$v_a = \frac{24.51 q}{D_2^2 - D_1^2} \text{ [ft/min]}$
$\gamma_w = \frac{1.6 * G * v}{D_R} \text{ [sec}^{-1}\text{]}$	
$\tau_w = \left[\left(\frac{4 - \alpha}{3 - \alpha} \right) \right] \tau_0 + k \gamma_w^n \text{ [lbf/100ft}^2\text{]}$	
$N_{Re} = \frac{\rho v_p}{19.36 \tau_w}$	$N_{Re} = \frac{\rho v_e}{19.36 \tau_w}$
$f_{laminar} = \frac{16}{N_{Re}}$ $f_{transient} = \frac{16 N_{Re}}{(3470 - 1370 n_p)}$ Turbulent : $f_{turbulent} = \frac{a}{N_{Re}^b}$ $a = \frac{\log(n) + 3.93}{50}$ $b = \frac{1.75 - \log(n)}{7}$	$f_{laminar} = \frac{24}{N_{Re}}$ $f_{transient} = \frac{16 N_{Re}}{(3470 - 1370 n_p)}$ Turbulent : $f_{turbulent} = \frac{a}{N_{Re}^b}$ $a = \frac{\log(n) + 3.93}{50}$ $b = \frac{1.75 - \log(n)}{7}$
$f_{partial} = (f_{transient}^{-8} + f_{turbulent}^{-8})^{-1/8}$	
$f_p = (f_{partial}^{12} + f_{laminar}^{12})^{1/12}$	$f_a = (f_{partial}^{12} + f_{laminar}^{12})^{1/12}$
$\left(\frac{dp}{dL} \right) = 1.076 \cdot \frac{f_p \cdot v_p^2 \cdot \rho}{10^5 \cdot D_p} = \text{[psi/ft]}$ $\Delta p = \left(\frac{dp}{dL} \right) \cdot \Delta L = \text{[psi]}$	$\left(\frac{dp}{dL} \right) = 1.076 \cdot \frac{f_a \cdot v_a^2 \cdot \rho}{10^5 \cdot (D_2 - D_1)} = \text{[psi/ft]}$ $\Delta p = \left(\frac{dp}{dL} \right) \cdot \Delta L = \text{[psi]}$
$\Delta p_{Nozzles} = \frac{156 \cdot \rho \cdot q^2}{(D_{N1}^2 - D_{N2}^2 - D_{N3}^2)^2} = \text{[psi]}$	

2.9.1 ECD

The pressure exerted by a drilling fluid is dependent on several factors such as the true vertical depth (TVD) and geometry of the wellbore, as well as the density of the drilling fluid. Moreover, the resulting pressure is contingent on whether the fluid is static or dynamic. A static drilling fluid simply exerts a pressure equivalent to the product of its mud weight and the TVD of the well, i.e. the hydrostatic pressure. When the drilling fluid is circulating in the well, a term called equivalent circulating density (ECD) is essential to describe the resulting pressure [55]. ECD is defined as the effective density exerted by a circulating fluid on the formation as it accounts for the pressure loss occurring due to friction between the wellbore wall and a flowing fluid [73, 74]. The equivalent circulating density is calculated as shown in the following equation:

$$ECD = MW + \frac{\Delta P_{annulus}}{0.0981 \cdot TVD} \quad (2.44)$$

Where:

- ECD = Equivalent circulation density, [sg]
- MW = Mud weight, [sg]
- $\Delta P_{annulus}$ = Pressure drop in annulus, [bar]
- TVD = True vertical depth, [m]

2.9.2 Pump Pressure

Prior to computing the pump pressure, knowledge about the complete path of which a drilling fluid is circulated is necessary. Figure 2.23 illustrates a typical circulation system and its major components. The circulation of the drilling fluid is generated by the mud pump and it is therefore a vital component of the system. Essentially, the pump can be thought of as the heart of a circulation system. [29, 75]

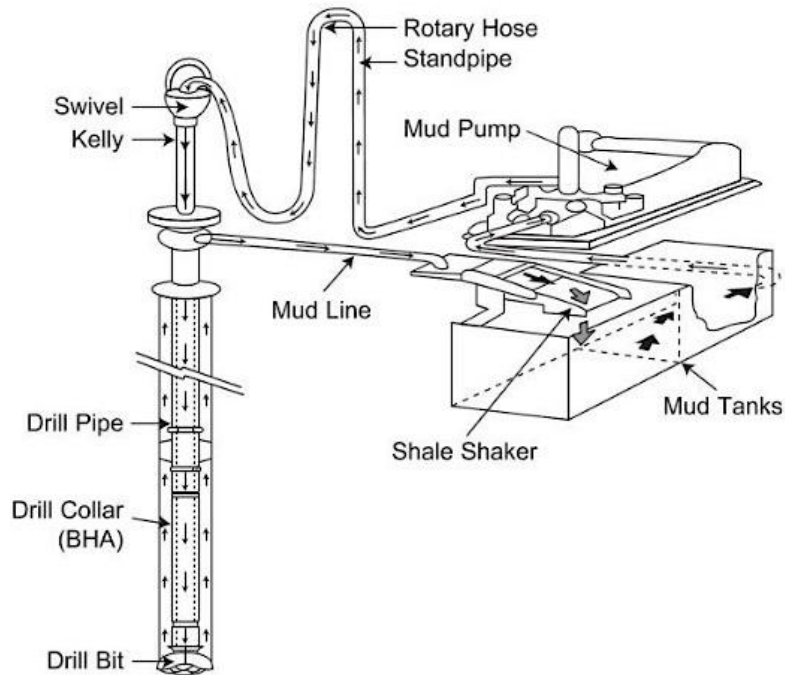


Figure 2.23: Illustration of a typical circulation system, [29]

At first, drilling fluid is extracted from the mud tanks and taken to the mud pump. Thereafter, the mud is circulated through the standpipe and kelly into the drill string. The drill string consists of drill pipes and a bottom hole assembly in which the mud flows prior to exiting the string through a bit with nozzles. Mud is then circulated up the annular space between the string and the wellbore wall to the surface. At this point, the mud is deposited over shale shakers which consists of vibrating screens to separate cuttings from the mud. In addition, the mud can be run through desanders, desilters and degassers to filter out smaller particles, air and gas. The clean mud is then drained back into the mud tanks where it can be reused by the system. [29, 76]

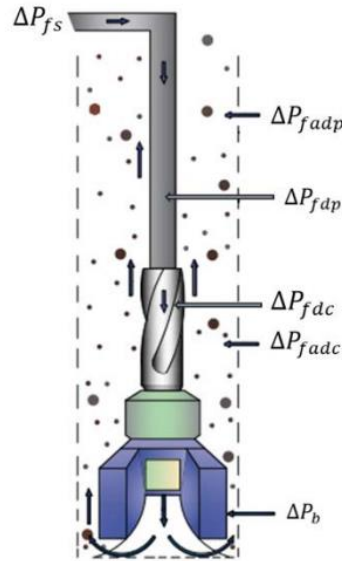


Figure 2.24: Frictional pressure losses in a circulation system,[77]

As the drilling fluid travels through the circulation system, pressure will be lost due to frictional resistance, i.e. the pump pressure is spent by frictional pressure losses in the components. To ensure fluid circulation all the way back to the surface, the pump pressure must overcome the total losses encountered in the system. Accordingly, the pump pressure is given as presented in equation 2.45. The frictional pressure losses defined in the equation are illustrated in figure 2.24. [70]

$$P_{pump} = \Delta P_{tot} = \Delta P_{fs} + \Delta P_{fadp} + \Delta P_{fdp} + \Delta P_{fdc} + \Delta P_b + \Delta P_{fadc} + \Delta P_{fadp} \quad (2.45)$$

Where:

- ΔP_{pump} = Pump pressure, [bar]
- ΔP_{tot} = Total frictional pressure loss, [bar]
- ΔP_{fs} = Pressure loss in surface flow lines, [bar]
- ΔP_{fdp} = Pressure loss in drill pipe, [bar]
- ΔP_{fdc} = Pressure loss in drill collar, [bar]
- ΔP_b = Pressure loss in nozzles of the drill bit, [bar]
- ΔP_{fadc} = Pressure loss in the annular space between the wellbore and drill collar, [bar]
- ΔP_{fadp} = Pressure loss in the annular space between the wellbore and drill pipe, [bar]

3 Literature Study

In this section, nanotechnology and its application in drilling fluids will be elaborated on. In addition, a literature review concerning previous application of nanoparticles in drilling fluids will be presented.

3.1 Nanotechnology

Nanotechnology is the development and application of materials, tools and devices on a nanoscopic scale using nanoparticles. Nanoparticles are defined as a substance whose diameter ranges from 1-100 nm and over the years, its application have brought several technical breakthroughs in a wide range of industries. In fact, nanotechnology has become one of the most active research topics of modern time. [78, 79]

Even though nanotechnology has provided numerous advances within areas such as medicine, biology and electronics for the past decades, it has only more recently been given an increasing interest in the petroleum industry. The technology is thought to have significant impact on several aspects of the industry and accordingly, the application of nanoparticles has been experiencing rapid growth [78, 80]. For instance, nanotechnology has been applied to attain advances on construction and materials, as well as enhancements of drilling fluids. [81]

3.2 Nanoparticle Drilling Fluids

As mentioned in section 2.1, the success and total cost of a drilling operation greatly depends on the performance of the applied drilling fluid and accordingly, the drilling fluid should be designed to provide efficient performance in the expected wellbore conditions. As the complexity of the drilling operation increases, the mud must be able to endure more extreme conditions and operational issues, such as clay swelling, narrow operational window, formation of gas hydrates, high temperatures, poor hole cleaning and stuck pipe situations. Typically, oil-based drilling fluids have been applied in such complicated operations due to their superior performance under said conditions. These systems are, however, more expensive and damaging to the environment compared to water-based mud. Thus, nanoparticle water-based drilling fluids are being developed and designed to tolerate said challenges and improve drilling performance in a more environmentally friendly manner. [5, 43, 82]

A nanoparticle drilling fluid is defined as any drilling fluid that contains one or more nanoparticle additives. Such systems have unique fluid properties which offer several modifications beyond that of conventional additives, like improved lubricity, fluid loss, shale inhibition and cuttings transport. The use of nanoparticles enable fit for purpose optimization, such that the fluid properties can be modified according to the wellbore conditions. The superior drilling performance of nanoparticle systems are to a large extent caused by the great surface area to volume ratio provided by the small size of the nanoparticles, illustrated in figure 3.1. Potentially, the application of nanoparticles can eliminate the use of other expensive additives and provide drilling fluids with improved functionality. [82, 83]

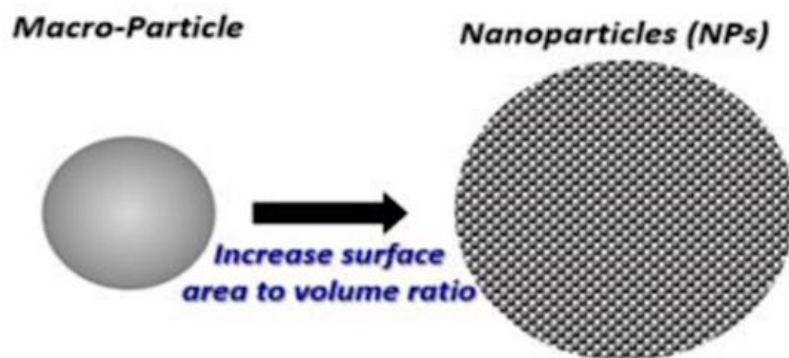


Figure 3.1: Illustration of the increase in the surface area to volume ratio with nanoparticles, [82]

Nanoparticles are, however, highly reactive substances which makes them very sensitive to changes in the wellbore and other fluid components. This provokes the current challenge of selecting the optimum nanoparticle type, concentration and size distribution. Typically, nanoparticle concentrations beyond the optimum amount will have a negative impact on the rheological and filtration properties of a fluid. Moreover, many nanoparticles exhibit poor dispersion properties, which causes instability and formation damage in the wellbore when the drilling fluid is degraded by changes in pH, salinity and/or temperature. [82, 83]

3.3 Literature Study: Application of Nanoparticles in Drilling Fluids

Nanoparticles can provide drilling fluids with unique properties which are superior to those of conventional drilling fluids. This have led to an increasing interest in the development of nanoparticle drilling fluids in order to eliminate the need for oil-based mud, as well as finding solutions to industry problems not yet solved with traditional methods. [82, 83]

Over the years, several studies have been conducted with the intention of developing modified drilling fluids with the application of nanoparticles. A literature review of some of the previous studies in nanoparticle drilling fluids is presented in the following paragraphs.

“Nanotechnology for Oilfield Applications – Hype or Reality?” by Friedheim et al., [84]

In a paper published by Friedheim et al. in 2012, carbon nanotubes (CNT) were applied to invert-emulsion muds to evaluate its effect as a stabilizer at ultra-HPHT conditions. Two CNT formulations were investigated and thus, exposed to 16 hours’ heat aging at 600°F (~315.5°C). Results were positive and showed that both CNTs were able to stabilize the rheological profile of the invert-emulsion fluid, even at low concentrations. The base fluid, however, was not able to tolerate the increased temperature and it was seen that its lower shear rheology was completely lost. The filtration properties of the CNT fluids were also examined and showed that fluid loss control still was an issue. [84, 85]

The paper also investigated the application of graphene oxide (GO) nanoparticles to a water-based mud containing bentonite. Quantities ranging from 2-6 pounds per barrels were added to the base fluid to examine the effect of GO as a viscosifier. Results showed that even an amount 2.0 lb/bbl caused a significant effect on the viscosity. Graphene oxide was also added to another water-based mud formulation to study its effect on both rheology and fluid loss after 16 hours’ heat aging at 150°F (~65.5°C). These results also showed that low concentrations of GO increase the viscosity of the base fluid substantially, whilst the amount of fluid loss was significantly lowered. Thus, the GO nanoparticle was considered to be a relatively effective additive in regard to both viscosity and fluid loss. [84]

“Nanoparticle-Based Drilling Fluids for Minimizing Formation Damage in HP/HT Applications” by Mahmoud et al., [86]

In 2016, Mahmoud et al. published a research paper which provided an extensive evaluation of modified water-based drilling fluids for HPHT application. In the study, a bentonite-based drilling fluid was modified with ferric oxide and silica, which are two commercially available nanoparticles. The fluids were then exposed to various temperatures ranging from 120-200°F (~50-90°C) and ambient pressure. It was observed that the addition of Fe₂O₃ resulted in improved rheological properties at increased temperatures and compared to the base fluid, higher yield stress values were obtained. Increased YS values provide the drilling fluid with better dynamic suspension of the cuttings, consequently increasing the cuttings transport

capacity. The application of silica, however, reduced the YS values of the drilling fluid. [85, 86]

Furthermore, the filtration properties of the two nanoparticle fluids were investigated under HPHT conditions. A HPHT filtration test was performed at 250°F (~129°C) with a differential pressure of 300 psi. Results showed that ferric oxide reduced the amount of fluid loss at lower concentrations, whereas silica increased both the filtrate volume and filter cake thickness. Both nanoparticle drilling fluids were also exposed to 16 hours' dynamic aging at 350°F (~177°C), in cells pressurized to 300 psi. It was observed that the rheological properties of the Fe₂O₃ fluid remained quite stable with only a minor loss of gel strength. The aged SiO₂ fluid, however, exhibited great losses of gel strength and higher YS values, which negatively impacts the cuttings transport capacity. [86]

“The Novel Approach for the Enhancement of Rheological Properties of Water-Based Drilling Fluids by Using Multi-Walled Carbon Nanotube, Nanosilica and Glass Beads” by Ismail et al., [87]

Ismail et al. researched the effect of multi-walled carbon nanotube and nanosilica in conventional water-based drilling fluids. The study examined the effect of various nanoparticle concentrations, in the range of 0.001-0.2 ppb, on the rheological, filtration and frictional properties of the base fluid. Results showed that the YS values increased with concentration for both nanoparticle fluids. Furthermore, it was observed that both MWCNT and nanosilica reduced the amount of fluid loss. In addition, the frictional properties of the nanoparticle systems were investigated. Measurements of the coefficient of friction (CoF) showed that all concentrations improved the lubricity of the base fluid significantly. It was, however, seen that the CoF decreased non-linearly with increasing nanoparticle concentration. [87]

“Effect of Nano-Silicon Dioxide (SiO₂) on Polymer/Salt Treated Bentonite Drilling Fluid Systems” by Belayneh et al., [88]

In 2016, Belayneh et al. published a paper focusing on the effect of silicon dioxide, SiO₂, in a water-based drilling fluid containing bentonite, polymer and salt. Three fluid systems were formulated with the use of xanthan gum, CMC and a mixture of LV-CMC and xanthan gum as the polymer additive. Various concentrations of silica, ranging from ~0.02-0.09 wt%, was applied to these systems to investigate its influence on the rheological and filtrations properties at room temperature. Overall, it was observed that the rheology profiles of the systems

increased non-linearly with the addition of silica, as well as becoming more shear thinning. In regard to fluid loss, most nanoparticle concentrations resulted in increased filtration volumes for the CMC and LV-CMC and xanthan gum mixture systems, excluding those containing ~0.06 wt% silica. In the xanthan gum polymer system, most of the concentrations resulted in a slightly reduced fluid loss. At an optimum concentration of silica, the following was observed for all polymer systems: [88]

- Improved rheology parameters
- Slightly improved filtration properties
- Efficient cuttings transport
- Reduced (CMC system) and increased ECD (xanthan gum and polymer mixture systems)

“Effect of Nanomaterial on the Rheology of Drilling Fluids” by Ismail et al., [89]

In a study conducted by Ismail et al. in 2014, focus was put on finding an optimum concentration of multi-walled carbon nanotube to improve the rheological properties of both water-based and ester-based drilling fluids. At first, the concentration of MWCNT was varied in both of the fluid systems and tested at room temperature. This resulted in little variance in the rheological properties of the water-based drilling fluid, whilst the gel strength and emulsion stability of the ester-based mud was slightly increased. [89]

Thereafter, the combined effect of multi-walled carbon nanotube and a conventional fluid loss additive was investigated by varying the amount of pac UL and confitrol in the water- and ester-based drilling fluid, respectively, whilst keeping the nanoparticle concentration constant. API and HPHT fluid loss tests were performed for the water-based and ester-based muds, respectively, and showed that the fluid loss volume of both fluids decreased with the addition of a conventional fluid loss additive. [89]

In addition, the effect of temperature on the rheological properties of the MWCNT treated fluids were examined. In the range of 80-250°F (~27-120°C), it was observed that PV, YS and gel strength of the water-based fluid decreases with increasing temperature. The plastic viscosity, in particular, is significantly affected by the increasing temperature, though its values are still found to be within the acceptable limit. The opposite trend was observed for the ester-based drilling fluids with increasing temperature. [89]

“Effect of Al₂O₃ Nanoparticles on Rheological Properties of Water Based Mud” by Amarfio and Abdulkadir, [90]

Amarfio and Abdulkadir researched the performance of aluminum oxide nanoparticles in a water-based drilling fluid containing bentonite. In the study, four systems were formulated with an Al₂O₃ concentration varying from 0.0-1.5 g and by increasing the temperature from 40-90°C, the temperature stability was investigated. Results showed minor variations in the PV and YS values, as well as maintained shear stresses with increasing temperatures. Thus, it was concluded that aluminum oxide provides thermal stabilization of the water-based mud under high temperature conditions. [90]

“Water Based Mud Lifting Capacity Improvement by Multiwall Carbon Nanotube Additive” by Samsuri and Hamzah, [91]

In a research paper published in 2011, Samsuri and Hamzah studied the use of MWCNTs to improve the carrying capacity of water-based drilling fluids. By varying the nanoparticle concentration from 0.0-0.01 %, it was observed that the viscosity of the water-based system increased with increasing concentration. The same trend was also seen for the fluid’s carrying capacity, where the addition of 0.01 % MWCNT resulted in a 15 % increase in the cuttings recovery. This was, however, the case for smaller cuttings sizes, whereas the medium and big cuttings sizes exhibited lower values of cuttings recovery with the same amounts of MWCNT. Moreover, it was observed that the carrying capacity exhibited less improvement with increasing nanoparticle concentration for cuttings of bigger sizes. [91]

“Multifunctional Nanoadditive in Water Based Drilling Fluid for Improving Shale Stability” by Taraghikhah et al., [92]

Taraghikhah et al. examined the application of silica nanoparticles in water-based drilling fluids. Their main goal was to improve the shale inhibition and wellbore stability, though other fluid properties was also investigated. The silica concentration was varied from 0.5-2.0 wt% and the results were compared to the base fluid, as well as the base fluid containing conventional shale inhibitors. Results showed that the nanoparticle had a positive effect on the shale recovery and it even produced values better than that of the base fluid containing conventional shale inhibitors. In regard to rheological properties, it was observed that both PV and YS values increased with the addition of silica. At lower concentrations, the fluid loss did not change considerably, but showed slightly lower values. At the highest concentration, however, the

amount of fluid loss increased significantly. Overall, it was seen that quantities of silica below 1.0 wt% would be the most economical and effective concentrations of the nanoparticle. At these quantities, the drilling fluid provided acceptable shale inhibition, as well as efficient lubrication. [92]

“Impact of Nanomaterials on the Rheological and Filtration Properties of Water-Based Drilling Fluids” by Salih et al., [82]

In a paper published in 2016 by Salih et al., the effect of colloidal nanosilica in water-based mud was investigated. Focus was put on finding the optimum concentration of the nanoparticle to enhance drilling fluid properties and hydraulics. The addition of silica at lower concentrations, below 0.7 wt%, improved the rheological and filtration properties of the base fluid. Higher nanoparticle concentrations, however, had a negative impact on some of the rheological properties. Results showed that the addition of 0.1 wt% silica yielded the most significant reduction of the ECD and circulating pressure loss. Overall, the optimum silica concentration was found to be in the range of 0.1-0.3 wt%. [82]

4 Experimental Work Study

This section presents the formulations of the various drilling fluid systems to be experimentally examined in this thesis, as well as descriptions of all the chemical additives. Moreover, the experimental equipment and methodology for the rheological, viscoelastic, frictional and fluid loss testing is introduced.

4.1 Description of Drilling Fluid Additives

4.1.1 Bentonite

Bentonite is a plastic and highly colloidal clay formed by alteration of volcanic material. Primarily, it contains montmorillonite, a three-layer clay of the smectite group. Since bentonite has no definite mineralogical composition, it is a generic term and not an exact mineralogical name [12, 25, 93, 94]. Though, table 4.1 presents a typical chemical composition of a commercial Wyoming bentonite clay. [95]

Table 4.1: Chemical composition of bentonite, [95]

Component	Percentage of chemical composition
Silica, SiO ₂	64.32
Alumina, Al ₂ O ₃	20.74
Cumulative water	5.14
Ferric oxide, Fe ₂ O ₃	3.03
Soda, Na ₂ O	2.59
Magnesia, MgO	2.30
Lime, CaO	0.50
Ferrous Oxide, FeO	0.46
Potash, K ₂ O	0.39
Sulfuric Anhydride	0.35
Titanium Oxide, TiO ₂	0.14
Phosphoric Anhydride	0.01
Other minor constituents	0.01

The content of montmorillonite provides the swelling and thixotropic properties of the bentonite, making it useful as a viscosity enhancer in drilling fluids. Thus, bentonite can increase the carrying capacity and improve the suspension of weight materials in a fluid. In addition, it can improve the fluid loss and filter cake properties [15, 17, 25]. The basic structure

of a montmorillonite clay is illustrated in figure 4.1 and as seen, it consists of three-layer minerals where a central octahedral layer is sandwiched by two tetrahedral layers.

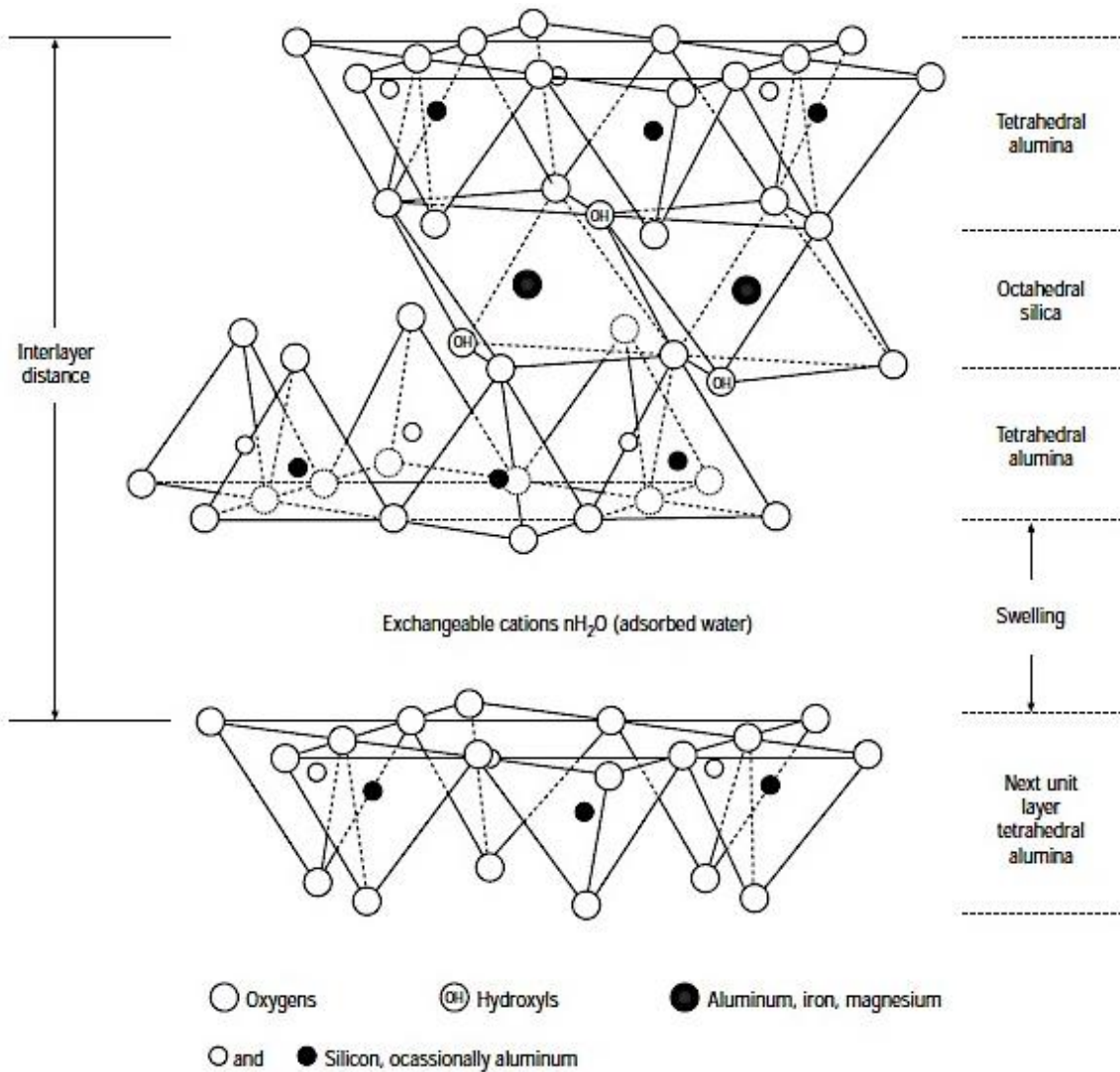


Figure 4.1: Illustration of the basic structure of montmorillonite, [25]

4.1.2 Soda Ash

Soda ash is an alkali water soluble salt with the chemical formula Na_2CO_3 . It is also known as sodium carbonate and is used in drilling fluids to increase the pH. Furthermore, the additive is useful in order to treat calcium ion contamination of water-based drilling fluids from gypsum or anhydrite formations. Such contamination can cause reduced pH, clay flocculation and precipitation of polymers. In this thesis, both hydrated (60-100 %) and anhydrous (100 %) soda ash was used. [96]

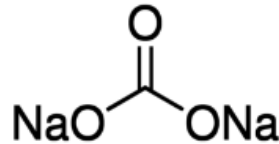


Figure 4.2: Molecular structure of anhydrous sodium carbonate, [97]

4.1.3 Barite

Barite is a naturally occurring mineral with the chemical formula BaSO₄. It is a non-toxic and non-reactive solid with high specific gravity, thus it is commonly used as an additive in drilling fluids to increase density. Due to its specific gravity of 4.2-4.5, barite has been able to weight-up a WBM to as high as 2.6 sg, while maintaining a low viscosity, and is therefore a widely used weighting material. The addition of weighting materials in drilling fluids is valuable to provide a sufficient hydrostatic head in the wellbore. [8, 13, 17, 25]

4.1.4 Polymer Additives

Polymers are large molecules made up from one or several repeating units, called monomers, which are connected to one another in long chains. In situations where the clay additive, such as bentonite, gives undesirable or insufficient drilling fluid properties, polymer additives should be used instead of or together with the clay. There are various polymers available that perform different functions such as: [8, 13]

- Increasing the viscosity and gelation properties
- Reducing fluid loss
- Operating as a flocculant or deflocculant
- Acting as a surfactant

The area of application depends on the molecular weight, i.e. length, and charge of the polymer. By changing the monomers, their coupling and/or the number of monomers, they can be tailored to specific drilling situations. In this case, the polymers are synthetic and almost an endless number of combinations are available. Polymers also occur naturally. [8, 13, 25]

4.1.4.1 Polypac

Polypac is a polyanionic cellulose polymer used for fluid loss control in water-based drilling fluids. The polymer is effective even at low concentrations and is applicable in all WBMs. However, higher concentrations are required to encapsulate shales and cuttings when applied in, among others, saltwater systems. When polypac is applied to drilling fluids, the filter cake formed is thin with low permeability, thus the risk of differential sticking and flow from the wellbore into the formation is minimized. Polypac does in general function as a fluid loss reducer, however, there are different types available, such as M-I Swaco's polypac ELV or polypac UL, which presents slightly different additional qualities. [98]

4.1.4.2 Pac

Polyanionic cellulose, pac, is used to increase viscosity and control the fluid loss of water-based fluids. According to IRO Group Inc. [99], the polymer can also be used as a stabilizer, suspending agent and colloid protector. Hence, the additive will improve the cuttings transport efficiency and suspension properties of drilling fluids. Pac, as well as the polymer polypac mentioned above, is bacteria resistant and effective over a wide range of pH levels. Its chemical formula is $[C_6H_7O_2(OH)_2CH_2COONa]_n$ and like polypac, there are various forms of pac exerting different levels of viscosity control. [99, 100]

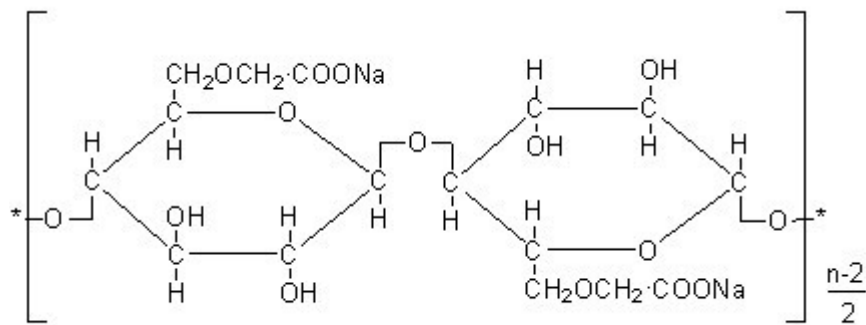


Figure 4.3: Chemical structure of pac, [99]

4.1.4.3 Carbopol

Carbopol is a family of polyacrylic acid polymers, also known as carbomers, commonly used to increase the viscosity of liquids in several industries. All carbopol solutions have high molecular weight and polyacrylic acid polymers that are crosslinked. According to Priscilla et al. [101], the polymer also functions as an agent for suspension, dispersion and stabilization. However, the dispersion properties are strongly affected by the reagents, water properties and

mixing process of the fluid. Thus, a strict procedure of its implementation is fundamental to attain reproducibility. [101, 102]

The rheological effect of carbopol is a function of its concentration, as well as the following fluid properties: composition, pH, temperature, preparation process and ageing. The effect of temperature is minor; however, neutralization of the polymer is necessary for it to attain its maximum thickening capacity. Then, it is common to use bases such as sodium hydroxide, also known as caustic soda, or potassium hydroxide, NaOH and KOH respectively. [101, 103]

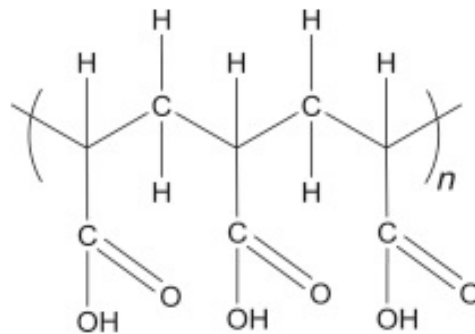


Figure 4.4: Typical chemical structure of carbopol polymers, [104]

4.1.4.4 Lignosulfonate

Lignosulfonate is a highly anionic polymer derived from by-products created during the production of sulphite paper from coniferous woods. It is a dispersant primarily used in drilling fluids to control the flocculation of bentonite, thus it functions as a thinning agent. However, lignosulfonate is also used to reduce fluid loss. The polymer is considered to perform better at pH > 10 and is temperature stable up until 200°C. [8, 12]

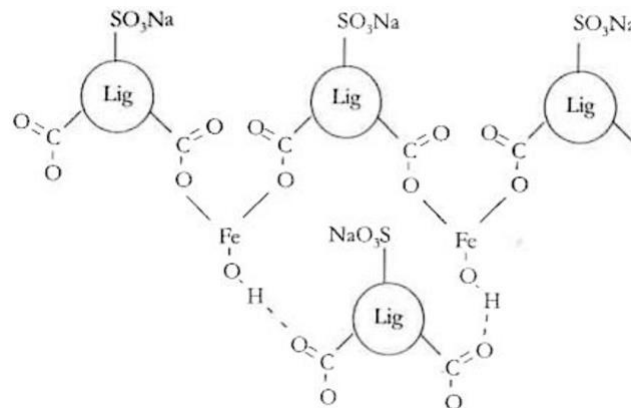


Figure 4.5: Chemical structure of lignosulfonate, [8]

4.1.5 Nanoparticle Additives

Nanoparticles were added to the best performing flat rheology system in order to modify the fluid properties. All nanoparticles to be applied in this thesis are described in this subsection. It is to be noted that the nanoparticles studied in this thesis are in liquid dispersion and not in powder form.

4.1.5.1 Multi-Walled Carbon Nanotube

Carbon nanotubes exist as single-walled or multi-walled structures, SWCNT and MWCNT respectively. The multi-walled carbon nanotube simply consists of concentric single-walled carbon nanotubes which are held together by weak van der Waals forces. Thus, the two structures are merely cylinders with one or several layers of graphene sheets. A multi-walled carbon nanotube modified with the carboxyl group, MWCNT-COOH, was used in this thesis. It provides an additional property in the form of increased dispersibility in water. [105, 106]

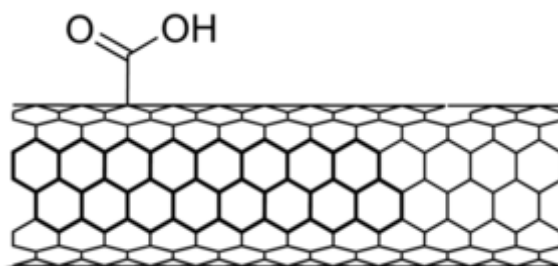


Figure 4.6: Chemical structure of MWCNT-COOH, [107]

In general, CNTs have shown exceptional physical and mechanical properties. Its stiffness, strength and resilience have been reported to exceed that of any current material. In addition, carbon nanotubes possess unique thermal and electronic properties. It is known to be thermally stable up until 2800°C in vacuum and has a thermal conductivity almost twice that of diamonds. These properties do, however, depend on the atomic arrangement, diameter and length of the nanotubes, as well as its morphology and structure. [106]

The MWCNT-COOH used in this thesis was purchased from US Research Nanomaterials in a 3 wt% water solution. The outside diameter of the nanoparticles is between 20-30 nm, whilst the inside diameter is between 5-10 nm. Furthermore, it has a length of 10-30 µm and a density of ~2.10 g/cm³ [108]. Figure 4.7 shows the solution of 0.07 g MWCNT-COOH dispersed in 350 ml freshwater. As seen, the nanoparticle suspension displays good dispersion properties both at the time of mixture and after ~24 hours.



Figure 4.7: MWCNT-COOH solution dispersed in water, immediately (left) and after 24 hours (right)

4.1.5.2 Silicon Dioxide

Silicon dioxide, more commonly known as silica, is a naturally occurring compound of silicon and oxygen [109]. The nanoparticle has the chemical formula SiO_2 and is widely used in several industries. For instance, the particle is added as a strengthening filler in concrete and other construction composites. In addition, it is used as an additive in many other products, such as plastics, ceramics, glass and fibers. [110]

In this thesis, a colloidal silica called NYACOL DP9711 is used and it is obtained at a 30 % weight concentration from Nyacol Nano Technologies. This silica is surface modified, which means that it provides polymer systems with reactive surfaces [111]. The nominal particle size of the product is 20 nm and it is known to exhibit great stability over a wide range of pH values. In regards to application in drilling fluids, the nanoparticle is typically used for fluid loss control. [112]

Figure 4.8 presents the mixture of 0.13 g SiO_2 and 350 ml freshwater. As seen, the silica suspension display great dispersion properties both immediately and after 24 hours. It is to be noted, that the darker spots are leftover markings on the glass container.



Figure 4.8: Silica solution dispersed in water, immediately (left) and after 24 hours (right)

4.1.5.3 Aluminum Oxide

Aluminum oxide, also known as alumina, is a synthetic nanoparticle with the chemical formula Al_2O_3 [113]. It is used in a wide range of industries and is found in for example fillers, ceramics, paint and rubber. Depending on the area of application, the nanoparticle could be utilized to improve the lubricity, hardness and thermal properties of materials [114].

In this thesis, an alpha aluminum oxide water dispersion is to be tested. The product is provided by US Research Nanomaterials with a 20 % weight concentration, original particle size of 30 nm and particle density of 3.95 g/cm^3 [115]. Previous studies have shown that aluminum oxide nanoparticles could improve the rheological and filtration properties of drilling fluids. However, little research has been conducted regarding application in mud and therefore, it is still relatively unknown how the product will impact its properties. [1]

The dispersion properties of 0.13 g aluminum oxide in 350 ml freshwater is displayed in figure 4.9. As seen, the nanoparticle suspension appears to disperse well immediately, but particles settle with time. The poor dispersion in water could be due to the higher density of the nanoparticles of the suspensions. Though, the particles might still be suspended in the drilling fluid because of its viscous properties.

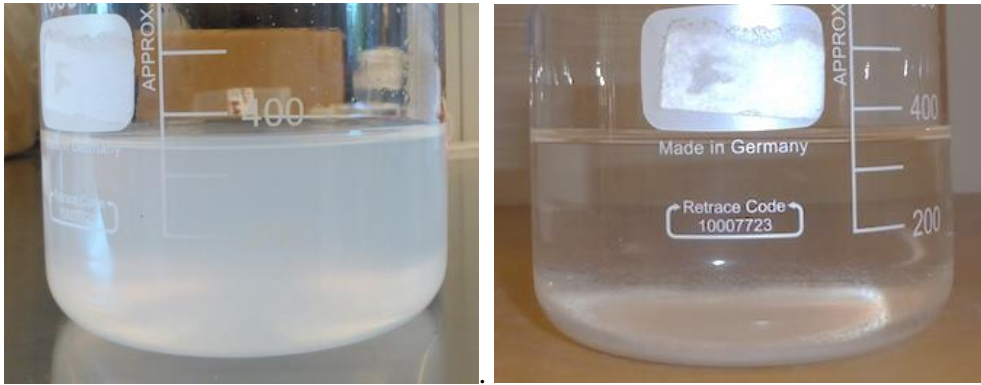


Figure 4.9: Aluminum oxide solution dispersed in water, immediately (left) and after 24 hours (right)

4.2 Experimental Equipment and Methodology

4.2.1 Hamilton Beach Mixer

A Hamilton Beach Mixer and mixing cup was used to mix all drilling fluid formulations in this thesis. The mixing procedure of the fluids are presented in table 4.2, 4.5 and 4.9. As seen in the procedures, the apparatus has three speed settings from low to high. These are represented with I, II and III and are switched between using a button on the upper surface of the device. The fluids were mixed for approximately 2 minutes prior to performing any experimental tests. This was to regain a homogeneous blend of particles in the fluid.



Figure 4.10: Hamilton Beach Mixer (with mixing cup)

4.2.2 OFITE Viscometer and Rheology Measurements

An OFITE Model 800 8-Speed viscometer was used to determine the rheological characteristics of all drilling fluids in this thesis. The viscometer has eight test speeds: 600, 300, 200, 100, 60, 30, 6 and 3 RPM. Measurements were taken for all shear rates and when performing the test, the respective shear stress for each shear rate was displayed in the dial window on the top surface of the apparatus.

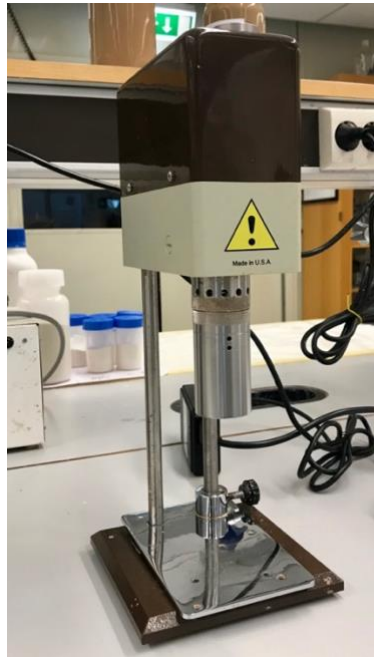


Figure 4.11: OFITE Model 800 8-Speed viscometer

A heating device was used to control the temperature of the fluid while taking the measurements. An OFITE Thermocup with a removable stainless steel cup was applied for this purpose. Measurements were taken at 22°C, 50°C and 80°C to observe how the fluids rheological properties varied with temperature. The procedure to carry out the test is as follows:

1. Place fluid in heating cup. When measuring at room temperature, keep the heater off.
2. Use a digital thermometer to measure the temperature of the fluid.
3. When the fluid reaches the desired fluid temperature, measure shear stress at all shear rates.
4. Repeat steps above for all test temperatures.

4.2.3 Anton Paar Rheometer

An Anton Paar MCR 302 rheometer was used to investigate the rheological and viscoelastic properties of the drilling fluid systems. The apparatus can be used for both shear and torsional

tests, meaning that the rotation is either continuous or oscillatory. Furthermore, tests can be performed with a parallel plate or a “cup and bob” setup. Figure 4.12 shows an Anton Paar rheometer in its test position with a parallel plate.



Figure 4.12: Anton Paar MCR 302 rheometer with parallel plate setup

The Anton Paar rheometer was used to perform amplitude sweep and temperature sweep tests. A parallel plate setup was used when performing the oscillatory amplitude sweep tests. These tests were carried out at increasing amplitudes from 0.1-1000 % while keeping the angular frequency, ω , and temperature constant at 10 rad/s and 22°C respectively. The results from the amplitude sweep tests were used to determine the linear viscoelastic range, as well as the fluid systems structural stability, strength and dynamic yield point. Temperature sweep tests were conducted to investigate how the stability and structure of fluids were dependent on temperature. These tests were conducted using both the parallel plate and “cup and bob” setup with temperatures ranging from 20-80°C and constant continuous rotation.

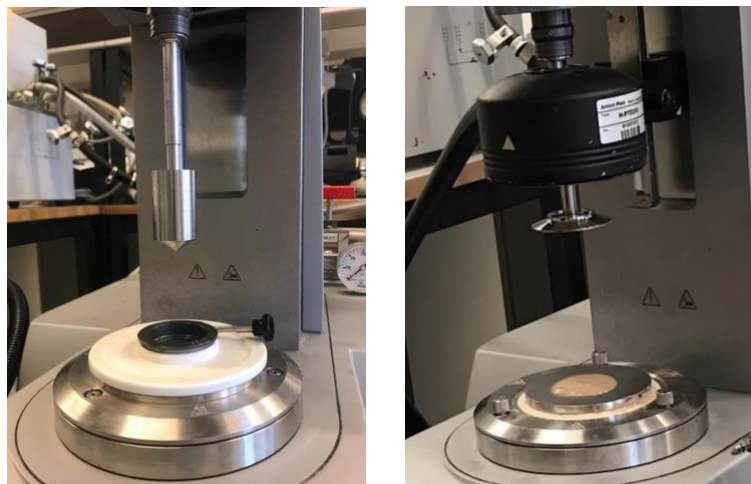


Figure 4.13: “Cup and bob” (left) and parallel plate (right) setup with test sample

4.2.4 API Static Filter Press and Fluid Loss Measurement Procedure

An API static filter press was used to measure the fluid loss of the drilling fluid systems. The test is performed at room temperature while subjecting the mud to a pressure of 100 psi. As illustrated in figure 4.14, the apparatus is constructed of several elements which must be assembled prior to performing the test.

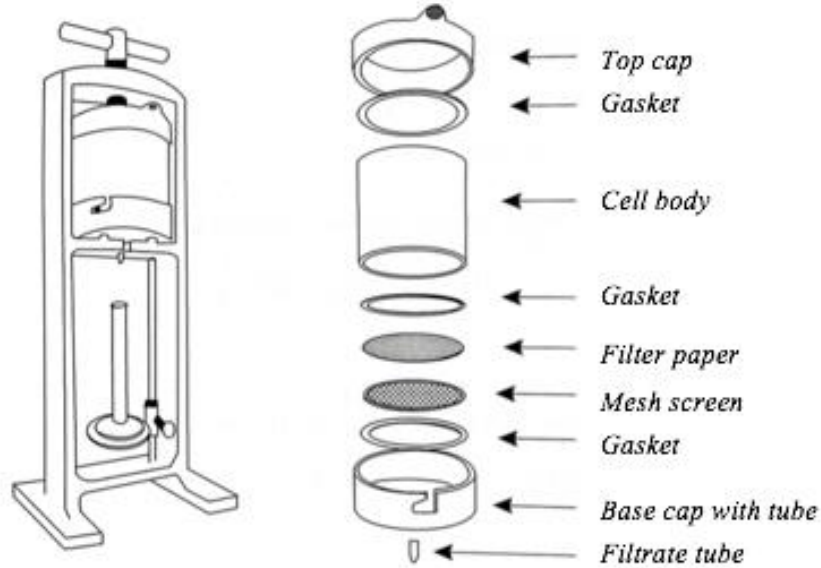


Figure 4.14: API static filter press setup and elements, [8]

A measuring cylinder is used to gather the fluid loss and usually, the collected filtrate volume is measured after 30 minutes. However, previous research has shown that doubling the amount of fluid loss measured after seven and a half minutes will result in a volume equivalent to that measured after 30 minutes. Since volume is proportional to the square root of time, the relation is found as seen the equations below. In this thesis, the fluid loss is measured after 7.5 minutes and then doubled according to the following relation. [8]

$$V_{7.5 \text{ min}} = x \cdot \sqrt{7.5} \quad \text{and} \quad V_{30 \text{ min}} = x \cdot \sqrt{30}$$

$$\begin{aligned} \frac{V_{30 \text{ min}}}{V_{7.5 \text{ min}}} &= \sqrt{\frac{30}{7.5}} \\ &= \sqrt{4} \\ &= 2 \end{aligned}$$

$$V_{30 \text{ min}} = 2 \cdot V_{7.5 \text{ min}} \tag{4.1}$$

4.2.5 Baroid Mud Balance and Density Measurement Procedure

Figure 4.15 illustrates a Baroid mud balance. This apparatus is used to measure the density of the drilling fluid systems in this thesis. The procedure of the test is as follows:

1. Place fluid in measuring cup. Make sure to fill it completely.
2. Clean all excess mud.
3. Move rider along the balance arm.
4. When the level glass shows that the weights are equivalent, the density can be read off the balance arm at the rider's position.

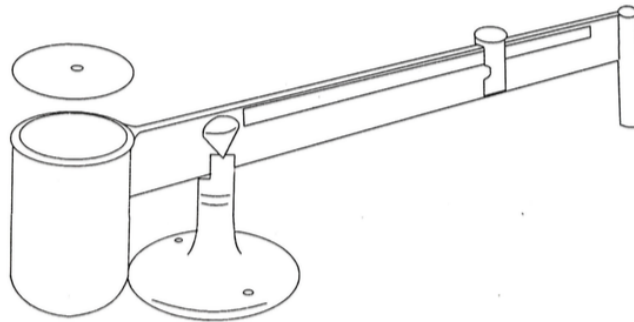


Figure 4.15: Baroid mud balance, [8]

4.2.6 pH-meter

A Mettler Toledo FiveEasy™ pH meter was used to measure the pH of the water-based drilling fluid formulations. The apparatus is presented in figure 4.16 and measures the hydrogen ion potential of the fluids using the glass-membrane electrode seen in the cup to the right. The following list presents the procedure of the test. [116, 117]

1. Remove electrode from storage solution and rinse it with deionized water.
2. Place electrode in sample and stir slowly.
3. When pH reading has stabilized, read of the value.
4. Rinse electrode with deionized water prior to placing it back in the storage solution again.

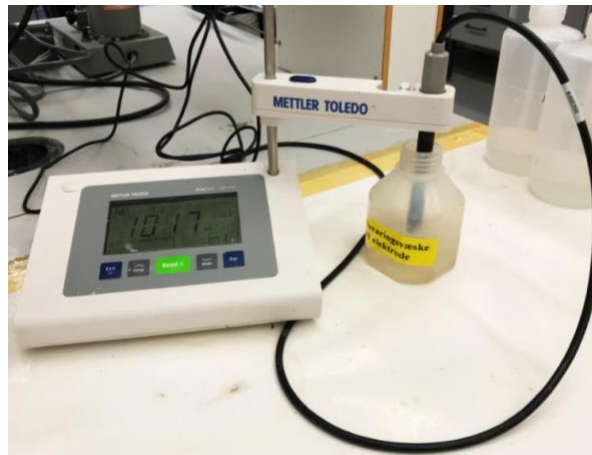


Figure 4.16: Mettler Toledo FiveEasy™ pH meter

4.2.7 Tribometer and Frictional Measurement

A CSM tribometer was used to investigate the frictional properties of the drilling fluid systems containing nanoparticle suspensions. The ball-on-disc tribometer is computer controlled and the test is conducted by loading a sphere onto the sample with a known force. In this thesis, a load of 5 N is applied to the ball-plate surface and the disc is rotating with a speed of 3 cm/s, resulting in a total test length of 9.8 minutes. During the test, the deflection of the elastic arm is measured and thus, the coefficient of friction can be obtained [118]. The test is performed at room temperature and is repeated at least twice for each system to attain representative average values. Figure 4.17 illustrates the ball-on-disc technology and its elements, while figure 4.18 shows the actual CSM tribometer used in this thesis.

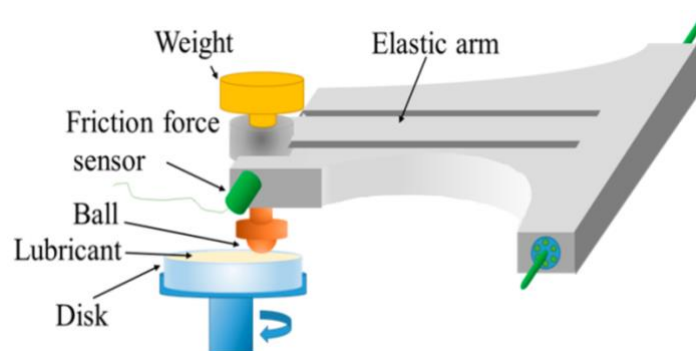


Figure 4.17: Illustration of ball-on-disc tribometer, [119]

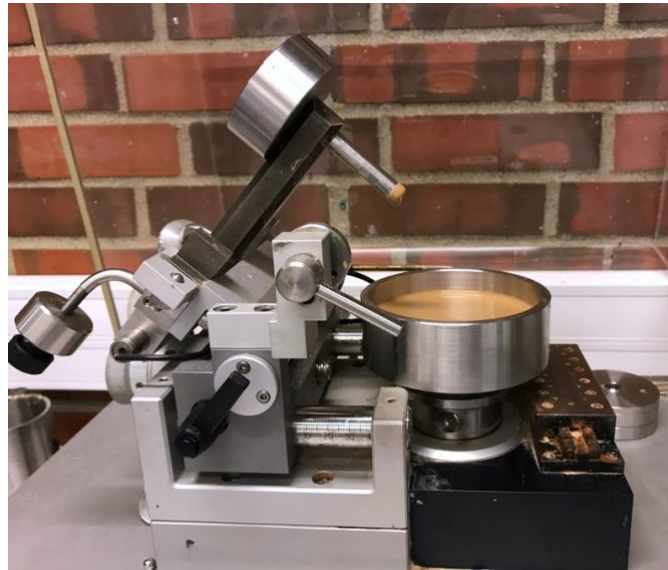


Figure 4.18: CSM tribometer with test fluid (lift position)

4.2.8 Scanning Electron Microscope

A Scanning Electron Microscope, SEM, was used to investigate the filter cake structure of the drilling fluids. The microscope is able to deliver high-resolution images and information about the element composition by scanning the surface of the sample with an electron beam. Though, the electrons of the beam are only able to interact with the sample if it is conductive and therefore, the filter cakes are coated with a palladium solution prior to utilizing the microscope. [120, 121]

4.3 Drilling Fluid Formulation with Flat Rheology

All water-based fluids formulated in this thesis were mixed and tested using the University of Stavanger’s laboratory facilities. The control formulation, referred to as the reference fluid, was mixed with water, polypac, pac, soda ash, bentonite and barite. The system was mixed in the following order and each chemical was mixed with the corresponding amount of time:

Table 4.2: Mixing order and times for the reference formulation

	Chemical	Mixing method and time
1.	Water	-
2.	Soda Ash	Stirred manually into water with a spoon until uniform.
3.	Polypac + Pac	Mixed at low speed for 5 minutes.
4.	Bentonite	Mixed at low to high speed for 5 minutes.
5.	Barite	Mixed at high speed for 10 minutes.

To achieve the desirable concentration of each additive, a Mettler Toledo Precision Weight Balance was utilized. As seen in the table above, soda ash was mixed with water and stirred manually using a spoon. Polypac and pac was blended together with a dry spoon prior to being added to the system. To minimize the amount of polymer flocculating and sticking to the cup’s wall, smaller amounts of the polymer mixture was carefully added in steps in between mixing. Further, the bentonite, which was gradually added while mixing, and barite was added. To create a well-blended fluid system, a Hamilton Beach mixer was used to mix the polymers and the rest of the additives together. Prior to performing any tests, all formulations were stored in glass bottles for 24 hours to ensure some bentonite swelling.

To increase the rheology of the reference fluid, 0.5 g carbopol was added to the mixture ex-situ. This means that the polymer was added and mixed together with the reference fluid after it was completed. While keeping the amount of these additives constant, the amount of lignosulfonate was varied to identify how the added lignosulfonate will affect the fluid system. The amounts of lignosulfonate added to the reference fluid containing 0.5 g carbopol (ex-situ) was 0.6, 0.7, 0.8 and 0.9 grams. The recipes for these fluid systems are listed in table 4.3 below.

Table 4.3: Recipe for WBM systems containing 0.5 g carbopol and various amounts of lignosulfonate

Chemical		Ref + 0.5 g CP			
		+ 0.6 g LS	+ 0.7 g LS	+ 0.8 g LS	+ 0.9 g LS
Water	[g]	350	350	350	350
Polypac	[g]	1	1	1	1
Pac	[g]	0.5	0.5	0.5	0.5
Soda Ash	[g]	4	4	4	4
Bentonite	[g]	10	10	10	10
Barite	[g]	150	150	150	150
Carbopol	[g]	0.5	0.5	0.5	0.5
Lignosulfonate	[g]	0.6	0.7	0.8	0.9
wt% lignosulfonate		0.116 %	0.135 %	0.155 %	0.174 %

Table 4.4: Recipe for WBM systems with 0.5 g carbopol added ex-situ and in-situ

Chemical		Ref	Ref + 0.5 g CP	Ref (No polypac and pac) +	Ref + 0.5 g
			(ex-situ)	0.5 g CP (in-situ) + 0.7 g LS	CP (in-situ) + 0.9 g LS
Water	[g]	350	350	350	350
Polypac	[g]	1	1	0	1
Pac	[g]	0.5	0.5	0	0.5
Soda Ash	[g]	4	4	4	4
Bentonite	[g]	10	10	10	10
Barite	[g]	150	150	150	150
Carbopol	[g]	0.0	0.5	0.5	0.5
Lignosulfonate	[g]	0.0	0.0	0.7	0.9
wt% lignosulfonate		-	-	0.136 %	0.174 %

Carbopol was also added to the reference fluid in-situ, to compare whether the method of application had any effect on the fluid system’s behavior. This was checked for two fluid systems; the reference fluid containing 0.9 g lignosulfonate and another system containing 0.7 g lignosulfonate, but no polypac and pac. The latter fluid system was of interest in order to observe the effect of carbopol alone. Table 4.4 lists the recipes for these formulations and the following table shows the order of mixing when adding lignosulfonate and carbopol (in-situ):

Table 4.5: Mixing order and times for lignosulfonate and carbopol (in-situ)

Chemical		Mixing method and time
1.	Water	-
2.	Soda Ash	Stirred manually into water with a spoon until uniform.
3.	Polypac + Pac	Mixed at low speed for 5 minutes.
4.	Carbopol	Mixed at low speed for 5 minutes.
5.	Lignosulfonate	Mixed at low speed for 5 minutes.
6.	Bentonite	Mixed at low to high speed for 5 minutes.
7.	Barite	Mixed at high speed for 10 minutes.

Based on the results obtained when testing the WBM systems specified in table 4.3 and 4.4, another three fluids were formulated with varying amounts of lignosulfonate. In addition, four fluid system with varied amounts of carbopol, added ex-situ, were formulated to observe if a smaller amount of the polymer would be sufficient to increase the systems rheology. The recipes of these various fluid systems are given in table 4.6 and 4.7.

Table 4.6: Recipe for WBM systems with 0.5 g carbopol and various amounts of lignosulfonate (1.0-1.5 g)

Chemical		Ref + 0.5 g CP		
		+ 1.0 g LS	+ 1.3 g LS	+ 1.5 g LS
Water	[g]	350	350	350
Polypac	[g]	1	1	1
Pac	[g]	0.5	0.5	0.5
Soda Ash	[g]	4	4	4
Bentonite	[g]	10	10	10
Barite	[g]	150	150	150
Carbopol	[g]	0.5	0.5	0.5
Lignosulfonate	[g]	1.0	1.3	1.5
wt% lignosulfonate		0.193 %	0.252 %	0.291 %

Table 4.7: Recipe for WBM systems with various amounts of carbopol (ex-situ)

Chemical		Ref + 0.1 g CP	Ref + 0.2 g CP	Ref + 0.3 g CP	Ref + 0.4 g CP
Water	[g]	350	350	350	350
Polypac	[g]	1	1	1	1
Pac	[g]	0.5	0.5	0.5	0.5
Soda Ash	[g]	4	4	4	4
Bentonite	[g]	10	10	10	10
Barite	[g]	150	150	150	150
Carbopol	[g]	0.1	0.2	0.3	0.4
Lignosulfonate	[g]	0	0	0	0
wt% carbopol		0.019 %	0.039 %	0.058 %	0.078 %

At this stage in the process, the UiS facilities ran out of hydrated (60-100 %) soda ash, which was the type of soda ash used in all the formulations up until this point. The UiS facilities could provide an anhydrous (100 %) soda ash, which is stronger due to absence of water. Thus, two formulations, both containing 0.1 g carbopol, were mixed with 3.2 g and 4.0 g soda ash anhydride. Based on results obtained previously, carbopol was added ex-situ. Furthermore, the reference fluid was remixed and is referred to as “REF”. The recipes for these fluid systems are given in table 4.8.

Table 4.8: Recipe for WBM systems with varied amounts of soda ash anhydride and carbopol

Chemical		REF	REF + 0.05 g CP	REF + 0.08 g CP	REF + 0.1 g CP	REF (3.2 g SA) + 0.1 g CP
Water	[g]	350	350	350	350	350
Polypac	[g]	1	1	1	1	1
Pac	[g]	0.5	0.5	0.5	0.5	0.5
Soda Ash Anhydride	[g]	4	4	4	4	3.2
Bentonite	[g]	10	10	10	10	10
Barite	[g]	150	150	150	150	150
Carbopol	[g]	0.0	0.05	0.08	0.1	0.1
wt% carbopol		-	0.010 %	0.016 %	0.019 %	0.019 %

4.4 Modification of Flat Rheology Drilling Fluid with Nanoparticles

At this stage in the process, it was decided to modify the best performing drilling fluid by adding nanoparticles. Primarily, the nanoparticles were added to investigate whether the performance of the system could be enhanced, especially by observing the fluid loss. The effect of multi-walled carbon nanotube, silica and aluminum oxide was analyzed. In this section, the REF + 0.08 g carbopol system is referred to as the reference fluid and will be denoted as REF. Furthermore, multi-walled carbon nanotube, silica and aluminum oxide will be denoted with MW, Si and Al, respectively, in the following tables and results.

Table 4.9: Mixing order and times for nanoparticle and carbopol (ex-situ)

Chemical		Mixing method and time
1.	Water	-
2.	Nanoparticle	-
3.	Soda Ash	Stirred manually into water with a spoon until uniform.
4.	Polypac + Pac	Mixed at low speed for 5 minutes.
5.	Bentonite	Mixed at low to high speed for 5 minutes.
6.	Barite	Mixed at high speed for 10 minutes.
7.	Carbopol	Mixed at high speed for 5 minutes.

Table 4.9 shows the order of mixing when adding nanoparticles and carbopol (ex-situ). All nanoparticles were added directly into the water using a 1 ml pipette. As seen in the table, the nanoparticles were not mixed into the water in any way and besides the addition of nanoparticles, the drilling fluid systems were mixed as before. The tables below list the recipes of the drilling fluid systems containing varied amounts of MWCNT-COOH, SiO₂ and Al₂O₃.

Table 4.10: Recipe for reference system with varied amounts of multi-walled carbon nanotube

Chemical		REF + 0.07 g MW	REF + 0.13 g MW	REF + 0.18 g MW	REF + 0.24 g MW
Water	[g]	350	350	350	350
Polypac	[g]	1	1	1	1
Pac	[g]	0.5	0.5	0.5	0.5
Soda Ash	[g]	4	4	4	4
Bentonite	[g]	10	10	10	10
Barite	[g]	150	150	150	150
Carbopol	[g]	0.08	0.08	0.08	0.08
MWCNT-COOH	[g]	0.07	0.13	0.18	0.24
wt% MWCNT-COOH		0.014 %	0.025 %	0.035 %	0.047 %

Table 4.11: Recipe for reference system with varied amounts of silica

Chemical		REF + 0.08 g Si	REF + 0.13 g Si	REF + 0.18 g Si	REF + 0.25 g Si
Water	[g]	350	350	350	350
Polypac	[g]	1	1	1	1
Pac	[g]	0.5	0.5	0.5	0.5
Soda Ash	[g]	4	4	4	4
Bentonite	[g]	10	10	10	10
Barite	[g]	150	150	150	150
Carbopol	[g]	0.08	0.08	0.08	0.08
SiO ₂	[g]	0.08	0.13	0.18	0.25
wt% SiO ₂		0.016 %	0.025 %	0.035 %	0.049 %

Table 4.12: Recipe for reference system with varied amounts of aluminum oxide

Chemical		REF + 0.07 g Al	REF + 0.13 g Al	REF + 0.19 g Al	REF + 0.24 g Al
Water	[g]	350	350	350	350
Polypac	[g]	1	1	1	1
Pac	[g]	0.5	0.5	0.5	0.5
Soda Ash	[g]	4	4	4	4
Bentonite	[g]	10	10	10	10
Barite	[g]	150	150	150	150
Carbopol	[g]	0.08	0.08	0.08	0.08
Al ₂ O ₃	[g]	0.07	0.13	0.19	0.24
wt% Al ₂ O ₃		0.014 %	0.025 %	0.035 %	0.047 %

As before, the silica and aluminum oxide systems were stored in glass bottles for 24 hours prior to performing any tests, whereas the multi-walled carbon nanotube systems were stored for 46 days due to the Covid-19 pandemic. Fortunately, a reference fluid formulation was stored for a longer period of time as well, 48 days to be exact, and made it possible to study the effect of aging on the MWCNT-COOH systems. For this purpose, a reference fluid system containing 0.07 g MW was tested after being stored for 24 hours.

Furthermore, a reference fluid system was aged at 62°C for nine hours prior to being stored for 48 days due to the pandemic. In addition, another sample of the reference fluid system was aged at the same temperature for 20 hours prior to performing any tests. This static aging was performed to investigate how the reference fluid would endure exposure to higher temperatures over time.

5 Results

This section presents all experimental results obtained from the rheological, viscoelastic, frictional, pH, fluid loss and mud weight measurements of the flat rheology formulations, as well as the nanoparticle modified fluids.

5.1 Effect of Hydrated versus Anhydrous Soda Ash on Rheological Parameters

As mentioned in section 4.3, hydrated (60-100 %) soda ash was initially used as the pH control agent in the system. After running out of this chemical, the UiS facilities provided an anhydrous (100 %) soda ash which was further used in the experimental study to achieve a flat rheology drilling fluid. Thus, there are two reference fluids referred to as “Ref” and “REF” containing hydrated and anhydrous soda ash, respectively. The reference fluid formulations are provided in table 4.4 and table 4.8.

The reference fluid containing hydrated soda ash, “Ref”, was not experimentally tested. This was because a visual inspection clearly showed that the fluid did not possess the required rheological properties to suspend particles. Thus, the effect of hydrated and anhydrous soda ash was investigated by comparing fluid systems containing 0.1 g carbopol. In figure 5.1, the shear stress responses of the fluid systems containing 0.1 g carbopol are plotted as a function of RPM.

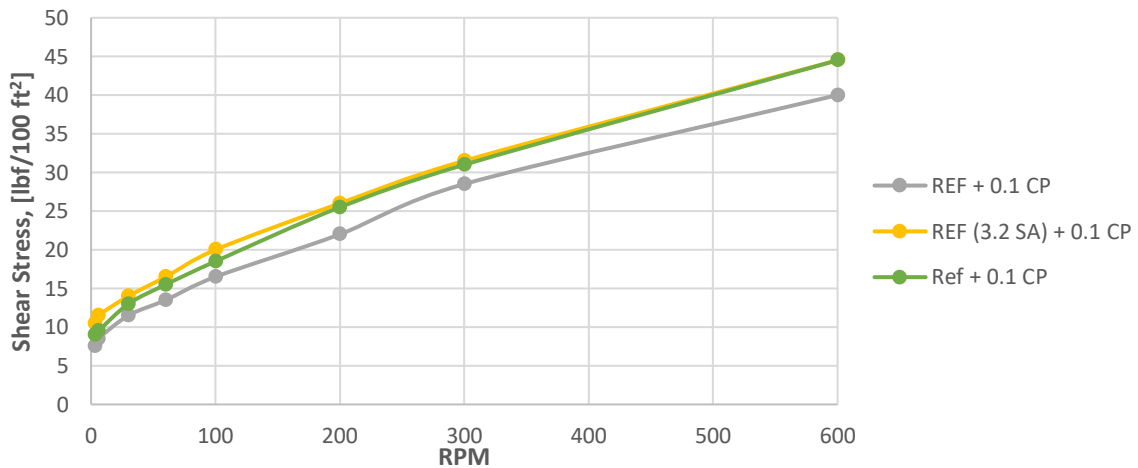


Figure 5.1: Viscometer data at 22 °C for fluids with hydrated and anhydrous soda ash

As expected, results show that the anhydrous soda ash is stronger than the hydrated one. In fact, both pH and shear stress responses measured at room temperature suggests that 3.2 g anhydrous soda ash is an approximate equivalent to 4.0 g hydrated soda ash. These results are presented in figure 5.1 and 5.2 and indicate that the two chemicals are comparable.

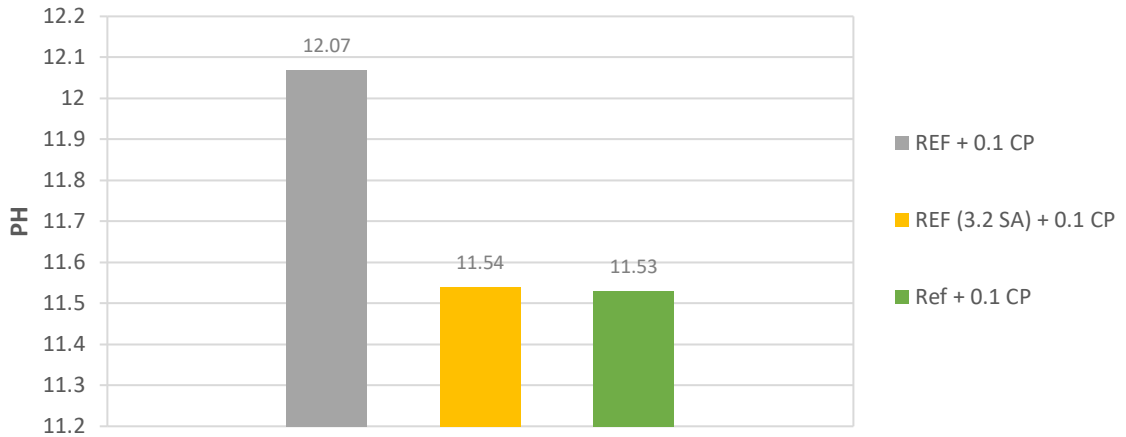


Figure 5.2: pH data at 22 °C of fluids with hydrated and anhydrous soda ash

From figure 5.3 and 5.4 below, it is seen that hydrated and anhydrous soda ash has a similar effect on the viscous properties of the drilling fluid system when measured at 50°C and 80°C as well. Thus, the systems containing hydrated and anhydrous soda ash are assumed to be comparable. Furthermore, it is seen that increasing the amount of additive from 3.2 g to 4.0 g reduces the systems rheological properties, though the effect is minor. The reason for the reduction is not investigated further due to absence of equipment. It was decided to continue the experimental research with an amount 4.0 g anhydrous soda ash. This was because the rheological properties of the fluid containing 4.0 g anhydrous soda ash were more alike those of the fluid containing 4.0 g hydrated soda ash at increasing temperatures.

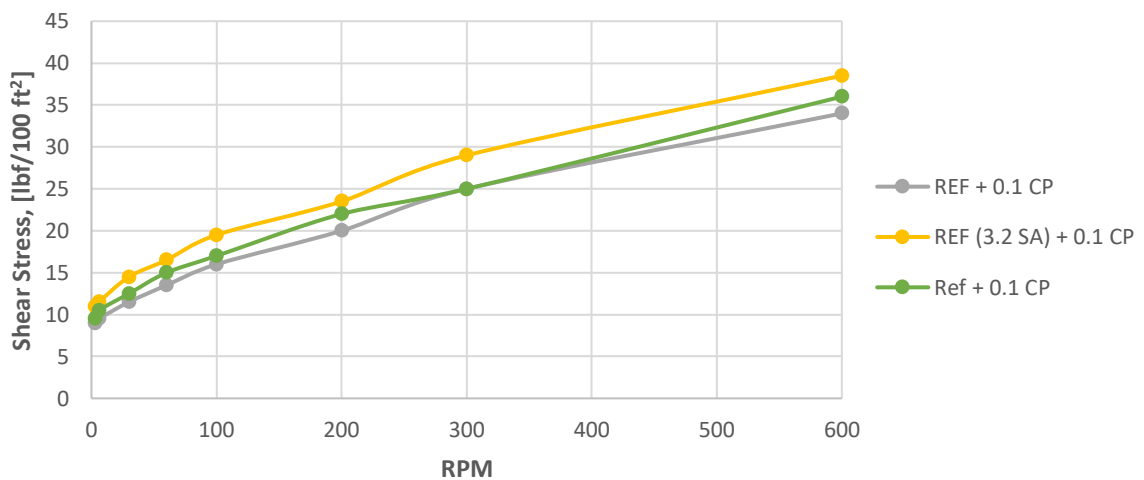


Figure 5.3: Viscometer data at 50 °C of fluids with hydrated and anhydrous soda ash

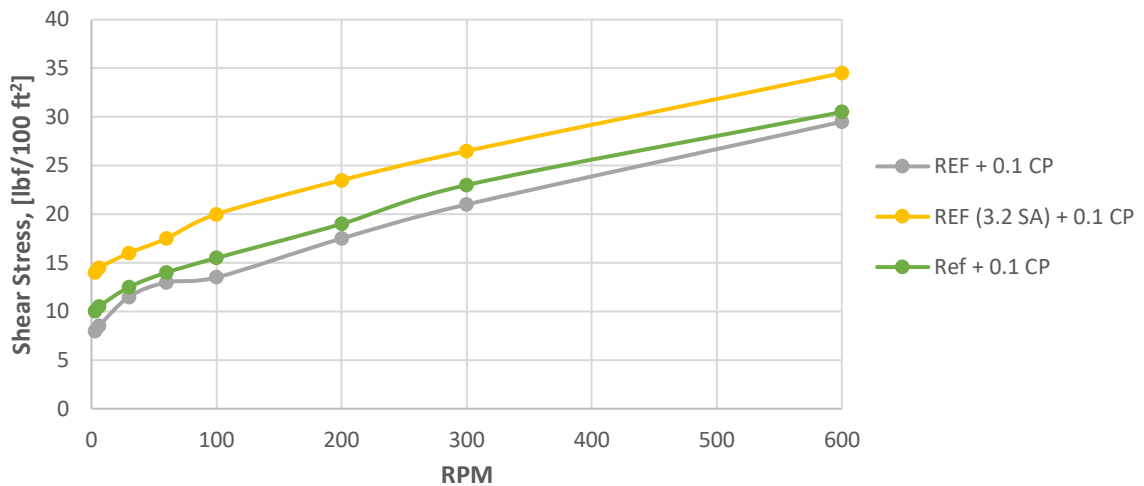


Figure 5.4: Viscometer data at 80 °C for fluids with hydrated and anhydrous soda ash

5.2 Effect of Carbopol's Method of Application on Rheological Parameters

As previously mentioned, a strict procedure of implementation is essential to attain reproducibility of carbopol fluids. This is due to the strong effect reagents, water properties and mixing procedure has on the dispersion properties of the fluid. Therefore, how the method of application will affect rheological parameters will be investigated in this subsection.

Carbopol is known to be a highly effective viscosifier, an ability demonstrated in section 5.4.1 when the viscosity of the reference fluid is increased significantly. This viscometer response is, however, a result of adding carbopol ex-situ. In figure 5.5, it is observed that two carbopol fluids with an identical composition of chemicals do not exhibit the same viscometer dial readings. Both viscosity profiles are provided by a reference fluid containing 0.5 g carbopol and 0.9 g lignosulfonate, however, the order of carbopol's application is different. Fundamentally, the distinction between the two viscosity profiles is due to them having different dispersion properties which could be a result of differing bentonite-polymer interaction. Though, there can be several factors affecting how the fluid structure will differ depending on the method of application.

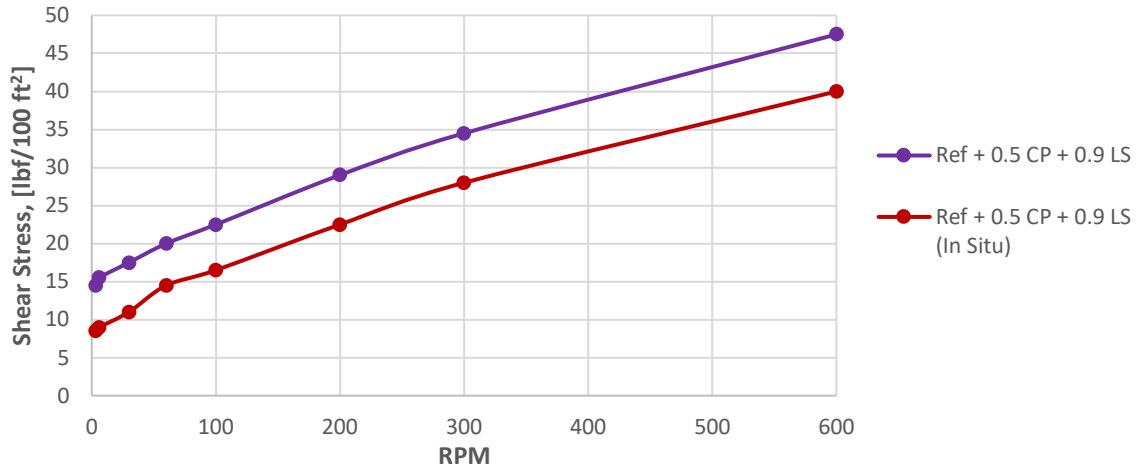


Figure 5.5: Viscometer data at 50°C to compare ex-situ and in-situ application of carbopol (1)

It is clearly seen that adding carbopol ex-situ induce greater viscometer dial readings compared to adding the polymer in-situ. The same trend is observed in figure 5.6, where the calculated yield stresses are presented at varied temperatures. Furthermore, a greater amount of foam was generated while mixing the in-situ system compared to the ex-situ one. This is related to the amount of water available when adding the polymer. When carbopol is added ex-situ, most of the water has already been consumed by other products, while the polymer will have easy access to water when added in-situ. The formation of foam hinders entrapment of water within the clay structure and consequently, free fluid will be present in the system. To limit the formation of foam, approximately 12 drops of anti-foam was added to the in-situ system, however, a complete removal was not obtained. Thus, both the presence of bubbles and addition of anti-foam could be contributing factors to why the rheological parameters of the fluid systems differ.

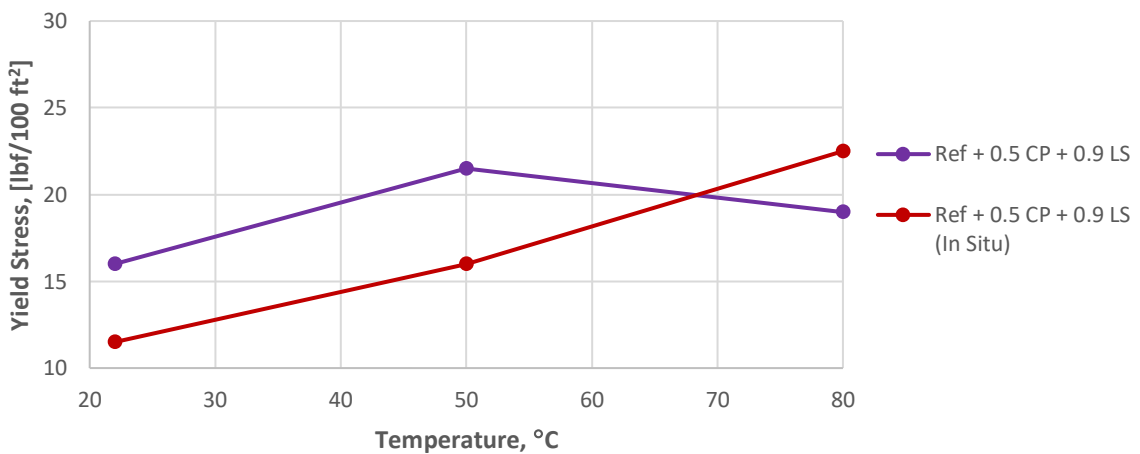


Figure 5.6: Bingham yield stress to compare ex-situ and in-situ application of carbopol

5.3 Effect of Carbopol

A reference fluid without polypac and pac was mixed to investigate the effect of carbopol alone. An amount of 0.5 g carbopol, added in-situ, and 0.7 g lignosulfonate was added to the system, whose recipe is presented in table 4.4. As discovered in section 5.2, the method of carbopol's application do influence the rheological properties of the system. Thus, the viscometer dial readings are also compared to the in-situ system containing 0.9 g lignosulfonate.

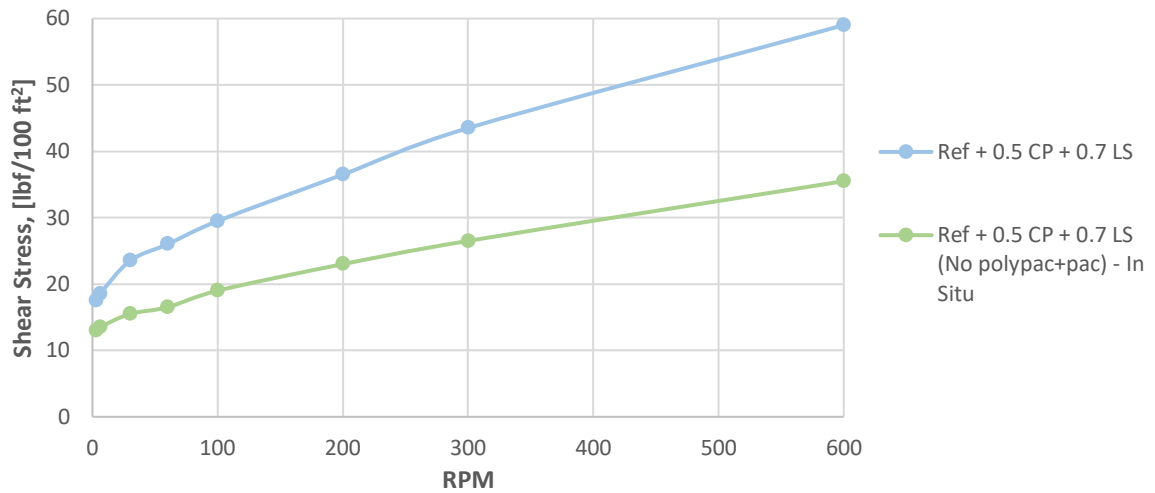


Figure 5.7: Viscometer data at 50 °C to compare ex-situ and in-situ application of carbopol (2)

In figure 5.5 and 5.7, it is observed that the viscosity profile is lower when adding carbopol in-situ. Comparing the two figures reveals that the gap between the viscosity profiles of the systems containing 0.7 g lignosulfonate is greater than that of the systems containing 0.9 g lignosulfonate. Most likely, this difference is due to the absence of polypac and pac. Consequently, the same trend is observed in figure 5.8, which illustrates the yield stresses of the 0.7 g lignosulfonate fluids.

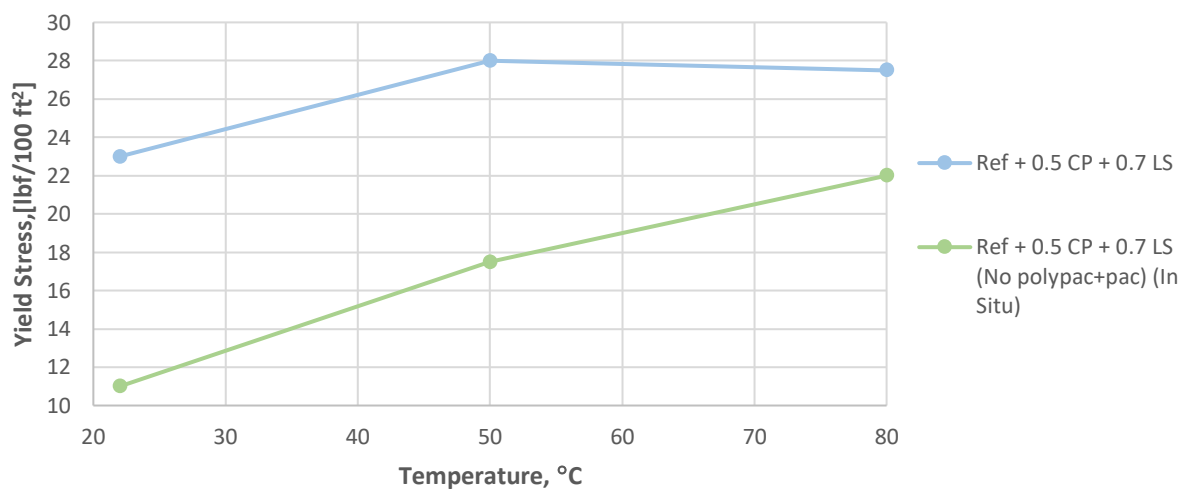


Figure 5.8: Bingham yield stress to investigate the effect of carbopol alone

Furthermore, it is observed that the fluid system without polypac and pac contains a considerable amount of free fluid. Figure 5.9 shows the ex-situ (left) and in-situ (right) systems containing 0.7 g lignosulfonate after being aged static for one hour at 22°C. It is seen that free fluid has accumulated rapidly at the surface and that the amount of free fluid of the in-situ system increases significantly with time. This is shown in figure 5.10, where the two in-situ systems containing 0.9 g (left) and 0.7 g (right) lignosulfonate, respectively, have been aged for approximately 24 hours under the same conditions as before.



Figure 5.9: Free fluid accumulating at the surface after ~1 hour



Figure 5.10: Free fluid accumulated at surface after ~1 day

In figure 5.10, it is seen that the system with polypac and pac hardly has any free fluid at its surface, while a greater amount is present for the system without these products. In addition to the considerable amount of free fluid accumulating at the surface, some free fluid is also detected within the 0.7 g lignosulfonate system. This indicates that the fluid loss of this drilling fluid will be high as well. Since polypac and pac is added for viscosity and fluid loss control, these results are as expected and justify the application of these polymers in the drilling fluid.

5.4 Flat Rheology Drilling Fluid Formulation

In this subsection, the experimental results obtained while constructing a thermally stable system is presented. The drilling fluid formulations examined to achieve such a system are presented in section 4.3.

5.4.1 Increasing the Viscosity of the Reference Fluid

As mentioned, the reference fluid did not possess the required property of suspending particles, thus its viscosity had to be increased using a polymer called carbopol. An amount of 0.5 g was used for this purpose and, as seen in the figure below, the viscometer response increased significantly. In addition, a visual inspection of the fluid indicated that its ability to suspend particles was improved. Since carbopol is known to function as a suspension agent and to increase the viscosity of fluids, these results were as expected.

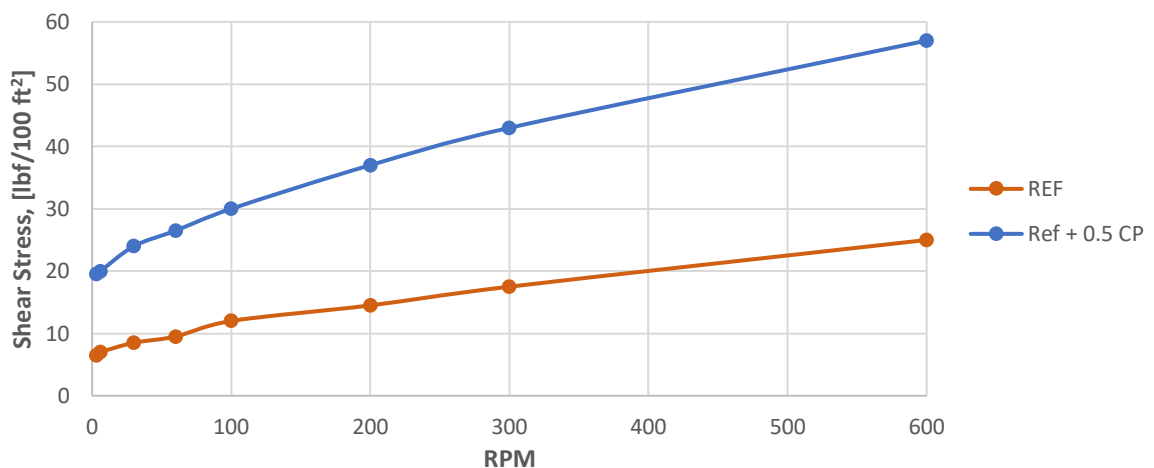


Figure 5.11: Viscometer data at 50°C for reference fluid containing 0.5 g carbopol

5.4.2 Effect of Lignosulfonate and Temperature on Rheological Parameters

After increasing the viscosity of the reference fluid with carbopol, varied amounts of lignosulfonate were added to investigate its influence on the fluid system. Primarily, the polymers effect on the viscometer readings and calculated yield stresses were analyzed.

In figure 5.12, the viscometer results are presented for the drilling fluids containing 0.6-0.9 g lignosulfonate. It is seen that the viscosity of the fluid generally decreases with added lignosulfonate, however the trend is nonlinear. Lignosulfonate is known to work as a dispersant

in clay fluids and functions as thinning agent as it prevents flocculation of bentonite. Thus, the results of less viscous fluids are as expected.

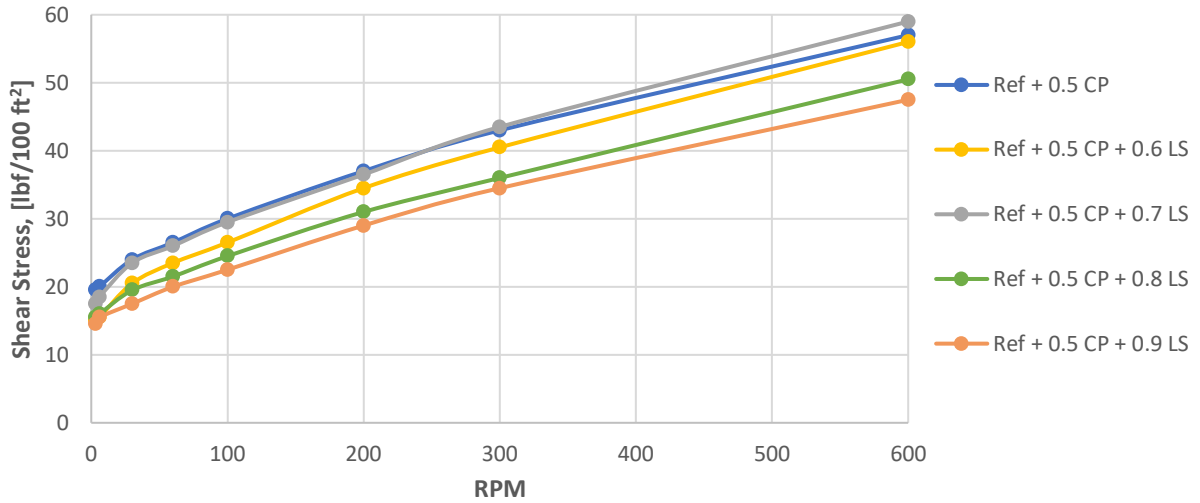


Figure 5.12: Viscometer data at 50°C for lignosulfonate fluids (0.6-0.9 g)

Figure 5.13 illustrates the calculated yield stresses at varied temperatures for the fluid systems presented in the figure above. The yield stress calculations are based on the Bingham Plastic model and are computed using viscosity measurements obtained at 22°C, 50°C and 80°C. Thus, the line connecting the three points is merely used to provide a visual representation of the anticipated yield stress profile of the fluid systems. This is the case for all Bingham yield stress plots presented in this thesis.

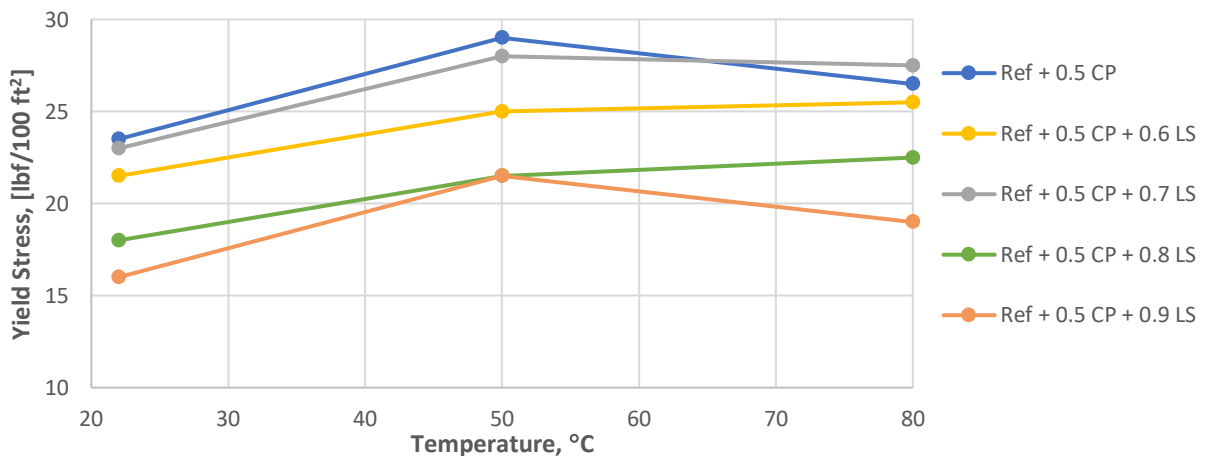


Figure 5.13: Bingham yield stress of lignosulfonate fluids (0.6-0.9 g) at varied temperatures

As observed in figure 5.13, the yield stress decreases non-linearly with added lignosulfonate. However, the system containing 0.7 g lignosulfonate produces a higher yield stress and viscosity, as seen in figure 5.12, compared to the systems with a lower amount of polymer.

Even with these reduced yield stresses, none of the fluids are within the range of 11-20 lbf/100 ft² which is commonly applied in the field to ensure efficient cuttings transport. Furthermore, the fluid systems do not exhibit a stable yield stress within the entire temperature range, though most of the fluids exhibit flat rheology characteristics at temperatures above 50°C. To reduce the yield stress values further and to investigate whether thermal stability could be obtained at lower temperatures as well, it was decided to investigate the effect of larger quantities of lignosulfonate.

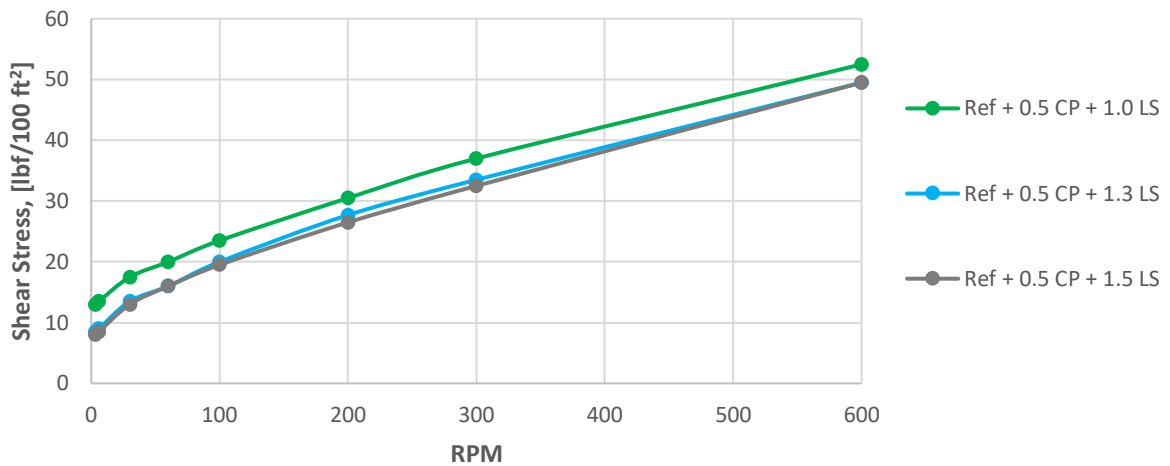


Figure 5.14: Viscometer data at 50°C for lignosulfonate fluids (1.0-1.5 g)

The viscometer dial readings for the drilling fluid systems containing 1.0 – 1.5 g lignosulfonate are presented in figure 5.14, while the corresponding Bingham yield stresses are presented in figure 5.15. It is observed that increasing the amount of lignosulfonate further results in less stable yield stresses with increasing temperature. In addition, the yield stress values of the systems still exceed the recommended range of Bingham yield stress values.

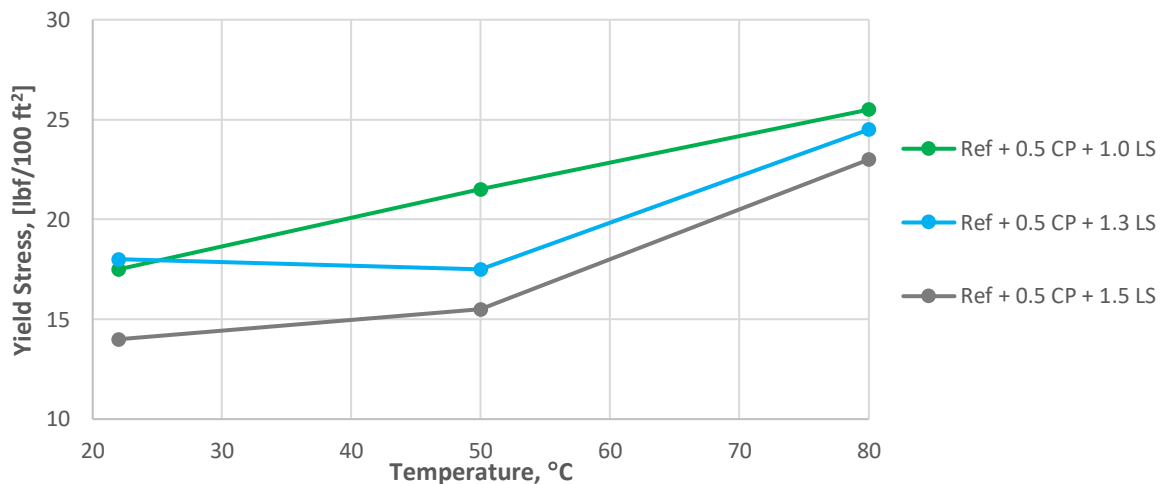


Figure 5.15: Bingham yield stress of lignosulfonate fluids (1.0-1.5 g)

At this point, the fluid systems containing 0.6, 0.7 and 0.8 grams appears to be amongst the most stable fluids as they are quite stable at temperatures above 50°C. However, none of the fluids containing lignosulfonate are stable throughout the entire temperature interval, as well as having yield stresses exceeding the recommended range for water-based drilling fluids. Thus, it was decided to further investigate varied quantities of carbopol in order to lower the yield stress of the system, as well as obtaining stable yield stress values as a function of temperature.

5.4.3 Effect of Lignosulfonate on Viscoelastic Properties

Figure 5.16 and 5.17 illustrates the results from the amplitude sweeps of the lignosulfonate fluids presented in table 4.3 and 4.6, respectively. The resulting storage and loss modulus are presented on the y-axis, while the shear strain is shown on the x-axis. Both axes have a logarithmic scale and in the following figures, it is observed that the storage modulus is greater than the loss modulus for all formulations. This indicates that the fluids have a more gel-like character than a liquid one in the linear viscoelastic range.

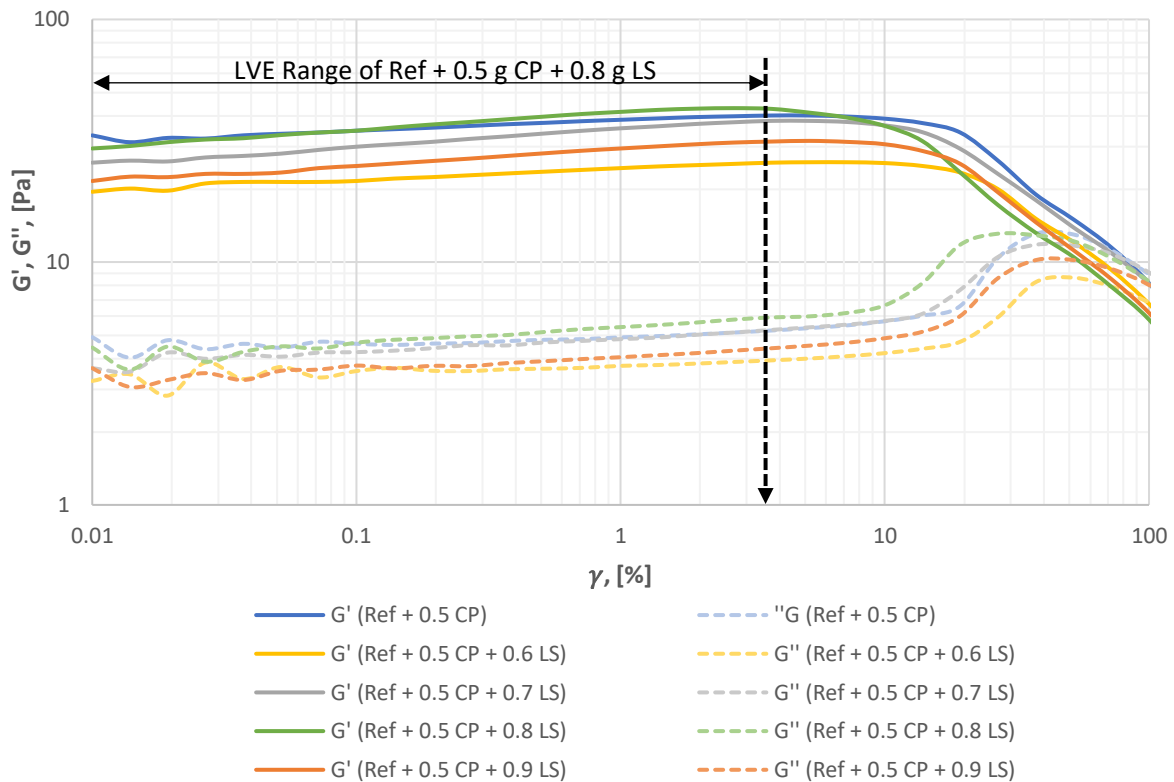


Figure 5.16: Amplitude sweep results for lignosulfonate fluids (0.6-0.9 g)

In figure 5.16, the LVE range of the reference fluid containing 0.5 g carbopol and 0.8 g lignosulfonate is illustrated. The upper limits of the other fluids in this diagram are slightly greater than that of the illustrated system and their values are presented in table 5.1. It is seen

that the reference fluid containing 0.5 g carbopol and 1.3 g lignosulfonate has the topmost upper limit with a value of 5.07 %. Furthermore, the loss modulus curves of these fluids all show a high peak before the viscous portion of viscoelastic behavior prevails. Such an increase in the loss modulus is also observed for the fluids in figure 5.17, however the peak is not as substantial for these lignosulfonate systems.

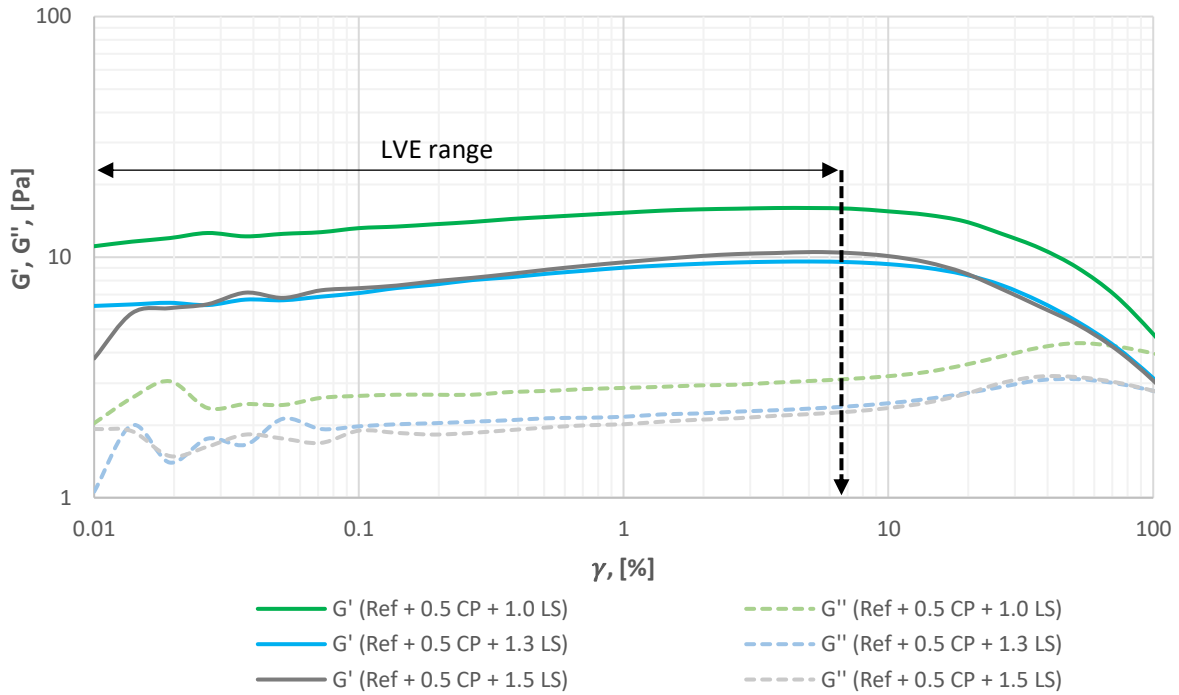


Figure 5.17: Amplitude sweep results for lignosulfonate fluids (1.0-1.5 g)

An approximate region of linear viscoelasticity is illustrated for the 1.0-1.5 g lignosulfonate fluids in figure 5.17 and the limiting values, γ_L , for each of the fluids are presented in table 5.1. It is observed that the storage and loss modulus curves of these lignosulfonate fluids are lower than those of the systems containing 0.6-0.9 g lignosulfonate. In general, it is seen the addition of lignosulfonate reduces the G' and G'' . It is also observed that the yield point of the reference fluid decreases with increasing amounts of lignosulfonate. This is the case for all fluids except the one containing 0.7 g lignosulfonate, which is the system whose yield stress and viscometer measurements also deviated from those of the other fluids.

Furthermore, the yield point, τ_y , and flow point, τ_f , of the fluid systems can be obtained from the strain amplitude sweep results. In subsection 2.6.2.2, it is described how these parameters can be estimated from a diagram where the measuring curves, G' and G'' , are plotted versus shear stress. However, τ_y and τ_f can also be obtained using a diagram with the phase shift angle and shear stress presented on the y- and x-axis respectively. It is known that the viscous and

elastic behavior of a sample are balanced when the phase shift angle is equal to 45° and therefore, the flow point can be obtained as illustrated in figure 5.18. To get more accurate numbers than those read of the graph, the flow points have been identified using interpolation. These values are presented in table 5.1.

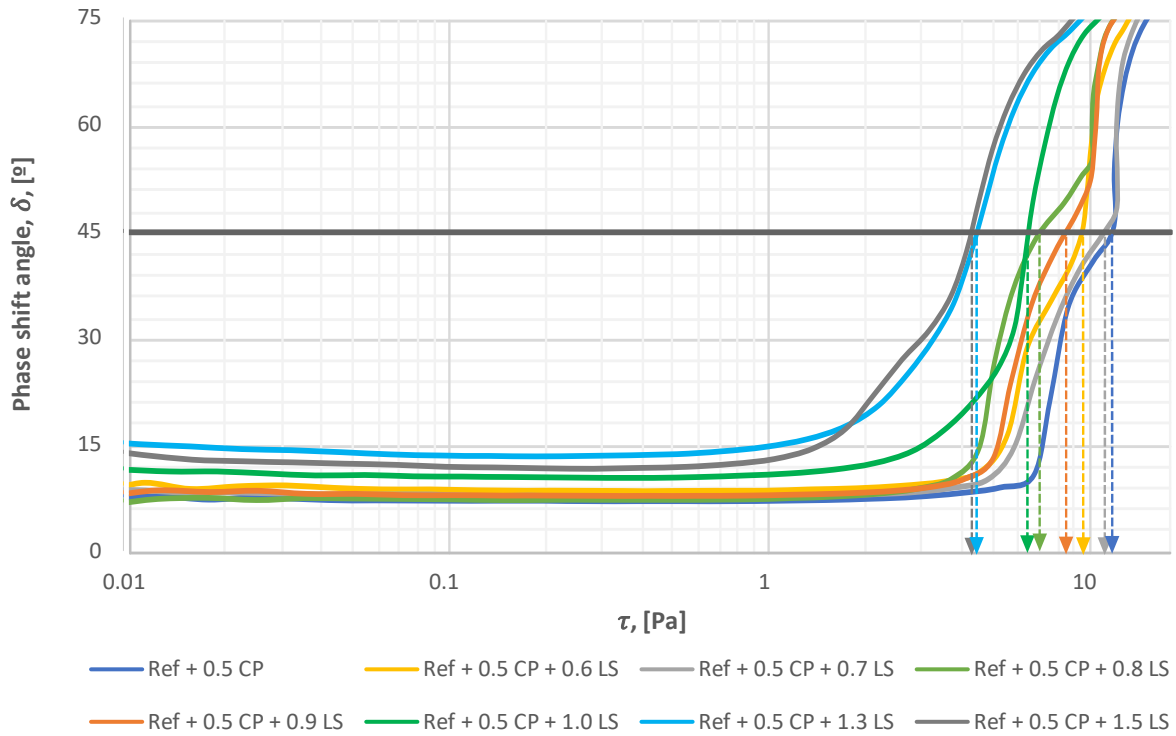


Figure 5.18: Phase shift angle vs. shear stress for lignosulfonate fluids

Section 2.6.2.2. also describes how the G' and G'' versus shear stress plot could be used to determine the yield point of a sample. However, the diagram presented in figure 5.18 was used to establish this parameter as well. In this diagram, the yield point is obtained by defining the shear stress value at which the phase shift angle begins to increase. Like the other parameters obtained from the amplitude sweeps of the lignosulfonate fluids, the yield point is presented in table 5.1. Here it is observed that the yield point and flow point of the reference fluid decreases with increasing amounts of lignosulfonate. To be noted, the limiting values, γ_L , are obtained using interpolation after determining the yield points.

Table 5.1: Summary of important parameters obtained from the amplitude sweeps of lignosulfonate fluids

Fluid system	ν_L , [%]	τ_y , [Pa]	τ_f , [Pa]
Ref + 0.5 CP	4.93	2.00	11.73
Ref + 0.5 CP + 0.6 LS	3.85	1.00	9.53
Ref + 0.5 CP + 0.7 LS	3.26	1.25	11.18
Ref + 0.5 CP + 0.8 LS	2.30	1.00	7.03
Ref + 0.5 CP + 0.9 LS	2.55	0.80	8.46
Ref + 0.5 CP + 1.0 LS	4.29	0.70	6.47
Ref + 0.5 CP + 1.3 LS	5.07	0.50	4.42
Ref + 0.5 CP + 1.5 LS	4.68	0.50	4.29

5.4.4 Effect of Carbopol and Temperature on Rheological Parameters

Desirable characteristics of the fluid system were not achieved by adding lignosulfonate, thus the effect of varying amounts of carbopol was investigated. As for the fluids containing lignosulfonate, the viscometer readings and calculated yield stresses were analyzed.

In section 5.4.2 it was established that the initial amount of 0.5 g carbopol should be decreased in order to obtain yield stresses within 11 and 20 lbf/100 ft². Figure 5.19 presents the viscometer response of the fluid systems containing 0.1-0.4 g carbopol. As expected, the viscosity of the system declines non-linearly when the amount of polymer is reduced. Consequently, the corresponding yield stresses, which are presented in figure 5.20, are also lowered. The system containing 0.1 g carbopol is the only fluid within the recommended range of yield stresses. However, a more stable yield stress profile with increasing temperature is desirable and thus, it was decided to reduce the quantity of carbopol further.

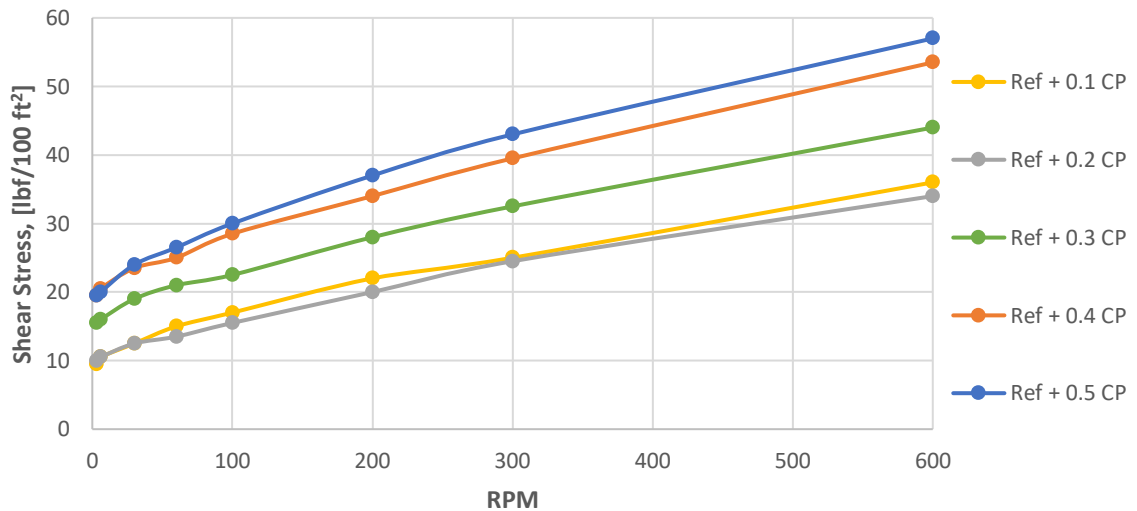


Figure 5.19: Viscometer data at 50°C for carbopol fluids (0.1-0.5 g)

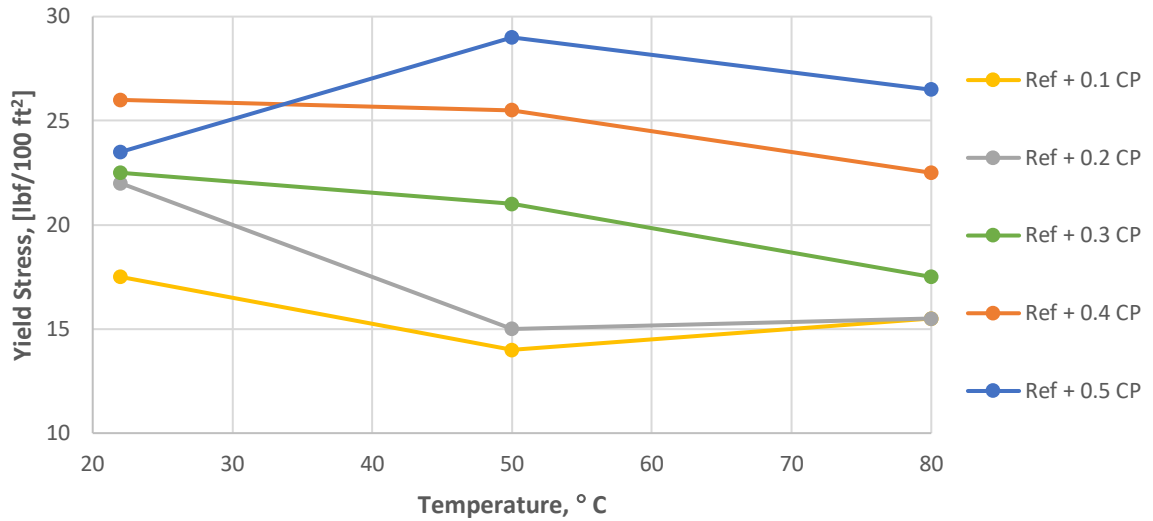


Figure 5.20: Bingham yield stress of carbopol fluids (0.1-0.5 g)

As observed in figure 5.21, reducing the added amount of carbopol further did not have a significant impact on the viscometer response. However, the corresponding yield stress profiles exhibit stable yield stress with increasing temperature. Figure 5.22 illustrates the calculated yield stresses of the fluid systems containing 0.05-0.1 g carbopol. From these results, it was found that adding 0.08 g carbopol to the reference fluid provides the system with the most temperature stable yield stress values. Therefore, it was decided to proceed with this fluid as the best performing drilling fluid with regards to obtaining a flat rheology system.

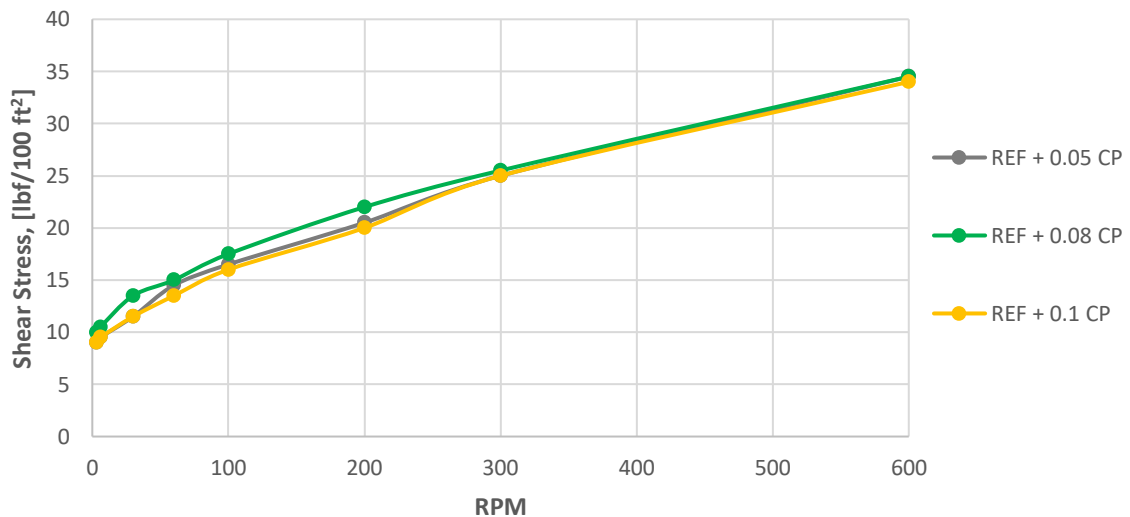


Figure 5.21: Viscometer data at 50 °C for carbopol fluids (0.05-0.1 g)

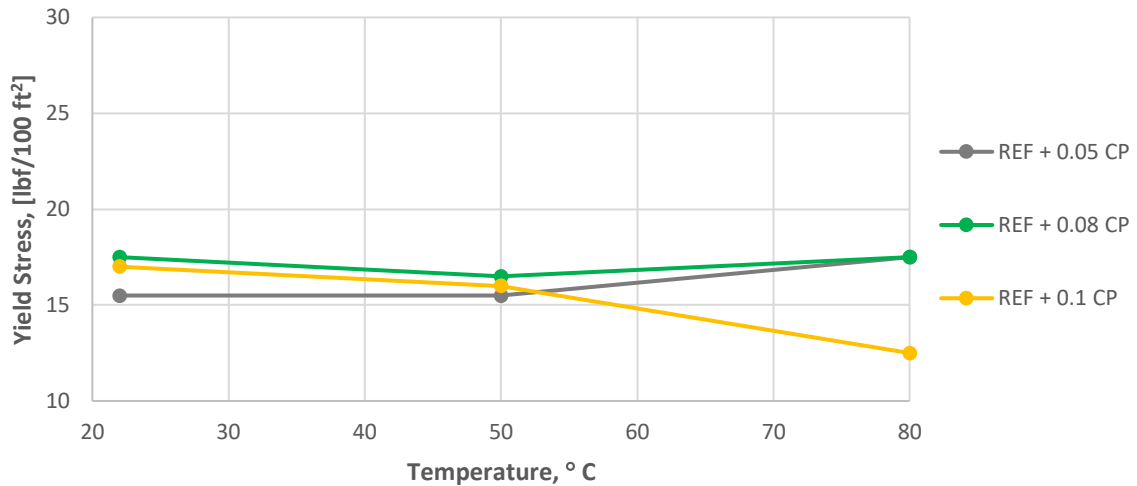


Figure 5.22: Bingham yield stress of carbopol fluids (0.05-0.1 g)

5.4.4.1 Rotational Temperature Sweep

Rotational temperature sweeps were conducted to further investigate the effect of temperature on the structure and stability of the fluids. Sweeps were performed on the systems containing 0.05 g, 0.08 g and 1.0 g carbopol, where the latter system contains 3.2 g soda ash. Both the parallel plate and “cup and bob” setup was used with constant continuous rotation.

At first, the reference fluid system containing 0.05 g carbopol was tested using the parallel plate setup. With this setup, the sweep is performed on a small amount of sample and therefore, two sweeps were conducted due to concerns that water evaporation would cause the sample to completely dry out at increasing temperatures. The two sweeps were performed at temperatures ranging from 20-50°C and 50-80°C. As observed in figure 5.23, water began to evaporate from the sample when surpassing a temperature of 50°C, even though the second sweep with a new sample had just been initiated. From the figure, it is seen that the resulting viscosity is increasing with temperature prior to dropping rapidly at around 70°C. This indicates that water is evaporating from the sample until it is completely dried out at the dropping point. Thereafter, the attained viscosity is equal to zero implying that there is no contact between the moving plate and the sample. Thus, the measurement is merely the viscosity of air. Figure A.1 in appendix A shows the dried-out sample after completing the temperature sweep.

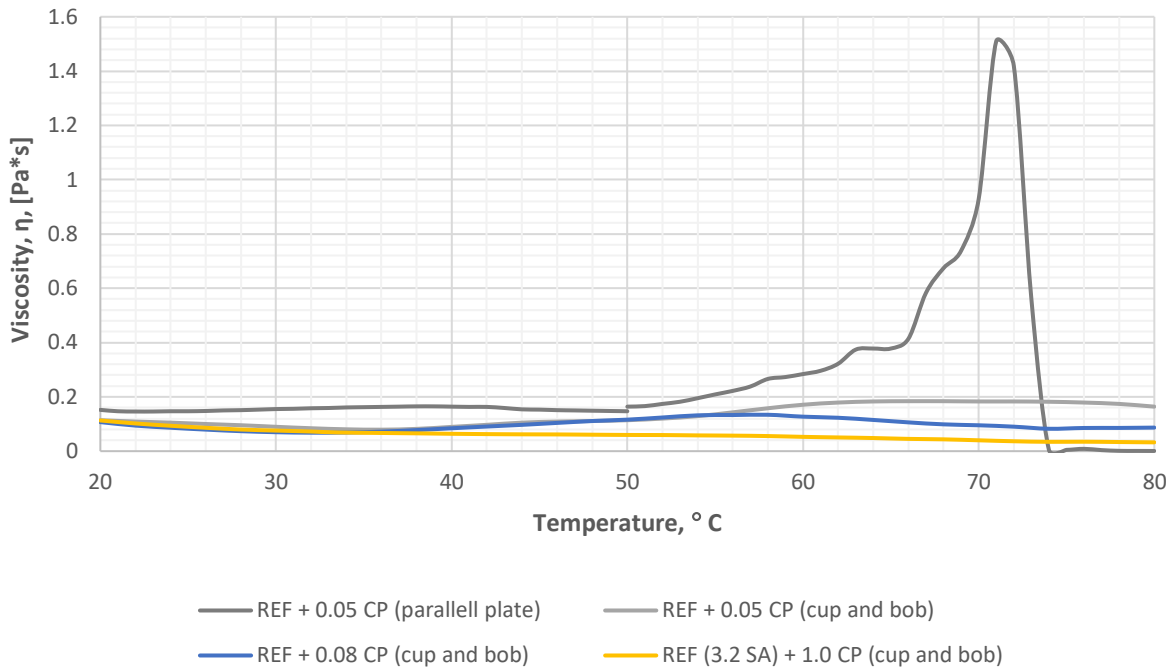


Figure 5.23: Temperature sweep results for some carbopol fluids

As described above, the parallel plate setup could not be used due to the sample drying out at increased temperatures, which results in a measured viscosity not representative for the drilling fluid. A larger amount of fluid is needed to perform tests using the “cup and bob” setup and therefore, it was decided to implement this setup instead. The temperature sweeps were carried out using the same program as before, however, only one sweep with a temperature ranging from 20°C to 80°C was performed for each system. Changing the setup enabled the Anton Paar MCR 302 rheometer to measure the viscosity of the sample at numerous temperatures within the studied range. Hence, it delivers knowledge about the stability of the system going beyond that obtained from the three temperatures of 22°C, 50°C and 80°C frequently used in this thesis. In figure 5.23, it is observed that the fluid systems tested are relatively stable in regard to temperature, verifying what yield stress plots have shown previously.

Primarily, the “cup and bob” setup enabled the rheometer to measure the viscosity of the sample at greater temperatures due to implementing a larger test sample. The amount of test sample was increased from 2-3 teaspoons to around 20 ml, which was used in the parallel plate and “cup and bob” setup, respectively. Increasing the amount of fluid reduced the impact of evaporation on the resulting viscosity measurements, however, water still evaporated from the sample when using the latter setup as well. Figure A.2 in appendix A shows the appearance of the sample after completing the temperature sweep with the “cup and bob” setup.

5.4.5 Effect of Carbopol on Viscoelastic Properties

Amplitude sweeps were performed for all carbopol systems as well. The diagrams and parameters in this subsection are presented and obtained in the same manner as for the lignosulfonate systems. This means that τ_y is read off from the graph, while γ_L and τ_f are determined using interpolation. All values obtained from these sweeps are presented in table 5.2.

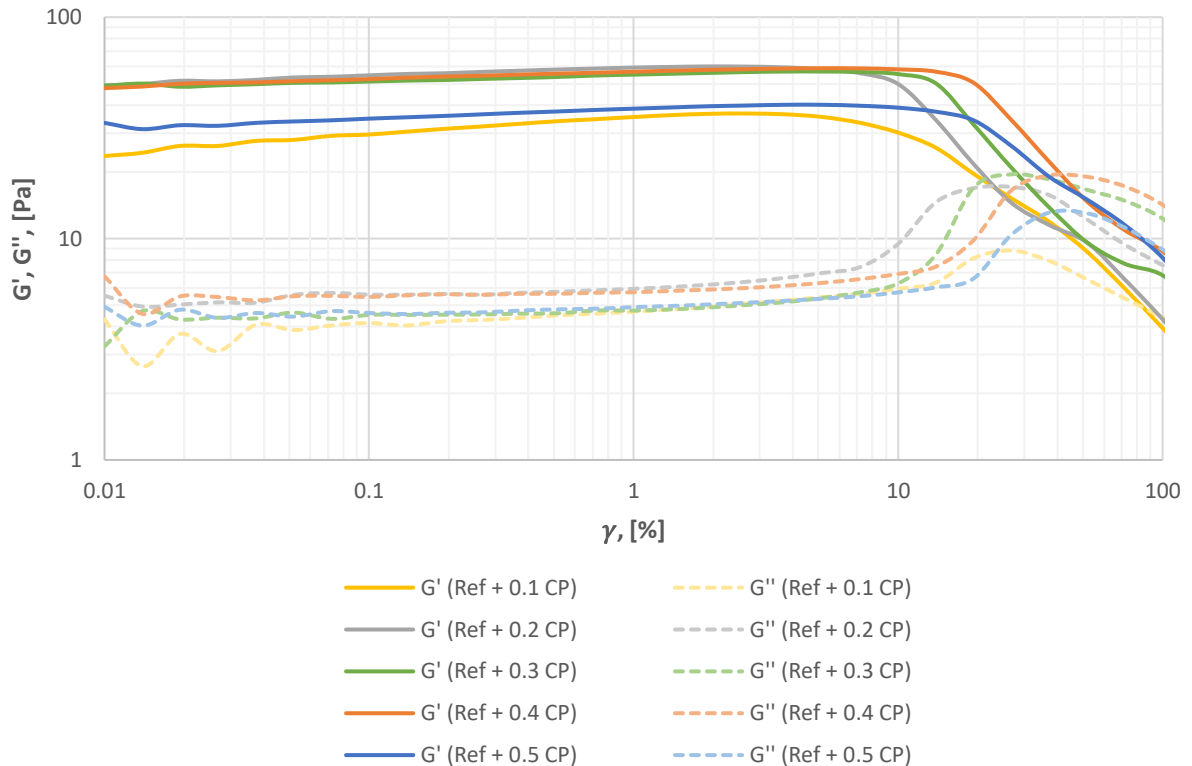


Figure 5.24: Amplitude sweep results for carbopol fluids (0.1-0.5 g)

Figure 5.24 and 5.25 presents the resulting storage and loss modulus curves of the carbopol fluids containing 0.1-0.5 and 0.05-0.08 g carbopol, respectively. The latter diagram also displays the resulting curves from testing the reference fluid containing a lower amount of anhydrous soda ash, i.e. the REF (3.2 g SA) + 0.1 g CP system. All the formulations show a gel-like character in the LVE range since their storage modulus are greater than their loss modulus in this region. Furthermore, the occurrence of a so-called G'' -peak can be observed for all fluids except the one containing 0.05 g carbopol. However, it is observed that the G'' -peaks of the reference fluid systems containing 0.08 and 0.1 g carbopol are less significant as well, excluding the system containing 3.2 g soda ash.

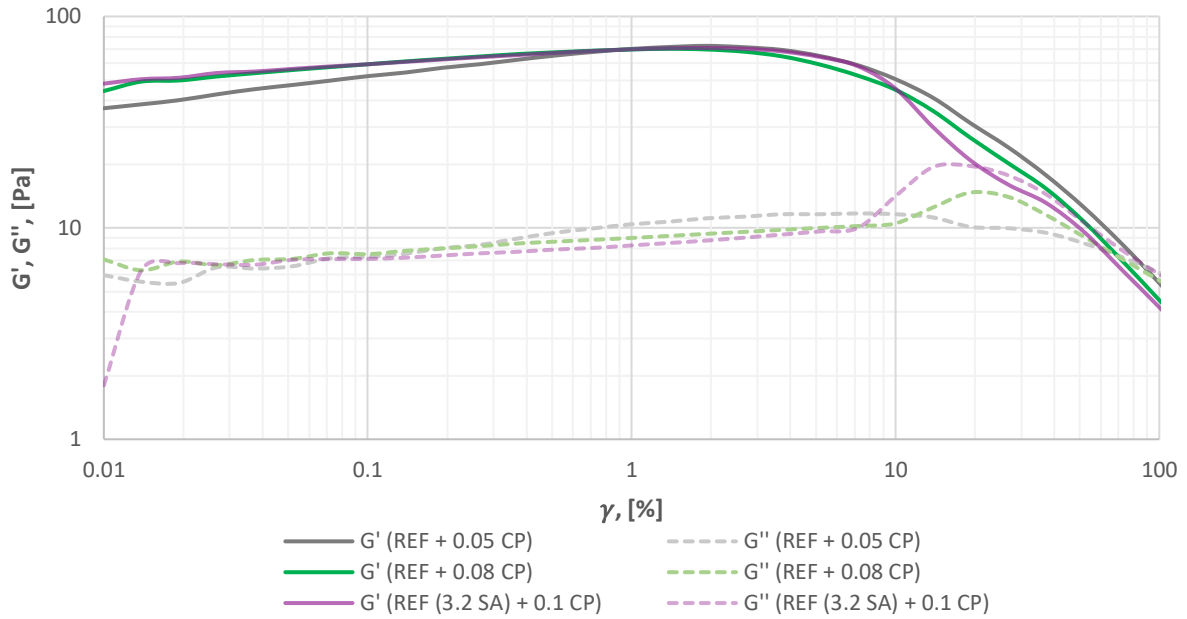


Figure 5.25: Amplitude sweep results for carbopol fluids (0.05-0.1 g)

Comparing figure 5.24 and 5.25, it is seen that the systems containing hydrated soda ash in general have a lower loss modulus curve than that of the fluids with anhydrous soda ash. As a reminder, the reference fluids containing hydrated and anhydrous soda ash are denoted as “Ref” and “REF”, respectively. Moreover, it is observed that the measuring curves of the anhydrous soda ash formulations are slightly increasing towards the upper limit of the LVE range, whereas those of the hydrous systems seems to be flatter. Furthermore, it is observed that the limiting value of the linear viscoelastic region in general increases with the addition of carbopol. This is reasonable since the application of carbopol is known to make the fluid more viscous and accordingly, greater shear rates must be applied to initiate flow.

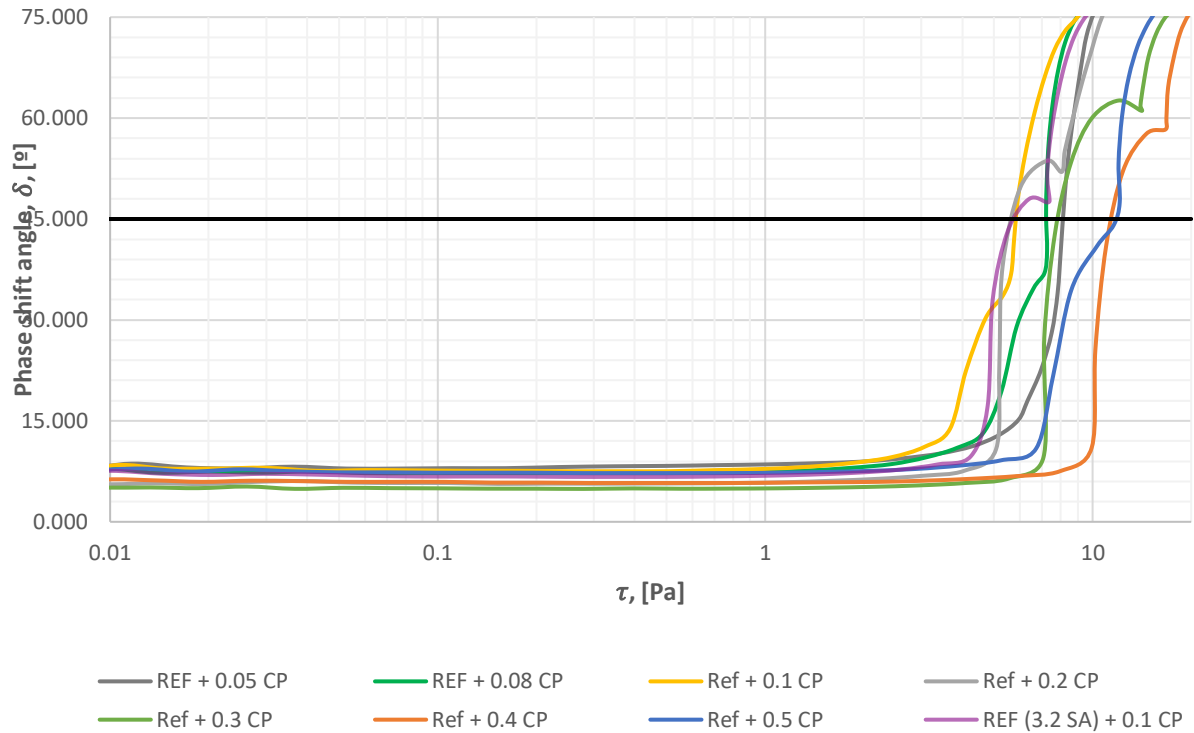


Figure 5.26: Phase shift angle vs. shear stress for carbopol fluids

As mentioned, the yield point of the carbopol fluids is determined using a diagram with the phase shift angle and shear stress presented on the y- and x-axis, respectively. Such a plot is illustrated in figure 5.26 and it presents the phase shift angle of all carbopol fluids versus shear stress. In general, it is observed that the flow point of the reference fluid increases with increasing amount of carbopol, however, this is merely the case at quantities greater than 0.1 g. When decreasing the amount of carbopol to 0.05 g and 0.08 g, it is seen that the flow point is greater than that of the 0.1 g carbopol fluid. The region where the phase shift curves remain constant with increasing shear stress represents the elastic behavior of the drilling fluid. When exceeding a phase shift angle of 45°, the fluid's behavior becomes mixed and viscous dominated.

Table 5.2: Summary of important parameters obtained from the amplitude sweeps of carbopol fluids

Fluid system	γ_L, [%]	τ_y, [Pa]	τ_f, [Pa]
REF + 0.05 CP	0.32	0.20	8.12
REF + 0.08 CP	1.47	1.00	7.22
REF (3.2 SA) + 0.1 CP	1.49	1.00	5.84
Ref + 0.1 CP	2.18	0.75	5.84
Ref + 0.2 CP	1.76	1.00	5.74
Ref + 0.3 CP	3.64	2.00	7.86
Ref + 0.4 CP	3.40	2.00	11.50
Ref + 0.5 CP	4.93	2.00	11.73

5.5 Best Performing Flat Rheology Drilling Fluid System

The reference fluid system containing 0.08 g carbopol was selected as the best performing flat rheology drilling fluid system. In this section, it is investigated how static aging will influence the rheological, filtration and viscoelastic properties of the formulation.

As mentioned, the reference fluid system containing 0.08 g carbopol was exposed to static aging at room temperature for 48 days. However, the system was also exposed to static aging at 62°C to investigate how it endures being exposed to increased temperatures for an extended period of time. In fact, the system was split into two samples which were aged in an oven for nine and 20 hours. The sample aged for nine hours in an oven was, however, aged for 48 days in total prior to performing any tests due to the Covid-19 pandemic.

5.5.1 Effect of Static Aging at Room Temperature on Rheological and Filtration Properties

Figure 5.27 presents the viscometer dial readings for the reference fluid containing 0.08 g carbopol when tested at 50°C after 24 hours and 48 days of static aging. It is observed that the viscosity of the system increases when stored for a longer period of time, however, its viscosity profile is still relatively parallel to that of the sample tested after one day. The increased viscosity could be caused by changes in the internal structure, density and pH.

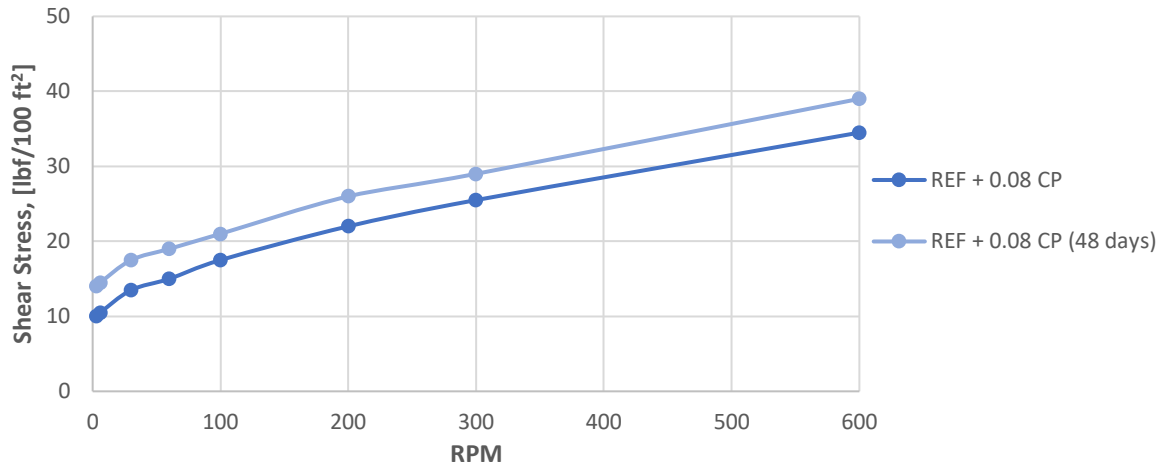


Figure 5.27: Viscometer data at 50°C for best performing flat rheology fluid

In figure 5.28, the Bingham yield stress calculated for measurements obtained at 22°C, 50°C and 80°C are illustrated for the two samples of the reference fluid containing 0.08 g carbopol. It is observed that the system becomes less stable with regards to temperature after static aging at room temperature for 48 days, however, this is merely the case at lower temperatures. The sample is still stable at temperatures above 50°C, although the yield stresses are slightly increased compared to the short time aging results.

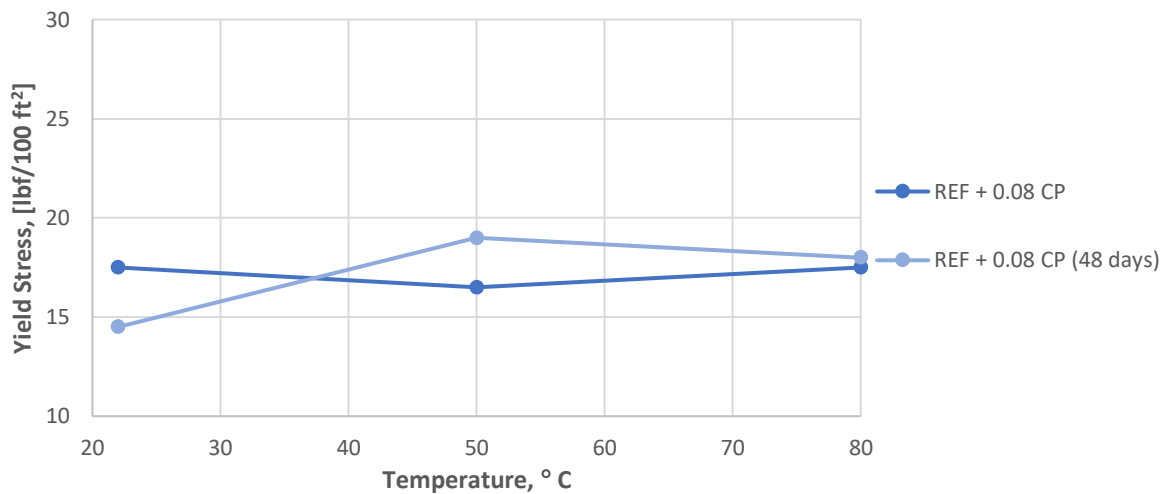


Figure 5.28: Bingham yield stress of best performing flat rheology fluid

Furthermore, it is observed that the filtration properties of the system changes with time. This is illustrated in figure 5.29, where it is seen that long-time aging and the changes in the mud properties it brings causes the fluid loss to increase. This indicates that the system is degrading over time and possibly, the increased fluid loss is due to less water being trapped within the clay particles. However, there could be several contributing factors to why the properties of the

mud changes with time, such as change in the internal structure, density, pH, evaporation of water or growth of bacteria.

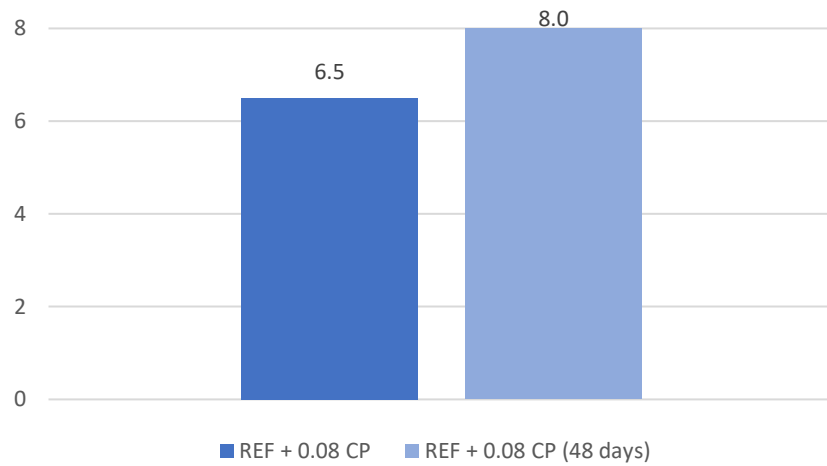


Figure 5.29: Fluid loss measurement of the best performing flat rheology fluid (in ml)

5.5.2 Effect of Static Aging at Room Temperature on pH and Density

When aging a water-based drilling fluid, it is to be expected that some of the water content will evaporate from the sample. By comparing the density of the short-time and long-time aged sample, one could determine whether some water have evaporated. After 24 hours, the density of the system is measured to be 1.33 sg, whereas it is at 1.37 sg after 48 days. Thus, a minor increase of the mud weight is observed, indicating that some water could have evaporated from the sample. Furthermore, the pH of the reference system containing 0.08 g carbopol is slightly lower after 48 days compared to the one attained after one day. The pH measurements of the short-time and long-time aged sample are illustrated in figure 5.30.

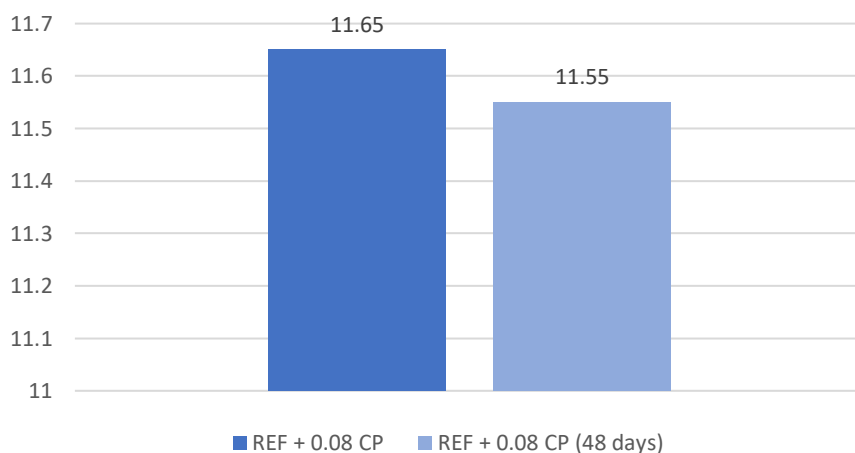


Figure 5.30: pH measurement of the best performing flat rheology fluid

5.5.3 Effect of Static Aging at Room Temperature on Viscoelastic Properties

In figure 5.31, the amplitude sweep results of the short-time and long-time aged samples are presented. It is seen that the storage modulus is greater than the loss modulus for both, indicating that the system, regardless of aging time, exhibit the character of a gel more than that of a liquid in the linear viscoelastic range. Furthermore, it is observed that the storage modulus is lower and the loss modulus is greater for the sample aged for 48 days compared to those of the short-time aged sample. In addition, it seen that the linear viscoelastic region of the system has been reduced with time. The upper limits of this region are presented in table 5.3. Moreover, the long-time aged sample also exhibit a G'' -peak, however, it is not as substantial as that of the reference fluid aged for 24 hours.

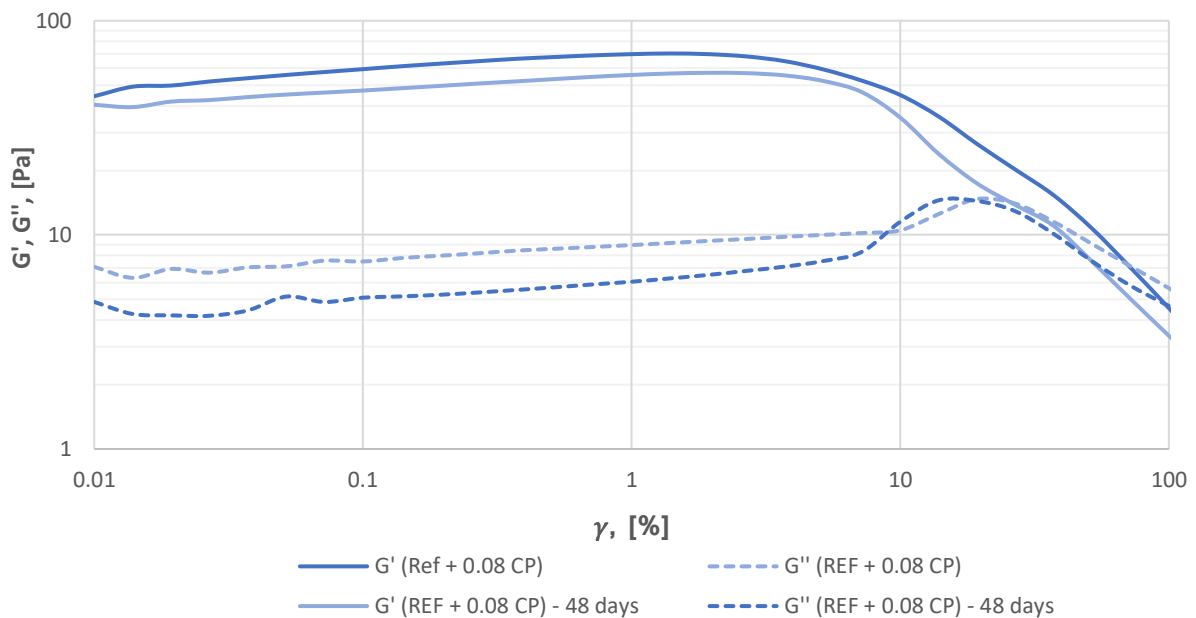


Figure 5.31: Amplitude sweep result for best performing flat rheology fluid

Figure 5.32 illustrates the phase shift angle as a function of shear stress for the short-time and long-time aged reference fluid containing 0.08 g carbopol. It is clearly seen that both the yield point and the flow point of the sample is reduced for the long-time aged sample. This indicates that the sample will be irreversibly deformed at lower shear rates and that the viscous portion of viscoelastic behavior prevails earlier when the system is aged for a longer period of time. The values of these parameters are presented in table 5.3.

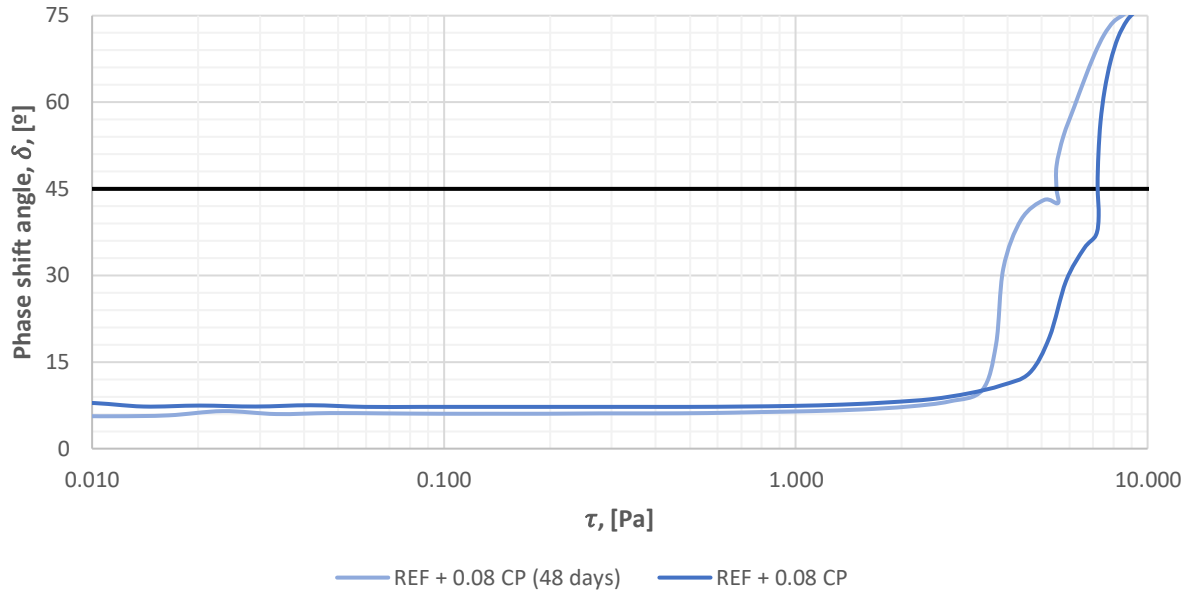


Figure 5.32: Phase shift angle vs. shear stress for best performing flat rheology fluid

Table 5.3: Summary of important parameters obtained from the amplitude sweeps of flat rheology fluid

Fluid system	γ_L , [%]	τ_y , [Pa]	τ_t , [Pa]
REF + 0.08 CP	1.47	1.00	7.22
REF + 0.08 CP (48 days)	1.23	0.70	5.51

5.5.4 Effect of Static Aging at 62°C on Rheological Properties

The viscometer dial readings for the best performing flat rheology system after nine and 20 hours at 62°C, as well as the ones after 24 hours and 48 days at room temperature, are presented in figure 5.33. Only a small increase in the viscosity profile of the system is observed at higher RPMs after exposure to 62°C for 20 hours and thus, results showed that this temperature exposure do not alter the viscosity to any significant extent. However, it is clearly seen that the properties of the mud are altered when storing the system for a total time of 48 days after exposing it to an increased temperature for nine hours. The viscosity profile of this sample has decreased with time, which is the opposite reaction to that of the system aged only at room temperature for the same duration.

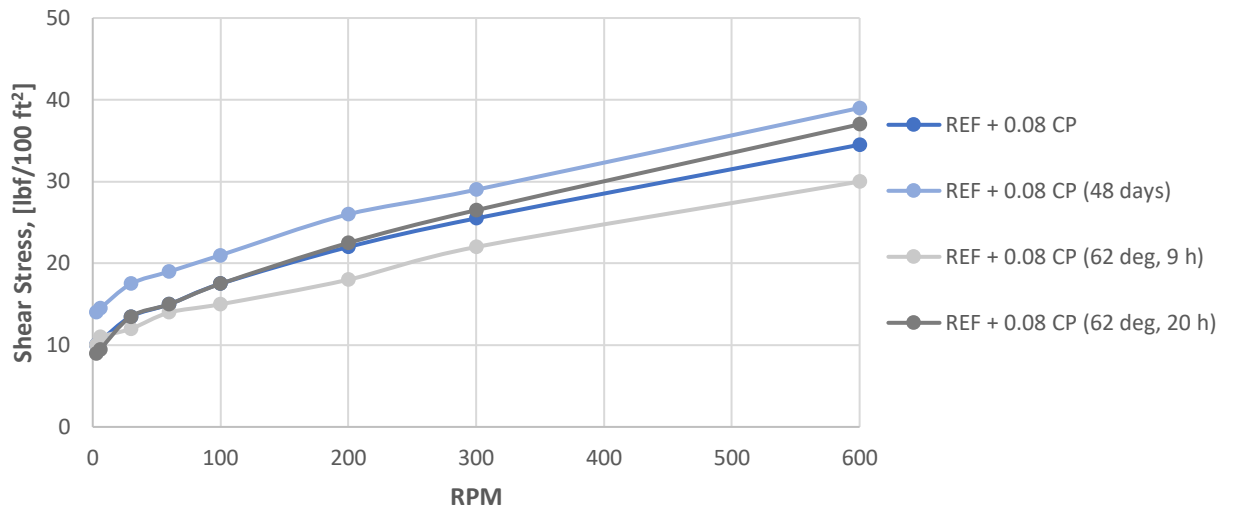


Figure 5.33: Viscometer data at 50°C for best performing flat rheology fluid after aging at 62 °C

Figure 5.34 illustrates the corresponding yield stresses calculated at 22°C, 50°C and 80°C. It is observed that exposing the system to 62°C for 20 hours have altered the yield stress of the fluid. In the range from 22°C to 50°C, the yield stresses are slightly lower after aging, whereas it has increased at 80°C. Furthermore, the sample has become less thermally stable at temperatures above 50°C. The sample aged both in an oven and at room temperature for 48 days in total is more stable with regards to temperature compared to the sample exposed to room temperature alone for the same duration. However, it is seen that the yield stress of this fluid slightly increases with temperature, which could indicate that the clay particles flocculate when exposed to higher temperatures after aging.

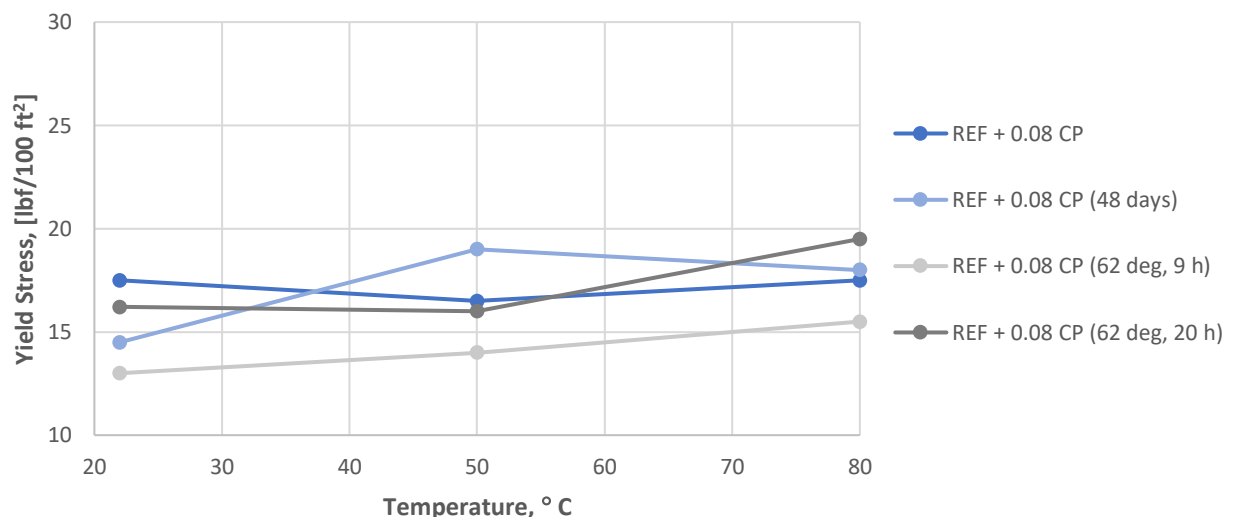


Figure 5.34: Bingham yield stress of best performing flat rheology fluid after aging at 62 °C

5.6 MWCNT-COOH Nanoparticle Based Drilling Fluid

Multi-walled carbon nanotube was the first nanoparticle suspension to be investigated in the best performing flat rheology drilling fluid obtained in subsection 5.4.4. The suspension was primarily added to enhance the filtration properties of the reference fluid. The recipe for the MWCNT-COOH fluid systems are presented in table 4.10.

As mentioned, these fluids were stored for 46 days prior to performing any tests and therefore, the effect of the nanoparticle suspension is investigated by comparing the results to those of a reference fluid which has been stored for 48 days. As a reminder, the best performing flat rheology system, i.e. the reference fluid system containing 0.08 g carbopol, is referred to as the reference fluid for all systems containing nanoparticles and is denoted as “REF”.

Unfortunately, the long-time stored reference fluid containing 0.07 g multi-walled carbon nanotube was spilled prior to measuring the viscosity at increased temperatures. Consequently, it will not be possible to investigate the thermal stability of this fluid.

5.6.1 Effect of MWCNT-COOH on Rheological Properties

Figure 5.35 presents the viscometer dial readings of the MWCNT-COOH treated fluids. It is observed that the viscosity of the system increases with the addition of multi-walled carbon nanotube, which indicates that the nanoparticle might have flocculated the bentonite system. Furthermore, it shows that adding 0.13 g induce a greater viscosity than an amount of 0.18 g. Hence, the effect of multi-walled carbon nanotube is non-linear

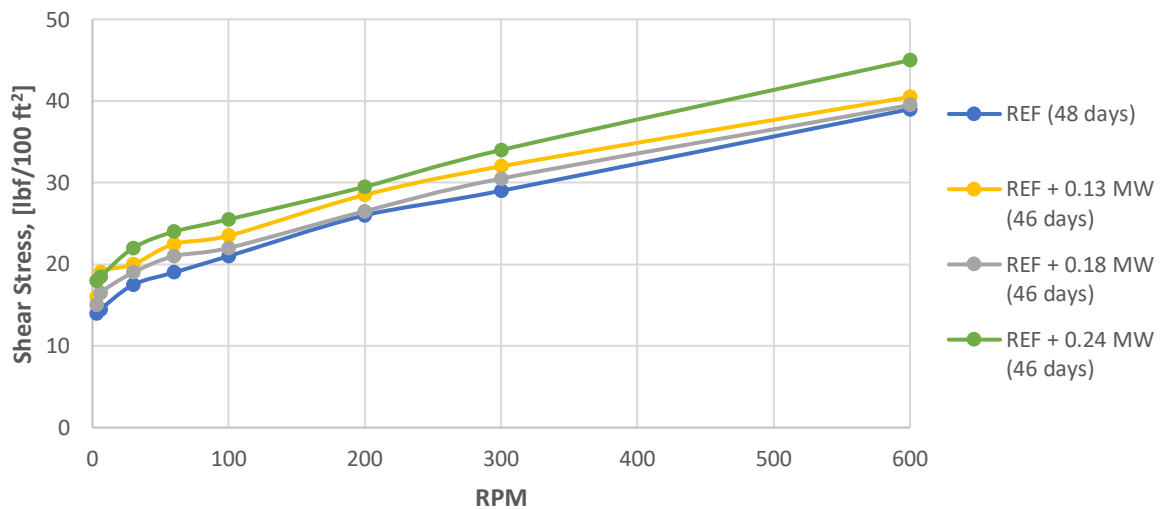


Figure 5.35: Viscometer data at 50°C for multi-walled carbon nanotube fluids (long-time aging)

The corresponding yield stress values of the fluid systems presented above are illustrated in figure 5.36. Like before, the Bingham yield stresses are calculated using the viscosity measurements obtained at 22°C, 50°C and 80°C and thus, the lines are merely an illustration of how the systems are thought to behave at other temperatures in between. Like viscosity, the yield stress of the system increases when adding MWCNT-COOH. In fact, it is observed that an amount of 0.13 g MW induce greater yield stresses than the addition of 0.18 g and that the addition of 0.13 g and 0.24 g has a similar effect on the system. Furthermore, the yield stresses of these formulations are relatively parallel to those of the reference fluid, which means that they are still temperature stable at temperatures above 50°C. The system containing 0.18 g, however, has become less temperature stable. It is also to be noted that the yield stress exhibited by the MWCNT-COOH fluids exceed the 11-20 lbf/100 ft² window commonly applied in the field.

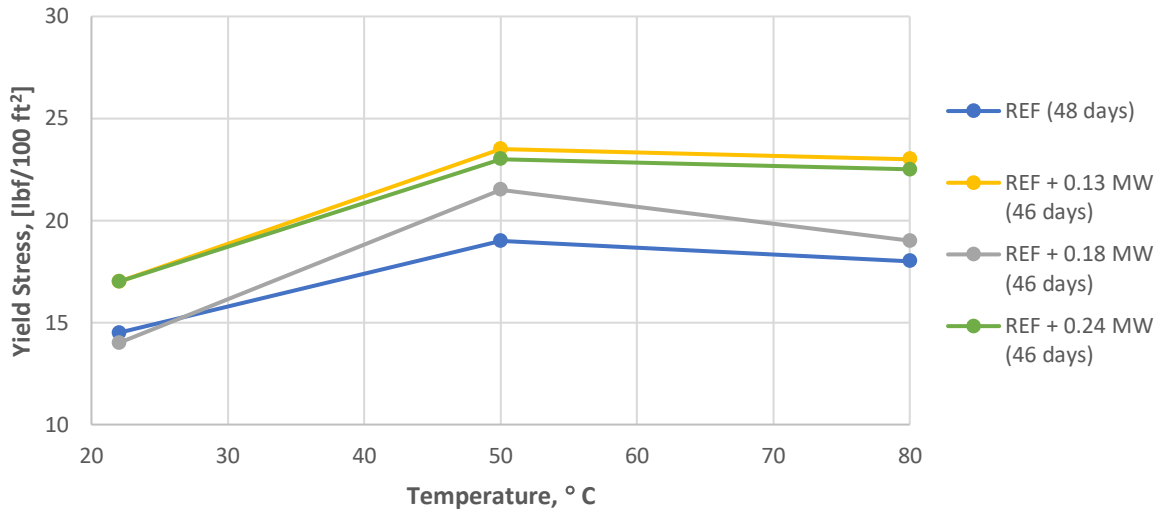


Figure 5.36: Bingham yield stress of multi-walled carbon nanotube fluids (long-time aging)

However, results have previously shown that storing the system for a longer period causes the mud properties to change. Figure 5.37 presents the viscosity profile of the reference fluid containing 0.07 g multi-walled carbon nanotube, as well as the reference fluid itself, when measured at 22°C after a shorter and longer period of aging. Results show that the viscosity of the REF + 0.07 g MW system has decreased with time and thus, the addition of multi-walled carbon nanotube might induce greater viscosity profiles than those presented in figure 5.35 when considering the effect of the nanoparticle suspension after short-time storing.

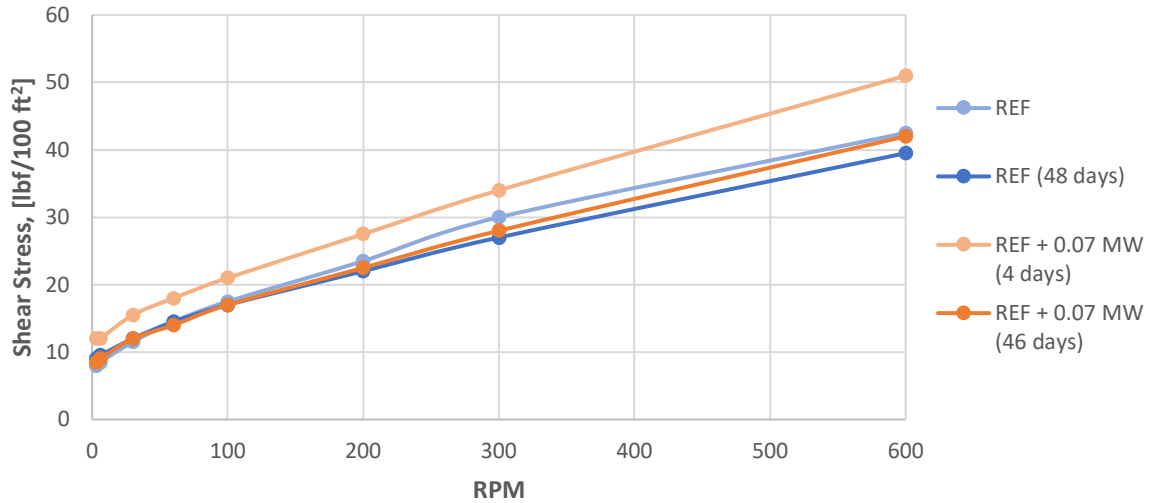


Figure 5.37: Viscometer data at 22 °C for multi-walled carbon nanotube fluids (short-time vs. long-time aging)

5.6.2 Effect of MWCNT-COOH on Fluid Loss

Figure 5.38 illustrates the effect of multi-walled carbon nanotube on the filtration properties of the best performing flat rheology fluid. Results show that lower quantities of the nanoparticle suspension reduce the fluid loss of the system more than the addition of larger quantities. In fact, it is seen that the fluid loss increases with added amounts of MWCNT-COOH which are greater than 0.07 g, at least within the amounts of chemical used in thesis. However, all quantities of the nanoparticle suspension improve the filtration properties of the reference fluid system.

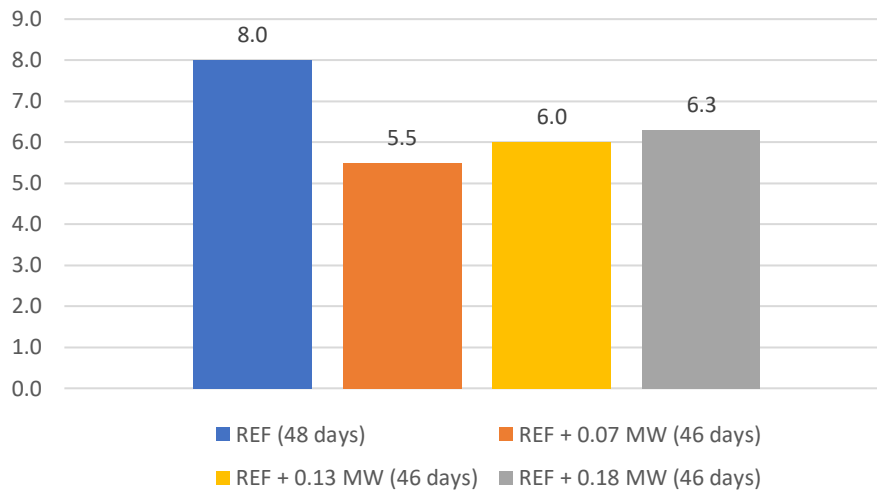


Figure 5.38: Fluid loss measurement of multi-walled carbon nanotube fluids (in ml)

Still, previous results have shown that the filtration properties of the reference fluid changes with time and therefore, the extent to which the fluid loss is reduced could differ depending on

the how long the system has been stored. It is clearly seen that the fluid loss increases after long-time aging when comparing figure 5.38 and 5.39. However, the difference between the amount of fluid loss measured for the reference fluid after short- and long-time aging is greater than that of the system containing 0.07 g multi-walled carbon nanotube. In fact, an increase of merely 0.5 ml is observed for the latter. This indicates that at least a quantity of 0.07 g improves the filtration properties of the best performing flat rheology fluid both after short- and long-time aging.

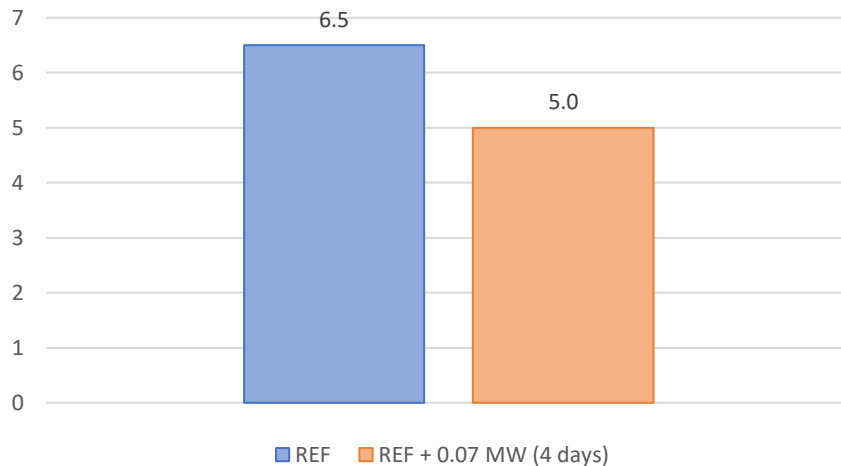


Figure 5.39: Fluid loss measurement of multi-walled carbon nanotube fluid after 4 days (in ml)

5.6.3 SEM Pictures and Element Analysis of Filter Cakes

The filter cakes of the reference fluid system and the reference fluid containing 0.07 g multi-walled carbon nanotube after short- and long-time aging were investigated using a Scanning Electron Microscope. The objective of this microscopic analysis was to examine the chemical and structural differences, if any, caused by the long-time aging of ~48 days. Additionally, the surface of the filter cakes was inspected for the presence of bacteria.

Figure 5.40 and 5.41 presents some of the SEM pictures of the filter cakes generated by the REF and REF + 0.07 g MW systems, respectively, after short- and long-time aging. Several SEM pictures were taken and are presented in appendix H. By a visual inspection of the figures, it is difficult to identify any major differences between the short- and long-time aged samples. However, differences in the internal structures can be observed when studying the SEM pictures to the very detail. This could be a reason why the fluid properties are altered after 46 and 48 days of aging. It has been previously mentioned that bacteria could alter the properties of a fluid, though none were spotted during the investigation.

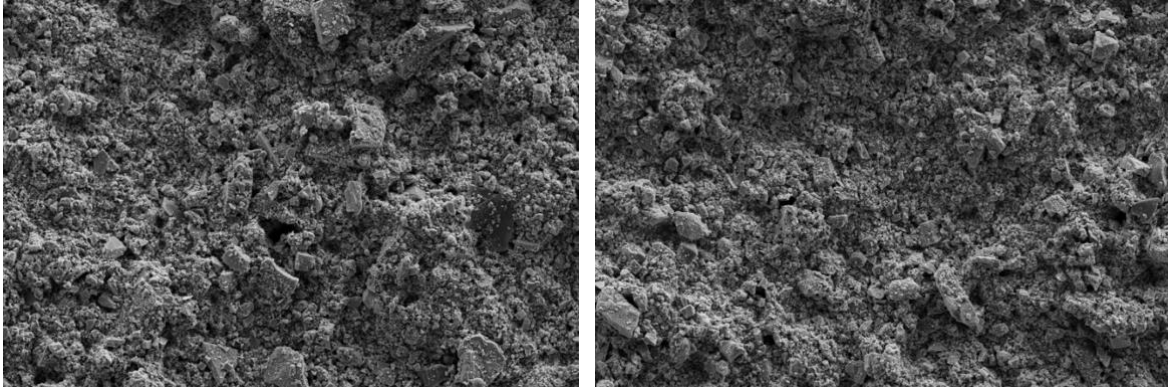


Figure 5.40: SEM pictures at 20 μm magnification of reference fluid after short- (left) and long-time aging (right)

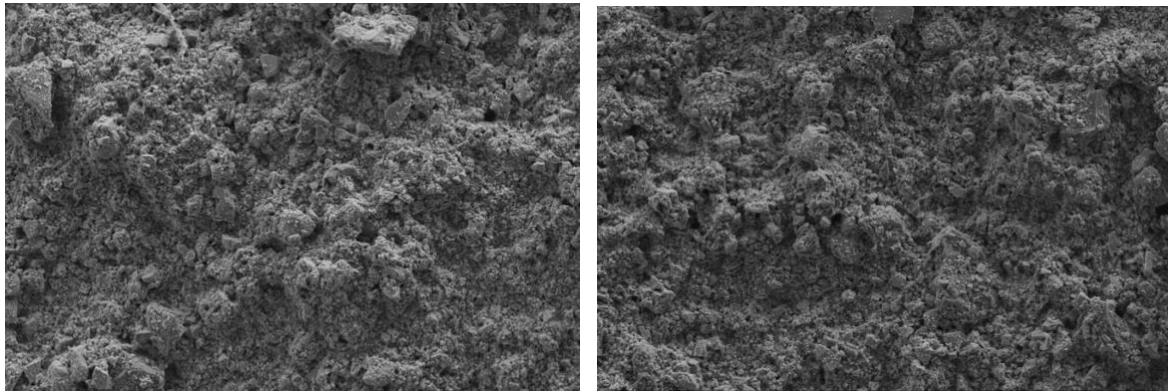


Figure 5.41: SEM pictures at 20 μm magnification of 0.07 g MW system after short- (left) and long-time aging (right)

Moreover, element mapping was conducted to determine and quantify the elements present in the filter cakes of the systems. Figure 5.42 and 5.43 presents a SEM picture of the filter cake's surface and the element concentration obtained from this surface for the reference fluid system after short- and long-time aging, respectively. Whereas figure 5.44 and 5.45 presents that of the 0.07 g MWCNT-COOH system after short- and long-time aging, respectively. Only minor changes in the chemical content of the filter cakes are observed due to aging. Thus, it was concluded that the alterations of the fluid properties are not caused by bacteria or changes in the element content of the fluids. The differing rheology and filtration volumes are most likely caused by the evaporation of water and degradation of the polymers.

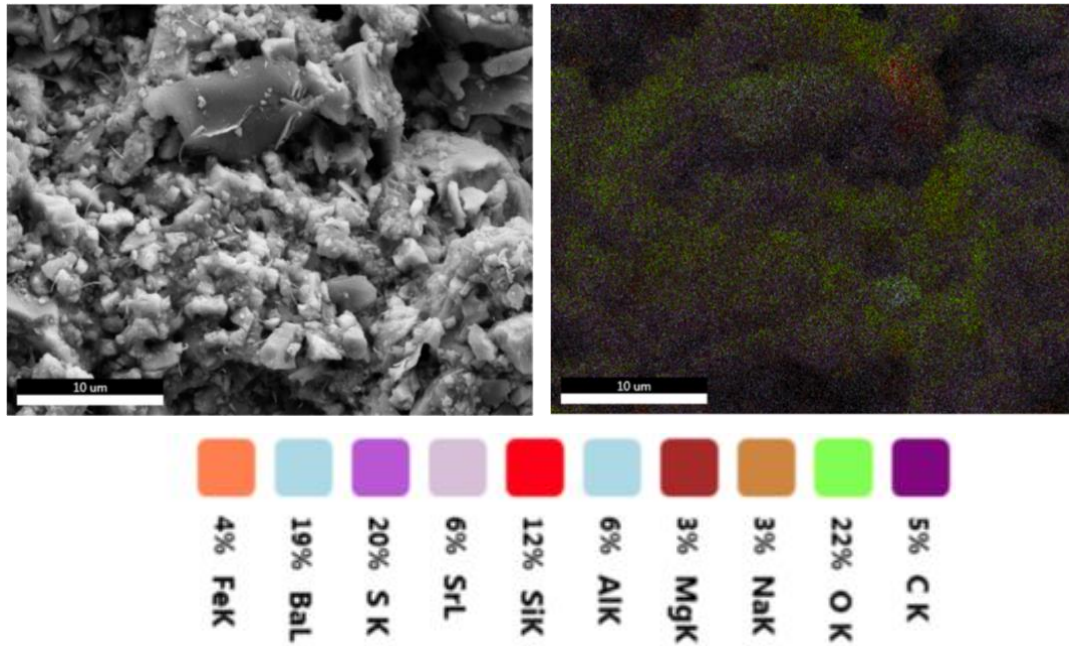


Figure 5.42: SEM picture at 10 µm magnification and element analysis for REF (short-time)

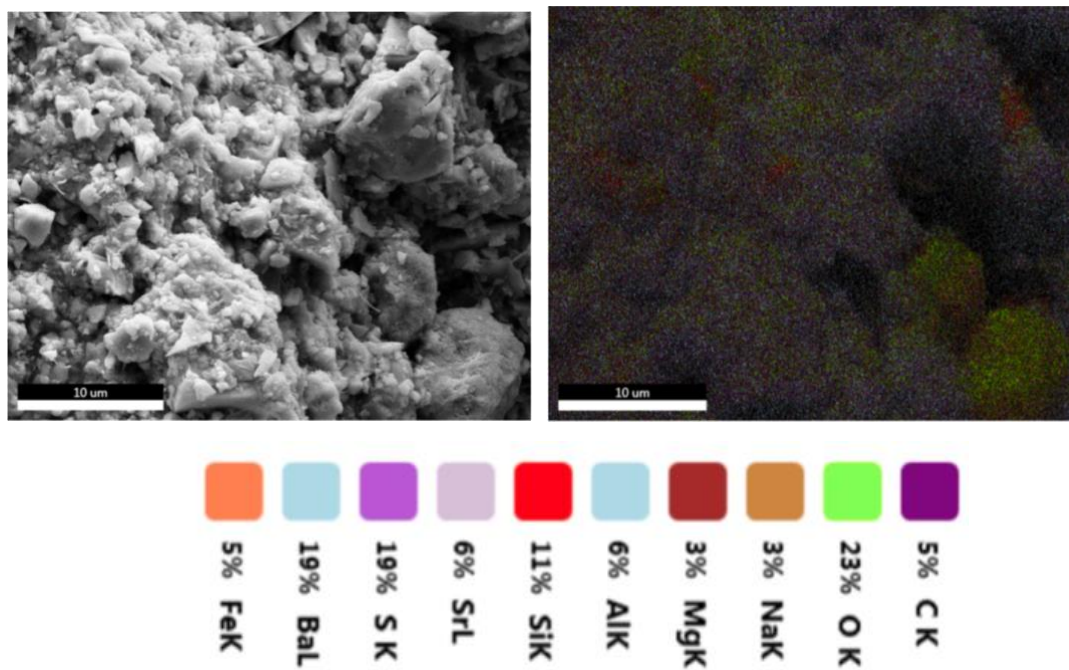


Figure 5.43: SEM picture at 10 µm magnification and element analysis for REF (long-time)

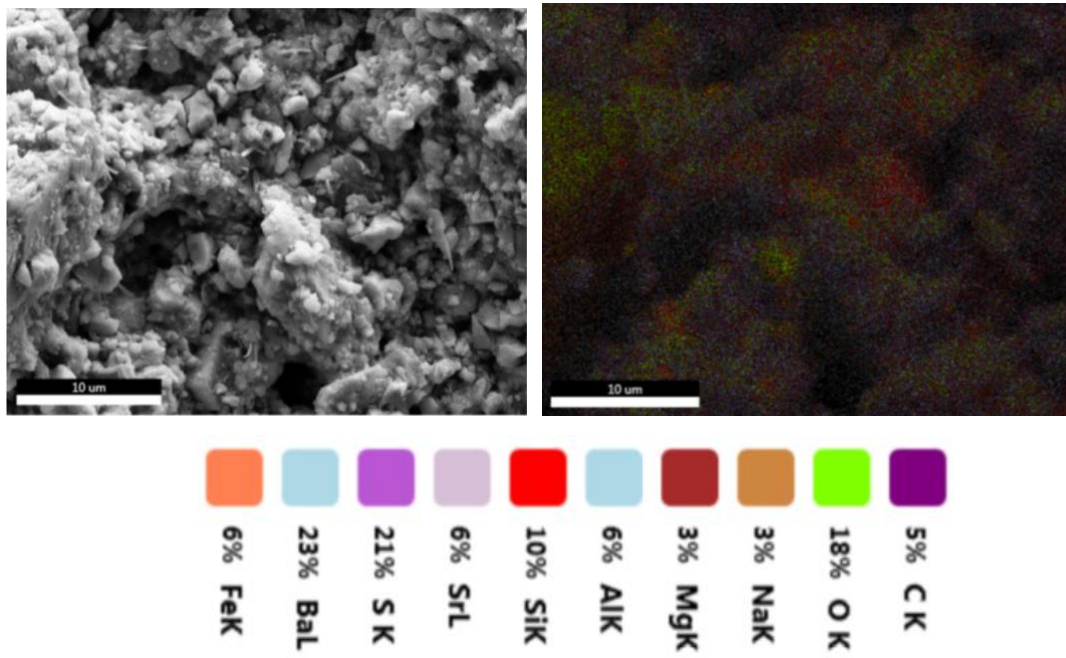


Figure 5.44: SEM picture at 10 μm magnification and element analysis for REF + 0.07 g MW (short-time)

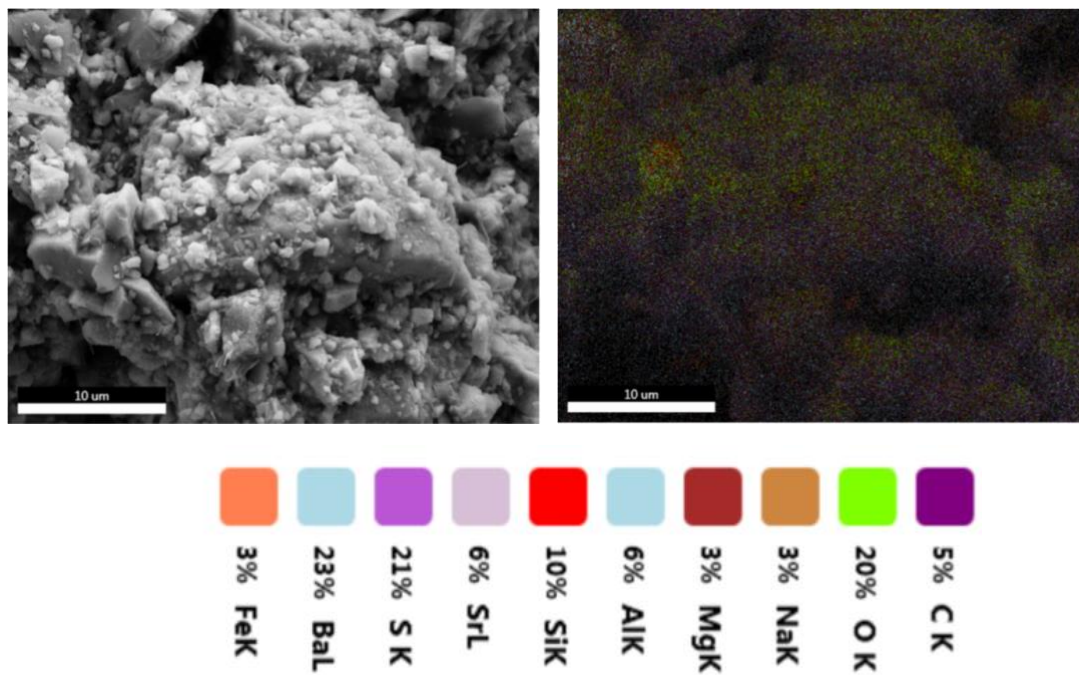


Figure 5.45: SEM picture at 10 μm magnification and element analysis for REF + 0.07 g MW (long-time)

5.7 SiO₂ Nanoparticle Based Drilling Fluid

The best performing flat rheology fluid was modified with a nanoparticle suspension known as silica. Primarily, the nanoparticle was added in order to improve the rheological and filtration properties of the fluid. The recipe for the SiO₂ fluid systems are presented in table 4.11.

5.7.1 Effect of SiO₂ on Rheological Properties

Figure 5.46 presents the viscometer dial readings of the silica fluids. It is observed that the addition of SiO₂ causes the viscosity of the reference fluid system to be slightly reduced for all quantities except for 0.18 g. However, the changes are not substantial and it is seen that most of the viscosity profiles are overlapping each other to some extent.

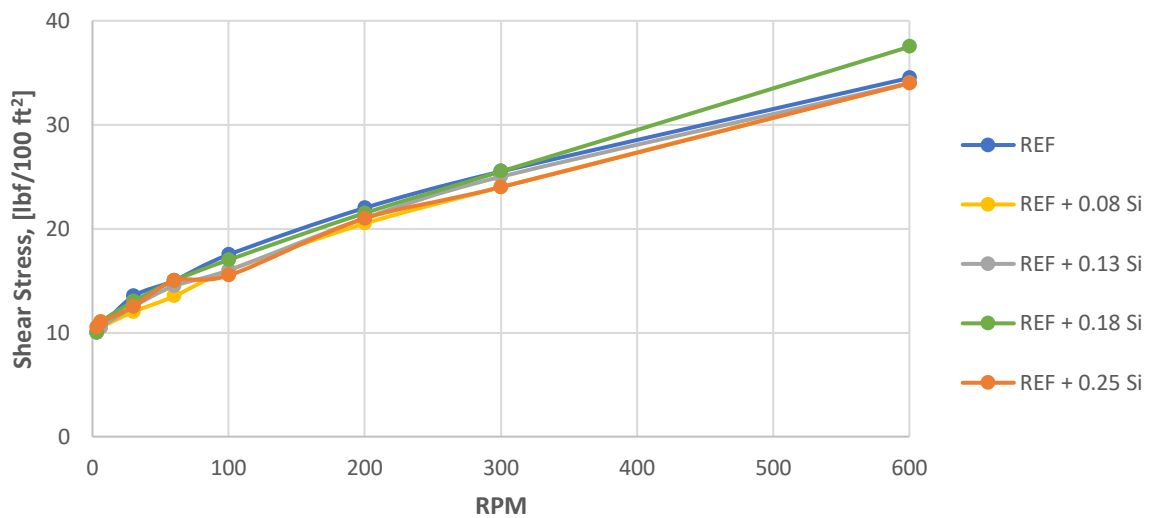


Figure 5.46: Viscometer data at 50 °C for silica fluids

The calculated yield stresses corresponding to the systems presented above are illustrated in figure 5.47. This figure shows that even though the viscosity profile of the system, obtained at 50 °C, do not change substantially with added silica, the temperature stability is indeed altered. Overall, the system becomes less stable for all quantities of silica, where an addition of 0.18 g leads to the most significant change and the least temperature stable system. However, it is seen that the system containing 0.13 g is still stable at temperatures above 50 °C. Furthermore, it is observed that the calculated yield stresses are reduced non-linearly with the addition of silica.

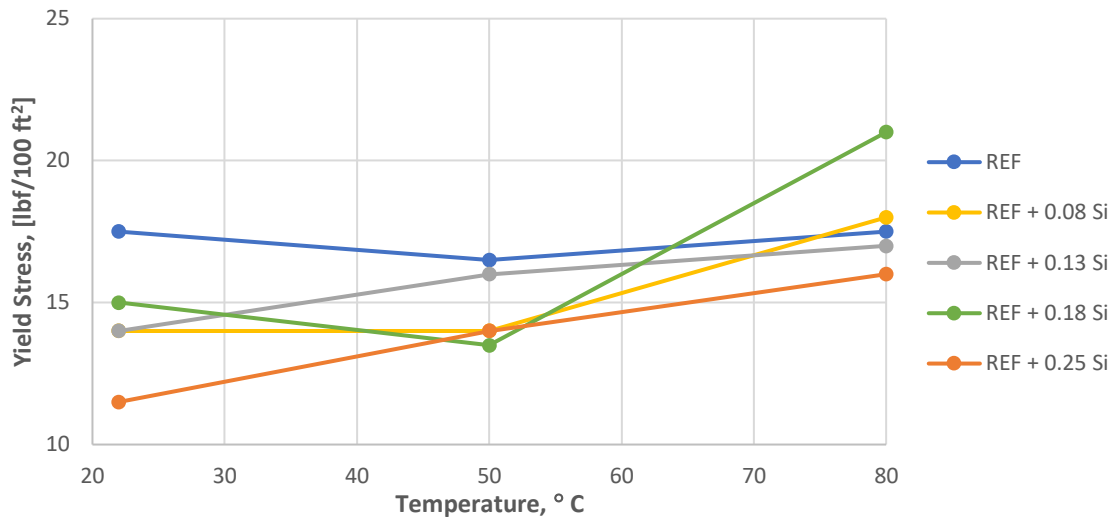


Figure 5.47: Bingham yield stress of silica fluids

5.7.2 Effect of SiO₂ on Fluid Loss

In figure 5.48 it is seen that the addition of silica improves the filtration properties of the best performing flat rheology fluid. All quantities applied in this thesis causes the fluid loss of the system to be reduced. However, the reduction is non-linear and a quantity of 0.13 g induce the greatest improvement. When increasing the amount of silica further than 0.13 g it appears as if the filtration volume increases slightly and then plateaus, though how the fluid loss of the system will change beyond quantities used in this thesis is unknown.

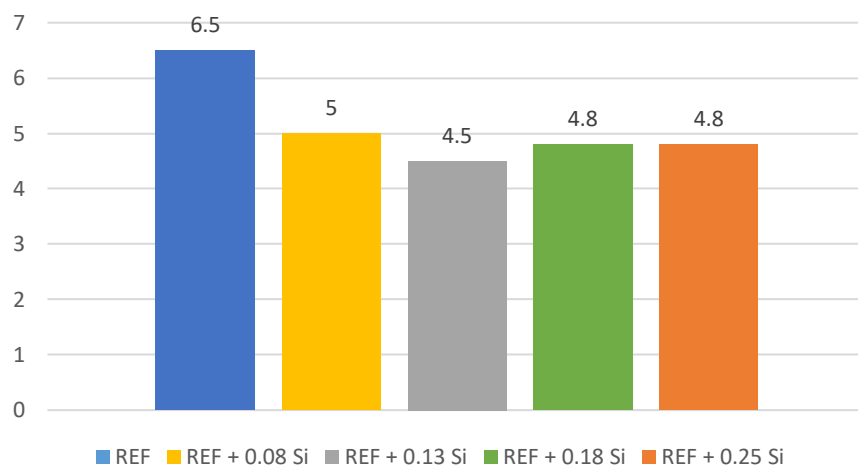


Figure 5.48: Fluid loss measurement of silica fluids (in ml)

5.8 Al₂O₃ Nanoparticle Based Drilling Fluid

Since little research has been conducted regarding the application of aluminum oxide in drilling fluids, its effect on mud properties is still relatively unknown. However, a previous study has shown that the nanoparticle could improve the rheological and filtration properties and therefore, this will be further investigated in this section. The recipe for the alumina fluid systems are presented in table 4.12.

5.8.1 Effect of Al₂O₃ on Rheological Properties

The viscometer dial readings of the aluminum oxide treated fluids are presented in figure 5.49. It is seen that the nanoparticle suspension causes little alteration of the viscosity profile of the reference fluid for all quantities except one, which is an amount of 0.07 g. Even though this is the smallest quantity of Al₂O₃ applied in this thesis, it causes the greatest change in regards to viscosity by increasing the viscosity profile of the reference fluid. Furthermore, it is observed that even though the alteration is minor, the viscosity of the system increases non-linearly with the addition of aluminum oxide.

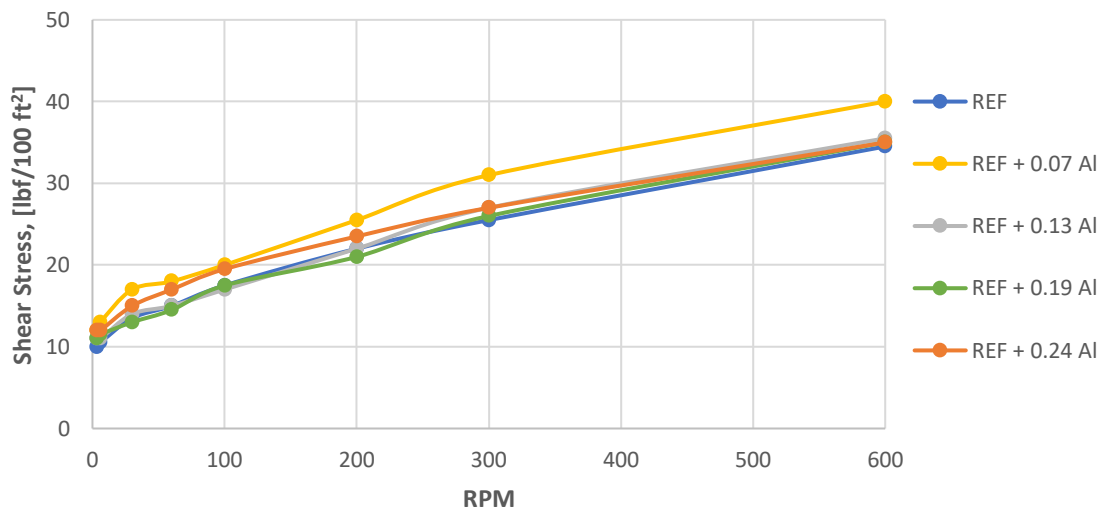


Figure 5.49: Viscometer data at 50°C for aluminum oxide fluids

Figure 5.50 illustrates the corresponding yield stresses of the fluids presented above and as before, these are calculated from viscosity measurements obtained at 22°C, 50°C and 80°C. For the quantities used in this thesis, there are two distinct effects of the aluminum oxide on the temperature stability of the reference fluid. It is observed that the addition of 0.13 g and 0.24 g Al₂O₃ causes the stability of the system to be improved at temperatures above 50°C, however, both have become less stable at lower temperatures. Furthermore, the addition of 0.07 g results

in a less temperature stable system overall. In addition, the lowest quantity produce yield stresses exceeding the range of 11-20 lbf/100 ft² commonly used in the field.

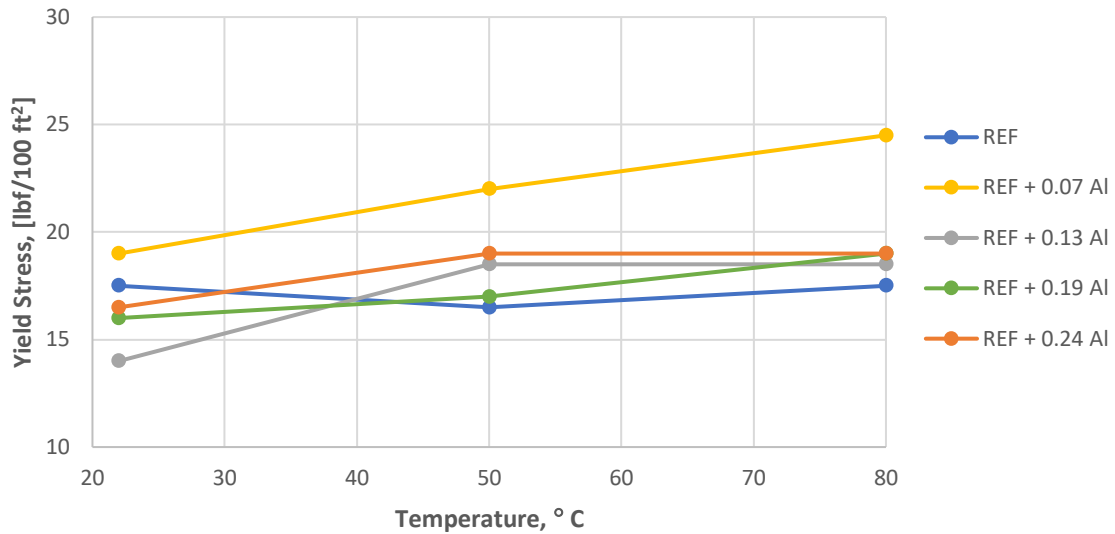


Figure 5.50: Bingham yield stress of aluminum oxide fluids

5.8.2 Effect of Al₂O₃ on Fluid Loss

In figure 5.51, it is seen that all quantities of Al₂O₃ used in this thesis improves the filtration properties of the reference fluid. Furthermore, it is observed that the effect of the nanoparticle suspension is non-linear and in fact, both the lowest and largest quantity produce an equally great reduction with a fluid loss of 4.4 ml. At quantities in between, the fluid loss seems to be slightly increasing until it drops again at the largest quantity of 0.24 g aluminum oxide.

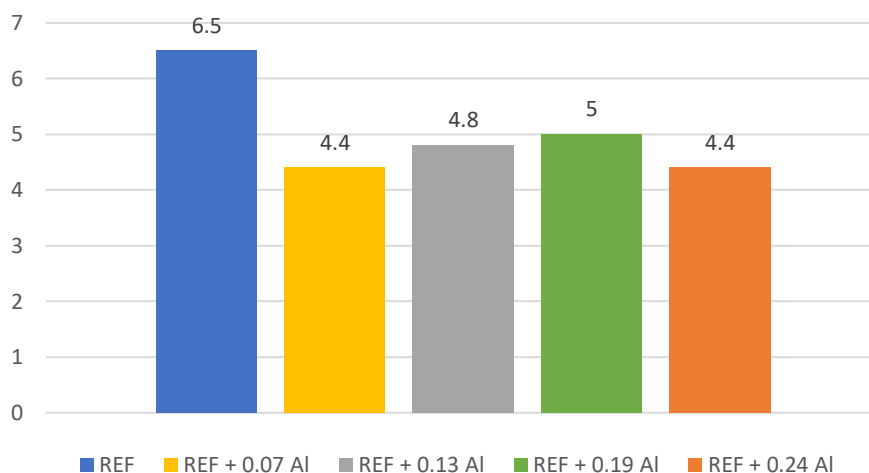


Figure 5.51: Fluid loss measurement of aluminum oxide fluids (in ml)

5.9 Effect of Nanoparticle Suspensions on Viscoelastic Properties

In general, it is observed that the storage and loss modulus curves decline with the addition of multi-walled carbon nanotube, silica and aluminum oxide suspensions. This is the case for all quantities tested in this thesis except for the lowermost amount of aluminum oxide, i.e. an amount of 0.07 g. The resulting storage and loss modulus curves of this system differs only slightly from those of the reference fluid. Furthermore, it is seen that the addition of silica causes the greatest reduction of both curves and in comparison, the other nanoparticle suspensions do not cause any significant changes to the storage and loss modulus curves. A summary of important parameters obtained from the amplitude sweeps of the MWCNT, SiO₂ and Al₂O₃ fluids are given in table 5.4, 5.5 and 5.6, respectively, whereas, the diagrams showing the amplitude sweep results are presented in the appendices.

Amplitude sweep results of the short- and long-time aged samples of the reference fluid containing 0.07 g multi-walled carbon nanotube show that the viscoelastic properties of the system changes with time. In appendix B, figure B.3, it is observed that both the storage and loss modulus curves decline when the system have been stored for a longer duration at room temperature. Moreover, the long-time storing causes the yield point and flow point of the system to decline, while the upper limit of the LVE range becomes greater. This indicates that the viscous portion of the viscoelastic behavior prevails at lower shear stresses and that the sample endures exposure to greater strains before being irreversibly deformed after 46 days of storing.

Overall, it is observed that the yield point of the reference fluid system, which is at 1.0 Pa, does not change much with the addition of various quantities of the nanoparticle suspensions. The upper limit of the linear viscoelastic region and the flow point of the reference fluid have previously been obtained as 1.47 % and 7.22 Pa, respectively. From the amplitude sweep results of the nanoparticle fluids, it is observed that the upper limit of the LVE range becomes greater for all systems except the one containing 0.07 g aluminum oxide. In the tables, it is also seen that the flow point of the system occurs at lower shear stresses when the reference fluid is blended with multi-walled carbon nanotube, silica and aluminum oxide.

Table 5.4: Summary of important parameters obtained from the amplitude sweeps of MW fluids

Fluid system	γ_L , [%]	τ_y , [Pa]	τ_f , [Pa]
REF + 0.07 MW (4 days)	1.53	1.25	6.67
REF + 0.07 MW (46 days)	2.17	1.00	5.63
REF + 0.13 MW (46 days)	2.14	1.00	5.80
REF + 0.18 MW (46 days)	2.10	1.00	5.77
REF + 0.24 MW (46 days)	1.95	0.90	6.08

Table 5.5: Summary of important parameters obtained from the amplitude sweeps of silica fluids

Fluid system	γ_L , [%]	τ_y , [Pa]	τ_f , [Pa]
REF + 0.08 Si (6 days)	2.64	1.25	5.84
REF + 0.13 Si (6 days)	2.51	1.00	5.33
REF + 0.18 Si (6 days)	2.98	1.00	4.90
REF + 0.25 Si (6 days)	2.74	1.00	4.96

Table 5.6: Summary of important parameters obtained from the amplitude sweeps of aluminum oxide fluids

Fluid system	γ_L , [%]	τ_y , [Pa]	τ_f , [Pa]
REF + 0.07 Al (3 days)	1.36	1.00	6.71
REF + 0.13 Al (3 days)	1.74	1.00	6.22
REF + 0.19 Al (3 days)	1.82	1.00	5.69
REF + 0.24 Al (3 days)	1.66	1.00	5.99

5.10 Effect of Nanoparticle Suspensions on Frictional Properties

The resulting coefficients of friction obtained from the tribometer tests of the multi-walled carbon nanotube, silica and aluminum oxide fluid systems are presented in figure 5.52, 5.53 and 5.54, respectively. As a reminder, the MWCNT-COOH fluids have been stored at room temperature for 46 days and are compared to the long-time aged reference fluid. The aluminum oxide and silica systems were stored for 3 and 6 days, respectively, prior to performing the test.

It is observed that the addition of all nanoparticle suspensions improves the lubricity of the system as it reduces the coefficient of friction. The reduction is non-linear and in general, lower amounts seems to cause the greatest improvement, excluding the system containing 0.08 g SiO₂. When considering the effect of multi-walled carbon nanotube on the lubricity of the system, it is seen that a quantity of 0.07 g and 0.13 g results in the greatest improvement after short- and long-time aging, respectively. Considering the effect of silica and aluminum oxide, the greatest improvement is presented with the addition of 0.13 g and 0.07 g, respectively. Results show

that increasing the amount of nanoparticle suspension beyond these quantities results in increasing coefficients of friction. However, this is merely the case for quantities tested in this thesis and the effect of the nanoparticle suspensions beyond this is unknown.

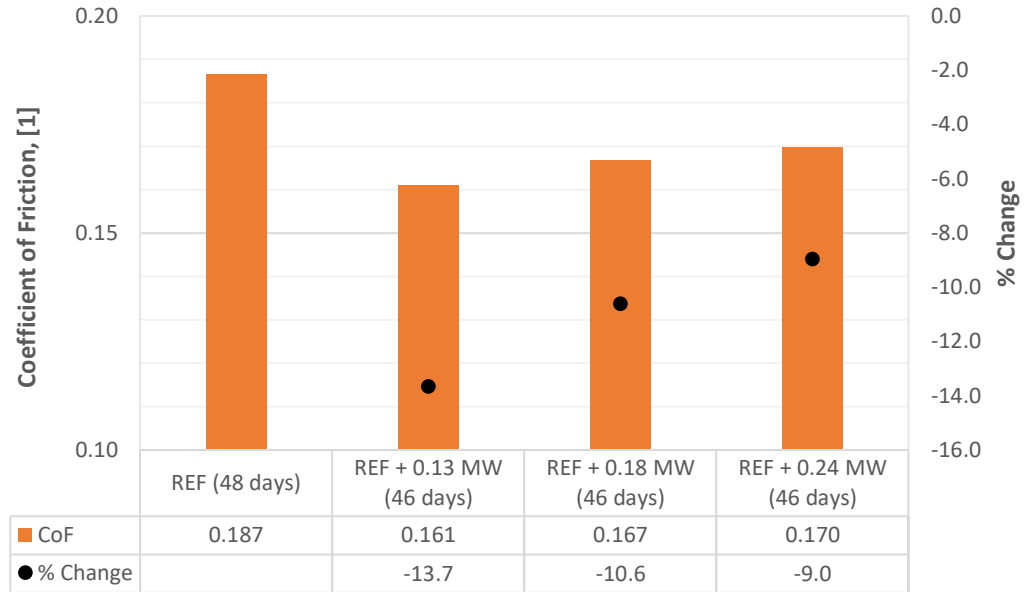


Figure 5.52: Tribometer results for multi-walled carbon nanotube fluids

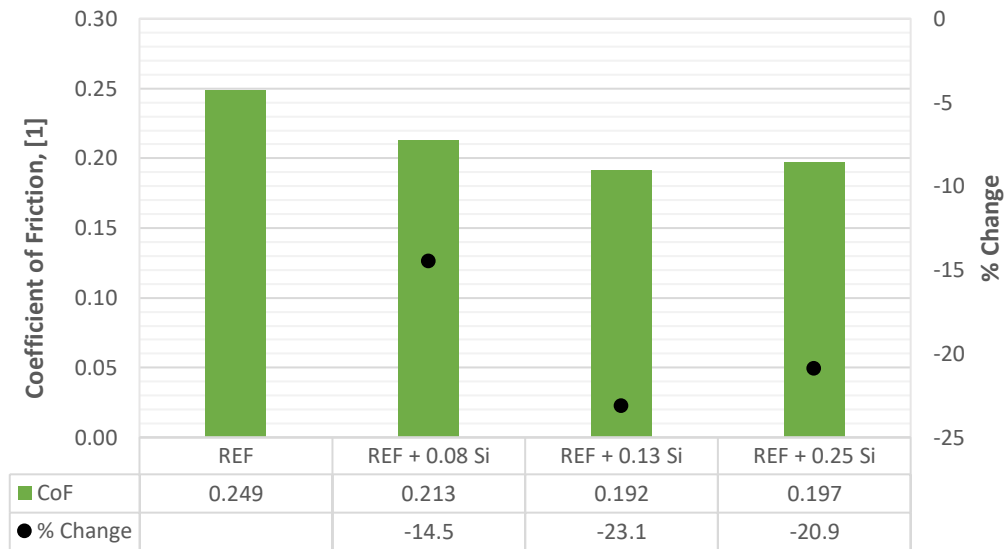


Figure 5.53: Tribometer results for silica fluids

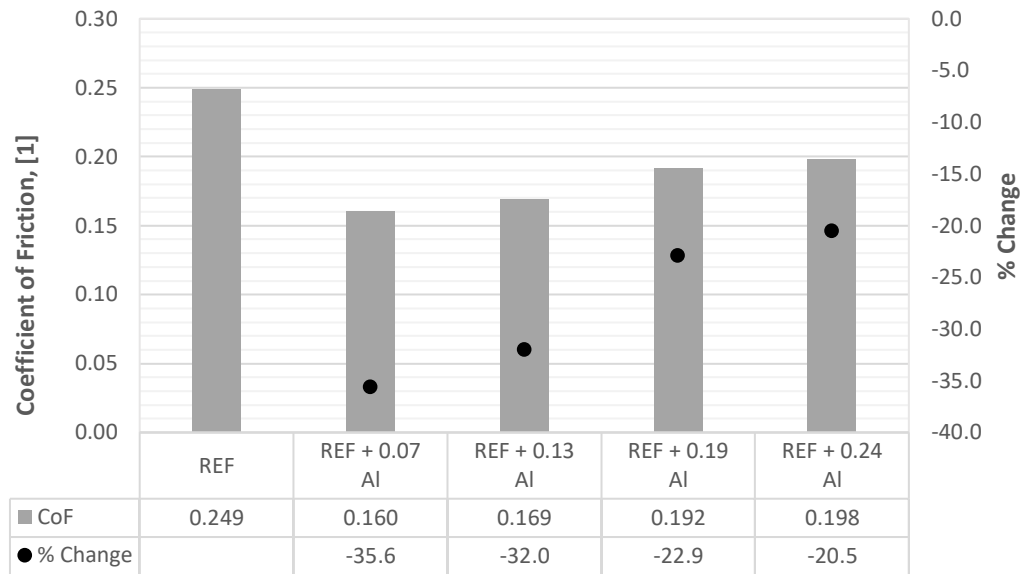


Figure 5.54: Tribometer results for aluminum oxide fluids

Overall, it is observed that aluminum oxide functions as the most effective friction-reducing additive in the best performing flat rheology system. It presents a maximum reduction of 35.6 %, whereas the lowest percentage change of the nanoparticle suspension is -20.5 %. In comparison, the greatest reduction produced by silica is a change of 23.1 %. In figure 5.52, it is seen that multi-walled carbon nanotube affects the coefficient of friction to a much lower extent with the greatest reduction being a change of 13.7 %. However, the CoF of the reference fluid itself has declined from 0.249 to 0.187 after 48 days. Thus, the percentage changes produced by MWCNT-COOH are minor even though the coefficients of friction presented are lower than those of the Al₂O₃ fluids overall.

Previous results have shown that the properties of the reference fluid and the MWCNT-COOH system changes with time. Figure 5.55 presents the coefficient of friction for the reference fluid containing 0.07 g multi-walled carbon nanotube after 6 days. It is observed that this system produce a percentage change of -36.8 % and thus, it goes beyond that of the fluid containing 0.07 g aluminum oxide. Seemingly, there will be a greater distinction between the obtained CoF of the MWCNT-COOH systems and the reference fluid after short-time storing.

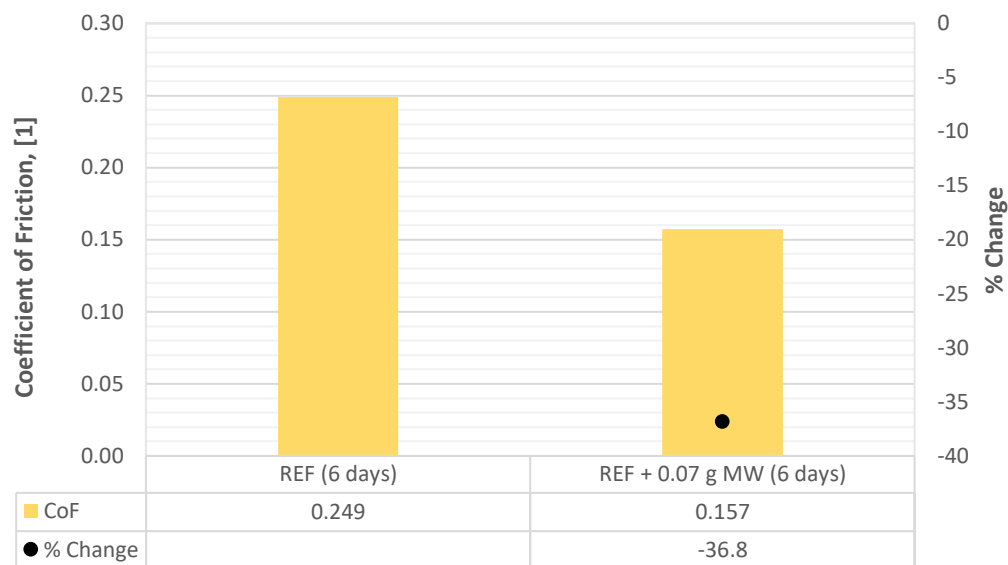


Figure 5.55: Tribometer results for multi-walled carbon nanotube fluid (short-time storing)

6 Modeling and Simulation Study

Rheological modelling was performed for the best performing flat rheology system, i.e. the reference fluid system containing 0.08 g carbopol, to determine the best-fit rheological model. Wellbore simulation studies in the form of hydraulics and T&D simulations were conducted by investigating the initial fluid formulation, reference fluid containing 0.08 g carbopol and some of the nanoparticle modified fluids. In the hydraulics simulation, the ECD and pump pressure of these fluids were examined based on the Unified hydraulics model as described in subsection 2.9.

6.1 Rheological Modeling

Rheological modeling was performed to find the rheological model most suited to describe the flow characteristics of the best performing flat rheology system, as well as investigating the effect of temperature on the rheological parameters. Calculations and modeling was conducted using an excel calculator which generated all model parameters from the given viscometer dial readings and shear rates. The viscosity of the reference fluid containing 0.08 g carbopol was then compared to each of the following models individually:

- Newtonian model
- Bingham Plastic model
- Power Law model
- Herschel-Bulkley model
- Unified model
- Robertson-Stiff model

All calculations are based on the equations presented in subsection 2.3, where the rheological models are presented and further described. The viscometer dial readings of the investigated fluid are presented in table 6.1.

Table 6.1: Viscometer dial readings of best performing flat rheology fluid

REF + 0.08 g CP			
RPM	22°C	50°C	80°C
θ_{600}	42.5	34.5	34.5
θ_{300}	30	25.5	26
θ_{200}	23.5	22	22
θ_{100}	17.5	17.5	18.5
θ_6	8.5	10.5	11.5
θ_3	8	10	11

6.1.1 Best-Fit Rheological Model

Figure 6.1 presents the percentage deviation between the actual measurements and the model prediction for each of the rheological models at 22°C, 50°C and 80°C, as well as the average percentage values of the three temperatures. It is clearly seen that the Herschel-Bulkley, Unified and Robertson-Stiff models provide quite accurate descriptions of the rheological properties, with an average deviation of 1.90 %, 2.44 % and 1.30 %, respectively. The Robertson-Stiff model describes the system with the smallest deviation, both overall and at each temperature, and thus, it is the best-fit rheological model for the reference fluid containing 0.08 g carbopol.

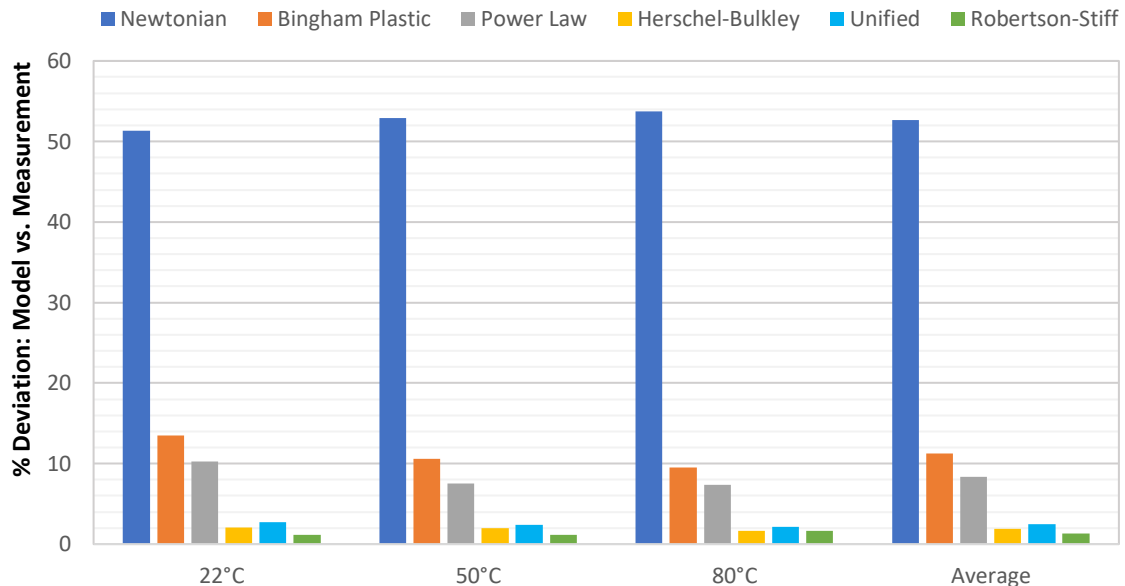


Figure 6.1: % Deviation between measurement and model for best performing flat rheology system

All predictions provided by the various rheological models versus the dial reading measurements are presented in appendix E, whereas the corresponding parameters and percentage deviations are presented in tables 6.2-6.4.

Table 6.2: Model parameters for best performing flat rheology system at 22°C

Model	Equation	Parameters				% Deviation	cP
		τ_0, τ_y, A	k, C	n, B	μ_p, μ		
Herschel-Bulkley	$7.896 + 0.190 \cdot \gamma^{0.772}$	7.896	0.190	0.772		2.1	
Unified	$8.003 + 0.156 \cdot \gamma^{0.804}$	8.003	0.156	0.804		2.7	
Power Law	$4.657 \cdot \gamma^{0.304}$		4.657	0.304		10.2	
Bingham Plastic	$0.036 \cdot \gamma + 10.684$	10.684			0.036	13.5	17.333
Robertson-Stiff	$1.003 \cdot (45.566 + \gamma)^{0.545}$	1.003	45.566	0.545		1.2	
Newtonian	$0.051 \cdot \gamma$				0.051	51.4	24.610

Table 6.3: Model parameters for best performing flat rheology system at 50°C

Model	Equation	Parameters				% Deviation	cP
		τ_0, τ_y, A	k, C	n, B	μ_p, μ		
Herschel-Bulkley	$10.061 + 0.207 \cdot \gamma^{0.711}$	10.061	0.207	0.711		2.0	
Unified	$10.137 + 0.179 \cdot \gamma^{0.734}$	10.137	0.179	0.734		2.4	
Power Law	$6.860 \cdot \gamma^{0.222}$		6.860	0.222		7.5	
Bingham Plastic	$0.025 \cdot \gamma + 12.609$	12.609			0.025	10.6	12.162
Robertson-Stiff	$2.019 \cdot (51.402 + \gamma)^{0.413}$	2.019	51.402	0.413		1.1	
Newtonian	$0.043 \cdot \gamma$				0.043	52.9	20.732

Table 6.4: Model parameters for best performing flat rheology system at 80°C

Model	Equation	Parameters				% Deviation	cP
		τ_0, τ_y, A	k, C	n, B	μ_p, μ		
Herschel-Bulkley	$11.092 + 0.225 \cdot \gamma^{0.691}$	11.092	0.225	0.691		1.7	
Unified	$11.204 + 0.183 \cdot \gamma^{0.724}$	11.204	0.183	0.724		2.2	
Power Law	$7.826 \cdot \gamma^{0.203}$		7.826	0.203		7.3	
Bingham Plastic	$0.024 \cdot \gamma + 13.606$	13.606			0.024	9.5	11.683
Robertson-Stiff	$2.613 \cdot (49.768 + \gamma)^{0.375}$	2.613	49.768	0.375		1.6	
Newtonian	$0.044 \cdot \gamma$				0.044	53.8	20.924

6.1.2 Effect of Temperature on Rheological Parameters

Table 6.5 presents a summary of all the rheological parameters for the best performing flat rheology fluid, as well as the percentage deviations caused by the increasing temperature. The following observations were made for each of the models based on the data presented in the table:

Herschel-Bulkley Model

From the rheological modelling, it is observed that the yield stress of the fluid increases with temperature. This indicates that the internal friction within the fluid increases and that greater shear stress values are required to initiate flow at higher temperatures. Exposing the fluid to 50°C and 80°C lead to higher consistency index values and lower flow behavior index values. Moreover, all n-values are below 1.0, which implies that the reference fluid containing 0.08 g carbopol is pseudoplastic.

Unified Model

The lower shear yield point of the Unified model increases with temperature and exhibit percentage deviations of 26.7 % and 40.5 % at 50°C and 80°C, respectively. The consistency index and flow behavior index follow the same trend as the Herschel-Bulkley model and thus, have slightly greater and lower values at higher temperatures, respectively. Overall, it is observed that the Unified model parameters are quite similar to those of the Herschel-Bulkley model, which most likely is related to the fact that both describe fluid flow with the same three-parameter equation.

Power Law Model

It is observed that the consistency index and flow behavior index of the Power Law model follows the same trend as the aforementioned models. However, higher percentage changes are observed for both parameters with increasing temperature. Moreover, it is seen that the n-values obtained using the Power Law model are significantly lower than those of the H-B and Unified model, whereas the k-values are larger. Smaller n-values imply that the fluid is more shear thinning and in appendix E, it is clearly seen that the Power Law model anticipate that the fluid is more shear thinning than it actually is.

Bingham Plastic Model

As for the H-B model, the Bingham yield stress increases with temperature, however, smaller percentage deviations of 18.0 % and 27.3 % are observed at 50°C and 80°C, respectively. The plastic viscosity of the fluid decrease with temperature, which indicates that the viscosity at the bit is reduced and results in a higher ROP. [122]

Robertson-Stiff Model

It is observed that the A parameter, which resembles the k-value of other models, increases significantly with temperature and shows percentage deviations of 101.2 % and 160.5 % at 50°C and 80°C, respectively. The B parameter, which can be thought of as the n-value of other models, decreases as the temperature of the fluid increases. These values are found to be higher than the n-values of the Power Law model and lower than those of the H-B and Unified Model. However, all B- and n-values are below 1.0, which indicates pseudoplastic fluid behavior.

Newtonian Model

The plastic viscosity of the Newtonian model decreases non-linearly with increasing temperature. A percentage deviation of -15.8 % is observed as the temperature yields 50°C, whereas the value slightly increases again with 0.8 % at 80°C.

Table 6.5: Summary of all rheological parameters for the best performing flat rheology fluid

Model		22°C	50°C	80°C
Herschel-Bulkley	τ_0	7.896	10.061	11.092
	% deviation		27.4 %	40.5 %
	k	0.190	0.207	0.225
	% deviation		8.7 %	18.0 %
	n	0.772	0.711	0.691
	% deviation		-7.9 %	-10.5 %
Unified	τ_{yL}	8.003	10.137	11.204
	% deviation		26.7 %	40.0 %
	k	0.156	0.179	0.183
	% deviation		14.7 %	17.0 %
	n	0.804	0.734	0.724
	% deviation		-8.7 %	-10.0 %
Power Law	k	4.657	6.860	7.826
	% deviation		47.3 %	68.0 %
	n	0.304	0.222	0.203
	% deviation		-27.2 %	-33.4 %
Bingham Plastic	τ_y	10.684	12.609	13.606
	% deviation		18.0 %	27.3 %
	μ_p	0.036	0.025	0.024
	% deviation		-29.8 %	-32.6 %
Robertson-Stiff	A	1.003	2.019	2.613
	% deviation		101.2 %	160.5 %
	C	45.566	51.402	49.768
	% deviation		12.8 %	9.2 %
	B	0.545	0.413	0.375
	% deviation		-24.2 %	-31.3 %
Newtonian	μ_p	0.051	0.043	0.044
	% deviation		-15.8 %	-15.0 %

6.2 Hydraulics Performance Simulation

Conducting hydraulics analyses of drilling fluids to be used in an operation is of great importance. As mentioned in subsection 2.9, the ECD is a critical parameter to consider in order to prevent the occurrence of lost circulation, kick and a potential blowout. To ensure a safe operation, the parameter should be kept below the fracture gradient and above the pore pressure. However, wellbore pressure is also dependent on the pump pressure required to circulate the drilling fluid and provide sufficient cuttings transport. Accordingly, it has become customary to perform hydraulics performance simulations in the industry. In this section, the performance of the best performing flat rheology system, as well as the nanoparticle fluids, is simulated in terms of ECD and pump pressure for a given experimental well and fluid flow rate.

6.2.1 Simulation Arrangement

All hydraulics performance simulations are conducted for the given experimental well setup presented in figure 6.2. An excel calculator is used to perform the simulations and it assumes an 8.5” vertical well with a total depth of 10000 ft. For simplicity, the mud pump and tank are assumed to be in direct contact with the drill string, which means that pressure loss due to surface equipment is neglected. In addition, the drill string simply consists of a 5” OD x 4.8” ID drill pipe and a bit with three nozzles. During the simulation, the flow rate of the drilling fluid is varied from 50 to 600 gpm, whilst the mud weight was set to 1.30 sg. As mentioned in subsection 2.9, the hydraulics performance simulations were conducted using the Unified model.

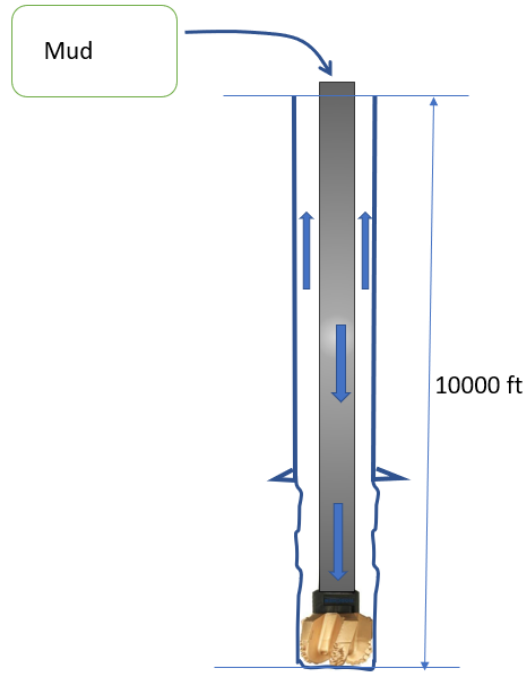


Figure 6.2: Well setup for the hydraulics performance simulation

The hydraulics performance simulation was conducted for the best performing flat rheology system, as well as the reference fluid containing no carbopol. These systems will be referred to as “REF + 0.08 g CP” and “REF”, respectively. Hence, when referring to the reference fluid in this subsection, 6.2, the initial system containing no carbopol is considered. Furthermore, the pump pressure and ECD exerted by the nanoparticle fluids are simulated. Since the viscosity of the system is a required input to perform the hydraulics simulation, this data is summarized in the following tables. As seen, the simulations will be performed at 22°C, 50°C and 80°C for all systems.

Table 6.6: Summary of viscometer dial readings applied in the hydraulics simulation (flat rheology system)

RPM	REF			REF + 0.08 g CP		
	22°C	50°C	80°C	22°C	50°C	80°C
600	26.5	25	28.5	42.5	34.5	34.5
300	18.5	17.5	22.5	30	25.5	26
200	13.5	14.5	19.5	23.5	22	22
100	9.5	12	17.5	17.5	17.5	18.5
6	3.5	7	13.5	8.5	10.5	11.5
3	3	6.5	13	8	10	11

Table 6.7: Summary of viscometer dial readings applied in the hydraulics simulation (nanoparticle fluids)

RPM	0.13 g MW			0.13 g Si			0.07 g Si		
	22°C	50°C	80°C	22°C	50°C	80°C	22°C	50°C	80°C
600	43	40.5	38	42	34	33	49	40	35.5
300	30	32	30.5	28	25	25	34	31	30
200	24.5	28.5	27	22	21	22	28	25.5	26.5
100	18	23.5	23	15.5	16	18.5	20.5	20	22
6	10	19	16.5	7.5	10.5	13.5	12	13	15.5
3	9.5	16	16	7.5	10	13	11.5	12	15

6.2.2 Pump Pressure Simulation Evaluation

As mentioned, the required pump pressure to circulate fluid through the circulation system is equivalent to the total pressure loss encountered in the system. For simplicity, the pump pressure simulations are performed assuming no rotation of the drill string, as well as no cuttings present in the wellbore. These assumptions do not reflect reality, but are acceptable in this thesis as the objective of the simulations is to compare the hydraulics performance of the fluids.

6.2.2.1 Best Performing Flat Rheology System

As mentioned, simulations were performed for the best performing flat rheology system, as well as the reference fluid, to investigate the effect of carbopol on the hydraulics performance. In figure 6.3, it is observed that the addition of 0.08 g carbopol lowers the total pressure loss encountered in the simulation system. Moreover, the pump pressure exhibited by the best performing flat rheology system, REF + 0.08 g CP, display relatively small changes with temperature. This is merely the case at flow rates above ~500 gpm for the reference fluid. Thus, the simulation verifies previous outcomes which indicated that the REF + 0.08 g CP system is temperature stable.

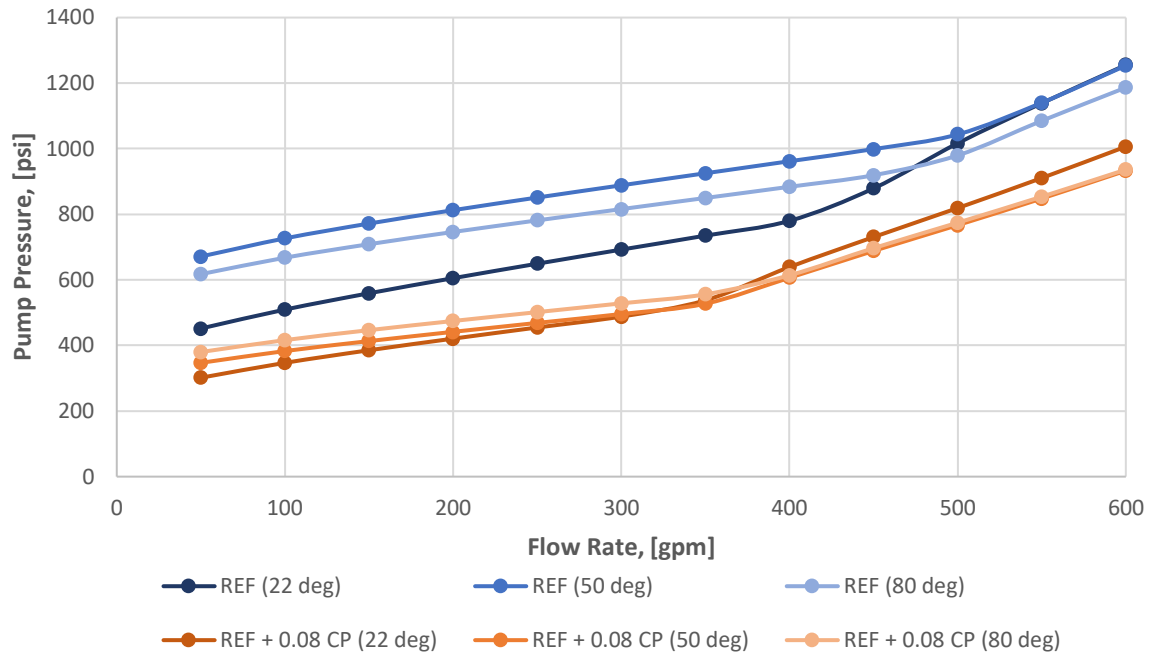


Figure 6.3: Pump pressures of flat rheology systems at 22°C, 50°C and 80°C

6.2.2.2 Nanoparticle Fluids

Hydraulics performance simulations were conducted for the nanoparticle fluids to investigate how the nanoparticle suspensions affected the hydraulics of the best performing flat rheology system. The resulting pump pressures of the 0.13 g MW, 0.13 g Si and 0.07 g Al systems are presented in this section, whilst the data for the remaining nanoparticle fluids are given in appendix F. It was decided to present the results of these particular fluids as they exhibit the best filtration and frictional properties when considering the nanoparticle suspensions separately, as well as only looking at the long-time effect of MWCNT-COOH. As the long-time stored 0.07 g MW system was spilled prior to measuring the CoF, this system is excluded. Additionally, the same trend was observed for most of the fluids containing the same nanoparticle in regards to total pressure loss at varied temperatures.

Figure 6.4, 6.5 and 6.6 presents the pump pressure as a function of flow rate for the multi-walled carbon nanotube, silica and aluminum oxide fluids, respectively. It is observed that the temperature's effect on the total pressure loss is relatively small, with the greatest deviation being exhibited by the 0.13 g multi-walled carbon nanotube fluid at 22°C. However, the difference caused by temperature is close to zero at flow rates above ~450 gpm for said system. All systems display a close to linear trend with increasing flow rate prior to more rapid growth at rates above 300-400 gpm. Overall, when considering the nanoparticle fluids presented in this

subsection, silica seems to produce the most stable system in regard to temperature. However, the best performing flat rheology system is still more stable.

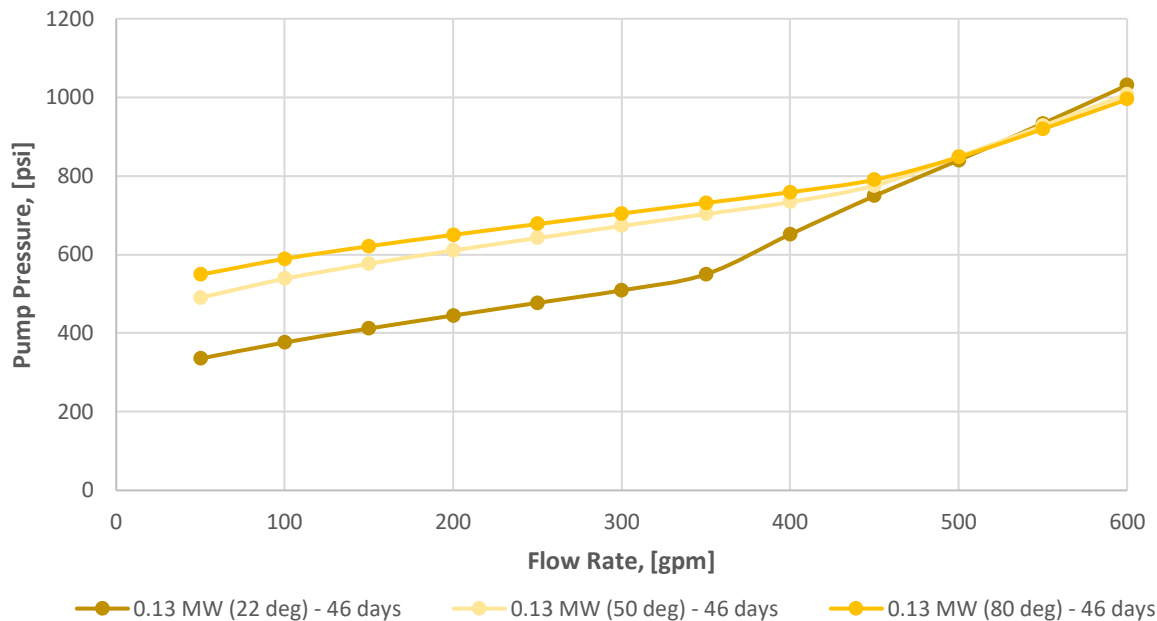


Figure 6.4: Pump pressure of 0.13 g MWCNT-COOH fluid at 22°C, 50°C and 80°C

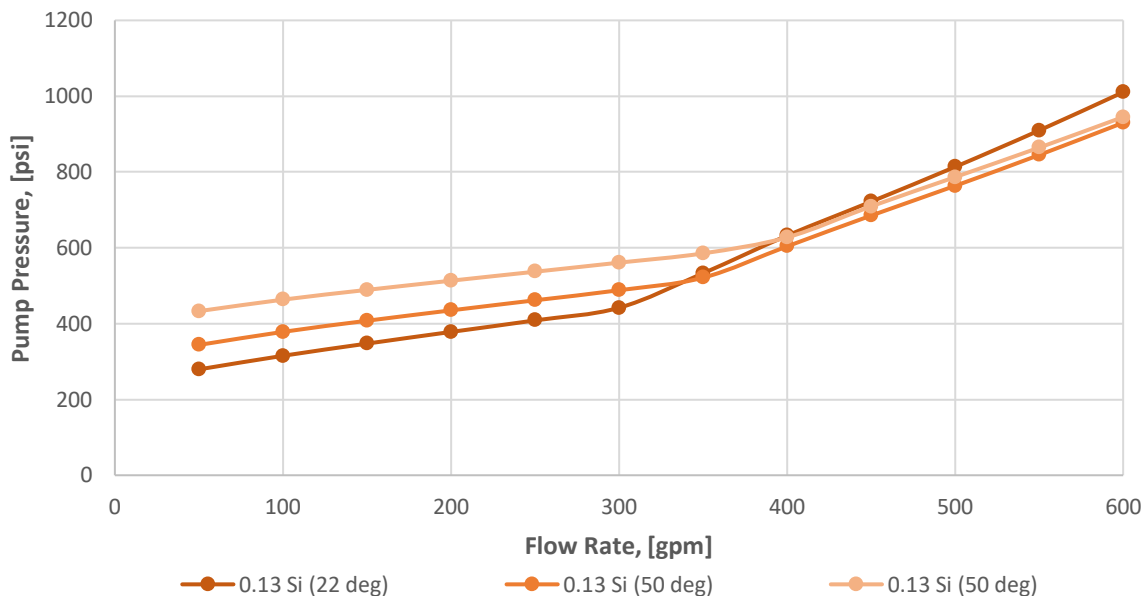


Figure 6.5: Pump pressure of 0.13 g silica fluid at 22°C, 50°C and 80°C

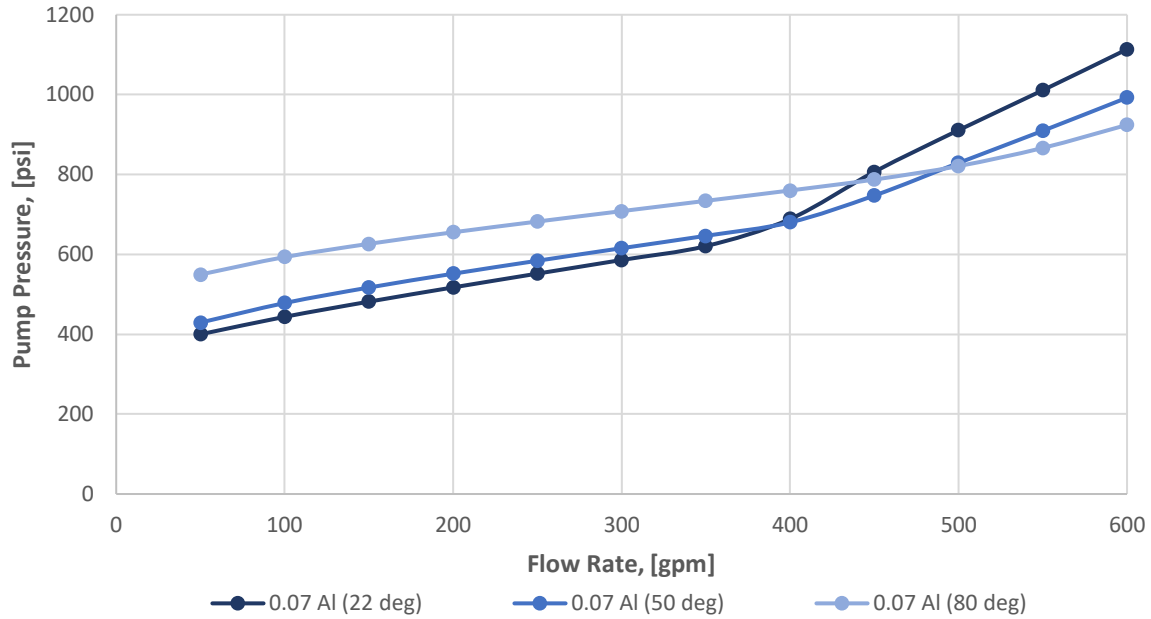


Figure 6.6: Pump pressure of 0.07 g aluminum oxide fluid at 22°C, 50°C and 80°C

Figure 6.7, 6.8 and 6.9 presents the change in total pressure loss for the multi-walled carbon nanotube, silica and aluminum oxide fluids, respectively, with the best performing flat rheology system as reference. It is observed that most of the nanoparticle fluids encounter greater pressure losses compared to the REF + 0.08 g CP system, whereas the 0.13 g silica fluid is the only system, presented in this subsection, that requires lower pump pressures for it to be circulated in the simulation well at 22°C and 50°C. Said fluid also produce the lowermost change in pressure as a function of flow rate overall, in addition to the 0.13 g MW fluid at 22°C.

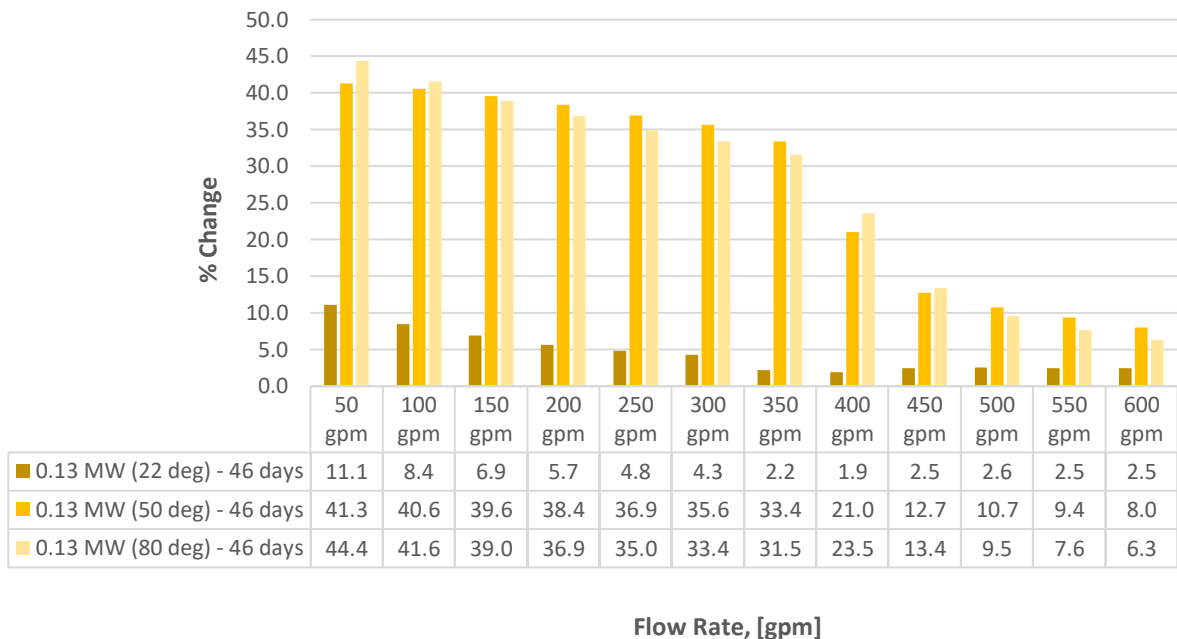


Figure 6.7: %Change in pump pressure for 0.13 g MW fluid at 22°C, 50°C and 80°C

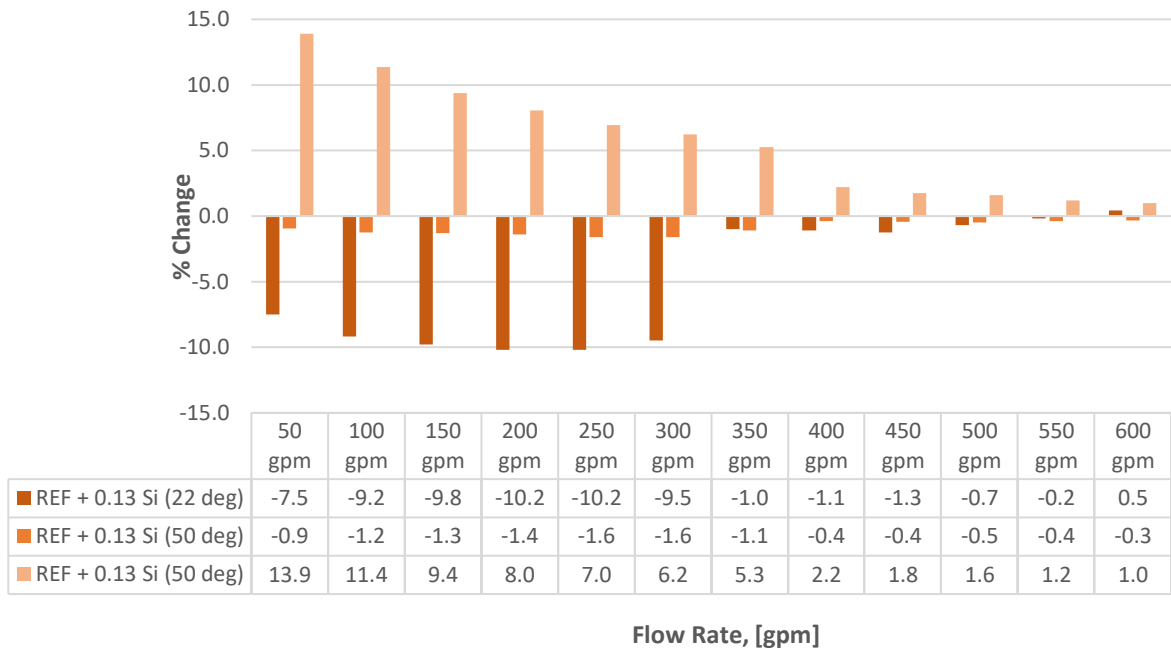


Figure 6.8: % Change in pump pressure for 0.13 g Si fluid at 22°C, 50°C and 80°C

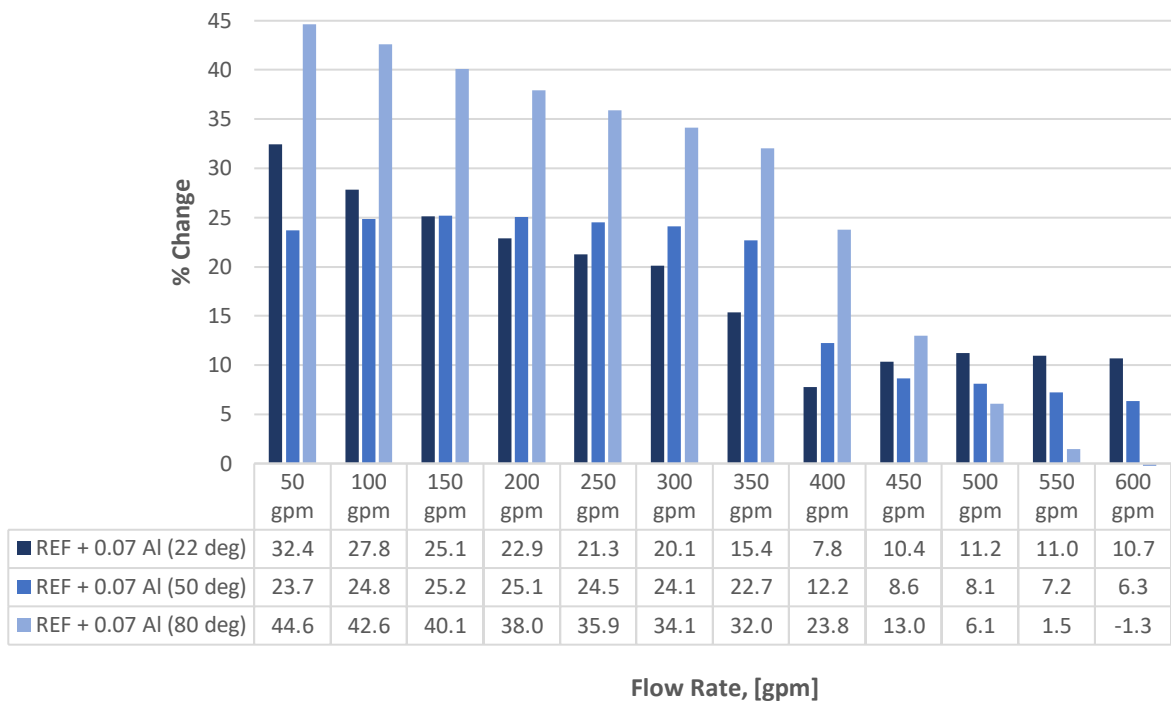


Figure 6.9: %Change in pump pressure for 0.07 g Al fluid at 22°C, 50°C and 80°C

6.2.3 ECD Simulation Evaluation

The ECD simulations are conducted with the use of equation 2.44, which is presented in subsection 3.9.1. To attain values for the equivalent circulation density, the annular pressure loss is a required input. This parameter is obtained at varied flow rates from the hydraulics performance simulation whilst keeping the fluid density constant. Furthermore, the assumptions of no cuttings and a non-rotating drill string, which was used in the pump pressure simulation, also applies for ECD simulation. It is to be noted that the units applied in the actual simulation differs from those presented in the ECD equation.

6.2.3.1 Best Performing Flat Rheology System

Figure 6.10 shows the ECD exhibited by the reference fluid and the best performing flat rheology system as a function of flow rate. Like the pump pressure, carbopol lowers the ECD of the system. In addition, it is observed the REF + 0.08 g CP system exhibit a stable ECD with increasing temperatures, when considering data obtained at 22°C, 50°C and 80°C. The values obtained for the reference fluid is also considered to be relatively stable, especially at temperatures above 50°C. However, as the flow rate is increasing, the difference between the resulting ECD at 22°C from those obtained at 50°C and 80°C declines.

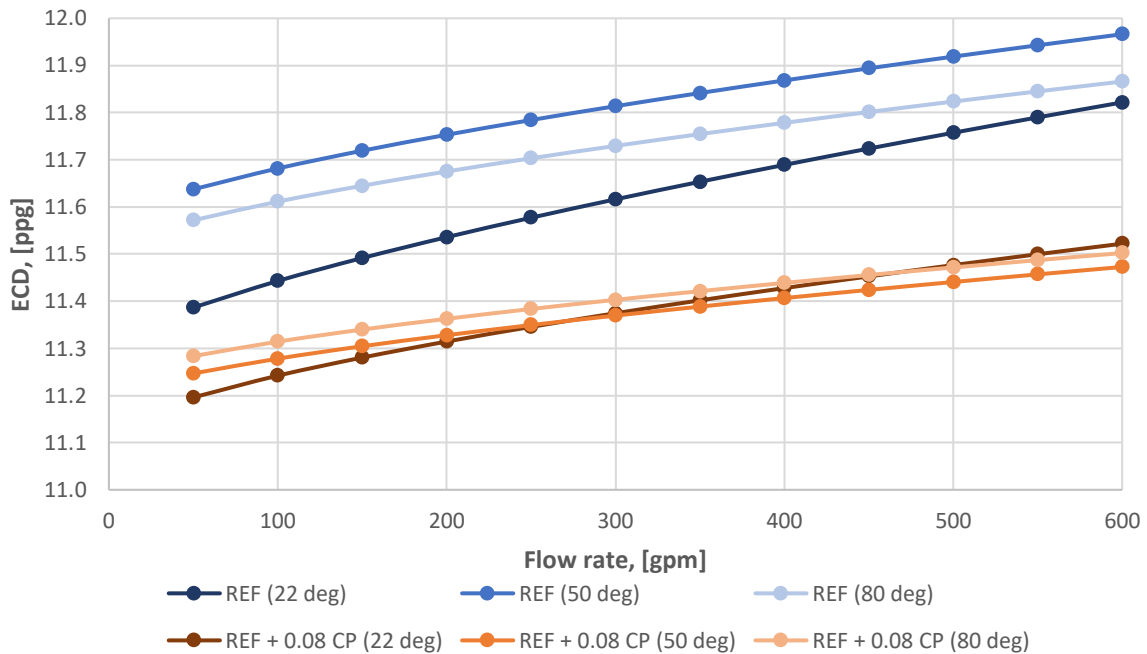


Figure 6.10: ECD plot for the flat rheology fluid

6.2.3.2 Nanoparticle Fluids

Similar to the pump pressure simulation described in subsection 6.2.2.2, the ECD simulations are performed for the 0.13 g multi-walled carbon nanotube, 0.13 g silica and 0.07 g aluminum oxide fluids. The resulting ECD as a function of flow rate for said systems are presented in figure 6.11, 6.12 and 6.13, respectively. Diagrams containing the simulated ECD for all nanoparticle quantities are given in appendix F.

The nanoparticle fluids display little change with temperature. This verify the previous results which indicated that the fluids are temperature stable. Furthermore, it is observed that the ECD's change with flow rate is minor within the simulation range for all nanoparticle suspensions. Having little growth in the ECD with increasing flow rate gives greater leeway in the process of selecting a proper pump rate to be applied in an operation. As mentioned, the flow rate should provide sufficient transport of cuttings to the surface whilst keeping the pressures within the safe operational window. Hence, it is observed that greater or lower flow rates can be applied accordingly without significantly influencing the resulting ECD. However, small changes are observed for all fluids when varying the flow rate. Table F.4, F.5 and F.6 in appendix F presents the percentage change from the initial mud weight of 10.83 ppg, which is equivalent to 1.30 sg, for the nanoparticle fluids.

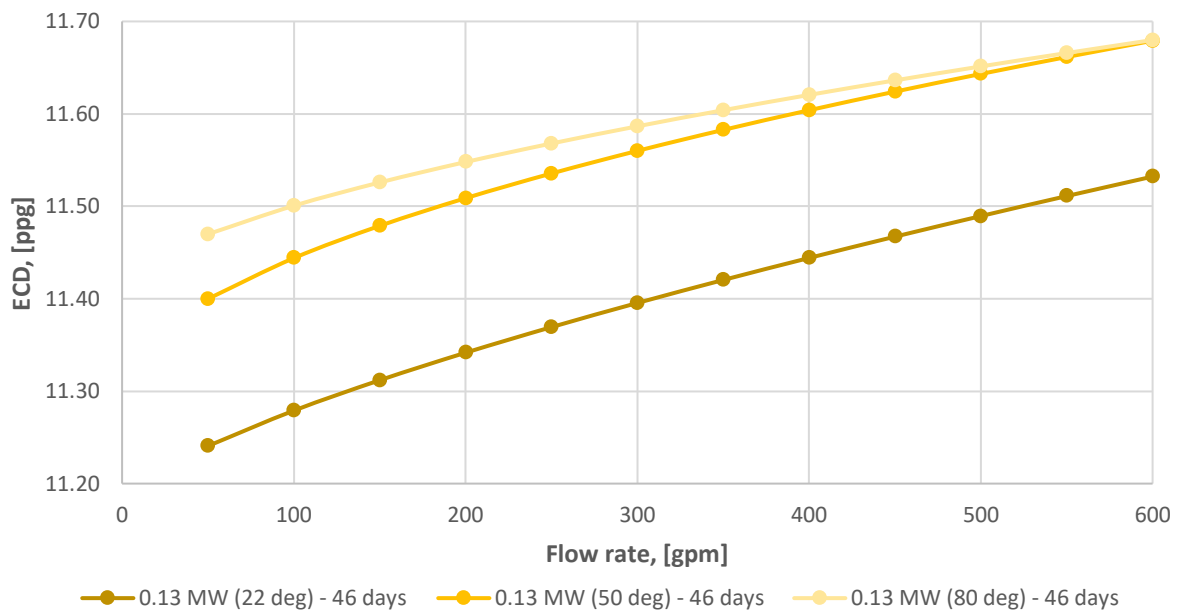


Figure 6.11: ECD plot for 0.13 g MWCNT-COOH fluid at 22°C, 50°C and 80°C

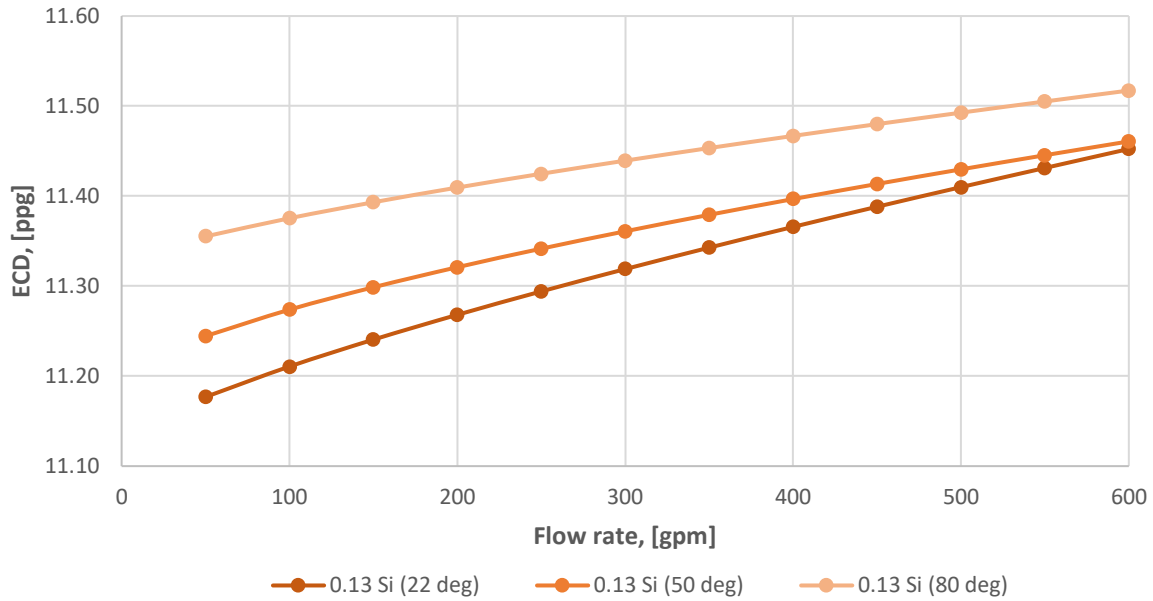


Figure 6.12: ECD plot for 0.13 g silica fluid at 22°C, 50°C and 80°C

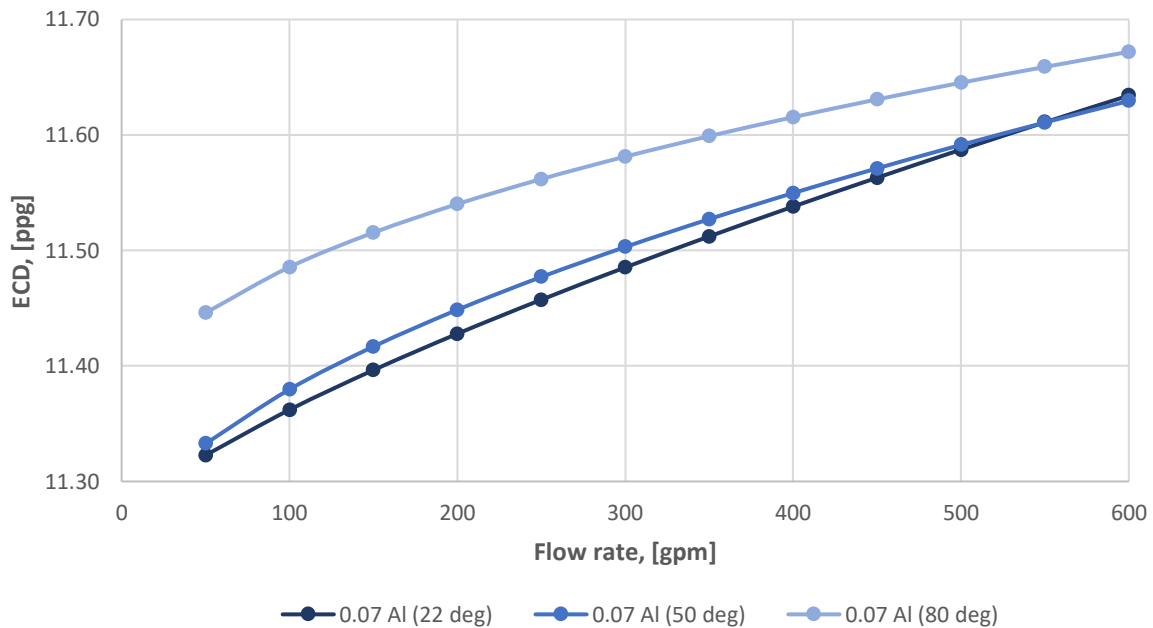


Figure 6.13: ECD plot for 0.07 g aluminum oxide fluid at 22°C, 50°C and 80°C

In figure 6.14, 6.15 and 6.16, it is observed that the addition of nanoparticle suspensions to the best performing flat rheology system induce little change in the resulting ECD. Both MWCNT-COOH and Al₂O₃ generates slightly greater ECD's, while silica also leads to relatively lower values when comparing to the REF + 0.08 g CP system. Results show that 0.13 g silica circulated at 50°C and 80°C, as well as 0.13 g MW at 22 °C, display the lowermost changes.

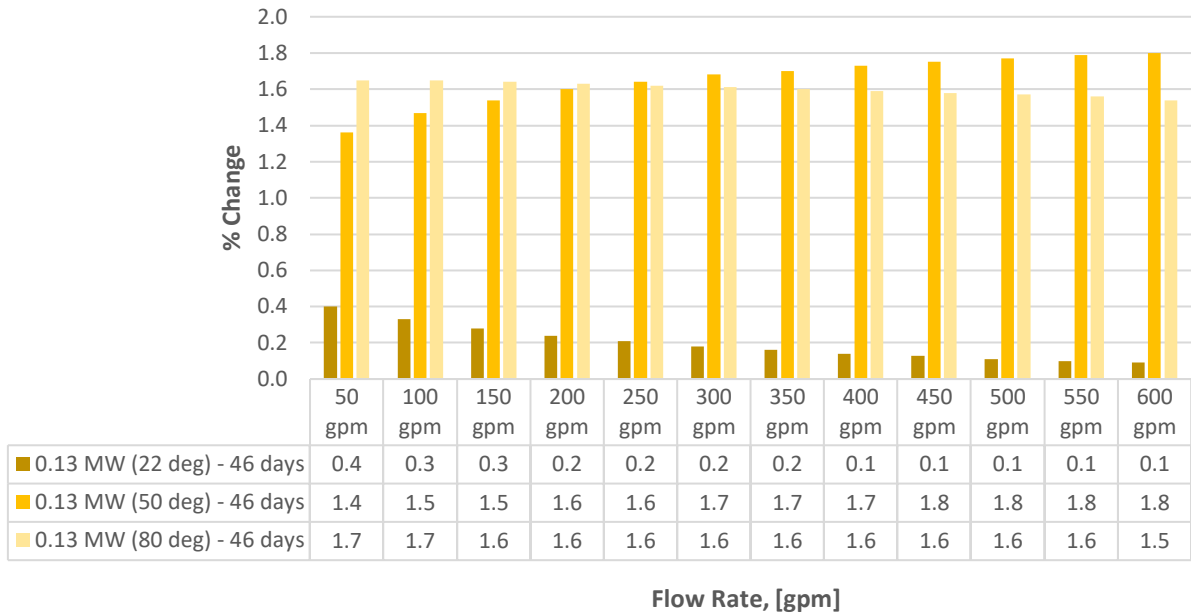


Figure 6.14: % Change of ECD from the REF + 0.08 g CP system for 0.13 g MW fluid

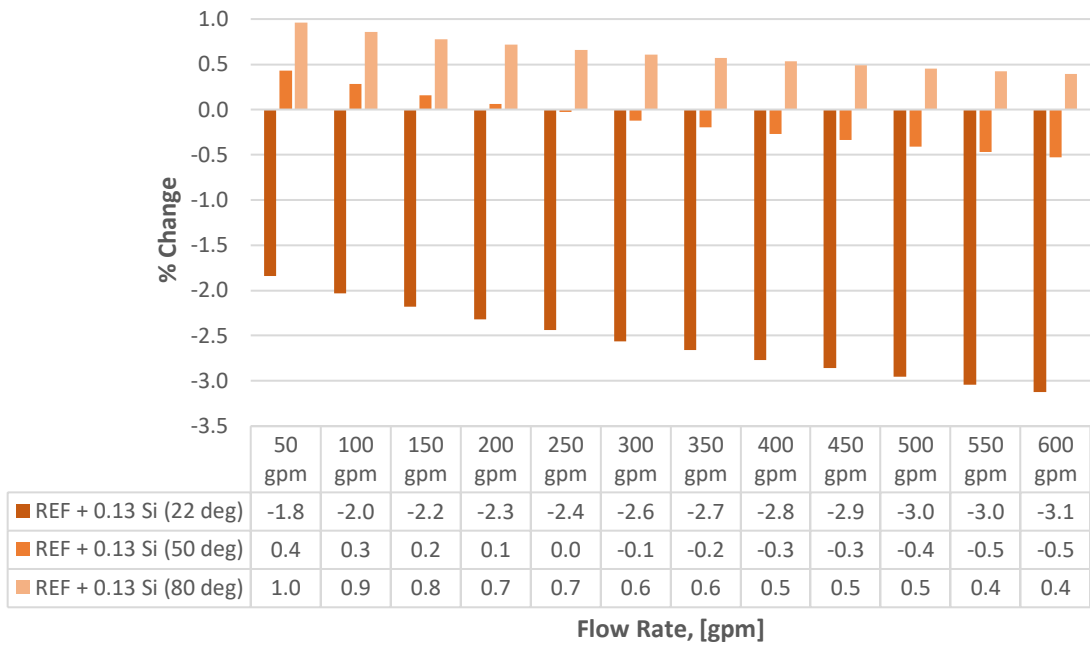


Figure 6.15: % Change of ECD from REF + 0.08 g CP system for 0.13 g silica fluid

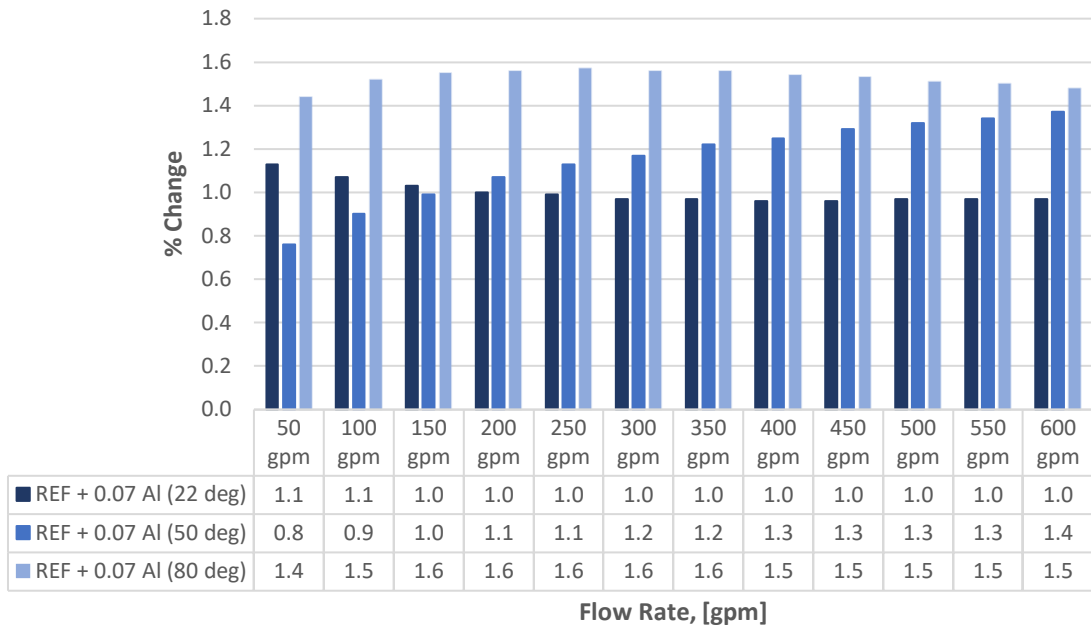


Figure 6.16: % Change of ECD from REF + 0.08 g CP system for 0.07 g Al fluid

6.3 Torque and Drag Simulation

Prior to drilling any well, simulations should be performed to ensure a successful drilling operation and reaching target depth. By defining a safe operational window, as presented in subsection 2.8.3, caution could be given to not exceeding the torsional and tensile limits when running into the well or tripping out of the hole, respectively. This is particularly important prior to drilling extended-reach, horizontal and deviated wells where contact between the drill string and the wellbore is more probable, resulting in increased friction resistance which makes torque and drag forces more critical.

Application of fluid systems with lower coefficients of friction will provide better lubrication of the drill string and bit, ultimately reducing the torque and drag values occurring in the wellbore. By implementing the friction results from the CSM tribometer test of the nanoparticle fluid systems, torque and drag simulations are performed to evaluate the effective tension, torque, stress trip in and stress trip out for each system. All simulations were executed using Halliburton Landmark’s WellPlan™ and the resulting plots are presented in appendix G.

6.3.1 Simulation Arrangement

The torque and drag simulation study was performed for the reference fluid, which is the one containing 0.08 g carbopol, as well as the best performing nanoparticle systems with regards to fluid loss. All simulations were completed using the same well design and keeping certain parameters constant. It consisted of a 13 3/8" casing with the casing shoe set at 4012 ft and a deviated 12.615" open hole section. However, the same coefficient of friction is used for both. Moreover, the applied drill string had an outside diameter of 5" and an inside diameter of 4.276". The rotational speed of the pipe was set to 50 RPM, while a tripping in and tripping out speed of 90 ft/min was utilized.

The experimental results obtained from the viscometer and tribometer tests at 22°C were registered to WellPlant™ and the simulations were conducted using the Herschel-Bulkley model. For each system, the measured depth was varied to investigate the effect of the nanoparticles on the maximum drilling depth. While increasing the depth in steps, the produced plots for effective tension, torque, stress trip in and stress trip out were observed. The objective was to obtain the greatest depth to which the well could be drilled without exceeding the safe operational window. Since it is common practice to implement an additional margin of security from the actual limits in the field, this was also applied when determining the maximum drilling depth from the plots.

6.3.2 Simulation Evaluation

When increasing the depth of the wellbore, as well as the drill string, for each of the fluid systems in the T&D simulation, two factors were found to repeatedly limit the drill string. This was the effective tension when tripping out and the torque when rotating of bottom. Accordingly, the maximum depths are found to be where these curves are approaching the torque and tensile limit with only a defined safety margin separating them. As mentioned, the resulting plots from the simulations are presented in appendix G, whereas the maximum drilling depths are presented in figure 6.18. All percentage changes are calculated as the change from the reference fluid measured after short-time aging, except the REF + 0.13 g MW (long-time) system which is compared to the reference fluid stored for a longer period.

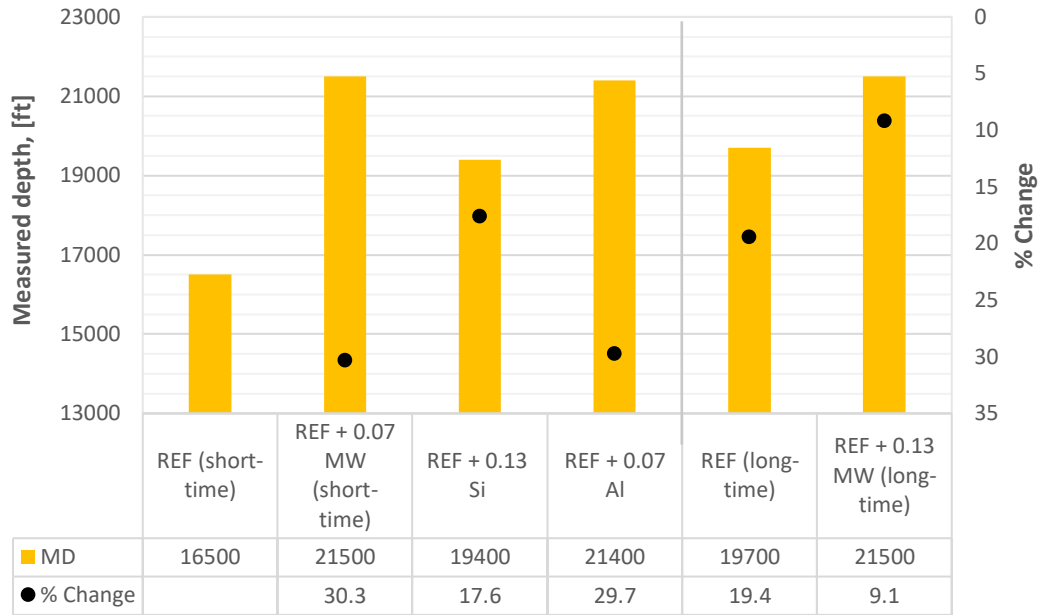


Figure 6.17: Maximum drilling depths from the T&D simulation

As presented in figure 6.17, application of the reference fluid after short-time aging enables the drill string to drill down to a measured depth of 16500 ft. Drilling any further would cause the torsional limit to be exceeded when rotating off bottom. Storing the reference fluid for a longer period, prior to performing the operation, allows drilling to proceed until a measured depth of 19700 ft, resulting in a 19.4 percent improvement. Since the tribometer test indicated a 25.2 % reduction of the coefficient of friction, better lubricity and an increased maximum drilling depth is as expected. Moreover, it is observed that the addition of all nanoparticle suspensions increase the measured depth to which the drill string can be utilized without exceeding the safe operational window. Overall, it is seen that the resulting maximum depths obtained from the T&D simulation corresponds with the tribometer results, which showed that the coefficient of friction of all nanoparticle fluids were reduced. A summary of the coefficients of friction, maximum depths and limiting factors for each system is presented in table G.1 and G.2.

7 Summary and Discussion

This section will provide a summary and some discussion of the results obtained from the experimental work and simulation studies. In addition, some limitations and uncertainties related to the measurements of the fluids will be elaborated on.

7.1 Characterization of Drilling Fluid

The water-based drilling fluids were characterized using rheological, filtration, viscoelastic and frictional measurements. Primarily, the rheological properties were obtained at 22°C, 50°C and 80°C using an OFITE Model 8 viscometer, whereas an Anton Paar MCR 302 rheometer was applied to attain the viscosity over the entire temperature range for some fluids. This apparatus was also applied to measure the viscoelastic properties by performing amplitude sweeps. The filtration and frictional properties of the fluids were obtained at room temperature using an API static filter press and a CSM tribometer, respectively. Further descriptions of this experimental equipment were presented in subsection 4.2.

7.1.1 Flat Rheology System

Rheological Measurements

Initially, various amounts of lignosulfonate were added to the water-based drilling fluid with the objective of obtaining a flat rheology fluid. The polymer is commonly used for this purpose in the industry and as seen in figure 7.1, it also provided such characteristics of the water-based fluid presented in this thesis. The addition of 0.6 g, 0.7 g and 0.8 g lignosulfonate provided the fluid with flat rheology characteristics at increased temperatures ranging from 50°C to 80°C, which are in fact closer to the temperatures encountered in conventional wellbores and thus, more realistic. Though, this is the effect of lignosulfonate together with 0.5 g carbopol.

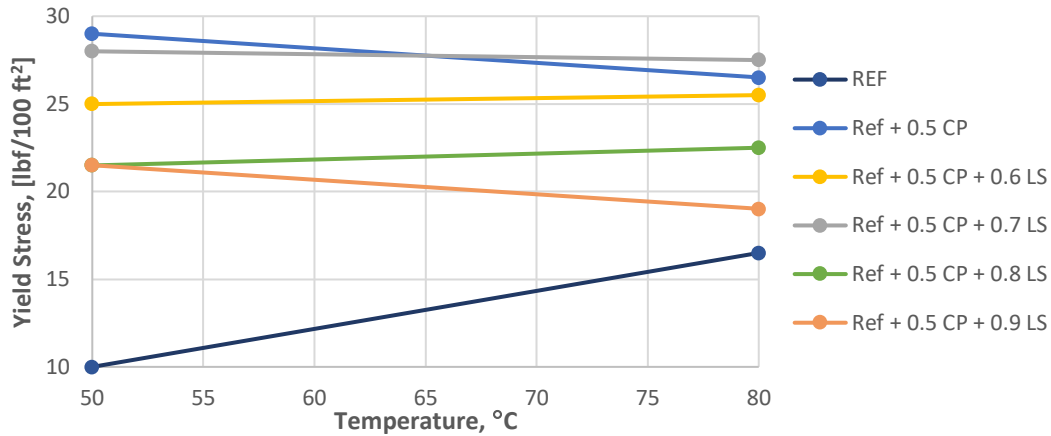


Figure 7.1: Bingham yield stress of lignosulfonate fluids (0.6-0.9 g) at 50°C and 80°C

However, lignosulfonate is known to function as a thinning agent and thus, it will reduce the rheological properties such as viscosity and yield stress. As expected and seen in figure 7.1, the yield stress values of the fluid formulation presented in this thesis decreased non-linearly with the addition of the polymer. This contradicts with the effect of carbopol, which was added to increase the viscosity of the initial fluid formulation. From the results presented in figure 7.1, it was observed that carbopol could act both as a viscosifier and provide flat rheology characteristics. Thus, the effect of carbopol was further investigated with the objective of attaining an additive providing temperature stability as well as increased viscosity.

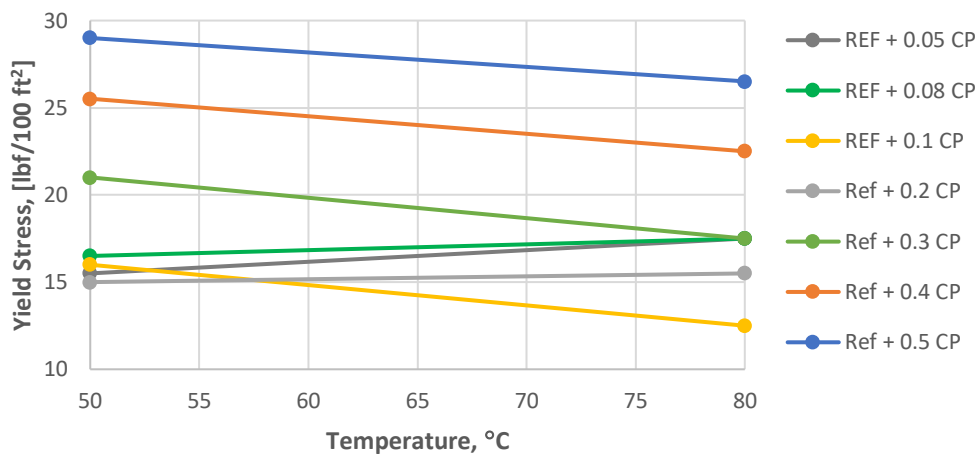


Figure 7.2: Bingham yield stress of carbopol fluids (0.05-0.5 g) at 50°C and 80°C

By reducing the amount of carbopol, it was observed that the Bingham yield stresses of the fluid became more stable. In addition, temperature sweeps of the fluids containing 0.05 g and 0.08 g carbopol showed that the viscosity was quite stable over the entire temperature range of 20-80°C. Thus, it was concluded that carbopol could provide flat rheology characteristics in the same manner as lignosulfonate, but act as a viscosifier instead of functioning as a thinning agent.

Viscoelastic Measurements

From the oscillatory amplitude sweeps it was observed that all fluids had a gel-like character at lower shear rates, in the LVE range, and thus, exhibited viscoelastic properties. This is an important property of drilling fluids for it to be able to suspend weight material and lift cuttings in the wellbore. However, too much gelling is undesirable as it might make the fluid unpumpable without exceeding the pump pressure limitations [123]. Though, the point of this analysis was not to evaluate whether the yield stress values are correct or not, but to investigate the changes caused by the additives.

In general, it was observed that the yield stress and flow point of the fluid decreased with the addition of lignosulfonate. This means that the fluid will be irreversibly deformed at lower shear rates and that the viscous portion of viscoelastic behavior prevails earlier with greater amounts of lignosulfonate. The opposite was observed with the addition of carbopol, which increased the yield stress and flow point values of the fluid. This trend, however, was non-linear and excluded the quantities of 0.1-0.3 g which resulted in lower flow point values. Moreover, carbopol tended to elongate the linear viscoelastic range, which is reasonable since the application of the polymer makes a fluid more viscous and accordingly, greater shear rates must be applied to initiate flow.

A so-called G'' -peak was observed for all lignosulfonate and carbopol fluids to a varying degree, when excluding the system containing 0.05 g carbopol. This increase of the loss modulus curve indicate that deformation energy is being used to irreversibly deform parts of the sample's internal structure prior to the final breakdown of the gel. Such a peak might occur due to relative motion between particles or the presence of long network bridges, to mention a few.

7.1.2 Nanoparticle Modified System

Both the calculated Bingham yield stresses and the temperature sweeps showed that 0.05 g and 0.08 g carbopol provided the system with flat rheology characteristics. In addition, both fluids exhibited Bingham yield stresses within the range of 11-20 lbf/100 ft² commonly applied in the field. However, the fluid system containing 0.08 g carbopol was thought to provide slightly better stability and was therefore chosen as the best performing flat rheology system. Thus, this became the reference fluid in which the effect of multi-walled carbon nanotube, silica and aluminum oxide would be investigated. The following concentrations were applied:

- 0.07 g, 0.13 g, 0.18 g and 0.24 g multi-walled carbon nanotube
- 0.08 g, 0.13 g, 0.18 g and 0.25 g silica
- 0.07 g, 0.13 g, 0.19 g and 0.24 g aluminum oxide

Rheological Measurements

From the rheological measurements, it was observed that the addition of multi-walled carbon nanotube increased the viscosity profile of the fluid, whilst silica and aluminum oxide displayed minor alterations. Moreover, both MWCNT-COOH and alumina resulted in greater yield stress values, while the opposite was observed for the silica fluids. The latter correlates well with results obtained by Mahmoud et al. in a previous study presented in section 3.3, where silica reduced the YS of a WBM formulation exposed to temperatures ranging from ~50-90°C.

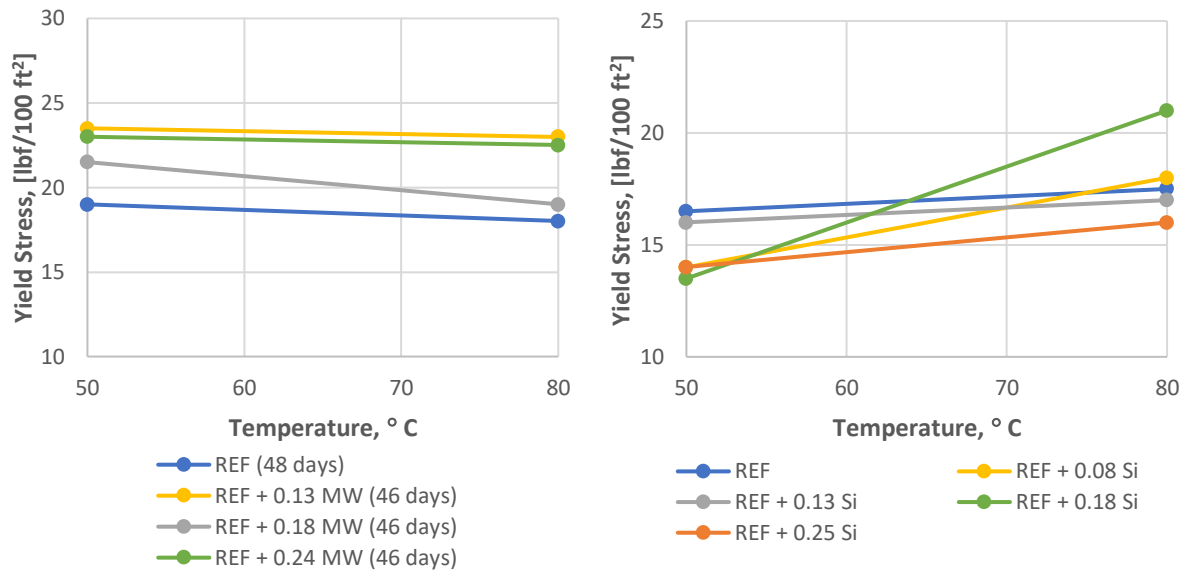


Figure 7.3: Bingham yield stress of MW (left) and silica fluids (right) at 50°C and 80°C

As seen in figure 7.3 and 7.4, the fluid remained quite temperature stable with the addition of most of the nanoparticle quantities. In fact, the addition of 0.13 g and 0.24 g aluminum oxide improved the stability of the system. This is analogous to the results presented by Amarfio and Abdulkadir, which concluded that aluminum oxide provided thermal stabilization of their WBM formulation. On the other hand, when considering temperatures above 50°C, silica displayed the largest alterations of the stability overall and at a concentration of 0.18 g, the stability was non-existent. It is to be noted, that all quantities of multi-walled carbon nanotube exhibited yield stress values beyond the 11-20 lbf/100 ft² range, in addition to the 0.18 g silica and 0.07 g alumina fluids.

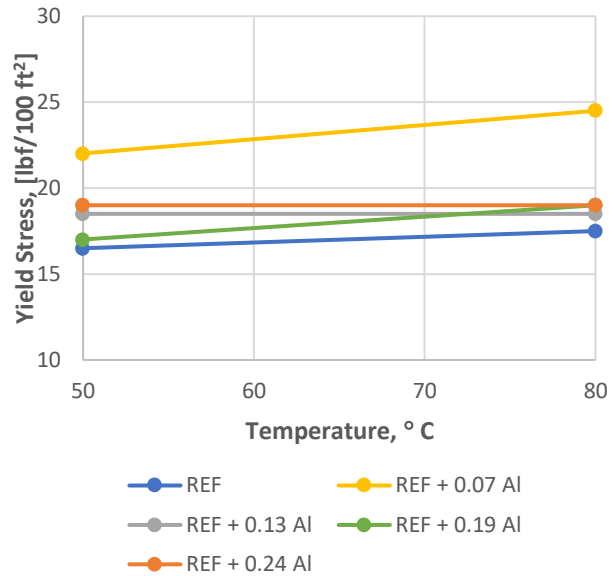


Figure 7.4: Bingham yield stress of aluminum oxide fluids at 50°C and 80°C

Viscoelastic Measurements

The amplitude sweeps showed that lower flow points and increased upper limits of the linear viscoelastic range were exhibited by all nanoparticle systems, excluding the 0.07 g alumina fluid which had a shorter LVE range. This indicates that a fluid modified with multi-walled carbon nanotube, silica and aluminum oxide tolerates larger shear rates prior to being irreversibly deformed and that the viscous portion of viscoelastic behavior prevails at lower shear stresses. Moreover, the yield stress remained relatively unaffected by the nanoparticle suspensions.

The best performing flat rheology system still exhibited structural stability with the addition of all nanoparticle suspensions and their quantities since the elastic portion dominated the viscous one in the LVE range. However, it was observed that the addition of silica reduced both the storage and loss modulus of the fluid. This implies that the silica systems exhibited less viscoelastic responses to the applied dynamic load, which is a result of lower gel strengths. The addition of MWCNT-COOH and alumina resulted in minor changes in the magnitudes of the G' and G'' values.

Filtration Measurements

Primarily, the nanoparticle suspensions were added to improve the filtration properties of the reference fluid containing 0.08 g carbopol. From the results, it was observed that all the nanoparticle suspensions and their quantities reduced the filtration volume. This indicate that the nanoparticle suspensions provide a less permeable buildup of solids and thus, a filter cake of higher quality and improved structure [88]. The increased fluid loss control is to a large degree provided by the small size of the nanoparticles, which provide the ability to physically plug nanometer-sized pores [82].

Table 7.1: Fluid loss results of best performing fluid loss control quantities

Fluid	REF	REF + 0.07 g MW	REF + 0.13 g Si	REF + 0.07 g Al
Fluid Loss, [ml] (7.5 min · 2)	6.5	5	4.5	4.4
% Change	---	-23 %	-31 %	-32 %

Moreover, it was seen that the addition of lower volumes of multi-walled carbon nanotube, silica and alumina induced the greatest reduction of the fluid loss. Table 7.1 presents a summary of the nanoparticle quantities who caused the greatest reduction, where all results are for short-time stored systems. As seen, the greatest fluid loss control was provided by 0.07 g aluminum oxide.

Frictional Measurements

In previous studies, as well as in this thesis, it has been demonstrated that low concentrations of nanoparticles are able to greatly impact the properties of a fluid. Because of this, in addition to the large surface area to volume ratio, nanoparticles are thought to function as efficient lubricant additives in drilling fluids. The ability of nanoparticles to improve the frictional properties of a fluid was investigated by Taraghikhah et al., presented in section 3.3, which concluded that silica functioned as an efficient lubricant in a water-based drilling fluid formulation. Thus, the effect of multi-walled carbon nanotube, silica and aluminum oxide on the frictional properties of the best performing flat rheology system was investigated.

Table 7.2: Tribometer results of best performing lubricant quantities

Fluid	REF	REF + 0.07 g MW	REF + 0.13 g Si	REF + 0.07 g Al
CoF	0.249	0.157	0.192	0.160
% Change	---	-36.8 %	-23.1 %	-35.6 %

The tribometer results showed that the nanoparticle suspensions and their quantities reduced the coefficient of friction significantly and thus, improved the lubricity of the reference fluid. Moreover, it was observed that lower concentrations enhanced the frictional properties the most and in fact, this was the same exact quantities that provided superior fluid loss control. Some possible reasons to why nanoparticles reduce the CoF, especially at lower concentrations, are presented in the following list: [54]

- A lubricating layer is formed between the ball and plate surface by the nanoparticles.
- Micro sized irregularities of the surface are filled by the nanoparticles, reducing the ball's ability to grip onto the surface. Exceeding the point at which all the gaps are filled, the addition of more NPs could increase the CoF again.
- Nanoparticles lift the ball off the plate surface, inhibiting direct contact between the two. Exceeding the number of NPs required to lift the ball induce more contact points and consequently, the CoF increase again.

7.2 Carbopol's Method of Application

As presented in section 5.2, the order in which carbopol was added had significant impact on the rheological properties of the initial fluid formulation. It was clearly seen that the system with carbopol added ex-situ resulted in greater viscometer dial readings than the one with in-situ application. The viscometer dial readings of the two systems, as well as the percentage deviation caused by ex-situ application, are presented in table 7.3.

Table 7.3: Viscometer dial readings at 50 °C comparing ex-situ and in-situ application of carbopol

RPM	Ref + 0.5 g CP + 0.9 g LS		% Deviation
	In-Situ	Ex-Situ	
600	40	47.5	19 %
300	28	34.5	23 %
200	22.5	29	29 %
100	16.5	22.5	36 %
60	14.5	20	38 %
30	11	17.5	59 %
6	9	15.5	72 %
3	8.5	14.5	71 %

From figure 5.6, which displayed the Bingham yield stress values obtained at 22°C, 50°C and 80°C, it was seen that the method of application also impacted the polymers ability to provide flat rheology characteristics. In fact, the yield stress values of the in-situ system indicated that the fluid would flocculate when exposed to higher temperatures and thus, carbopol showed little tendency of providing temperature stability when added in-situ. Table 7.4 presents the Bingham yield stress values calculated for the in-situ and ex-situ systems, as well as the percentage change caused by increasing the temperature.

Table 7.4: Bingham yield stresses comparing ex-situ and in-situ application of carbopol

Temperature, [°C]	Ref + 0.5 g CP + 0.9 g LS			
	In-Situ	% Change	Ex-Situ	% Change
22	11.5	---	16	---
50	16	39 %	21.5	34 %
80	22.5	96 %	19	19 %

Fundamentally, the distinction between the in-situ and ex-situ systems are related to the fact that the two methods of application results in different structural properties. By adding carbopol in-situ, the polymer will be dispersed well and become part of the water phase. Hence, carbopol will be able to interact with most of the clay platelets and so will the induced surface changes it brings, resulting in a certain degree of repulsion. When adding carbopol ex-situ, on the other hand, it will interact with the hydrated clay platelets, as well as the other polymer additives. In this situation, the surface charge of carbopol will not be able to have a strong interaction with

the clay. Though, the reason for the distinction between the fluid properties was not investigated and thus, this is merely one possible explanation.

7.3 Effect of Aging

The reference fluid, i.e. the initial fluid formulation containing 0.08 g carbopol, was stored statically at room temperature for 48 days, whereas the multi-walled carbon nanotube fluids were stored for 46 days under the same conditions.

Rheological and Filtration Measurements

From the viscometer dial readings obtained at 50°C, it was observed that the reference fluid had become more viscous with time. The results obtained at 22°C, on the other hand, showed that the viscosity profile of the long-time stored sample had declined, though the change was minor. Accordingly, from the Bingham yield stress values, it was seen that the long-time stored fluid had become less stable at lower temperatures, however, the fluid still exhibited flat rheology characteristics at temperatures above 50°C.

Figure 5.37 presented the viscometer dial readings obtained at 22°C for the short- and long-time stored reference fluid, as well as the 0.07 g MWCNT-COOH system. The results showed that the viscosity profile of the nanoparticle fluid had decreased with time and in fact, the long-time stored sample exhibited a viscosity quite similar to that of the reference fluid after both storing periods. Hence, it was observed that the long-time storing effected the multi-walled carbon nanotube fluid to a greater extent, when considering the rheological data obtained at 22°C. Moreover, both fluids exhibited increased fluid loss volumes after long-time aging.

These results show that the reference fluid and the MWCNT-COOH system are degrading with time. There could be several factors contributing to the alterations of the fluid properties and the following was further investigated:

- Mud weight measurements showed that the density of the reference fluid had increased with time.
- pH measurements of both the reference fluid and the MWCNT-COOH system showed minor changes with time, where ΔpH was 0.10 and 0.17 respectively.

- A SEM inspection of the filter cakes showed no bacteria and minor changes in the element content of the surface

Thus, it was concluded that the alterations of the fluid properties primarily were caused by evaporation of water and degradation of the polymer additives. This means that less water is being trapped within the clay particle structure, as well as the polymer’s tensile strength, color, shape and/or molecular weight could have been changed. [124]

Frictional Measurements

The tribometer results showed that the coefficient of friction of the reference fluid had declined after 48 days of storing at room temperature, as well as exposure to 80°C during the viscosity measurement. A possible reason for this reduction can be the degradation of the polymer additives, which often results in lower molecular weight due to changes in the chemical and/or physical structure of the polymer chain. As a result, the polymer could have formed smaller molecules [124]. As with the addition of nanoparticles, the smaller sized polymer molecules could reduce the CoF by being able to fill micro sized gaps or lift the ball off the plate surface. Though, this is just a possible explanation.

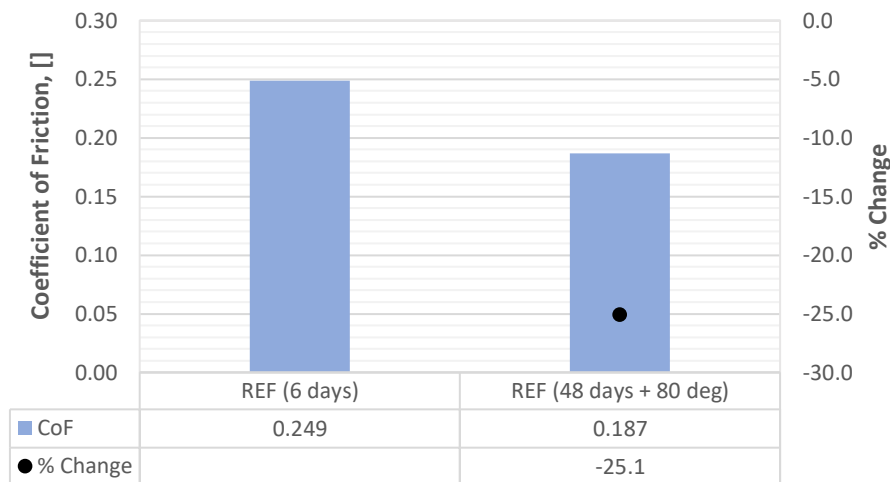


Figure 7.5: Tribometer results for reference fluid after short- and long-time storing

7.4 Performance Evaluation

Hydraulics and T&D simulations were performed to investigate the performance of the best performing flat rheology fluid and the nanoparticle systems. The simulations were conducted using the Unified and the H-B models, respectively. From the rheological modeling, it was found that both models provide a quite accurate description of the reference fluid at all test temperatures. To be noted, the initial fluid formulation was denoted as the reference fluid in subsection 6.2, though this notation is used for the flat rheology system containing 0.08 g carbopol in this section.

Hydraulics

The hydraulics performance of the fluids was investigated by simulating the pump pressure and ECD at 22°C, 50°C and 80°C for a given well, which was presented in subsection 6.2.1. From the resulting curves, it was observed that both the pump pressure and the ECD of the reference fluid was temperature stable. The nanoparticle fluids also exhibited relatively stable pump pressures and ECDs with increasing temperature, though none were as stable as the reference fluid itself.

Torque and Drag

Torque and drag simulations were performed to illustrate how the frictional properties of the applied drilling fluid affect the maximum drilling depth. By evaluating the effective tension, torque, stress trip in and stress trip out of the drill string, it was found that lower CoF values resulted in greater maximum depths. The addition of all nanoparticle suspensions improved the lubricity of the reference fluid and thus, reduce the torque and drag forces experienced in the well. Accordingly, the maximum depth to which a well can be drilled prior to exceeding the safe operational window becomes greater.

7.5 Rheological Model and Bingham Yield Stress

From the rheological modelling, the Robertson-Stiff model was found to provide the most accurate description of the reference fluid at all test temperatures. Though, the H-B and Unified models also provided relatively accurate predictions.

As mentioned in section 2.3, the applied rheological model should correlate well with the measured viscometer dial readings in order to attain an accurate description of the drilling fluid.

However, it was still decided to use the Bingham Plastic model to describe the rheological properties of the fluid formulations presented in this thesis. The reasons for doing so are related to the commonness of the model. Firstly, it is the rheological model most commonly applied in the petroleum industry [125]. Moreover, it is frequently used to describe fluid behavior and investigate the flat rheology characteristics in previously published papers. Some examples on experimental studies utilizing the Bingham Plastic model are presented in the following list:

- “Impact of Nanomaterials on the Rheological and Filtration Properties of Water-Based Drilling Fluids” by Salih et al., [82]
- “Experimental Investigations into the Performance of a Flat-Rheology Water-Based Drilling Fluid” by Xu et al., [126]
- “New Flat-Rheology Synthetic-Based Mud for Improved Deepwater Drilling” by van Oort et al., [127]
- “New Thermally Independent Rheology Invert Drilling Fluid for Multiple Applications” by Friedheim et al., [42]

7.6 Limitations and Uncertainties

All experimental measurements will have some degree of error due to limitations, uncertainties and assumptions related to the applied instruments and calculations. This will limit the reliability and reproducibility of the produced data and therefore, it is of utmost importance to minimize and account for sources of error. However, the extent to which the possible errors can be controlled varies and some factors are more easily controlled than others.

Chemical Additive Measurements

The application of an uncalibrated and/or low precision weight balance, with a low number of decimals, will impact the amount of chemical which is actually measured and applied to the drilling fluid. Thus, the possibility of error can be minimized by using a high precision weight balance, as well as performing calibrations on a regular basis. However, the amount of additive applied to the drilling fluids can still vary slightly due to small losses of particles to the environment, which for example occur during the mixing process.

Viscometer Measurements

In regards to the viscosity measurements of the fluids, the same procedure should be followed throughout the entire study and the applied viscometer should be calibrated regularly to minimize the possibility of errors. Other factors which can contribute to errors in the viscometer dial readings are the occurrence of:

- An inhomogeneous fluid,
 - As the properties of the fluids will vary depending on which part of the fluid is measured, the viscometer response can fluctuate.
- Dynamic sag,
 - Can result in lower viscometer dial readings as particles are settling to the bottom of the measuring cup.
- Temperature variations,
 - It is well known that temperature affects the resulting viscometer dial readings and for most bentonite fluids, the viscosity increases with temperature.

Rheometer Measurements

The Anton Paar MCR 302 rheometer was applied to perform oscillatory amplitude sweeps and rotational temperature sweeps. Some factors that could affect the accuracy of these measurements are:

- An inhomogeneous fluid,
 - As the viscoelastic properties could vary within the fluid, it could result in fluctuating data points.
- Dried out sample,
 - Depending on the extent to which the sample is dried out, other properties can be exhibited.
- Error in gap size
 - Could prevent the sample from interacting with both plates.
- Temperature offset,
 - With the application of the “cup and bob” setup, the set and actual temperature of the sample might differ slightly.
- Dynamic sag,

- With the application of the “cup and bob” setup, it can result in a less viscous fluid as particles settle and accumulate at the bottom of the measuring cup.

Hydraulics Simulations

For simplicity, several assumptions were made when performing the hydraulics simulations. These are stated in section 6.2 and ignore several aspects of a real drilling operation, making the simulated well unrealistic. Though, the objective of the simulation study was to compare the hydraulics performance of the drilling fluids relative to each other and thus, the assumptions were regarded as acceptable. However, the simulation study is based on the viscometer dial readings and the density of the drilling fluid and thus, the resulting pump pressure and ECD could be wrongful if these measurements contain errors.

8 Conclusion

The main objectives of this thesis were to design and characterize a flat rheology water-based drilling fluid and investigate the effect of multiple nanoparticle suspensions on the properties of this fluid. The rheological, filtration, viscoelastic and frictional properties of the fluids were measured and the resulting data was further applied in the simulation study to investigate the hydraulics and T&D performance.

Based on the results obtained from the experimental work and the simulation study, the following observations and conclusions were made;

In regards to the effect of carbopol and lignosulfonate:

- From the rheological measurements, it was observed that carbopol should be added ex-situ to attain flat rheology characteristics.
- The Bingham yield stress values indicated that both polymers could provide flat rheology characteristics, though carbopol functioned as a viscosifier and lignosulfonate as a thinning agent.
- Results from the rheological measurements indicated that the addition of ~0.016 wt% carbopol provided the most thermally stable fluid.
- From the oscillatory amplitude sweeps, it was observed that all fluids exhibited a gel-like structure in the linear viscoelastic range and thus, possess viscoelastic properties.
- The viscoelastic measurements showed that the application of carbopol increased the upper limit of the LVE range, as well as the flow point and the yield stress for most of the fluids.
- Long-time aging of the flat rheology fluid altered the fluid properties and the main reasons were found to be evaporation of water and polymer degradation.
- The hydraulics simulation verified the thermal stability of the flat rheology fluid as both the resulting pump pressure and ECDs were stable with increasing temperature.

Regarding the effect of the nanoparticle suspensions on the properties of the flat rheology fluid:

- Results from the rheological measurements showed that the addition of multi-walled carbon nanotube increased the viscosity of the fluid, whilst silica and aluminum oxide had minor impact on the viscometer dial readings.
- When considering temperatures above 50°C, the Bingham yield stress values indicated that the addition of silica made the flat rheology fluid less thermally stable, whilst MWCNT-COOH and alumina had minor impact on the stability of the fluid.
- The oscillatory amplitude sweeps showed that the flat rheology fluid still exhibited structural stability with the addition of all nanoparticle suspensions and their quantities.
- All nanoparticles improved the filtration and frictional properties of the flat rheology fluid and optimum concentrations of MWCNT-COOH, silica and alumina were found to be ~0.014 wt%, ~0.025 wt% and ~0.014 wt%, respectively.
- From the hydraulics performance simulations, it was observed that the nanoparticle fluids exhibited relatively stable pump pressures and ECDs with increasing temperature, though none were as stable as the reference fluid itself.
- The torque and drag simulation showed that the optimum concentrations of MWCNT-COOH, silica and aluminum oxide increased the maximum drilling depth with 30.3 %, 17.6 % and 29.7 %, respectively.

It should be noted that these observations and conclusions are based on the effect of the polymers and nanoparticle suspensions in the water-based drilling fluid formulated in this thesis. The chemical additives could behave differently when applied to other base fluids or exposed to other temperature and pressure conditions. Moreover, the effect of concentrations beyond the scope of this thesis remains unknown.

9 References

1. Smith, S.R., et al., *Application of aluminium oxide nanoparticles to enhance rheological and filtration properties of water based muds at HPHT conditions*. Colloids and Surfaces A: Physicochemical and Engineering Aspects, 2018. **537**: p. 361-371.
2. Alshubbar, G.D., et al., *The Effect of Barite Nanoparticles on the Friction Coefficient and Rheology of Water Based Mud*, in *51st U.S. Rock Mechanics/Geomechanics Symposium*. 2017, American Rock Mechanics Association: San Francisco, California, USA. p. 7.
3. *Drilling fluid*, in *Schlumberger Oilfield Glossary*. Schlumberger Oilfield Glossary.
4. *The Defining Series: Drilling Fluid Basics*. The Defining Series 2013 [cited 2020 19.02]; Available from: <https://www.slb.com/resource-library/oilfield-review/defining-series/defining-drilling-fluids>.
5. Lake, L.W. and R.F. Mitchell, *Petroleum Engineering Handbook : Drilling Engineering*. 2006, Richardson, UNITED STATES: Society of Petroleum Engineers.
6. *mud weight*, in *Schlumberger Oilfield Glossary*, G. Gillis, Editor., Schlumberger Oilfield Glossary: www.glossary.oilfield.slb.com.
7. *fluid loss*, in *Schlumberger Oilfield Glossary*, G. Willis, Editor., Schlumberger Oilfield Glossary www.glossary.oilfield.slb.com.
8. Strand, S., *Øvinger i bore-og brønnvæsker*. Høgskolen i Stavanger, Stavanger, 1998.
9. *Chapter 2 - Fluid loss additives*, in *Petroleum Engineer's Guide to Oil Field Chemicals and Fluids (Second Edition)*, J. Fink, Editor. 2015, Gulf Professional Publishing: Boston. p. 63-120.
10. Zakaria, M., M.M. Husein, and G. Harland, *Novel Nanoparticle-Based Drilling Fluid with Improved Characteristics*, in *SPE International Oilfield Nanotechnology Conference and Exhibition*. 2012, Society of Petroleum Engineers: Noordwijk, The Netherlands. p. 6.
11. *water-base mud*, in *Schlumberger Oilfield Glossary*, G. Gillis, Editor., Schlumberger Oilfield Glossary: Schlumberger Oilfield Glossary.
12. Steve, D., *Practical well planning and drilling manual*. 1st ed ed. 1998, S.I.]: S.I. : PennWell Corporation.
13. Devereux, S., *Drilling technology in nontechnical language*. 2nd ed. ed. 2012, Tulsa, Okla: PennWell.

14. *Drilling mud*, in *Encyclopædia Britannica*. Encyclopædia Britannica, inc. : Encyclopædia Britannica.
15. Fink, J.K., *Oil field chemicals*. 2003, Gulf Professional Pub.: Amsterdam Boston.
16. Fattnes, L., *Kick in OBM at HPHT conditions and gas in riser problems*, in *Faculty of Science and Technology*. 2018, University of Stavanger: Unpublished work. p. 35.
17. Chilingarian, G.V., *Drilling and drilling fluids*. Updated textbook ed. ed. Developments in petroleum science, ed. P. Vorabutr. Vol. 11. 1983, Amsterdam: Elsevier.
18. *rheology*, in *Schlumberger Oilfield Glossary*, G. Gillis, Editor., Schlumberger Oilfield Glossary: Schlumberger Oilfield Glossary.
19. Kolle, G. and R. Mesel, *Brønnevæsker: for VKI brønnteknikk*. 1998, Nesbru: Vett & viten. 214 s. ill.
20. *Basics of rheology*. [cited 3. May 2020]; Available from: <https://wiki.anton-paar.com/en/basics-of-rheology/>.
21. *yield point*, in *Schlumberger Oilfield Glossary*, G. Gillis, Editor., Schlumberger Oilfield Glossary: www.glossary.oilfield.slb.com.
22. *thixotropy*, in *Schlumberger Oilfield Glossary*, G. Gillis, Editor., Schlumberger Oilfield Glossary: www.glossary.oilfield.slb.com.
23. *shear stress*, in *Schlumberger Oilfield Glossary*, G. Gillis, Editor., Schlumberger Oilfield Glossary: www.glossary.oilfield.slb.com.
24. *shear rate*, in *Schlumberger Oilfield Glossary*, G. Gillis, Editor., Schlumberger Oilfield Glossary: www.gloassary.oilfield.slb.com.
25. Skjeggstad, O., *Boreslamteknologi : teori og praksis*. 1989, Bergen: Alma Mater.
26. *Rotational viscometry*. [cited 2020 16. June]; Available from: <https://wiki.anton-paar.com/en/rotational-viscometry/>.
27. *How to measure viscosity*. [cited 2020 16. May]; Available from: <https://wiki.anton-paar.com/en/how-to-measure-viscosity/-c16709>.
28. Mezger, T.G., *The rheology handbook : for users of rotational and oscillatory rheometers*. 3rd rev. ed. ed. European coatings tech files. 2011, Hannover: Vincentz.
29. Guo, B. and G. Liu, *Applied Drilling Circulation Systems: Hydraulics, Calculations and Models*. 2011: Gulf Professional Publishing.

30. Khataniar, S., G.A. Chukwu, and H. Xu, *Evaluation of rheological models and application to flow regime determination*. Journal of Petroleum Science and Engineering, 1994. **11**(2): p. 155-164.
31. *Newtonian fluid*, in *Schlumberger Oilfield Glossary*. Schlumberger Oilfield Glossary: www.glossary.oilfield.slb.com.
32. *Types of Flow and Rheology Models of Drilling Mud*. 2016 [cited 2020 17. June]; Available from: <http://www.drillingformulas.com/types-of-flow-and-rheology-models-of-drilling-mud/>.
33. *non-Newtonian fluid*, in *Schlumberger Oilfield Glossary*, G. Gillis, Editor., Schlumberger Oilfield Glossary: www.glossary.oilfield.slb.com.
34. *Bingham plastic model*, in *Schlumberger Oilfield Glossary*. Schlumberger Oilfield Glossary: www.glossary.oilfield.slb.com.
35. Belayneh, M., *Rheology, Hydraulics and cuttings transport*, in *Advanced Drilling Engineering and Technology*. 2019, University of Stavanger: PET580 Advanced Well and Drilling Engineering Lecture Notes.
36. *Herschel-Bulkley fluid*, in *Schlumberger Oilfield Glossary*. Schlumberger Oilfield Glossary: www.glossary.oilfield.slb.com.
37. Zamora, M. *Making a case for AADE hydraulics and the unified rheological model*. in *AADE Technology Conference" Drilling & Completion Fluids and Waste Management"*, April 2-3, Houston, Texas., 2002. 2002.
38. Vilorio Ochoa, M., *Analysis of drilling fluid rheology and tool joint effect to reduce errors in hydraulics calculations*. 2006, Texas A&M University.
39. Robertson, R.E. and H.A. Stiff, Jr., *An Improved Mathematical Model for Relating Shear Stress to Shear Rate in Drilling Fluids and Cement Slurries*. Society of Petroleum Engineers Journal, 1976. **16**(01): p. 31-36.
40. Hilfiger, M.G., C.J. Thaemlitz, and E. Moellendick, *Investigating the Chemical Nature of Flat Rheology*, in *SPE Deepwater Drilling and Completions Conference*. 2016, Society of Petroleum Engineers: Galveston, Texas, USA. p. 11.
41. Abdo, J. and M.D. Haneef, *Clay nanoparticles modified drilling fluids for drilling of deep hydrocarbon wells*. Applied Clay Science, 2013. **86**: p. 76-82.
42. Friedheim, J., et al., *New Thermally Independent Rheology Invert Drilling Fluid For Multiple Applications*, in *Offshore Mediterranean Conference and Exhibition*. 2011, Offshore Mediterranean Conference: Ravenna, Italy. p. 11.

43. Alcázar-Vara, L.A. and I.R. Cortés-Monroy, *Drilling fluids for deepwater fields: an overview*. Recent Insights in Petroleum Science and Engineering, 2018: p. 71.
44. Zhao, X., et al., *Flat-rheology oil-based drilling fluid for deepwater drilling*. International Journal of Heat and Technology, 2017. **35**: p. 19-24.
45. *Elasticity*, in *Encyclopædia Britannica*. 2016, Encyclopædia Britannica, inc.: www.britannica.com.
46. Bui, B., et al., *Viscoelastic properties of oil-based drilling fluids*. Annual Transactions of the Nordic Rheology Society, 2012. **20**: p. 33-47.
47. Sharman, T., *Characterization and performance study of OBM at various oil-water ratios*. 2015, University of Stavanger, Norway.
48. *Amplitude sweeps*. [cited 2020 11. May]; Available from: <https://wiki.anton-paar.com/en/amplitude-sweeps/>.
49. Yan, Y., *Bio-Tribocorrosion in Biomaterials and Medical Implants*. 2013: Elsevier Science.
50. *Tribology*, in *Encyclopædia Britannica*. 2017, Encyclopædia Britannica, inc. : www.britannica.com.
51. Kaarstad, E., B.S. Aadnoy, and T. Fjelde, *A Study of Temperature Dependent Friction in Wellbore Fluids*, in *SPE/IADC Drilling Conference and Exhibition*. 2009, Society of Petroleum Engineers: Amsterdam, The Netherlands. p. 10.
52. Nohava, J., *Applications of tribology on polymers*. www.anton-paar.com.
53. Johancsik, C.A., D.B. Friesen, and R. Dawson, *Torque and Drag in Directional Wells- Prediction and Measurement*. Journal of Petroleum Technology, 1984. **36**(06): p. 987-992.
54. Alvi, M.A.A., et al., *The Effect of Micro-Sized Boron Nitride BN and Iron Trioxide Fe₂O₃ Nanoparticles on the Properties of Laboratory Bentonite Drilling Fluid*, in *SPE Norway One Day Seminar*. 2018, Society of Petroleum Engineers: Bergen, Norway. p. 14.
55. Strømø, S.M., *Formulation of New Drilling Fluids and Characterization in HPHT*, M. Belayneh, Editor. 2019, University of Stavanger, Norway.
56. Mirhajmohammadabadi, S.A.A., et al., *New Aspects of Torque-and-Drag Modeling in Extended-Reach Wells*, in *SPE Annual Technical Conference and Exhibition*. 2010, Society of Petroleum Engineers: Florence, Italy. p. 13.
57. Sheppard, M.C., C. Wick, and T. Burgess, *Designing Well Paths To Reduce Drag and Torque*. SPE Drilling Engineering, 1987. **2**(04): p. 344-350.

58. Mitchell, R.F. and G.R. Samuel, *How Good is the Torque-Drag Model?*, in *SPE/IADC Drilling Conference*. 2007, Society of Petroleum Engineers: Amsterdam, The Netherlands. p. 9.
59. Mirhaj, A., E. Kaarstad, and B.S. Aadnoy, *Minimizing Friction In Shallow Horizontal Wells*, in *IADC/SPE Asia Pacific Drilling Technology Conference and Exhibition*. 2010, Society of Petroleum Engineers: Ho Chi Minh City, Vietnam. p. 7.
60. Mikalsen, A., *Analysis of drilled wells on the Norwegian Continental Shelf (NCS)*. 2013, University of Stavanger, Norway.
61. Aarrestad, T.V., *Torque and Drag-Two Factors in Extended-Reach Drilling*. *Journal of Petroleum Technology*, 1994. **46**(09): p. 800-803.
62. Belayneh, M., *Drill string mechanics design*, in *Advanced Drilling Engineering and Technology*. 2019, University of Stavanger: PET580 Advanced Well and Drilling Engineering Lecture Notes.
63. *Torque*, in *Encyclopædia Britannica*. 2019, Encyclopædia Britannica, inc. : www.britannica.com.
64. *Drill String Failure Prevention*. [cited 2020 2. June]; Powerpoint slides]. Available from: <https://www.slideshare.net/hshobeyri/slb-drill-stringfailure>.
65. Belkacem, L., et al. *Tensile and torsional loads stress distribution along the drill string for deep wells*. in *2nd International Congress on Energy Efficiency and Energy Related Materials (ENEFM2014)*. 2015. Springer.
66. *lock-up*, in *Schlumberger Oilfield Glossary*, G. Gillis, Editor., Schlumberger: www.glossary.oilfield.slb.com.
67. *Hydraulics*, in *Encyclopædia Britannica*. 2019, Encyclopædia Britannica, inc. : www.britannica.com.
68. Faber, T.E., *Fluid mechanics*, in *Encyclopædia Britannica*. Encyclopædia Britannica, inc.: www.britannica.com.
69. Whittaker, A. and Exlog, *Theory and application of drilling fluid hydraulics*. The EXLOG series of petroleum geology and engineering handbooks. 1985, Dordrecht: Reidel.
70. Mitchell, R. and S. Miska, *Fundamentals of drilling engineering*. 2011: Society of Petroleum Engineers.
71. Hossain, M.E. and R. Islam, *Drilling Engineering Problems and Solutions: 9781118998724*. 2018: Wiley-Scrivener.

72. Sadigov, J., *Comparisons of rheology and hydraulics prediction of mud systems in concentric and eccentric well geometry*. University of Stavanger, Stavanger, Rogaland, 2013.
73. ECD, in *Schlumberger Oilfield Glossary*, G. Gillis, Editor., Schlumberger Oilfield Glossary: www.glossary.oilfield.slb.com.
74. Huang, Z., et al., *Chapter Five - Flow Behavior and Friction Characteristics of Fluid Flow in Coiled Tubing*, in *Abrasive Water Jet Perforation and Multi-Stage Fracturing*, Z. Huang, et al., Editors. 2018, Gulf Professional Publishing. p. 153-190.
75. *circulation system*, in *Schlumberger Oilfield Glossary*, G. Gillis, Editor., Schlumberger Oilfield Glossary: www.glossary.oilfield.slb.com.
76. Belayneh, M., *Chapter 8 Drilling Equipment*, in *Advanced Drilling Engineering and Technology*. 2019, University of Stavanger: PET580 Advanced Well and Drilling Engineering Lecture Notes.
77. Zeynalov, T. and M. Belayneh, *Effect of Boron nitride (BN) and surface modified BN on the properties of laboratory water-based drilling fluid formulated in Duovis/XG polymers: Experimental and Simulation studies*. 2018, University of Stavanger, Norway.
78. Cocuzza, M., et al., *Is The Oil Industry Ready For Nanotechnologies?*, in *Offshore Mediterranean Conference and Exhibition*. 2011, Offshore Mediterranean Conference: Ravenna, Italy. p. 17.
79. Ali, J.A., et al., *A state-of-the-art review of the application of nanotechnology in the oil and gas industry with a focus on drilling engineering*. *Journal of Petroleum Science and Engineering*, 2020. **191**: p. 107118.
80. Rafati, R., et al., *Effect of nanoparticles on the modifications of drilling fluids properties: A review of recent advances*. *Journal of Petroleum Science and Engineering*, 2018. **161**: p. 61-76.
81. Hoelscher, K.P., et al., *Nanotechnology Application in Drilling Fluids*, in *Offshore Mediterranean Conference and Exhibition*. 2013, Offshore Mediterranean Conference: Ravenna, Italy. p. 11.
82. Salih, A.H., T.A. Elshehabi, and H.I. Bilgesu, *Impact of Nanomaterials on the Rheological and Filtration Properties of Water-Based Drilling Fluids*, in *SPE Eastern Regional Meeting*. 2016, Society of Petroleum Engineers: Canton, Ohio, USA. p. 14.

83. Li, L., et al., *Vital Role of Nanomaterials in Drilling Fluid and Reservoir Protection Applications*, in *Abu Dhabi International Petroleum Conference and Exhibition*. 2012, Society of Petroleum Engineers: Abu Dhabi, UAE. p. 8.
84. Friedheim, J.E., et al., *Nanotechnology for Oilfield Applications - Hype or Reality?*, in *SPE International Oilfield Nanotechnology Conference and Exhibition*. 2012, Society of Petroleum Engineers: Noordwijk, The Netherlands. p. 7.
85. Vryzas, Z. and V.C. Kelessidis, *Nano-based drilling fluids: A review*. *Energies*, 2017. **10**(4): p. 540.
86. Mahmoud, O., et al., *Nanoparticle-Based Drilling Fluids for Minimizing Formation Damage in HP/HT Applications*, in *SPE International Conference and Exhibition on Formation Damage Control*. 2016, Society of Petroleum Engineers: Lafayette, Louisiana, USA. p. 26.
87. Ismail, A.R., et al., *The novel approach for the enhancement of rheological properties of water-based drilling fluids by using multi-walled carbon nanotube, nanosilica and glass beads*. *Journal of Petroleum Science and Engineering*, 2016. **139**: p. 264-275.
88. Belayneh, M. and B.S. Aadnøy. *Effect of nano-silicon dioxide (SiO₂) on polymer/salt treated bentonite drilling fluid systems*. in *International Conference on Offshore Mechanics and Arctic Engineering*. 2016. American Society of Mechanical Engineers.
89. Ismail, A.R., et al., *Effect of nanomaterial on the rheology of drilling fluids*. *Journal of applied sciences*, 2014. **14**(11): p. 1192.
90. Amarfio, E.M. and M. Abdulkadir, *Effect of Al₂O₃ nanoparticles on the rheological properties of water based mud*. *Int. J. Sci. Eng. Appl*, 2016. **5**: p. 7-11.
91. Samsuri, A. and A. Hamzah, *Water based mud lifting capacity improvement by multiwall carbon nanotubes additive*. *Journal of Petroleum and Gas Engineering*, 2011. **5**(2): p. 99-107.
92. Taraghikhah, S., M. Kalhor Mohammadi, and K. Tahmasbi Nowtaraki, *Multifunctional Nanoadditive in Water Based Drilling Fluid for Improving Shale Stability*, in *International Petroleum Technology Conference*. 2015, International Petroleum Technology Conference: Doha, Qatar. p. 17.
93. *montmorillonite*, in *Schlumberger Oilfield Glossary*, G. Gills, Editor., Schlumberger Oilfield Glossary: Schlumberger Oilfield Glossary.
94. *bentonitt*. 2020 [cited 2020 26. March]; Available from: <https://snl.no/bentonitt>.
95. Kutlić, A., G. Bedeković, and I. Sobota, *Bentonite processing*. *Rudarsko-geološko-naftni zbornik*, 2012. **24**(1): p. 61-65.

96. *soda ash*, in *Schlumberger Oilfield Glossary*, G. Gillis, Editor., Schlumberger Oilfield Glossary: Schlumberger Oilfield Glossary.
97. *Sodium carbonate anhydrous*. [cited 2020 26. March]; Available from: <https://www.sigmaaldrich.com/catalog/substance/sodiumcarbonateanhydrous1059949719811?lang=en®ion=NO>.
98. *Polypac UL*. [cited 2020 2. April]; Available from: <https://www.slb.com/drilling/drilling-fluids-and-well-cementing/drilling-fluids/drilling-fluid-additives/filtration-reducers/polypac-ul-ultralow-viscosity-cellulose-related-information>.
99. *Viscosifier*. [cited 2020 2. April]; Available from: <https://www.irooildrilling.com/Viscosifier/PAC.htm>.
100. *PAC LV*. [cited 2020 2. April]; Available from: <http://www.oil-drilling-fluids.com/pac-lv>.
101. Priscilla, R.V., et al., *Rheological Characterization of Carbopol® Dispersions in Water and in Water/Glycerol Solutions*. *Fluids*, 2019. **4**(1): p. 3.
102. Lefrançois, P., et al., *Insights into Carbopol gel formulations: Microscopy analysis of the microstructure and the influence of polyol additives*. *Journal of Applied Polymer Science*, 2015. **132**(46): p. n/a-n/a.
103. *Neutralizing Carbopol and Pemulen Polymers in Aqueous and Hydroalcoholic Systems*. [Technical Data Sheet] 2009 16. September [cited 2020 3. April]; Technical Data Sheet]. Available from: https://www.lubrizol.com/-/media/Lubrizol/Life-Sciences/Documents/TDS/TDS-237_Neutralizing_Carbopol_Pemulen_in_Aqueous_Hydroalcoholic_Systems--PH.pdf.
104. Qiu, Y., et al., *Developing solid oral dosage forms: pharmaceutical theory and practice*. 2016: Academic press.
105. Ruoff, R.S. and D.C. Lorents, *Mechanical and thermal properties of carbon nanotubes*. *Carbon*, 1995. **33**(7): p. 925-930.
106. Thostenson, E.T., Z. Ren, and T.-W. Chou, *Advances in the science and technology of carbon nanotubes and their composites: a review*. *Composites Science and Technology*, 2001. **61**(13): p. 1899-1912.
107. *Carbon nanotube, multi-walled, carboxylic acid functionalized*. [cited 2020 4. April]; Available from:

- https://www.sigmaaldrich.com/catalog/product/aldrich/755125?lang=en®ion=NO&cm_sp=Insite-_recent_fixed-_recent5-1.
108. COOH Functionalized MWCNTs (>95%, OD: 20-30 nm). [cited 2020 11. July]; Available from: <https://www.us-nano.com/inc/sdetail/230>.
109. Britannica, T.E.o.E., *Silica*, in *Encyclopædia Britannica*. 2019, Encyclopædia Britannica, inc.: www.britannica.com.
110. *Silicon Dioxide (SiO₂)*. [cited 2020 1. May]; Available from: <https://nanografi.com/nanoparticles/silicon-dioxide-sio2-nanopowder-nanoparticles-p-type-purity-99-65-size-13-23-nm-nonporous-and-amorphous/>.
111. *Colloidal Silica*. [cited 2020 1. May]; Available from: <https://www.nyacol.com/products/silicon-dioxide/>.
112. *NYACOL DP9711*. [Data Sheet] [cited 2020 01. May]; Available from: <https://www.nyacol.com/wp-content/uploads/2015/04/DP9711-Data-Sheet-20130812.pdf>.
113. Britannica, T.E.o.E., *Alumina*, in *Encyclopædia Britannica*. 2018, Encyclopædia Britannica, inc.: www.britannica.com.
114. *Aluminum Oxide (Al₂O₃) Nanoparticles/Nanopowder*. [cited 2020 1. May]; Available from: <https://nanografi.com/blog/aluminum-oxide-al2o3-nanoparticlesnanopowder/>.
115. *Aluminum Oxide Al₂O₃ Nanopowder/ Nanoparticles Water Dispersion (Alpha, 20wt%, 30 nm)*. [cited 2020 1. May]; Available from: <https://www.us-nano.com/inc/sdetail/623>.
116. *pH*, in *Schlumberger Oilfield Glossary*, G. Gillis, Editor., Schlumberger Oilfield Glossary: www.glossary.oilfield.slb.com.
117. *pH test*, in *Schlumberger Oilfield Glossary*, G. Willis, Editor., Schlumberger Oilfield Glossary: www.glossay.oilfield.slb.com.
118. *Tribometer*. [cited 2020 25. May]; Available from: [http://www.asi-team.com/asi-team/csm/csm data/ht tribometer.pdf](http://www.asi-team.com/asi-team/csm/csm%20data/ht%20tribometer.pdf).
119. Lu, et al., *Tribological Properties of Alkyldiphenylethers in Boundary Lubrication*. Lubricants, 2019. 7(12): p. 112.
120. Arenas-Lago, D., et al., *Chapter 2 - A Multianalytical Approach for the Assessment of Toxic Element Distribution in Soils From Mine and Quarry Areas*, in *Assessment, Restoration and Reclamation of Mining Influenced Soils*, J. Bech, C. Bini, and M.A. Pashkevich, Editors. 2017, Academic Press. p. 33-62.

121. *Scanning Electron Microscopy*. [cited 2020 9. July]; Available from: <https://www.nanoscience.com/techniques/scanning-electron-microscopy/>.
122. Goud, D.M., *Mud Engineering Simplified*. 2017, www.becomeshakespeare.com: Becomeshakespeare.com.
123. *gelled mud*, in *Schlumberger Oilfield Glossary*, G. Gillis, Editor., Schlumberger Oilfield Glossary: www.glossary.oilfield.slb.com.
124. Speight, J.G., *Chapter 14 - Monomers, Polymers, and Plastics*, in *Handbook of Industrial Hydrocarbon Processes*, J.G. Speight, Editor. 2011, Gulf Professional Publishing: Boston. p. 499-537.
125. *CHAPTER 2 - Flow Drilling: Underbalance Drilling with Liquid Single-Phase Systems*, in *Underbalanced Drilling: Limits and Extremes*, B. Rehm, et al., Editors. 2012, Gulf Publishing Company. p. 39-108.
126. Xu, L., et al., *Experimental Investigations Into the Performance of a Flat-Rheology Water-Based Drilling Fluid*. SPE Journal, 2013. **19**(01): p. 69-77.
127. van Oort, E., et al., *New Flat-Rheology Synthetic-Based Mud for Improved Deepwater Drilling*, in *SPE Annual Technical Conference and Exhibition*. 2004, Society of Petroleum Engineers: Houston, Texas. p. 11.

APPENDICES

APPENDIX A – ROTATIONAL TEMPERATURE SWEEPS

When conducting the rotational temperature sweep with a parallel plate setup, the sample completely dried out at increasing temperatures. Figure A.1 shows the appearance of the sample at measurement and lift position after completing the temperature sweep.

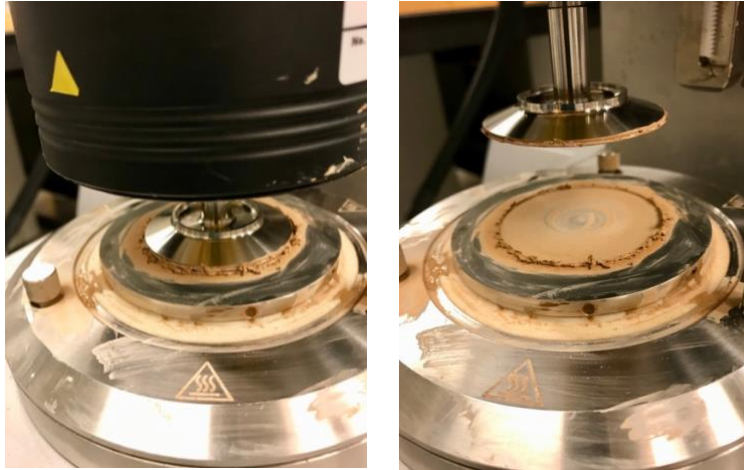


Figure A. 1: The dried-out sample at measurement (left) and lift position (right) after completing the temperature sweep

As described in section 5.4.4.1, changing the setup of the Anton Paar MCR 302 rheometer to “cup and bob” enabled it to measure the viscosity of the sample at numerous temperatures ranging within 22°C and 80°C. However, water still evaporates from the sample, its effect on the measurements is merely reduced as the amount of test sample is increased. The appearance of the sample after completing the temperature sweeps using the “cup and bob” setup is shown in figure A.2.

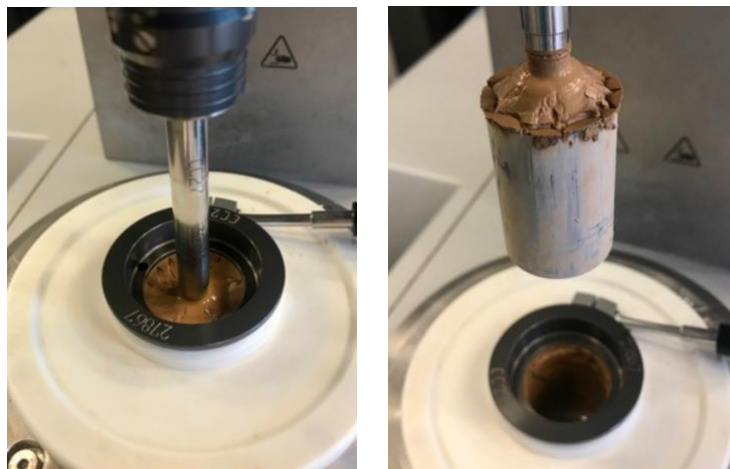


Figure A. 2: Sample at measurement (left) and lift position (right) after completing the temperature sweep (“cup and bob”)

APPENDIX B – EFFECT OF MWCNT-COOH ON VISCOELASTIC PROPERTIES

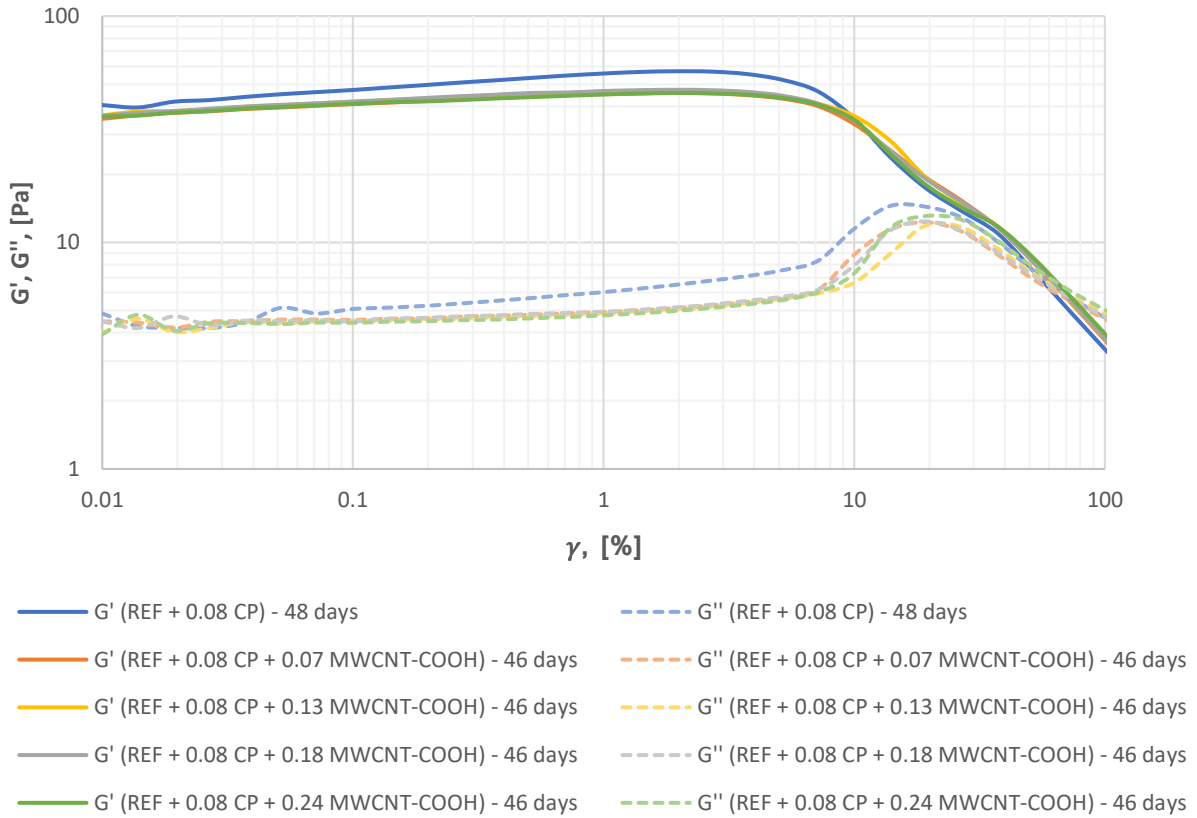


Figure B. 1: Amplitude sweep result for multi-walled carbon nanotube fluids

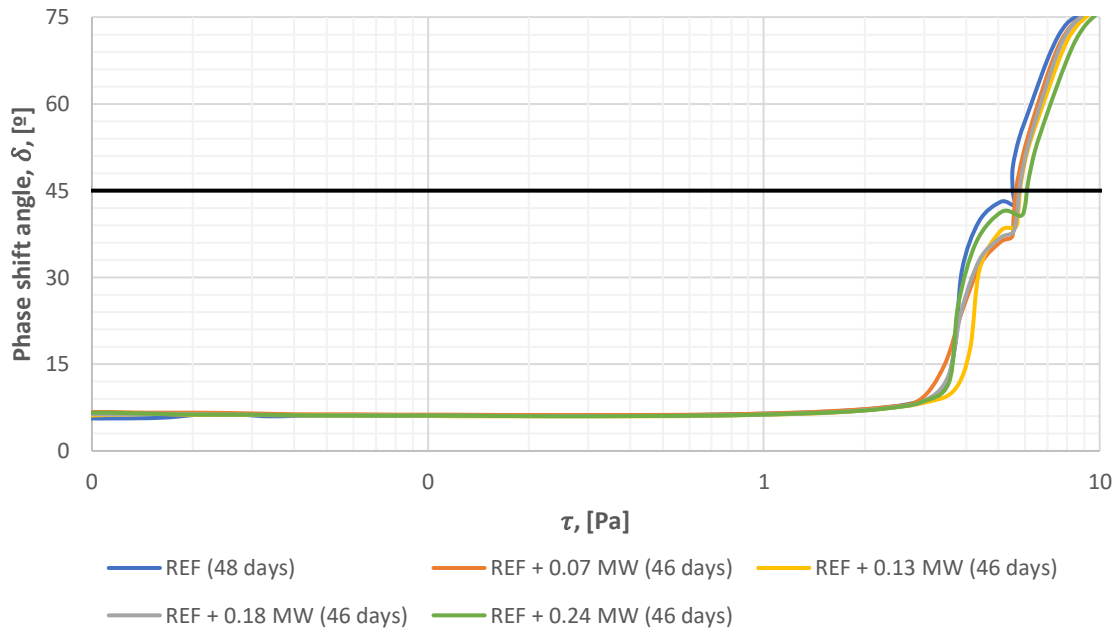


Figure B. 2: Phase shift angle vs. shear stress for multi-walled carbon nanotube fluids

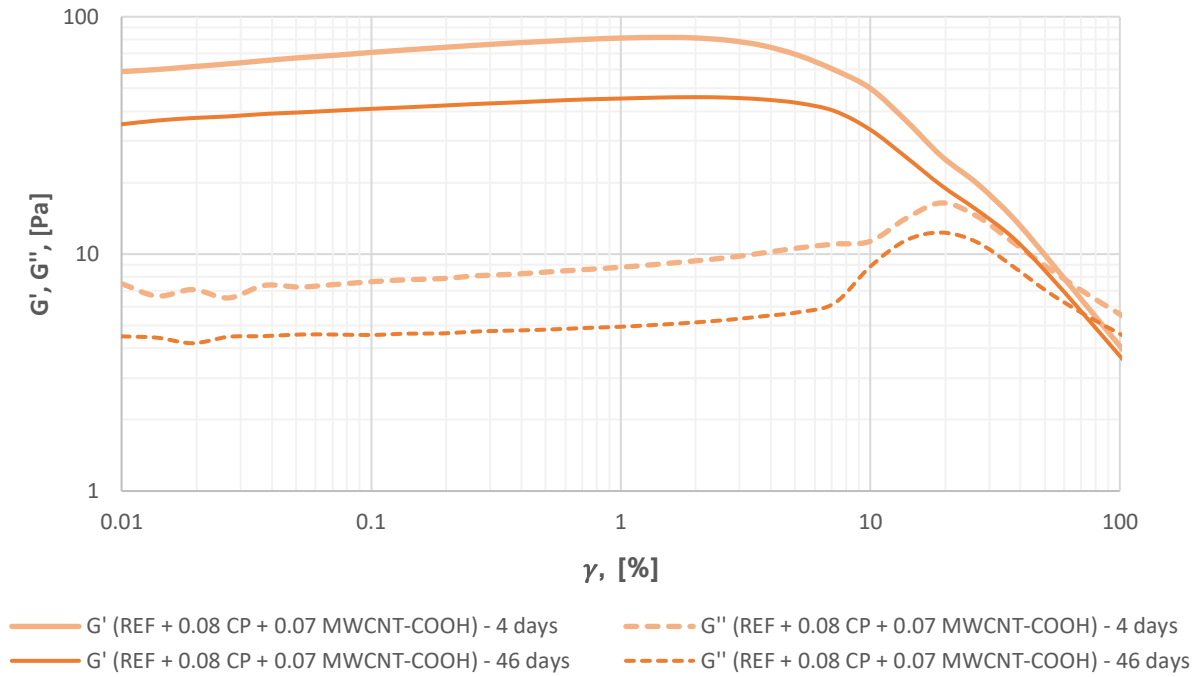


Figure B. 3: Amplitude sweep result for multi-walled carbon nanotube fluids (short-time vs. long-time aging)

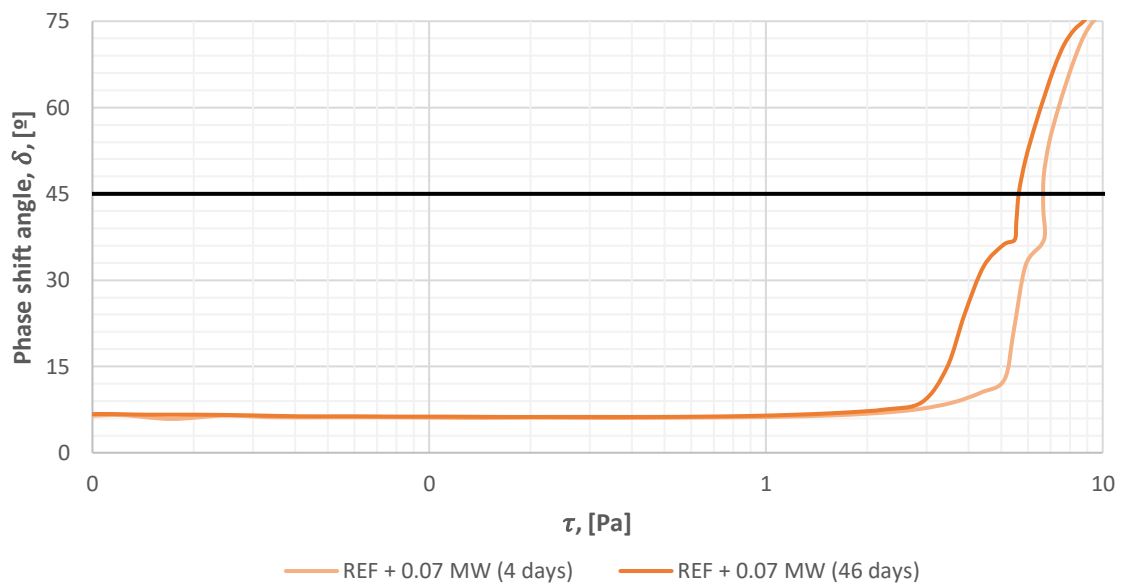


Figure B. 4: Phase shift angle vs. shear stress for multi-walled carbon nanotube fluids (short-time vs. long-time aging)

APPENDIX C – EFFECT OF SILICA ON VISCOELASTIC PROPERTIES

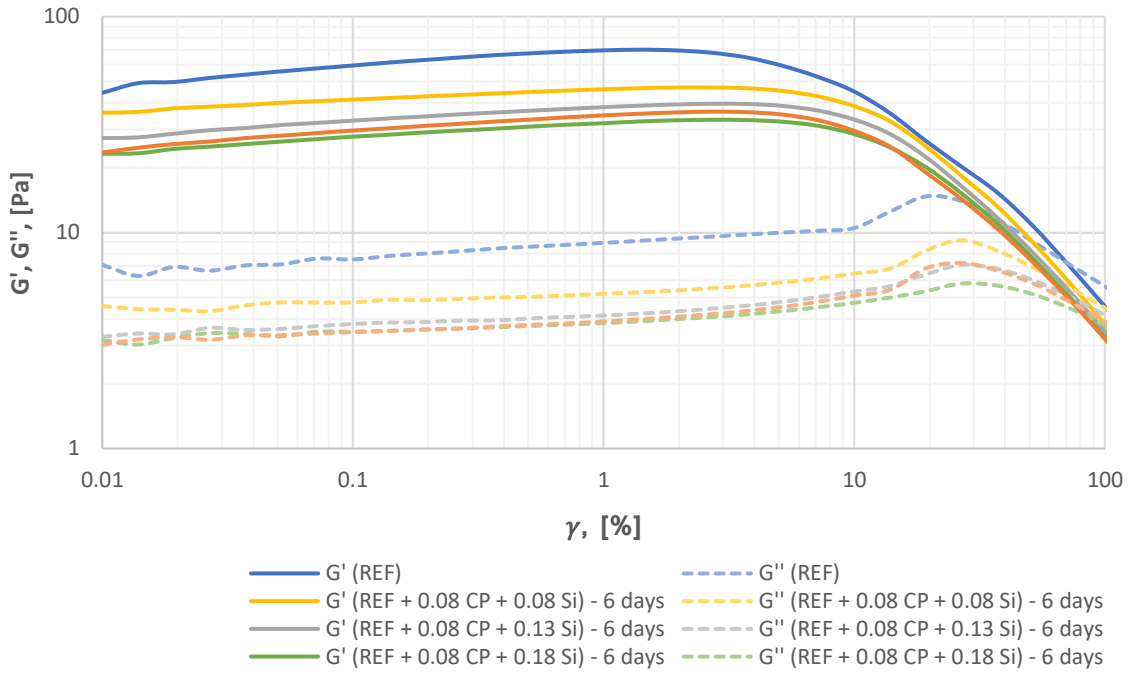


Figure C. 1: Amplitude sweep result for silica fluids

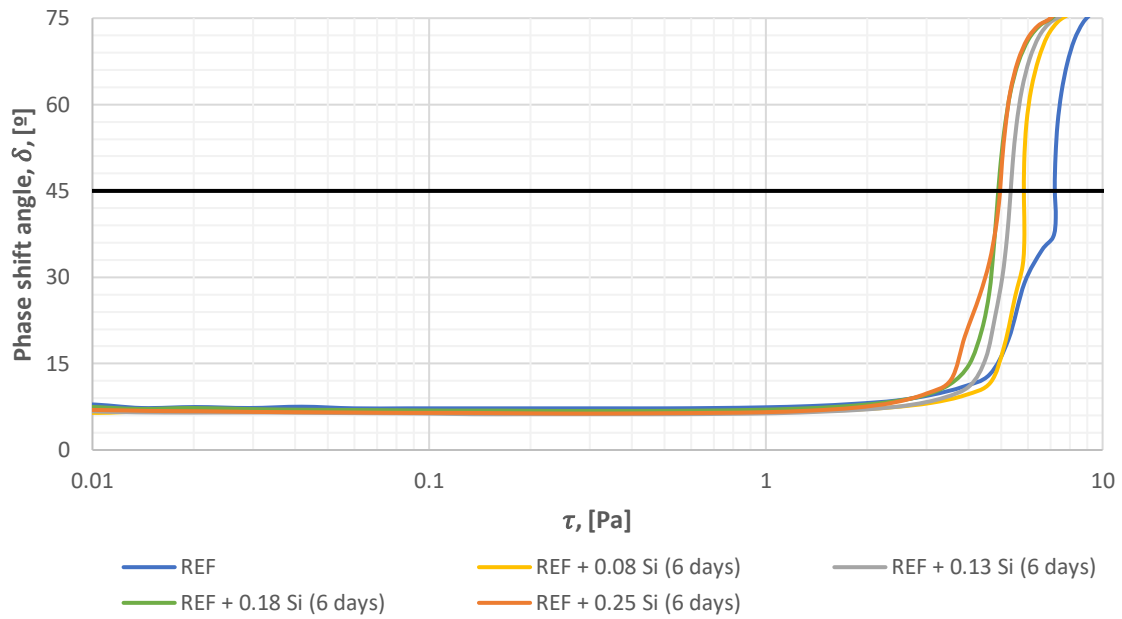


Figure C. 2: Phase shift angle vs. shear stress for silica fluids

APPENDIX D – EFFECT OF ALUMINUM OXIDE ON VISCOELASTIC PROPERTIES

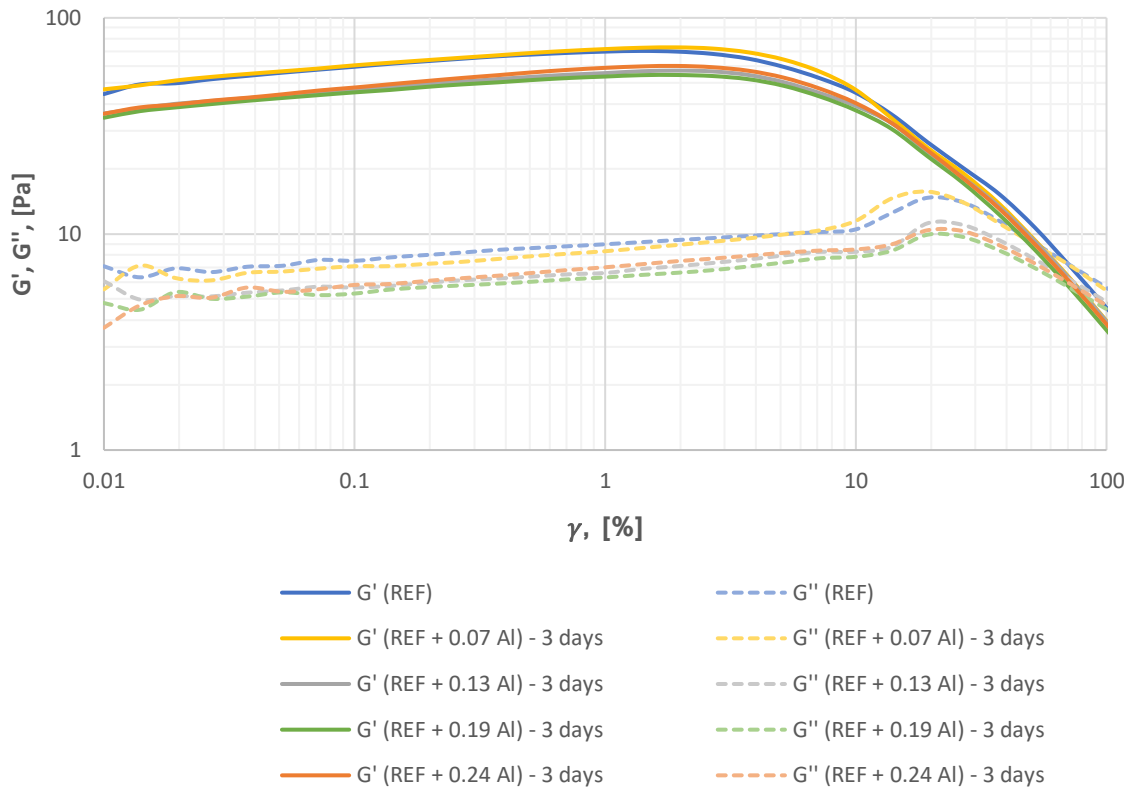


Figure D. 1: Amplitude sweep result for aluminum oxide fluids

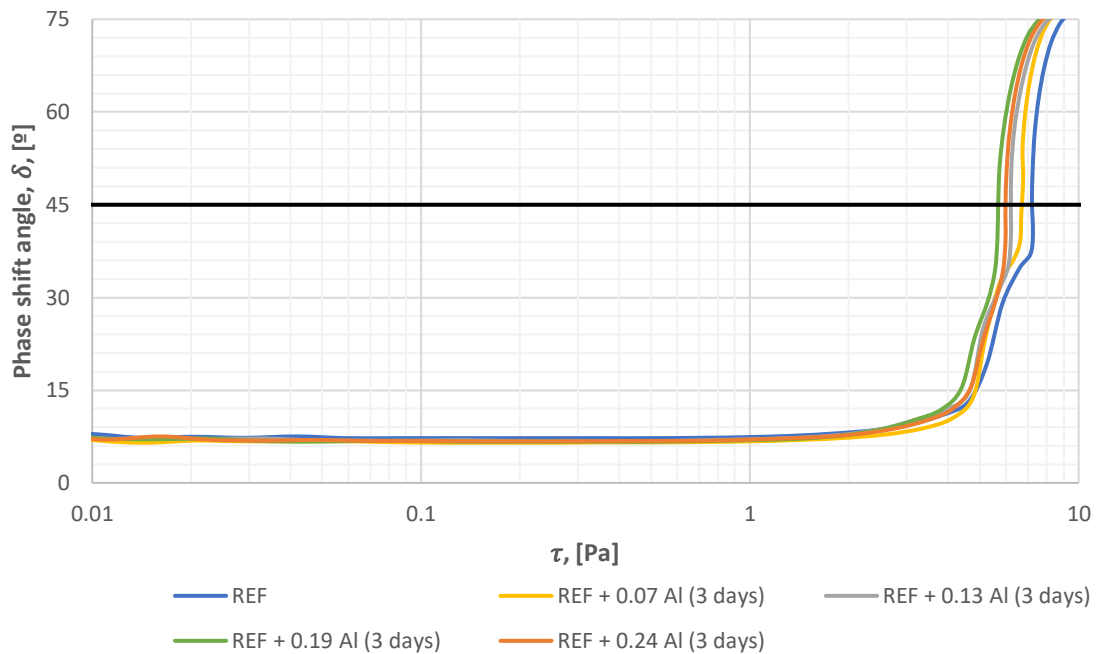


Figure D. 2: Phase shift angle vs. shear stress for aluminum oxide fluids

APPENDIX E – RHEOLOGICAL MODELLING DIAGRAMS

Newtonian Model

The Newtonian model assumes a linear shear stress-shear rate relation, which means that viscosity is independent of the shear rate. This does not reflect the flow characteristics of most drilling fluids, though it is known to describe the behavior of water, oil and gas well. In figure E.1, E.2 and E.3, the model is compared to viscometer readings obtained for the reference fluid containing 0.08 g carbopol at 22°C, 50°C and 80°C, respectively. There are significant deviations between the measured rheology profiles and the curves provided by the Newtonian model. Thus, the model describes the rheological properties of the drilling fluid poorly, which is as expected.

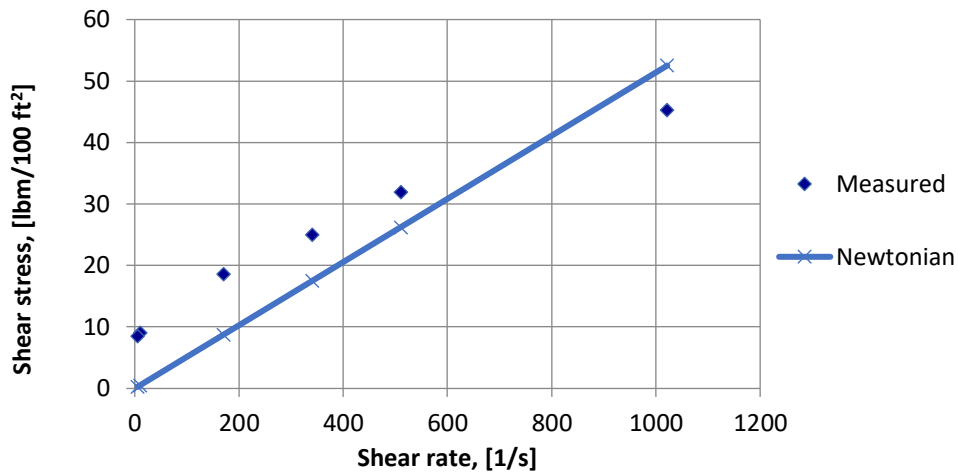


Figure E. 1: Newtonian model versus flat rheology fluid at 22 °C

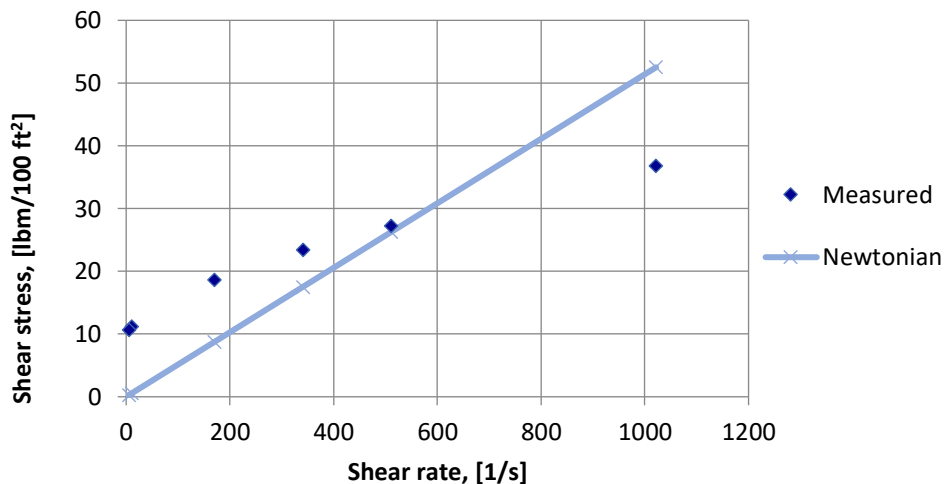


Figure E. 2: Newtonian model versus flat rheology fluid at 50 °C

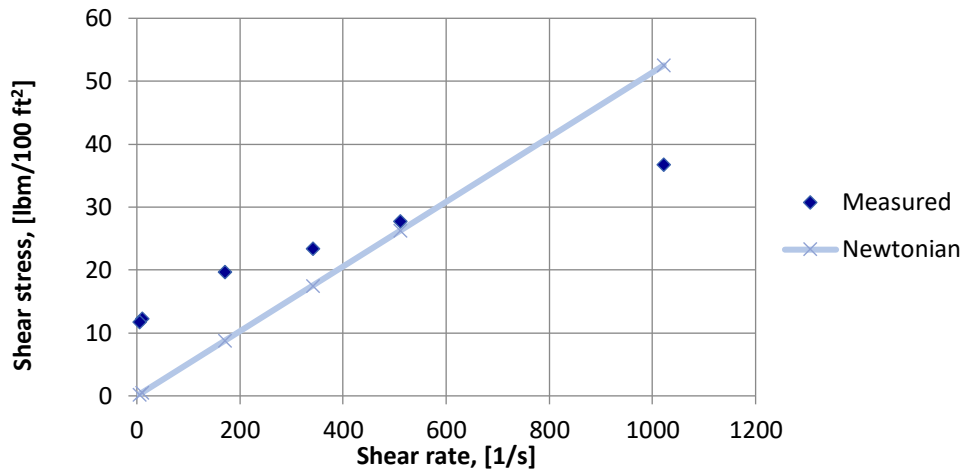


Figure E. 3: Newtonian model versus flat rheology fluid at 80 °C

Bingham Plastic Model

The Bingham Plastic model is a non-Newtonian model. It is quite similar to the Newtonian model in that it assumes a linear relationship between the shear stress and shear rate, however, it also considers the threshold shear rate typically required to make a fluid flow. Figure E.4, E.5 and E.6 presents the Bingham Plastic predictions and the measured viscometer dial readings of the formulated drilling fluid. Some deviations are still observed, though it provides a better description of the drilling fluid compared to the Newtonian model. This is because the model accounts for yield stress, making it capable of providing a description better fit with the rheological properties of most drilling fluids.

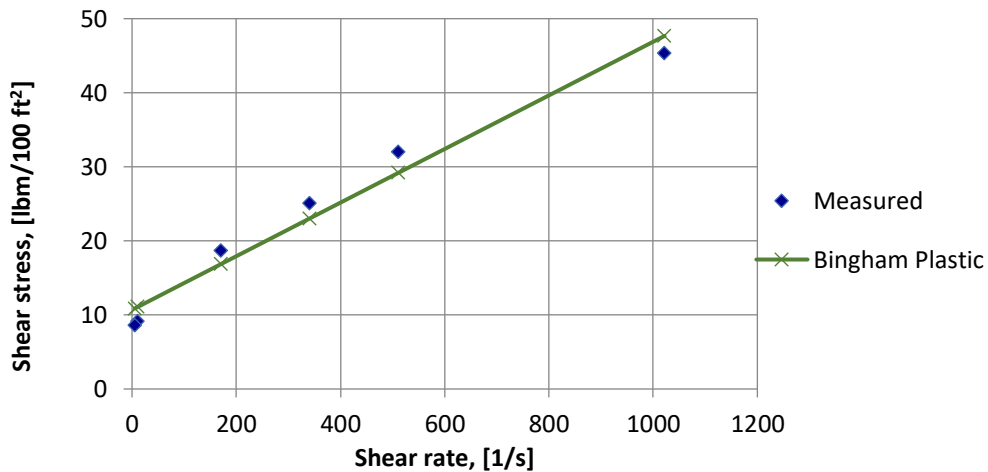


Figure E. 4: Bingham Plastic model versus flat rheology fluid at 22 °C

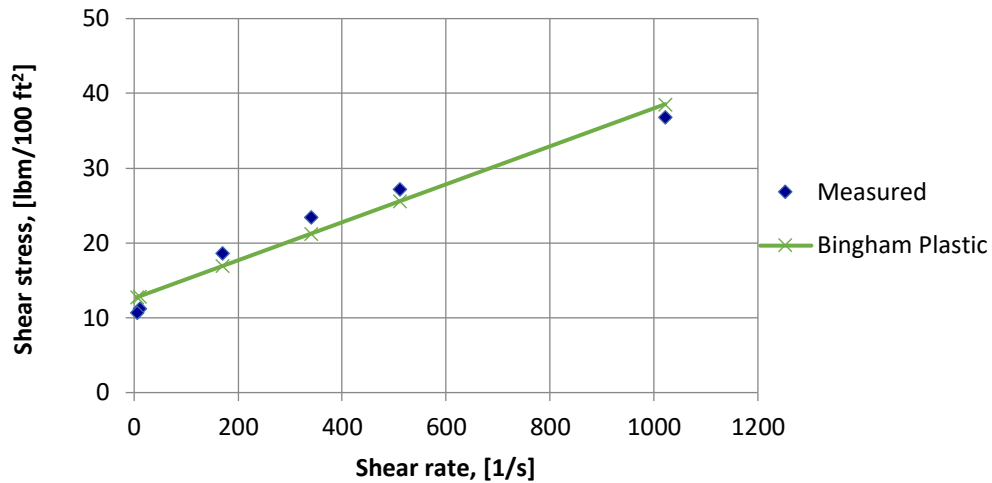


Figure E. 5: Bingham Plastic model versus flat rheology fluid at 50 °C

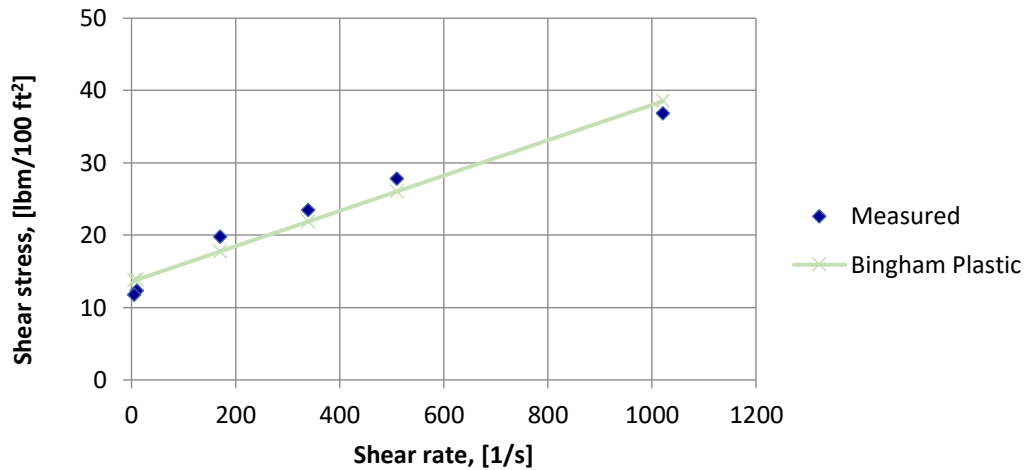


Figure E. 6: Bingham Plastic model versus flat rheology fluid at 80 °C

Power Law Model

The Power Law model is known to provide an accurate prediction of shear thickening and shear thinning drilling fluids, as well as Newtonian fluids. It is an exponential model which accounts for fluid flow behavior using the index denoted as n . Furthermore, it assumes a non-linear relation between shear stress and shear rate, which reflects the behavior of most drilling fluids. However, the model is limited by its assumption of no yield stress. Figure E.7, E.8 and E.9 displays the Power Law model predictions and the measured viscometer data at 22°C, 50°C and 80°C, respectively. It is observed that the model prediction describes a shear thinning fluid as the viscosity is reduced with increasing shear rates. Significant deviations are still seen between the model prediction and measured data, especially at greater shear rates where the model anticipated that the fluid would be more shear thinning than it actually is.

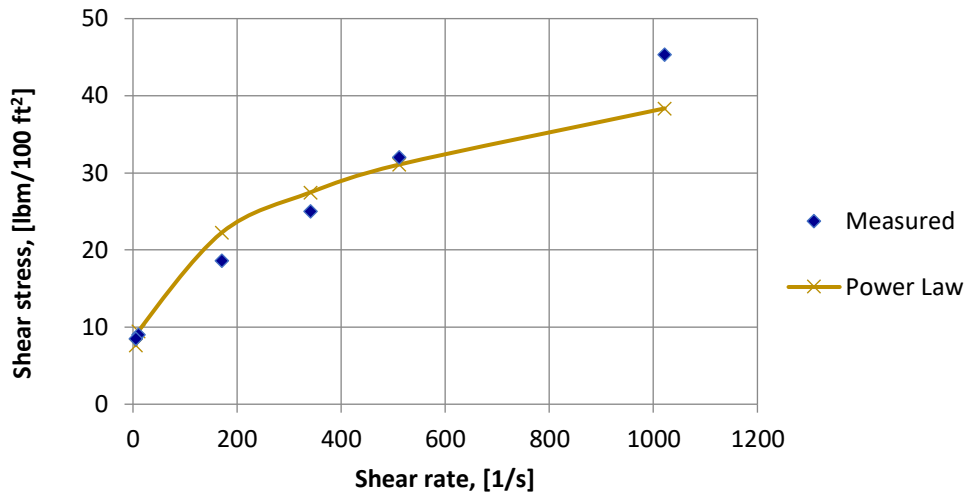


Figure E. 7: Power law model versus flat rheology fluid at 22 °C

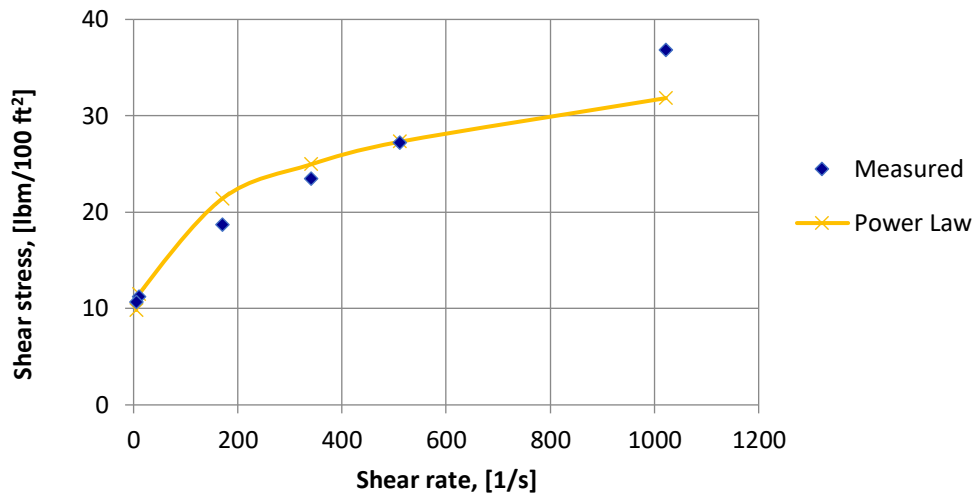


Figure E. 8: Power law model versus flat rheology fluid at 50 °C

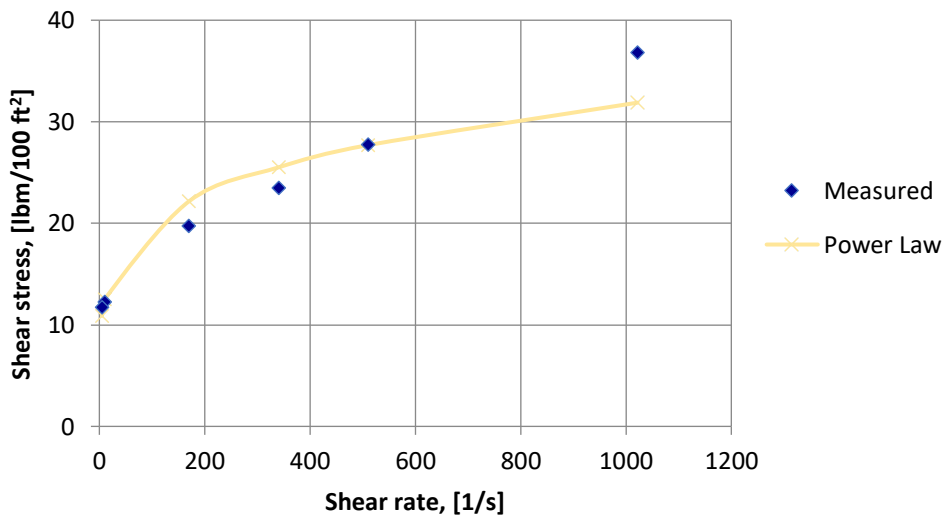


Figure E. 9: Power law model versus flat rheology fluid at 80 °C

Herschel-Bulkley Model

The H-B model is a modified Power Law model. It accounts for the yield stress exhibited by most drilling fluids and thus, provides a more realistic prediction of fluid flow. In figure E.10, E.11 and E.12, it is observed that the error deviation has been reduced significantly with the application of this model at all temperatures. In fact, the model provides a quite accurate description of the rheological properties of the best performing flat rheology fluid.

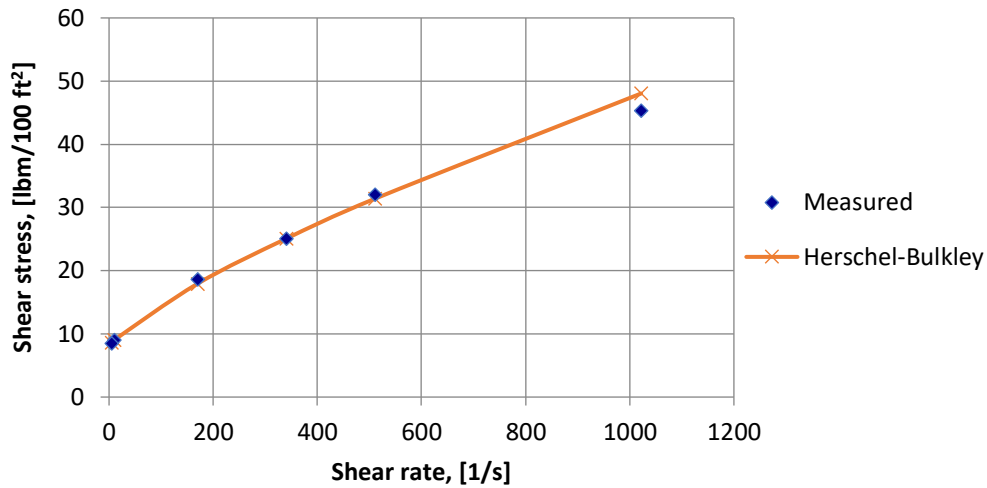


Figure E. 10: Herschel-Bulkley model versus flat rheology fluid at 22 °C

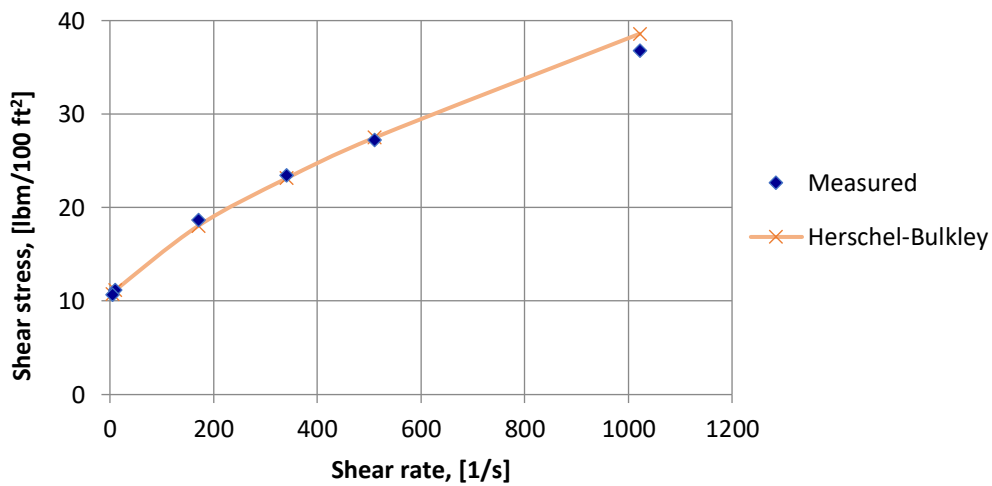


Figure E. 11: Herschel-Bulkley model versus flat rheology fluid at 50 °C

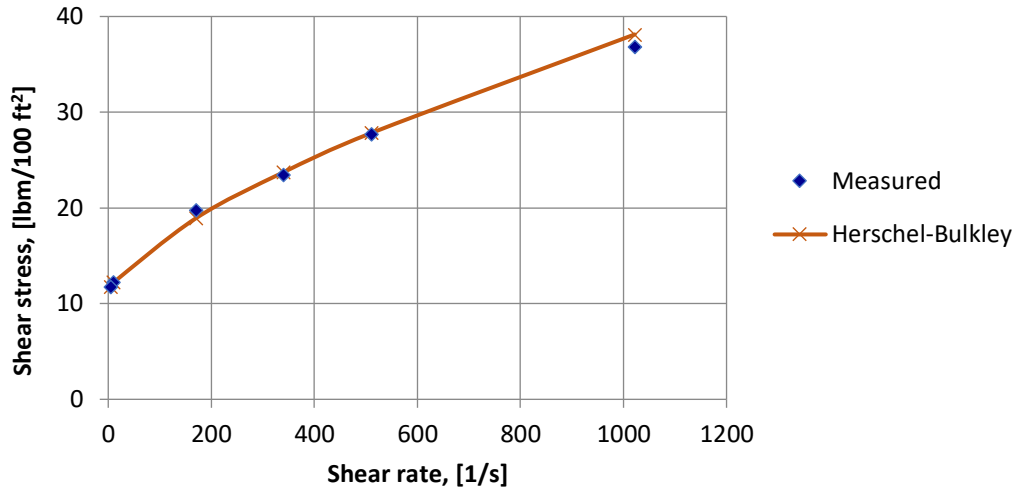


Figure E. 12: Herschel-Bulkley model versus flat rheology fluid at 80 °C

Unified Model

The Unified model, like the H-B model, is a modified Power Law model. It describes fluid flow using the same three-parameter equation as the H-B model, however, the two differ in their calculations of the yield stress, consistency- and flow behavior index. The Unified model predictions are presented in figure E.13, E.14 and E.15 for measurements at 22°C, 50°C and 80°C, respectively. It is observed that the flow behavior estimate is nearly the same as that of the H-B model.

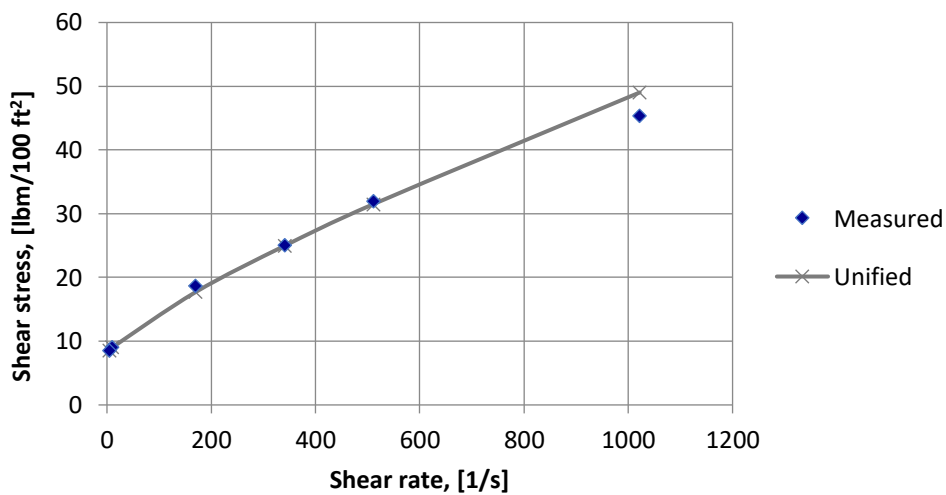


Figure E. 13: Unified model versus flat rheology fluid at 22 °C

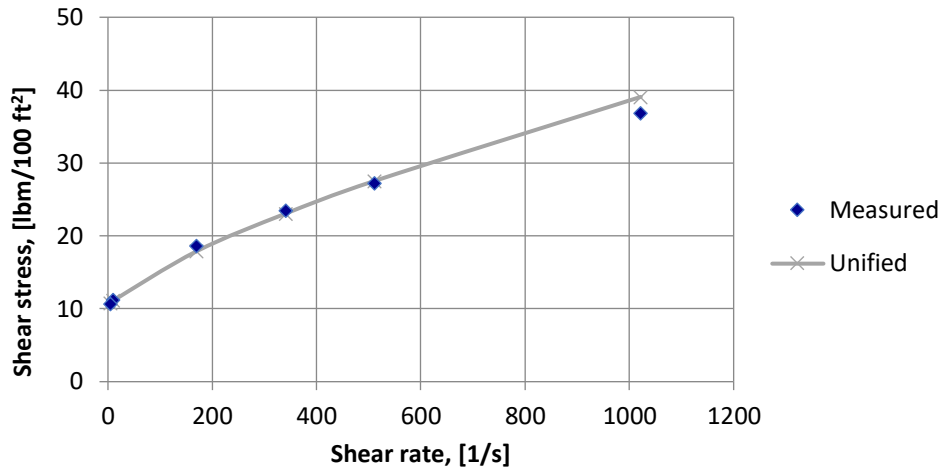


Figure E. 14: Unified model versus flat rheology fluid at 50 °C

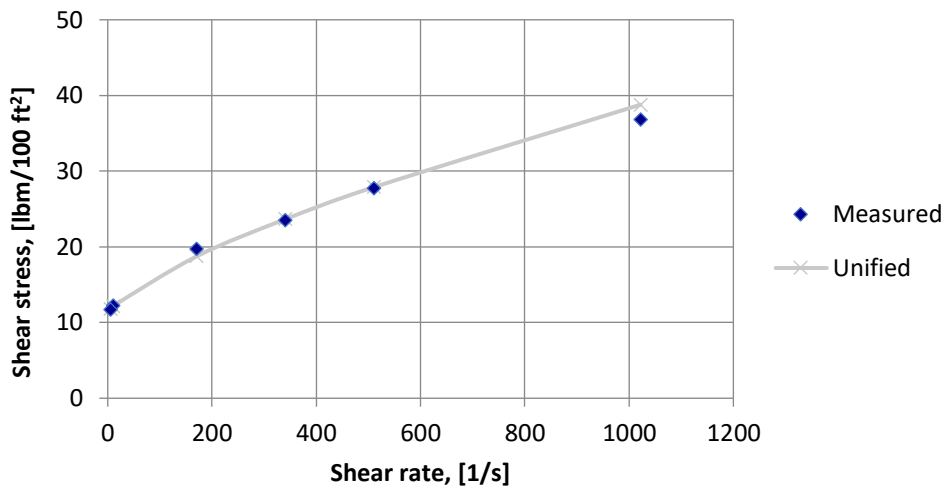


Figure E. 15: Unified model versus flat rheology fluid at 80 °C

Robertson-Stiff Model

The Robertson-Stiff model utilizes a four-parameter equation to describe the rheological behavior of drilling fluids. It differs from the other models as it has a more general approach of describing fluid flow and utilizes the constant parameters denoted as A, B and C. Figure E.16, E.17 and E.18 presents the predictions provided by the R-S model and the viscometer dial readings of the best performing flat rheology system at 22°C, 50°C and 80°C, respectively. It is observed that the model describes the flat rheology fluid almost perfectly with only very small error deviations from the actual viscometer data.

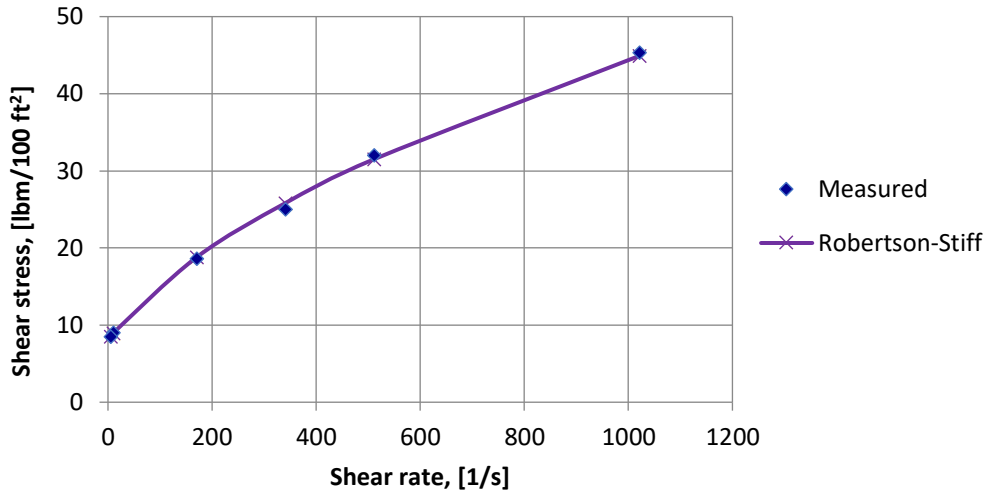


Figure E. 16: Robertson-Stiff model versus flat rheology fluid at 22 °C

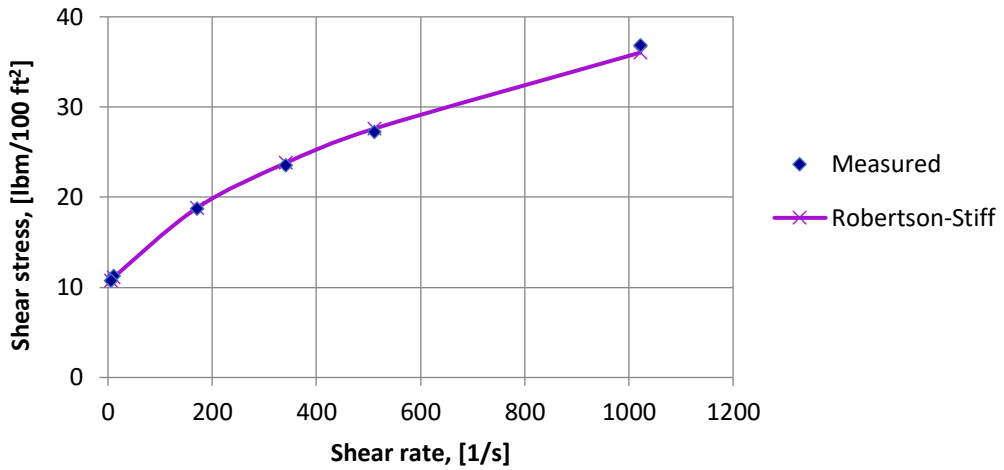


Figure E. 17: Robertson-Stiff model versus flat rheology fluid at 50 °C

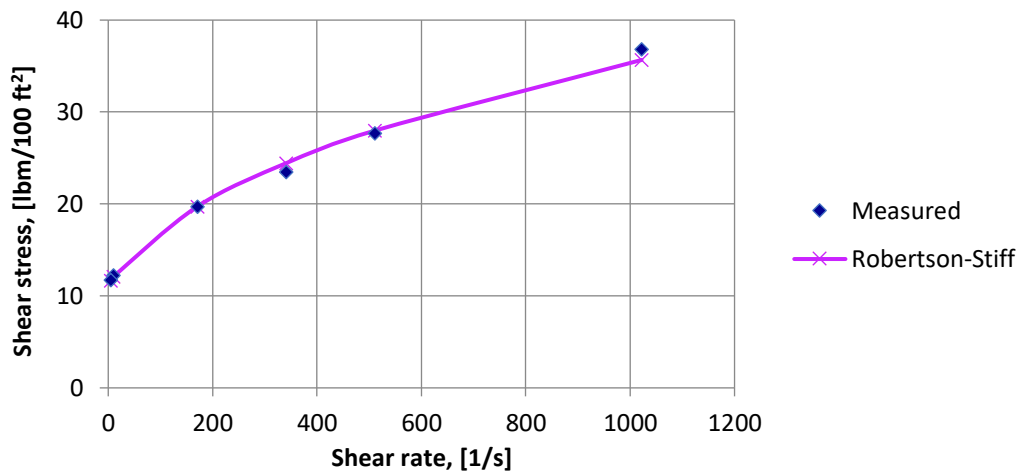


Figure E. 18: Robertson-Stiff model versus flat rheology fluid at 80 °C

APPENDIX F – HYDRAULICS PERFORMANCE SIMULATIONS

As mentioned, the viscosity of the applied fluid is a required input in order to perform a hydraulics performance simulation. Thus, the following tables presents the viscometer dial readings of the remaining nanoparticle fluids, i.e. those not already introduced in subsection 6.2.1.

Table F. 1: Summary of viscometer dial readings applied in the hydraulics simulation (MW fluids)

RPM	0.13 g MW			0.18 g MW			0.24 g MW		
	22°C	50°C	80°C	22°C	50°C	80°C	22°C	50°C	80°C
600	43	40.5	38	41	39.5	36	46	45	42.5
300	30	32	30.5	27.5	30.5	27.5	31.5	34	32.5
200	24.5	28.5	27	22	26.5	25	25	29.5	28.5
100	18	23.5	23	17	22	22	19	25.5	25
6	10	19	16.5	10	16.5	16	11	18.5	18
3	9.5	16	16	8.5	15	15	10.5	18	17.5

Table F. 2: Summary of viscometer dial readings applied in the hydraulics simulation (silica fluids)

RPM	0.08 g Si			0.13 g Si			0.18 g Si			0.25 g Si		
	22°C	50°C	80°C	22°C	50°C	80°C	22°C	50°C	80°C	22°C	50°C	80°C
600	42	34	32	42	34	33	44	37.5	34	41.5	34	31
300	28	24	25	28	25	25	29.5	25.5	27.5	26.5	24	23.5
200	22	20.5	22	22	21	22	24	21.5	24	21	21	21
100	16	16	18.5	15.5	16	18.5	17.5	17	19	15	15.5	17
6	8	10.5	13	7.5	10.5	13.5	9.5	11	13	7.5	11	13
3	7.5	10	13	7.5	10	13	9	10	13	7.5	10.5	13

Table F. 3: Summary of viscometer dial readings applied in the hydraulics simulation (Al fluids)

RPM	0.07 g Al			0.13 g Al			0.19 g Al			0.24 g Al		
	22°C	50°C	80°C	22°C	50°C	80°C	22°C	50°C	80°C	22°C	50°C	80°C
600	49	40	35.5	46	35.5	33.5	44	35	35	47.5	35	36
300	34	31	30	30	27	26	30	26	27	32	27	27.5
200	28	25.5	26.5	23.5	22	23	22.5	21	24	25	23.5	24
100	20.5	20	22	17	17	19	16	17.5	19.5	18	19.5	20.5
6	12	13	15.5	9	11	13.5	8.5	11.5	13.5	10	12	14
3	11.5	12	15	8.5	11	13	8	11	13	9.5	12	13.5

Pump Pressure Plots - Reference Fluid Containing Multi-Walled Carbon Nanotube

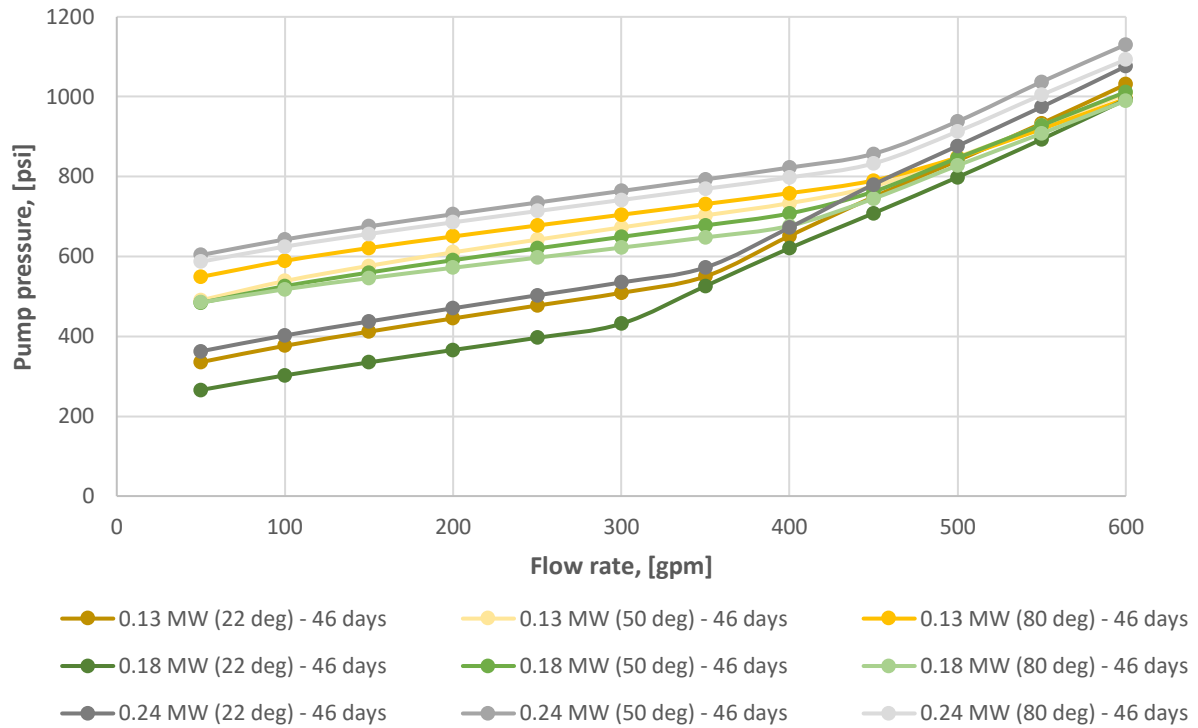


Figure F. 1: Pump pressure of MWCNT-COOH fluids at 22°C, 50°C and 80°C

Pump Pressure Plots - Reference Fluid Containing Silica

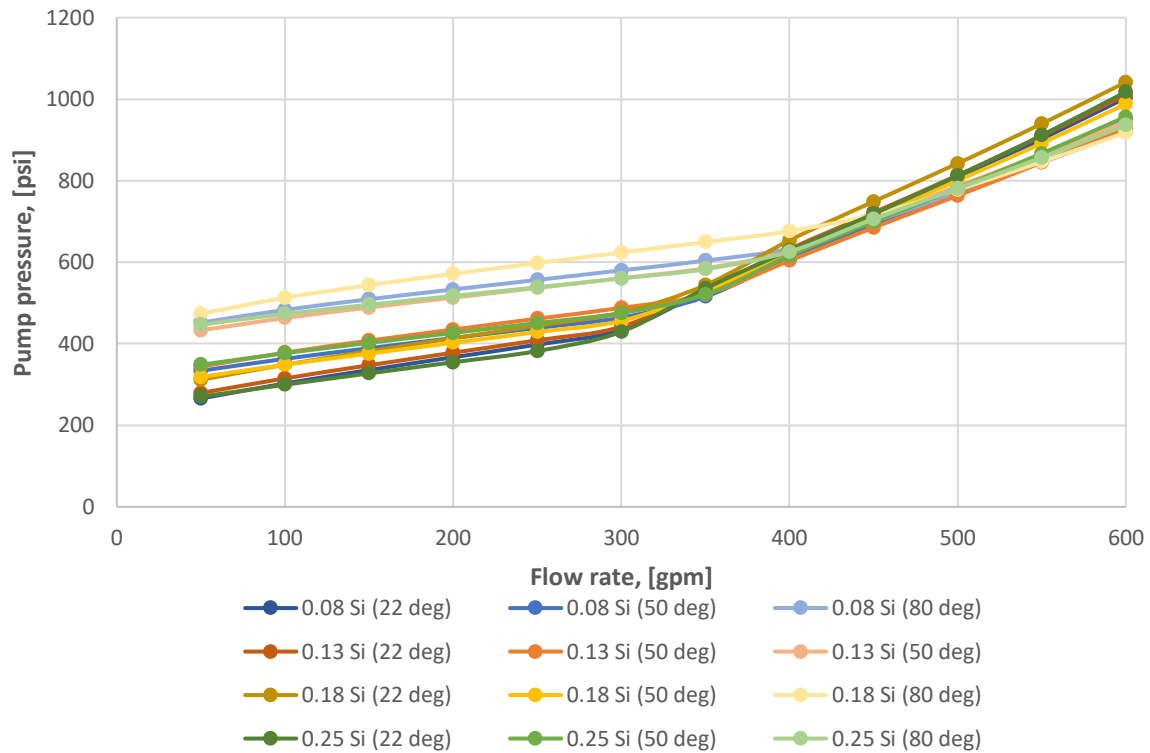


Figure F. 2: Pump pressure of silica fluids at 22°C, 50°C and 80°C

Pump Pressure Plots - Reference Fluid Containing Aluminum Oxide

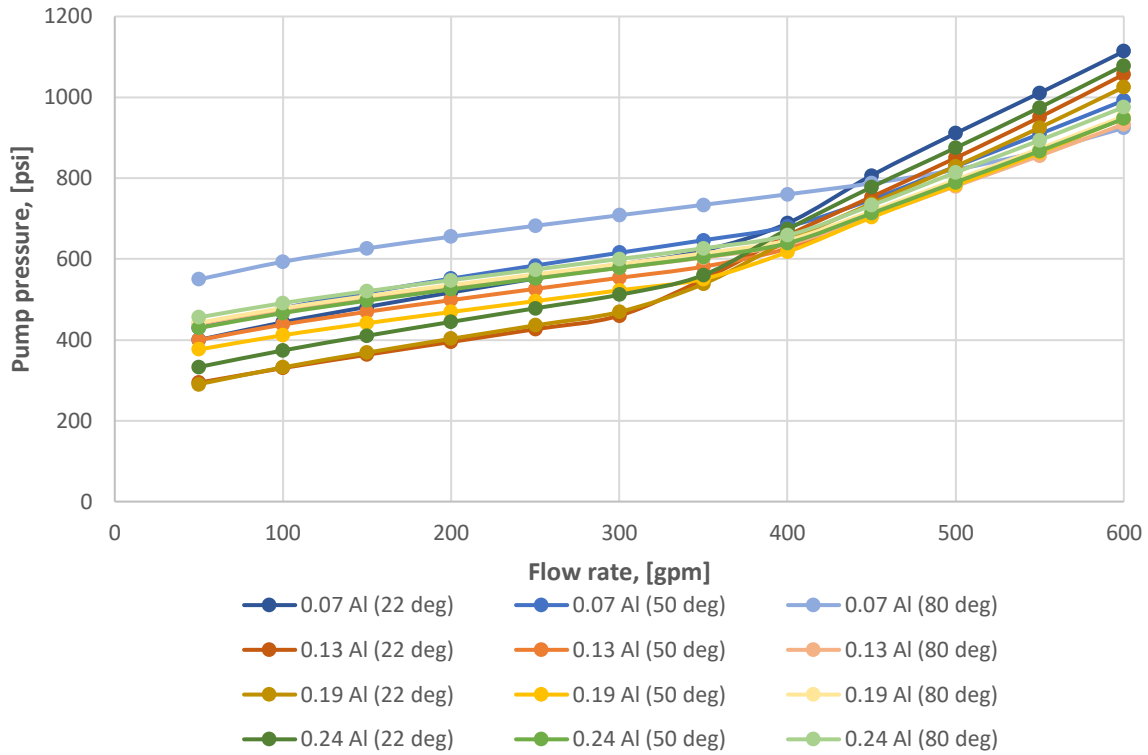


Figure F. 3: Pump pressure of aluminum oxide fluids at 22°C, 50°C and 80°C

ECD Plots - Reference Fluid Containing Multi-Walled Carbon Nanotube

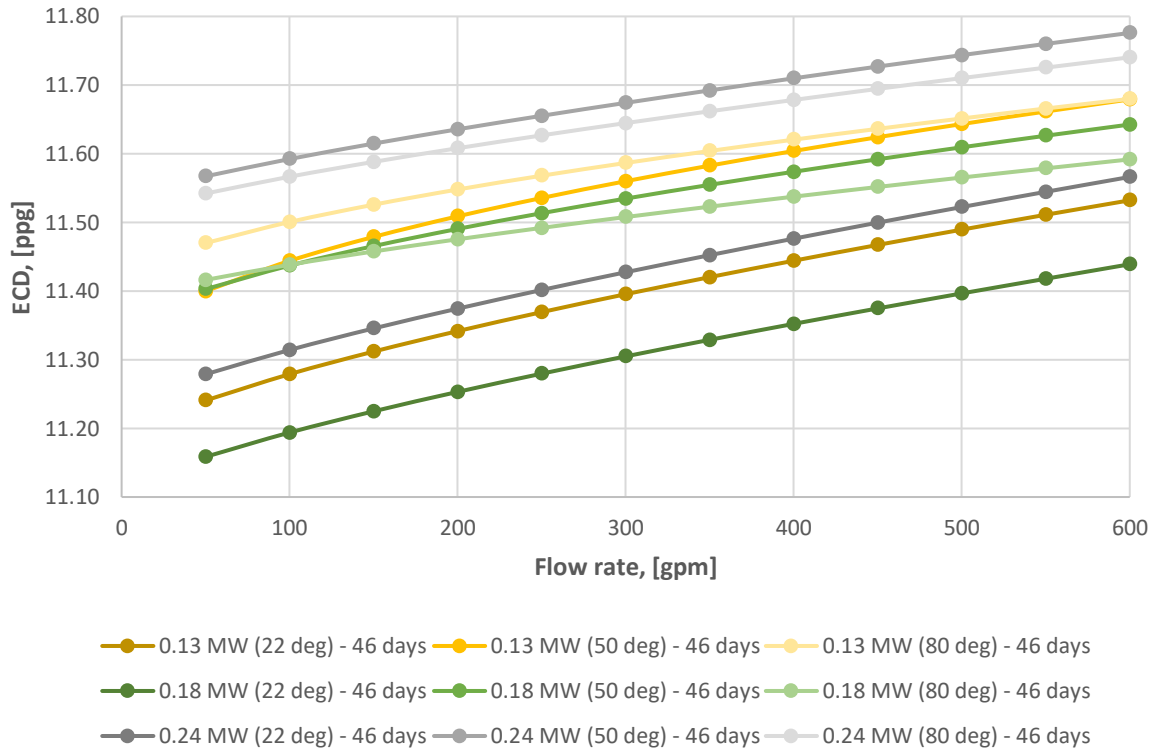


Figure F. 4: ECD of MWCNT-COOH fluids at 22°C, 50°C and 80°C

ECD Plots - Reference Fluid Containing Silica

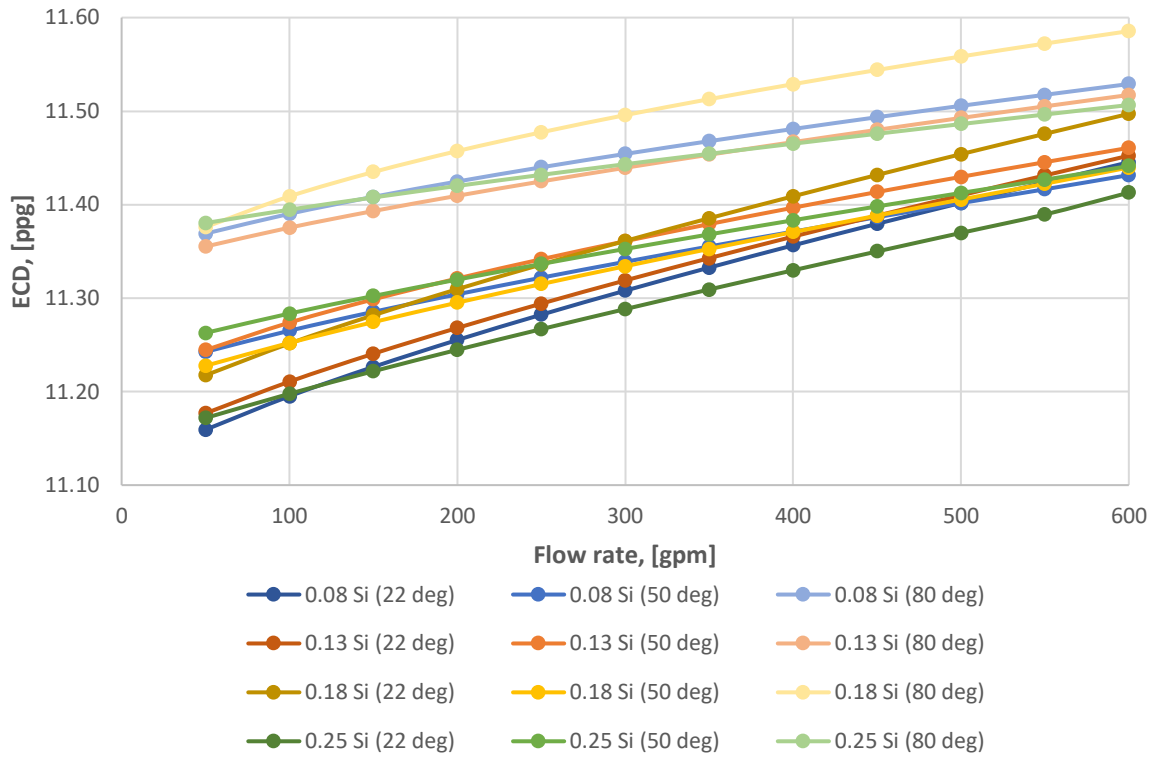


Figure F. 5: ECD of silica fluids at 22°C, 50°C and 80°C

ECD Plots - Reference Fluid Containing Aluminum Oxide

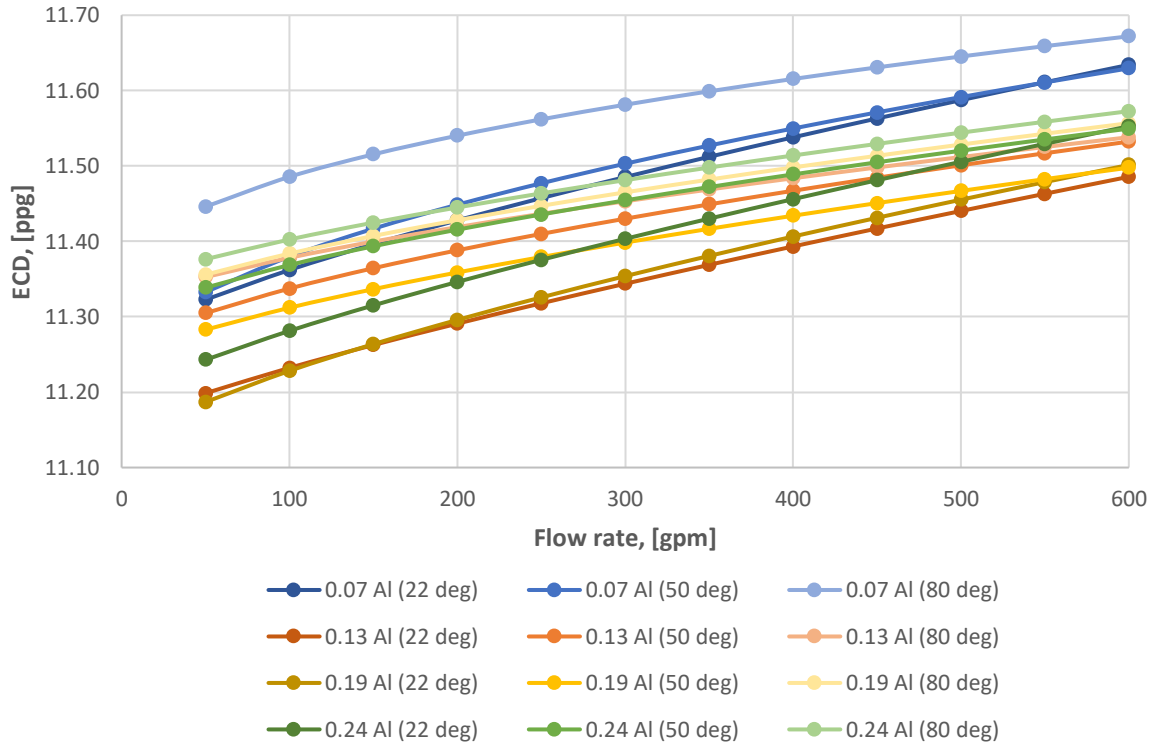


Figure F. 6: ECD of aluminum oxide fluids at 22°C, 50°C and 80°C

ECD Simulation - The Percentage Change from the Initial Mud Weight for Reference Fluid

Figure F.7 illustrates the percentage change from the initial mud weight for the best performing flat rheology system, i.e. the reference fluid containing 0.08 g carbopol.

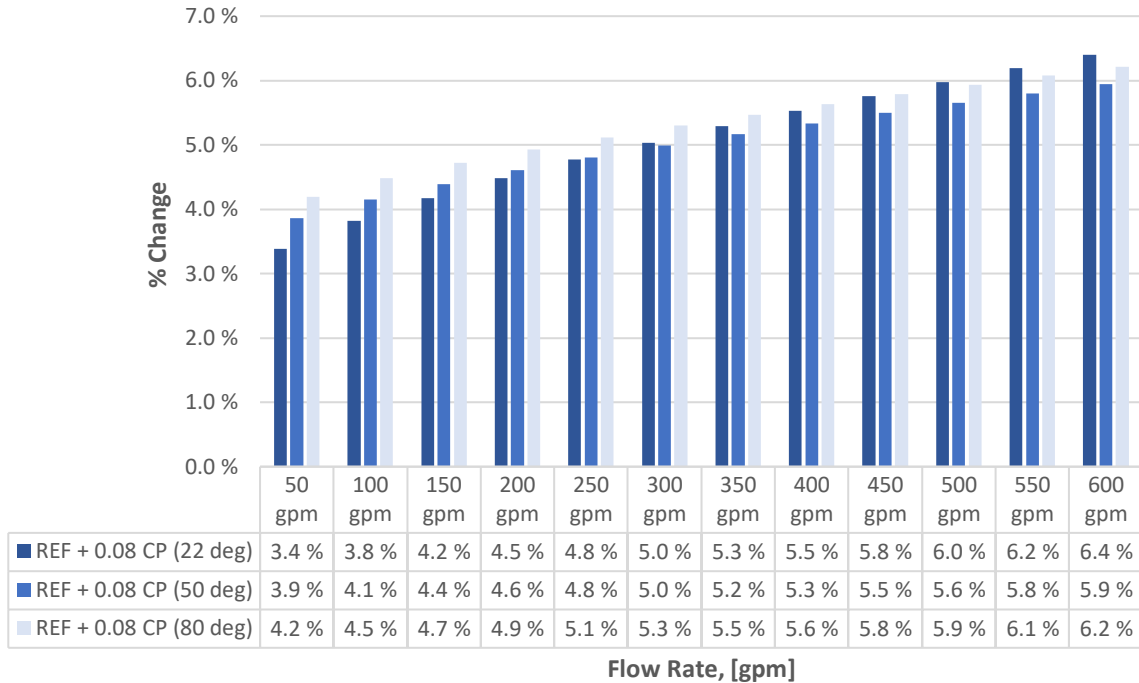


Figure F. 7: ECD simulation: % Change from initial mud weight (REF + 0.08 g CP system)

ECD Simulation - The Percentage Change from the Initial Mud Weight for Nanoparticle Fluids

In subsection 6.2.3.2, it was described how the ECD experienced minor change with increasing flow rate in the range considered in this thesis, i.e. 50-600 gpm. However, some change was observed for all fluids and it is presented in the tables below as a percentage change from the initial mud weight. As a reminder, the density was set as 1.30 sg for all fluids, which corresponds to 11.83 ppg. As seen in the tables, the 0.13 g MW, 0.13 g Si and 0.07 g Al fluids are “emphasized” with color. It is observed that the percentage changes are relatively alike for all nanoparticle fluids. However, the multi-walled carbon nanotube suspension produces a slightly greater change overall.

Table F. 4: ECD simulation: % Change from initial mud weight (MWCNT-COOH fluids)

Flow rate, [gpm]	0.13 g MW			0.18 g MW			0.24 g MW		
	22°C	50°C	80°C	22°C	50°C	80°C	22°C	50°C	80°C
50	3.8 %	5.3 %	5.9 %	3.0 %	5.3 %	5.4 %	4.2 %	6.8 %	6.6 %
100	4.2 %	5.7 %	6.2 %	3.4 %	5.6 %	5.6 %	4.5 %	7.0 %	6.8 %
150	4.5 %	6.0 %	6.4 %	3.7 %	5.9 %	5.8 %	4.8 %	7.3 %	7.0 %
200	4.7 %	6.3 %	6.6 %	3.9 %	6.1 %	6.0 %	5.0 %	7.4 %	7.2 %
250	5.0 %	6.5 %	6.8 %	4.2 %	6.3 %	6.1 %	5.3 %	7.6 %	7.4 %
300	5.2 %	6.8 %	7.0 %	4.4 %	6.5 %	6.3 %	5.5 %	7.8 %	7.5 %
350	5.5 %	7.0 %	7.2 %	4.6 %	6.7 %	6.4 %	5.8 %	8.0 %	7.7 %
400	5.7 %	7.2 %	7.3 %	4.8 %	6.9 %	6.5 %	6.0 %	8.1 %	7.8 %
450	5.9 %	7.3 %	7.5 %	5.0 %	7.0 %	6.7 %	6.2 %	8.3 %	8.0 %
500	6.1 %	7.5 %	7.6 %	5.2 %	7.2 %	6.8 %	6.4 %	8.4 %	8.1 %
550	6.3 %	7.7 %	7.7 %	5.4 %	7.4 %	6.9 %	6.6 %	8.6 %	8.3 %
600	6.5 %	7.8 %	7.9 %	5.6 %	7.5 %	7.0 %	6.8 %	8.7 %	8.4 %

Table F. 5: ECD simulation: % Change from initial mud weight (silica fluids)

Flow rate, [gpm]	0.08 g Si			0.13 g Si			0.18 g Si			0.25 g Si		
	22°C	50°C	80°C	22°C	50°C	80°C	22°C	50°C	80°C	22°C	50°C	80°C
50	3.1 %	3.8 %	5.0 %	3.2 %	3.8 %	4.9 %	3.6 %	3.7 %	5.1 %	3.2 %	4.0 %	5.1 %
100	3.4 %	4.0 %	5.2 %	3.5 %	4.1 %	5.0 %	3.9 %	3.9 %	5.4 %	3.4 %	4.2 %	5.2 %
150	3.7 %	4.2 %	5.3 %	3.8 %	4.3 %	5.2 %	4.2 %	4.1 %	5.6 %	3.6 %	4.4 %	5.3 %
200	3.9 %	4.4 %	5.5 %	4.1 %	4.5 %	5.4 %	4.4 %	4.3 %	5.8 %	3.8 %	4.5 %	5.5 %
250	4.2 %	4.6 %	5.6 %	4.3 %	4.7 %	5.5 %	4.7 %	4.5 %	6.0 %	4.0 %	4.7 %	5.6 %
300	4.4 %	4.7 %	5.8 %	4.5 %	4.9 %	5.6 %	4.9 %	4.7 %	6.2 %	4.2 %	4.8 %	5.7 %
350	4.7 %	4.9 %	5.9 %	4.7 %	5.1 %	5.8 %	5.1 %	4.8 %	6.3 %	4.4 %	5.0 %	5.8 %
400	4.9 %	5.0 %	6.0 %	5.0 %	5.2 %	5.9 %	5.4 %	5.0 %	6.5 %	4.6 %	5.1 %	5.9 %
450	5.1 %	5.1 %	6.1 %	5.2 %	5.4 %	6.0 %	5.6 %	5.2 %	6.6 %	4.8 %	5.3 %	6.0 %
500	5.3 %	5.3 %	6.2 %	5.4 %	5.5 %	6.1 %	5.8 %	5.3 %	6.7 %	5.0 %	5.4 %	6.1 %
550	5.5 %	5.4 %	6.4 %	5.6 %	5.7 %	6.2 %	6.0 %	5.5 %	6.9 %	5.2 %	5.5 %	6.2 %
600	5.7 %	5.6 %	6.5 %	5.8 %	5.8 %	6.4 %	6.2 %	5.6 %	7.0 %	5.4 %	5.7 %	6.3 %

Table F. 6: ECD simulation: % Change from initial mud weight (aluminum oxide fluids)

Flow rate, [gpm]	0.07 g Al			0.13 g Al			0.19 g Al			0.24 g Al		
	22°C	50°C	80°C	22°C	50°C	80°C	22°C	50°C	80°C	22°C	50°C	80°C
50	4.6 %	4.7 %	5.7 %	3.4 %	4.4 %	4.8 %	3.3 %	4.2 %	4.9 %	3.8 %	4.7 %	5.1 %
100	4.9 %	5.1 %	6.1 %	3.7 %	4.7 %	5.1 %	3.7 %	4.5 %	5.1 %	4.2 %	5.0 %	5.3 %
150	5.2 %	5.4 %	6.3 %	4.0 %	4.9 %	5.3 %	4.0 %	4.7 %	5.3 %	4.5 %	5.2 %	5.5 %
200	5.5 %	5.7 %	6.6 %	4.3 %	5.2 %	5.4 %	4.3 %	4.9 %	5.5 %	4.8 %	5.4 %	5.7 %
250	5.8 %	6.0 %	6.8 %	4.5 %	5.4 %	5.6 %	4.6 %	5.1 %	5.7 %	5.0 %	5.6 %	5.9 %
300	6.1 %	6.2 %	6.9 %	4.8 %	5.6 %	5.8 %	4.8 %	5.3 %	5.9 %	5.3 %	5.8 %	6.0 %
350	6.3 %	6.4 %	7.1 %	5.0 %	5.7 %	5.9 %	5.1 %	5.4 %	6.0 %	5.6 %	5.9 %	6.2 %
400	6.5 %	6.7 %	7.3 %	5.2 %	5.9 %	6.0 %	5.3 %	5.6 %	6.2 %	5.8 %	6.1 %	6.3 %
450	6.8 %	6.9 %	7.4 %	5.4 %	6.1 %	6.2 %	5.6 %	5.7 %	6.3 %	6.0 %	6.2 %	6.5 %
500	7.0 %	7.0 %	7.5 %	5.6 %	6.2 %	6.3 %	5.8 %	5.9 %	6.5 %	6.2 %	6.4 %	6.6 %
550	7.2 %	7.2 %	7.7 %	5.9 %	6.4 %	6.4 %	6.0 %	6.0 %	6.6 %	6.5 %	6.5 %	6.7 %
600	7.4 %	7.4 %	7.8 %	6.1 %	6.5 %	6.5 %	6.2 %	6.2 %	6.7 %	6.7 %	6.7 %	6.9 %

APPENDIX G – TORQUE AND DRAG SIMULATIONS

A torque and drag simulation study was performed for the reference fluid, which is the one containing 0.08 g carbopol, as well as the best performing nanoparticle systems in regard to fluid loss. Figure G.1 presents the well utilized in the simulations, however, its deviation is not illustrated and the shown depth will vary depending on the fluid system applied in the well. Further, the effective tension, torque, stress trip in and stress trip out plots obtained at the maximum depth for each fluid will be presented in the following subsections. Table G.1 and G.2 presents the maximum drilling depths and the limiting factors for each of the systems.

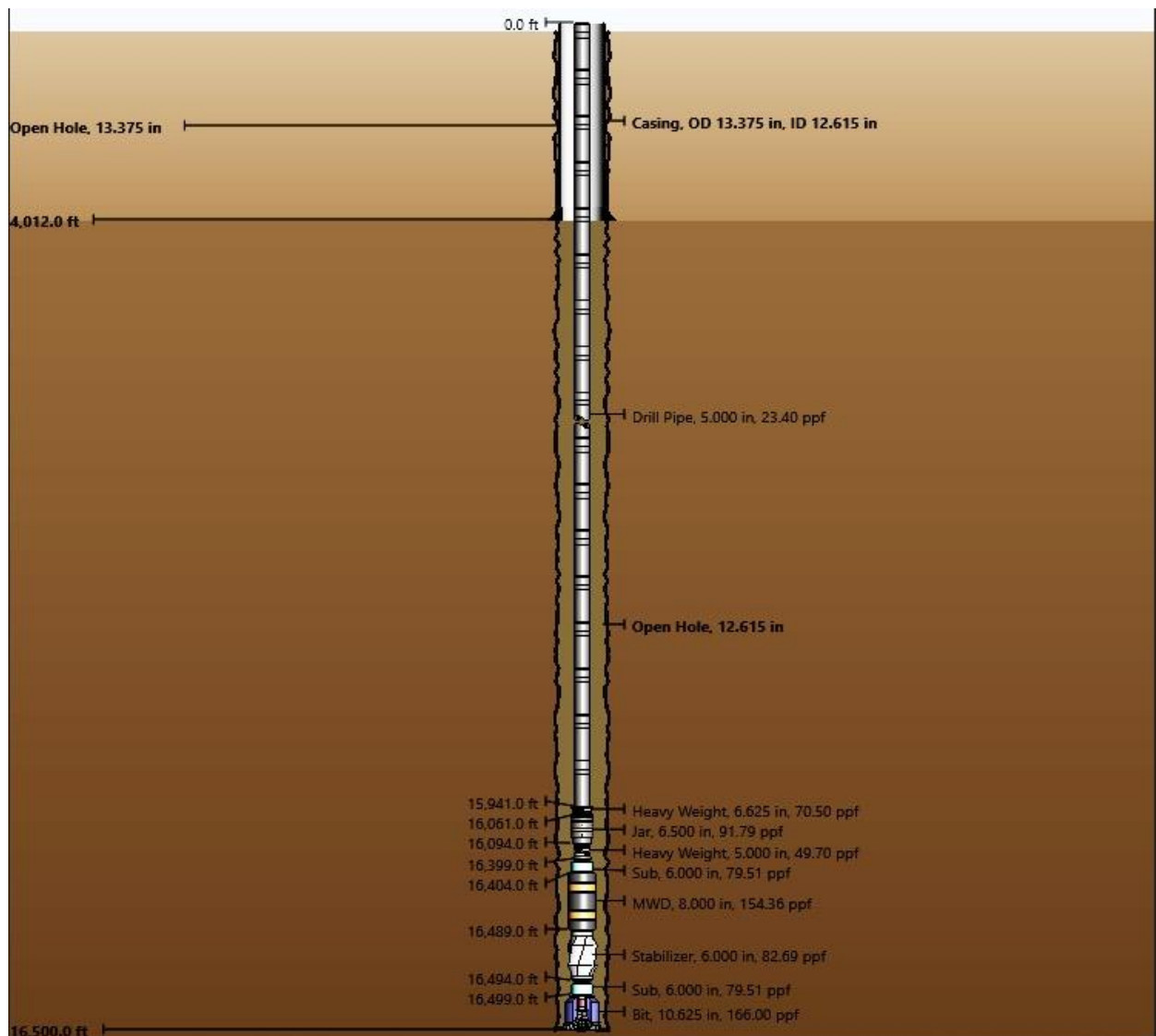


Figure G. 1: Illustration of the simulation well at the maximum depth for the reference fluid system

Table G. 1: Summary of the maximum depths obtained from the T&D simulation

Fluid	CoF	% Change CoF	Max. Depth, [ft]	% Change Depth
REF (short-time)	0.249	---	16500	---
REF + 0.07 MW (short-time)	0.157	-36.8	21500	30.3
REF + 0.13 Si	0.192	-23.1	19400	17.6
REF + 0.07 Al	0.160	-35.7	21400	29.7
REF (long-time)	0.187	-25.1	19700	19.4
REF + 0.13 MW (long-time)	0.161	-13.7	21500	9.1

Table G. 2: Summary of the factors limiting the maximum drilling depth of each fluid system

Fluid	Limiting Factor
REF (short-time)	Torque when rotation of bottom
REF + 0.07 MW (short-time)	Torque when rotation of bottom
REF + 0.13 Si	Effective tension when tripping out
REF + 0.07 Al	Effective tension when tripping out
REF (long-time)	Torque when rotation of bottom
REF + 0.13 MW (long-time)	Effective tension when tripping out

T & D Plots - Reference Fluid System (Short-Time)

Stress Trip Out Plot



Figure G. 2: Stress trip out plot for reference fluid system (short-time)

Stress Trip In Plot

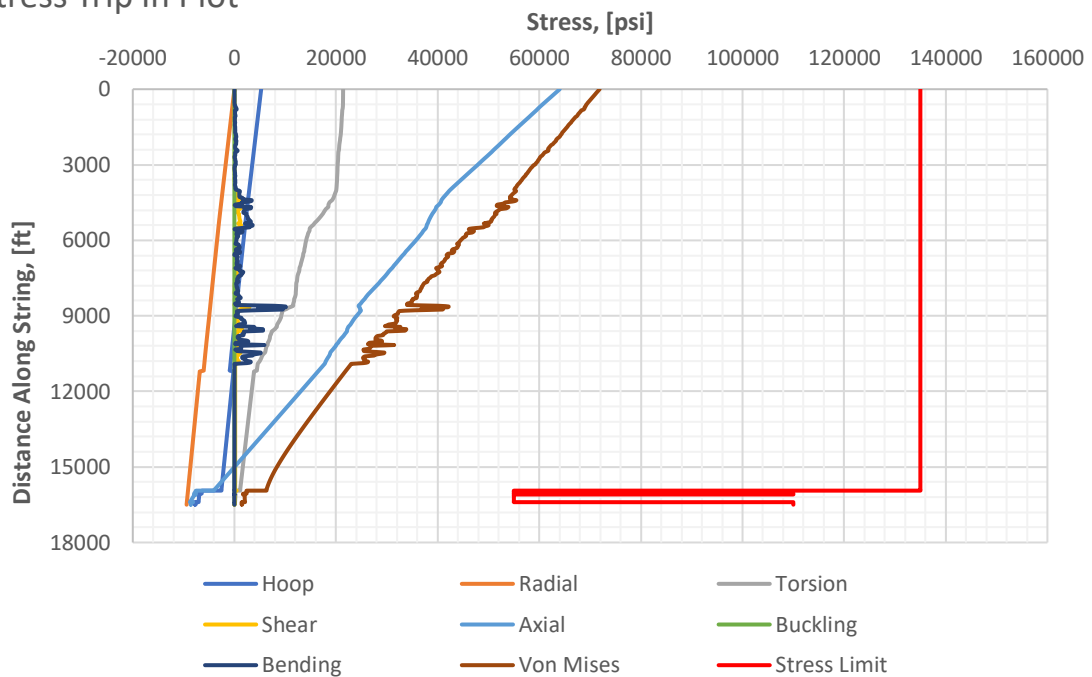


Figure G. 3: Stress trip in plot for reference fluid system (short-time)

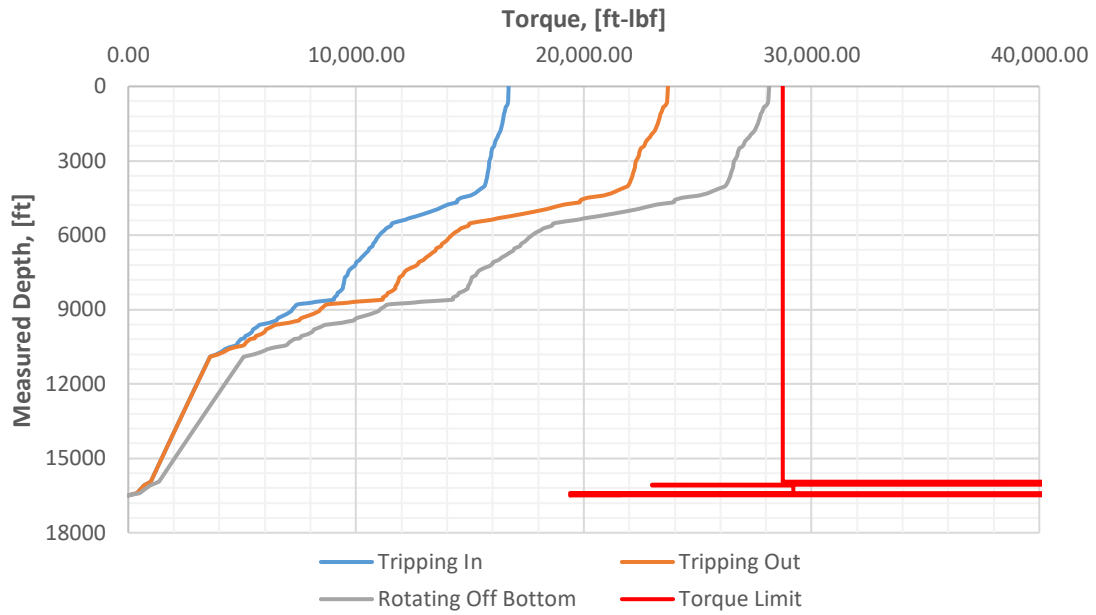


Figure G. 4: Torque plot for the reference fluid system (short-time)

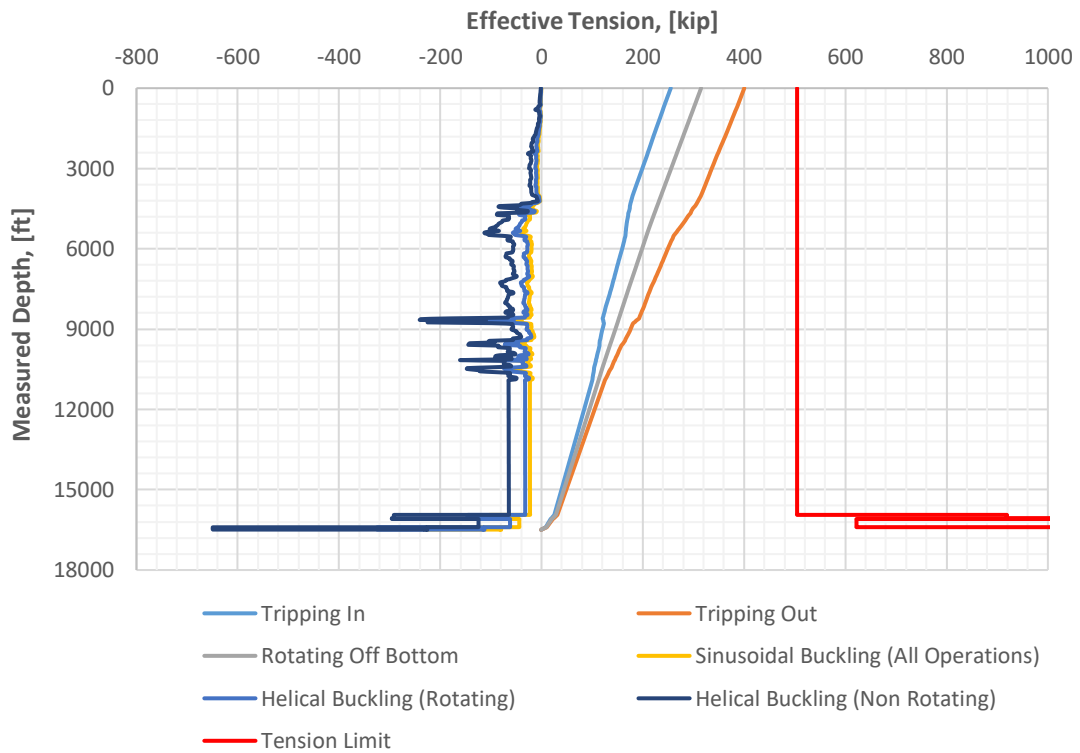


Figure G. 5: Effective tension plot for reference fluid system (short-time)

T & D Plots - Reference Fluid System (Long-Time)

Stress Trip Out Plot

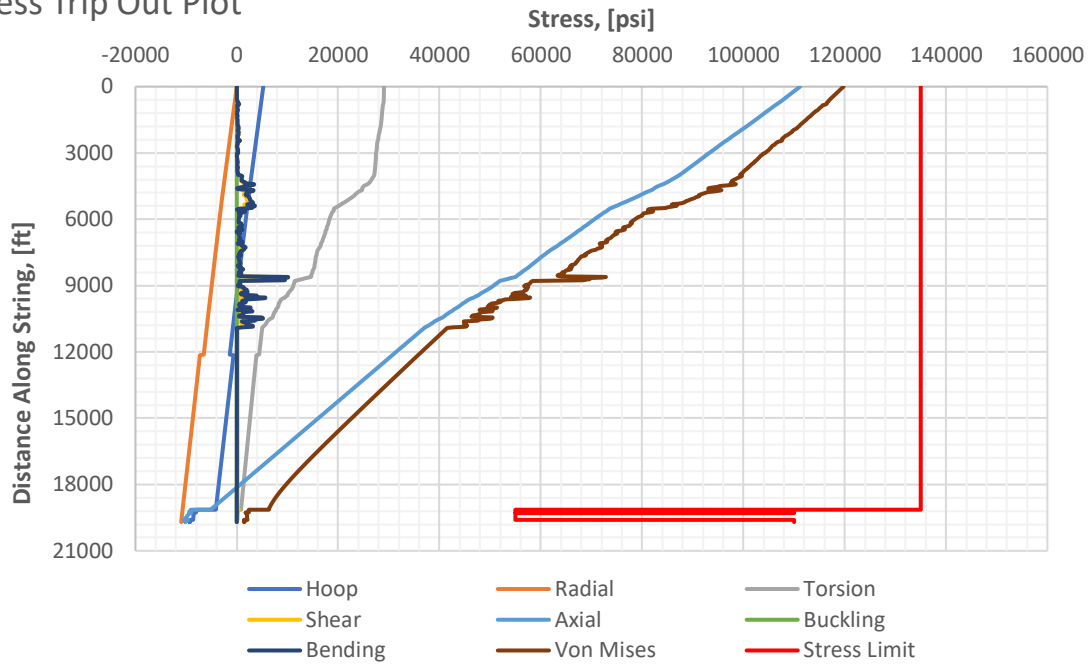


Figure G. 6: Stress trip in plot for reference fluid system (long-time)

Stress Trip In Plot

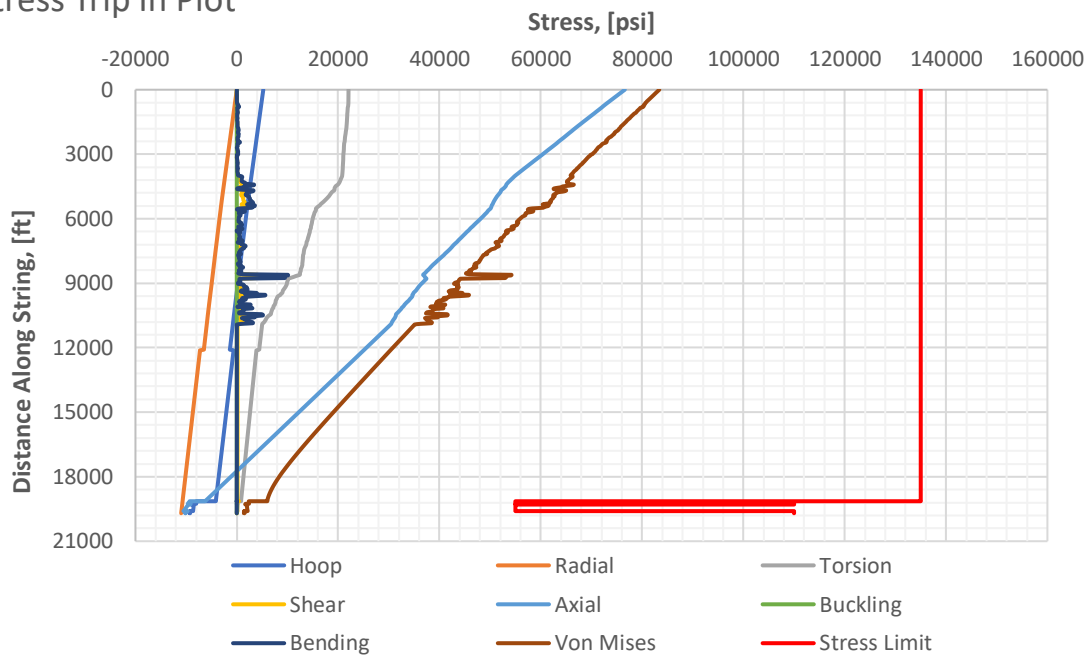


Figure G. 7: Stress trip in plot for reference fluid system (long-time)

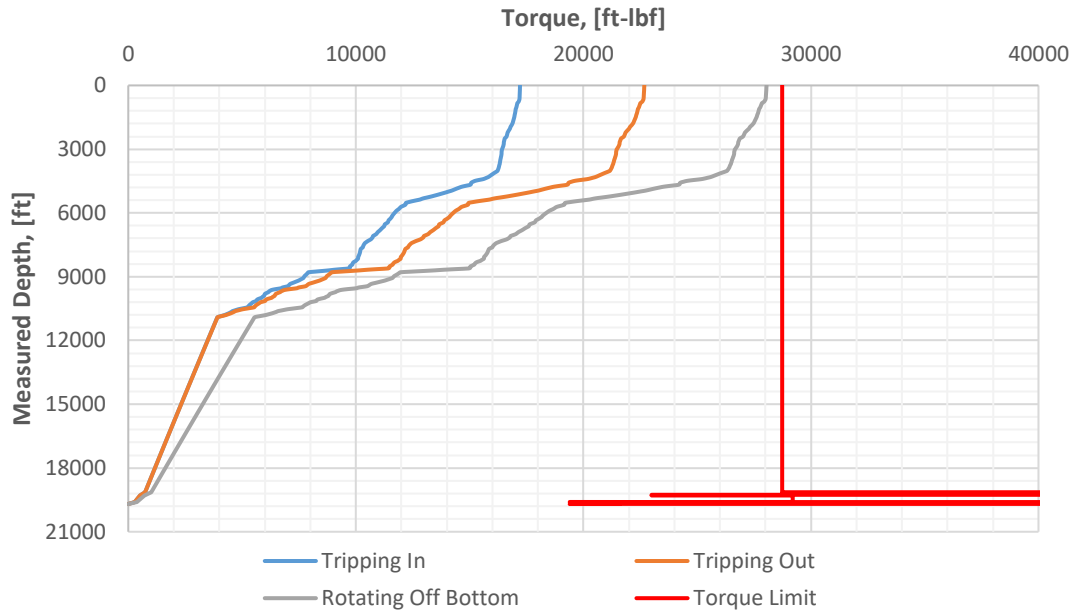


Figure G. 8: Torque plot for reference fluid system (long-time)

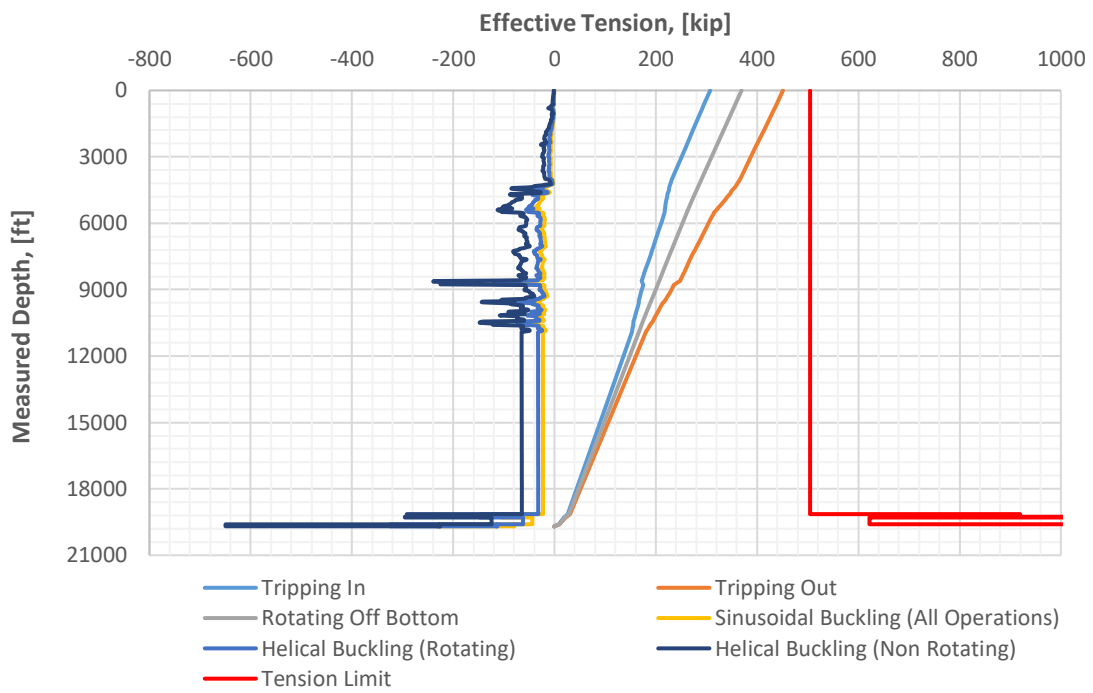


Figure G. 9: Effective tension plot for reference fluid system (long-time)

T & D Plots - Reference Fluid Containing 0.07 g MWCNT-COOH (Short-Time)

Stress Trip Out Plot

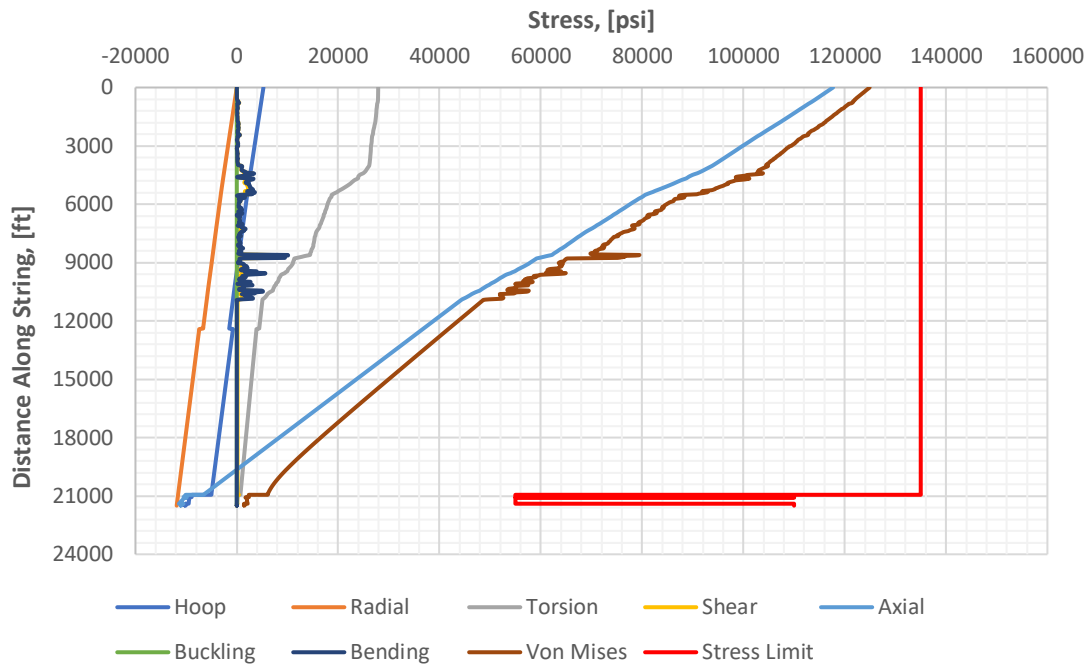


Figure G. 10: Stress trip out plot for REF + 0.07 g MW (short-time)

Stress Trip In Plot

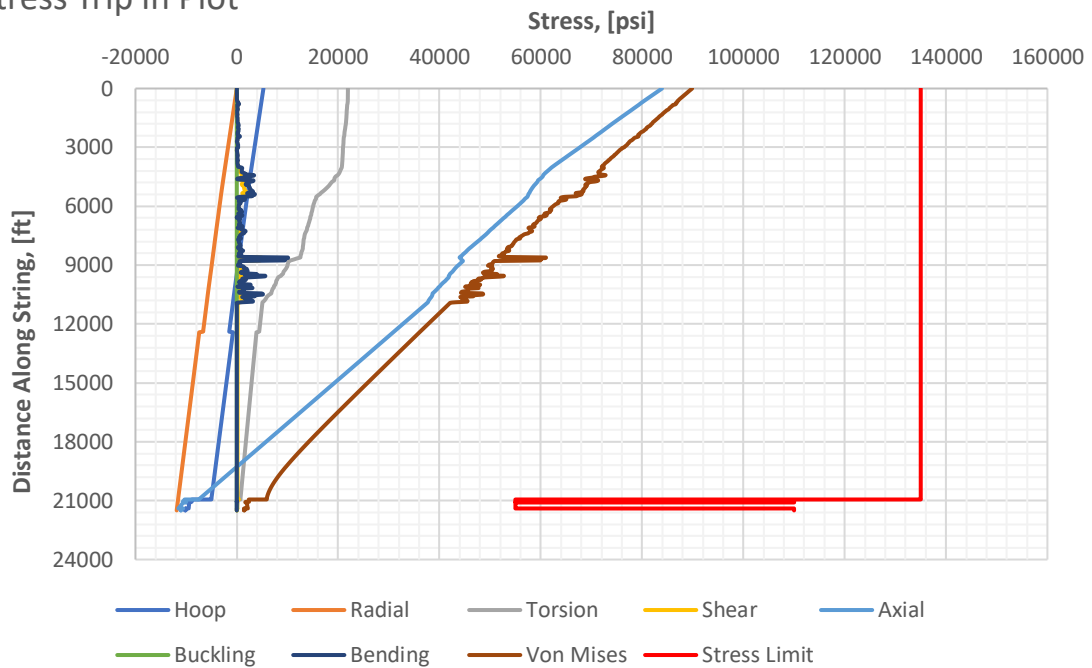


Figure G. 11: Stress trip in plot for REF + 0.07 g MW (short-time)

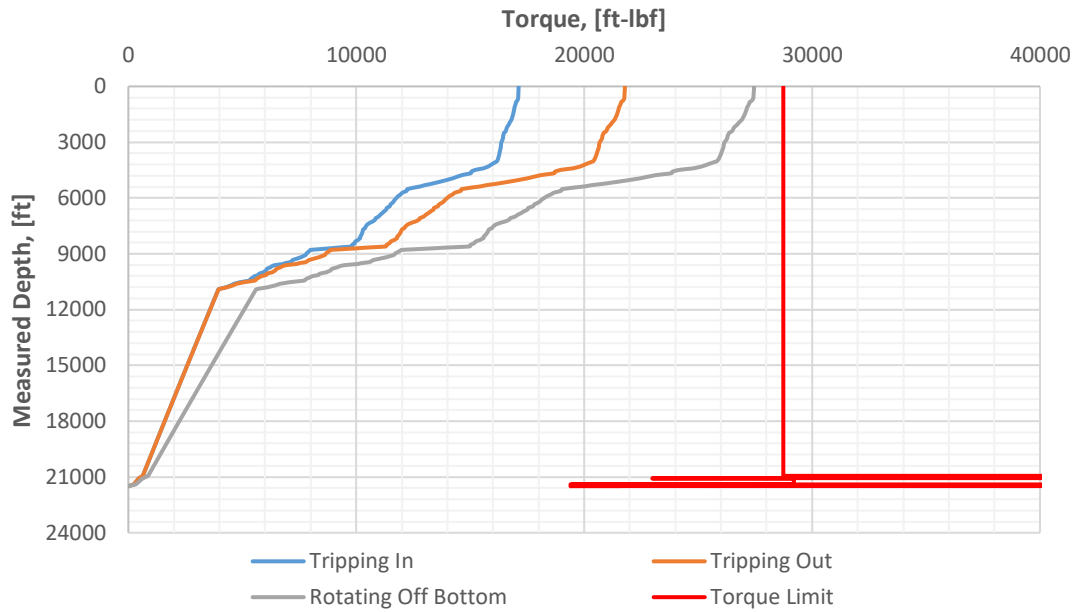


Figure G. 12: Torque plot for REF + 0.07 g MW (short-time)

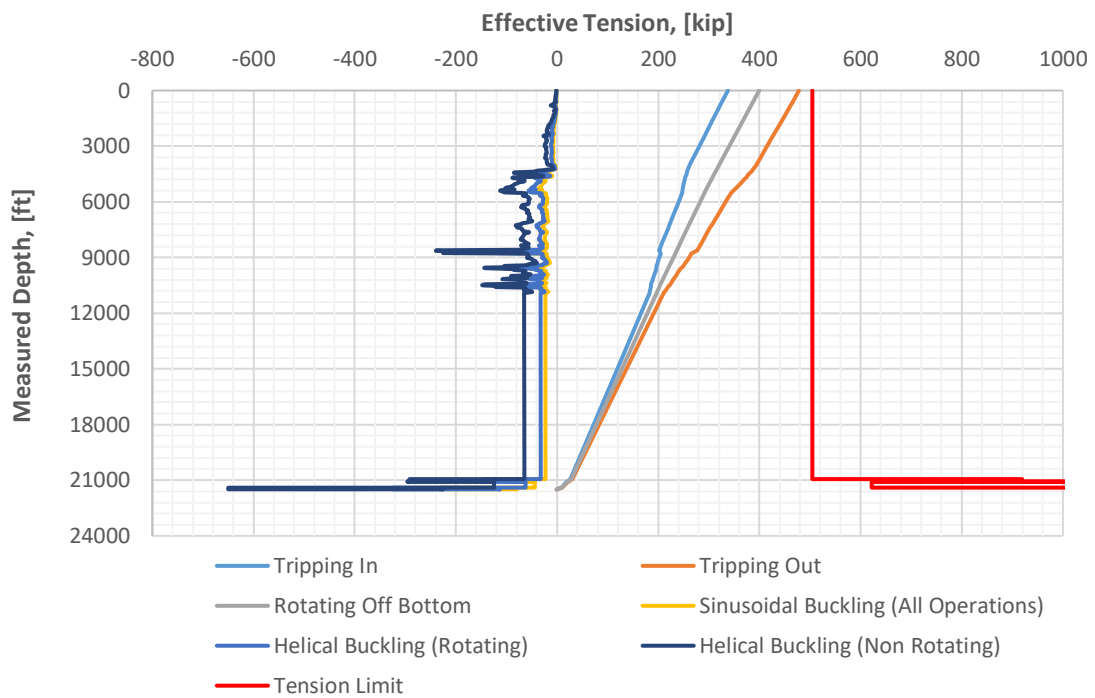


Figure G. 13: Effective tension plot for REF + 0.07 g MW (short-time)

T & D Plots - Reference Fluid Containing 0.13 g MWCNT-COOH (Long-Time)

Stress Trip Out Plot



Figure G. 14: Stress trip out plot for REF + 0.13 g MW (long-time)

Stress Trip In Plot



Figure G. 15: Stress trip in plot for REF + 0.13 g MW (long-time)

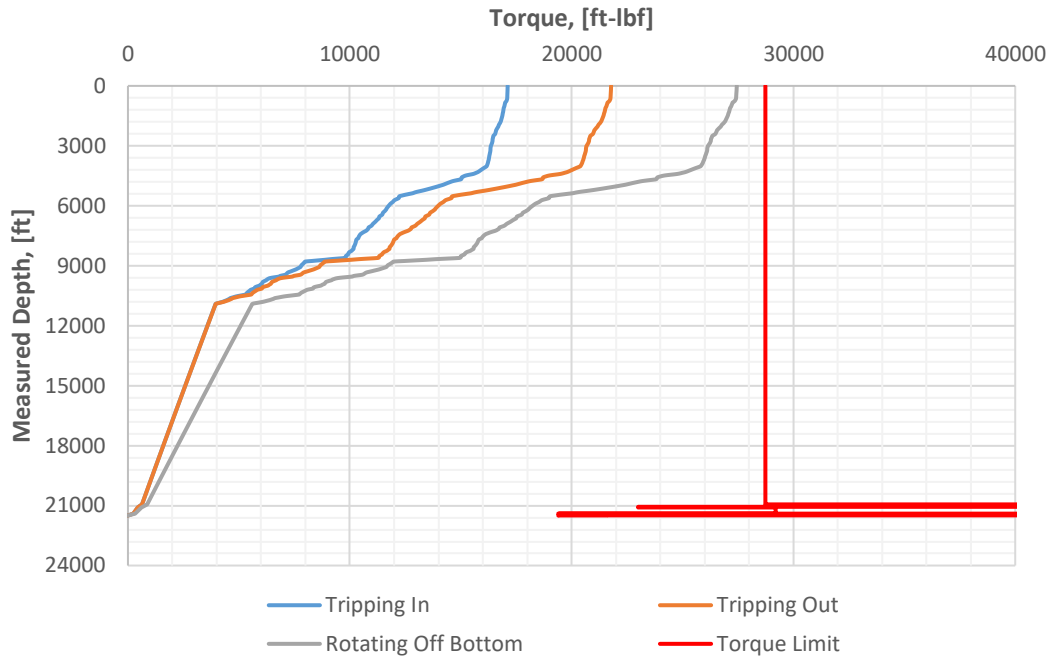


Figure G. 16: Torque plot for REF + 0.13 g MW (long-time)

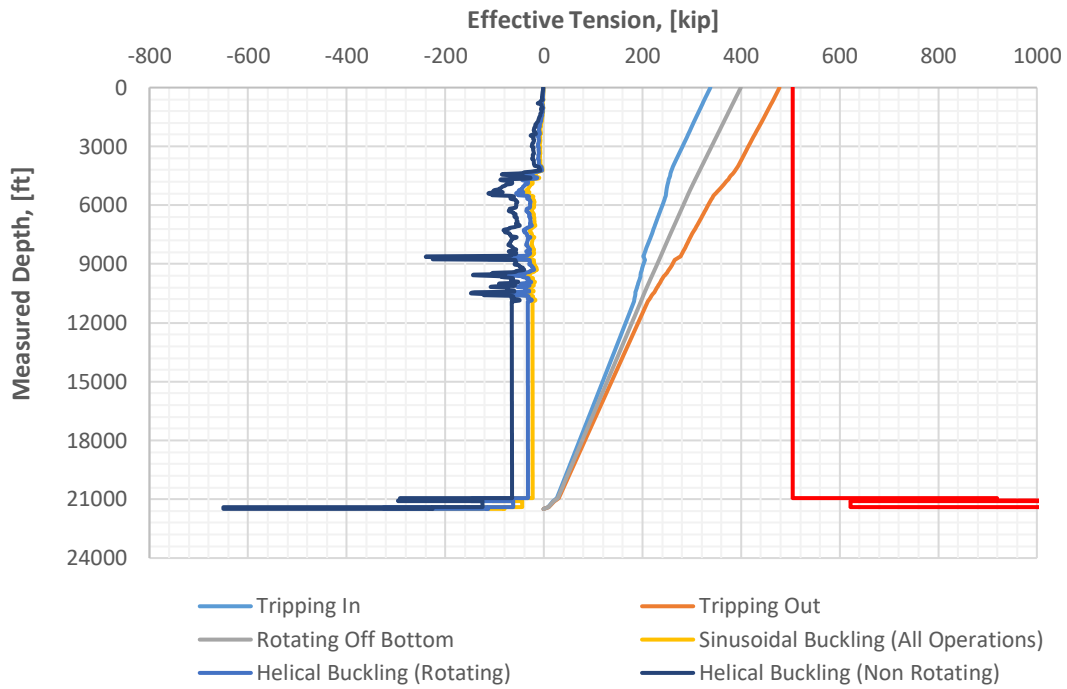


Figure G. 17: Effective tension plot for REF + 0.13 g MW (long-time)

T & D Plots - Reference Fluid Containing 0.13 g SiO₂

Stress Trip Out Plot

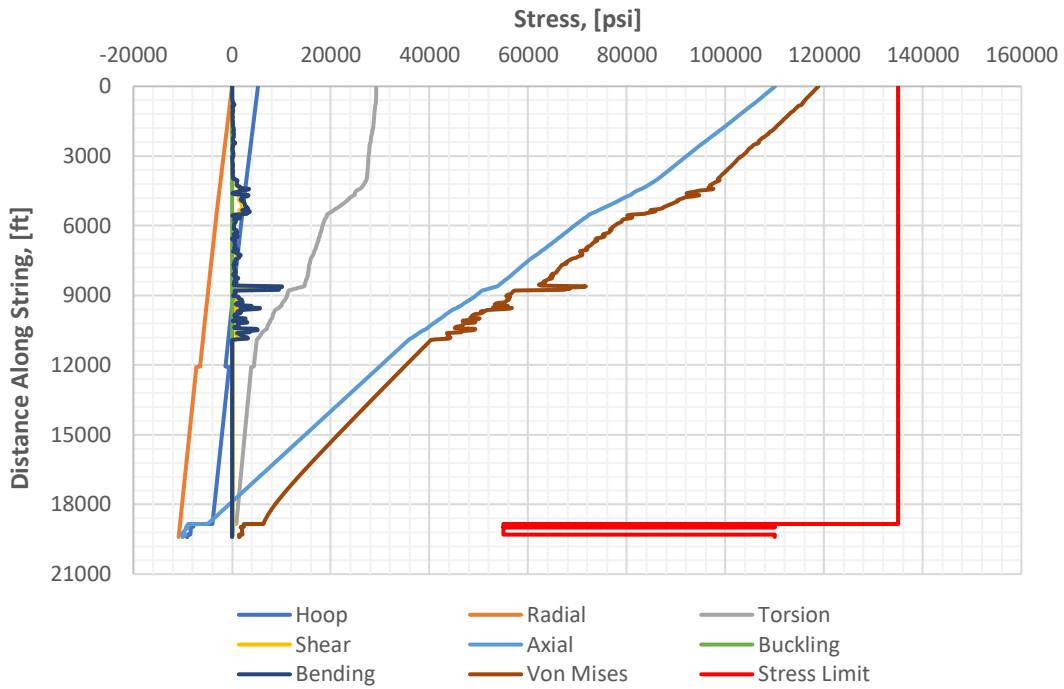


Figure G. 18: Stress trip out plot for REF + 0.13 g Si

Stress Trip In Plot

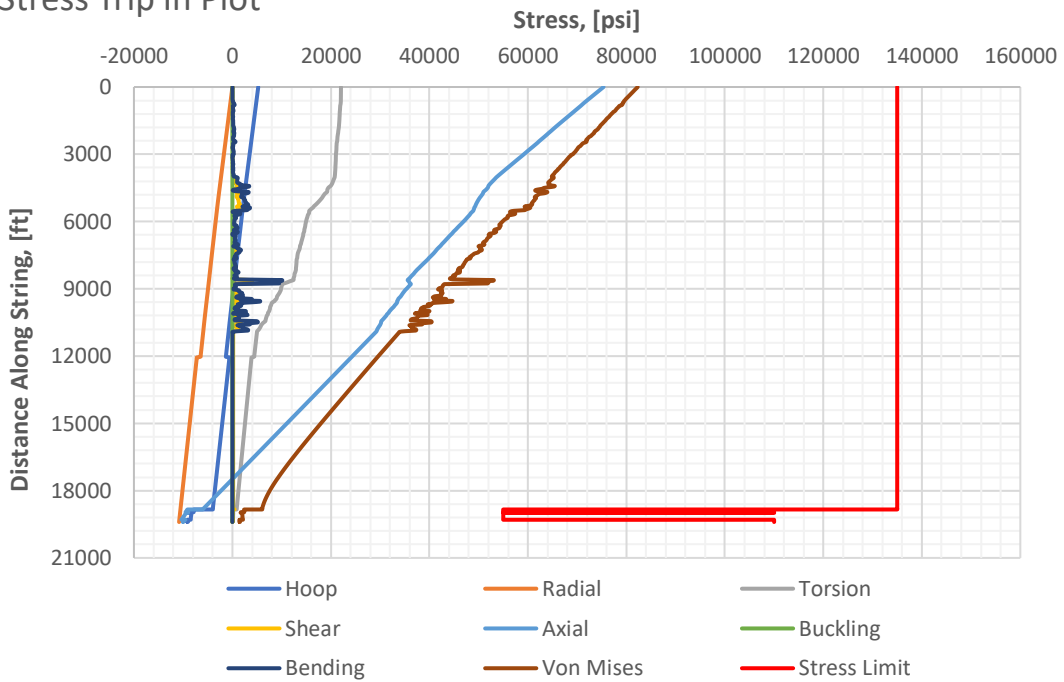


Figure G. 19: Stress trip in plot for REF + 0.13 g Si

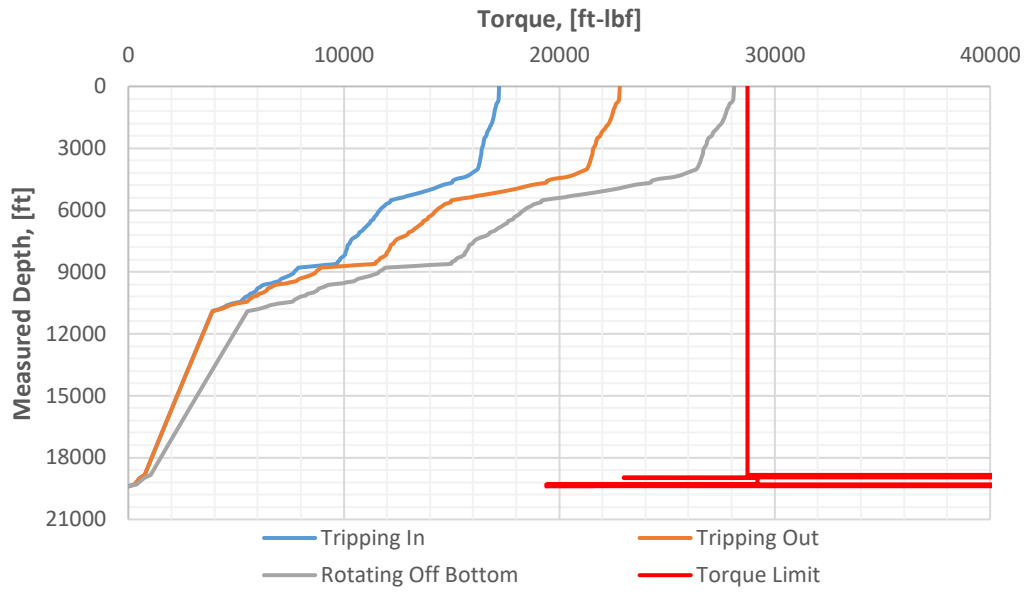


Figure G. 20: Torque plot for REF + 0.13 g Si

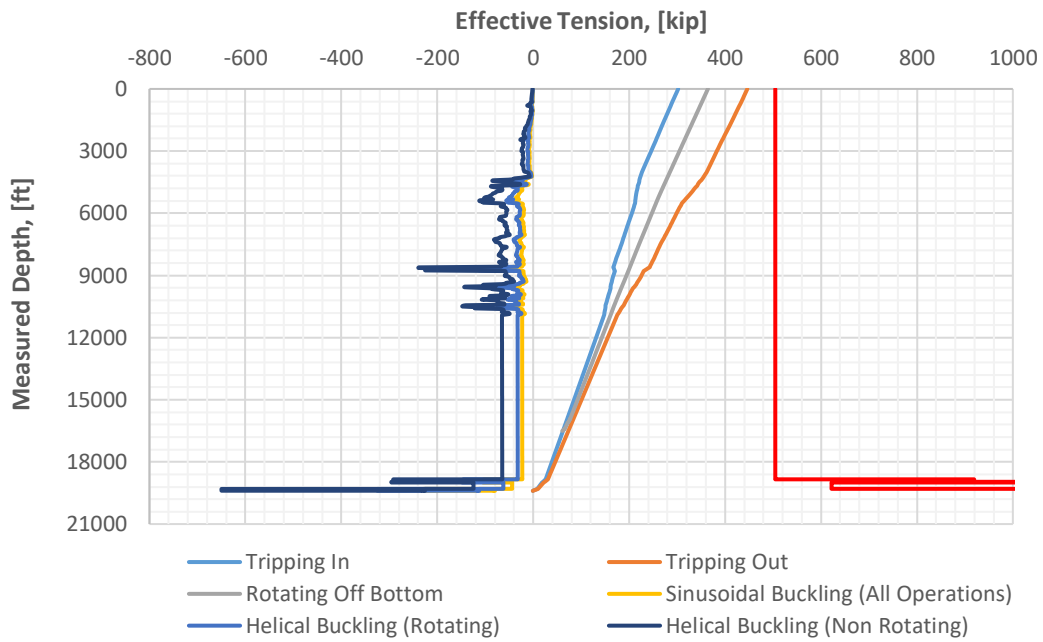


Figure G. 21: Effective tension plot for REF + 0.13 g Si

T & D Plots - Reference Fluid Containing 0.07 g Al₂O₃

Stress Trip Out Plot

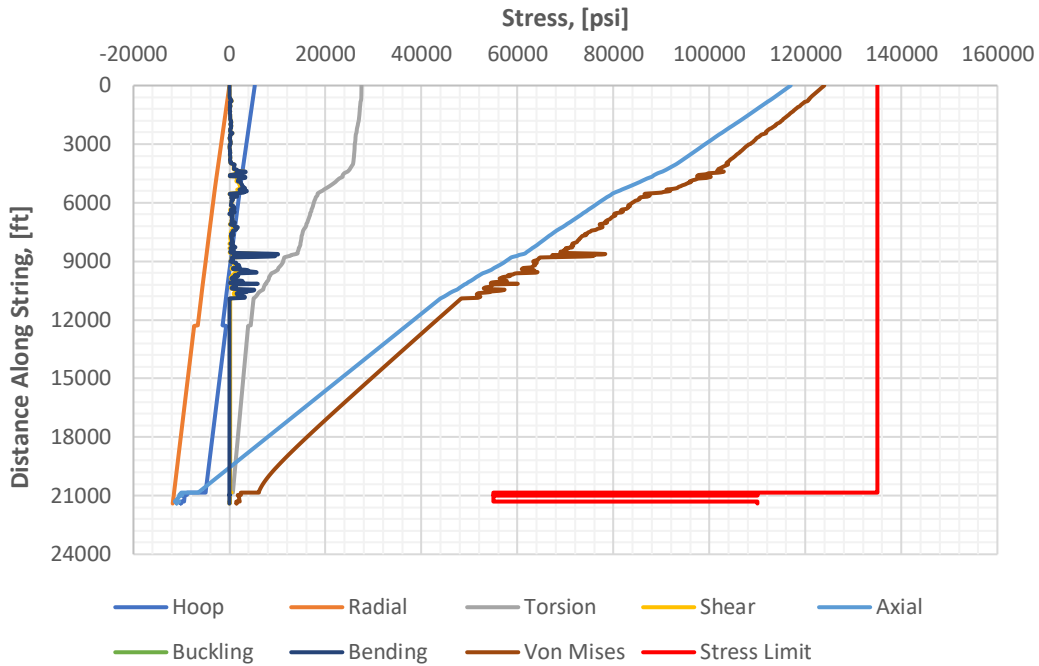


Figure G. 22: Stress trip out plot for REF + 0.07 g Al

Stress Trip In Plot

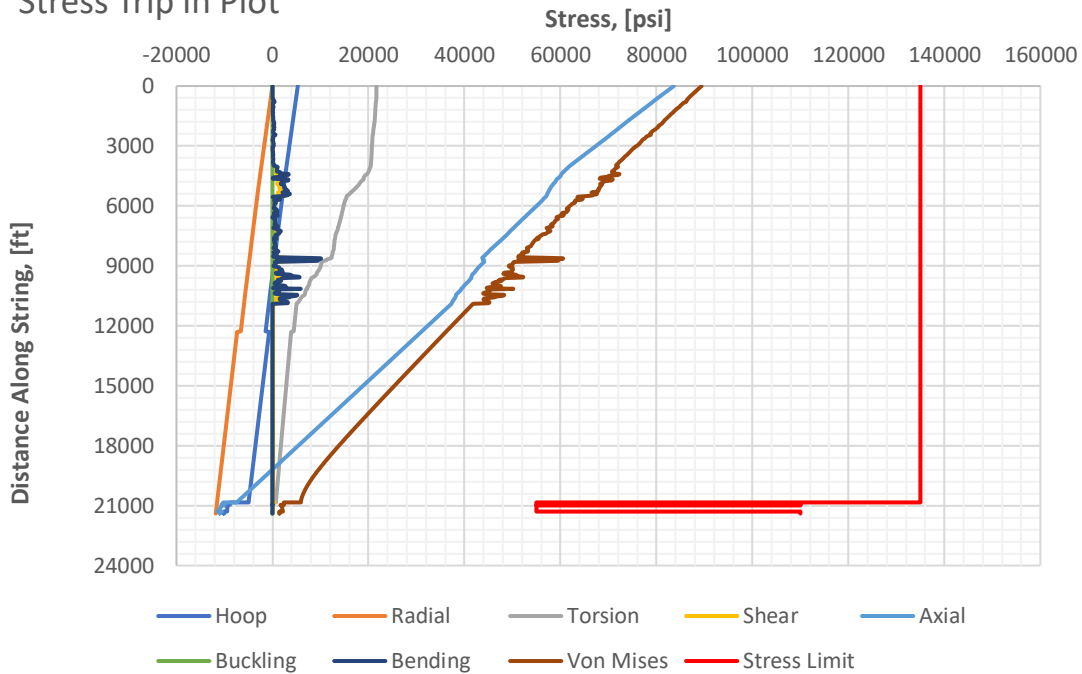


Figure G. 23: Stress trip in plot for REF + 0.07 g Al

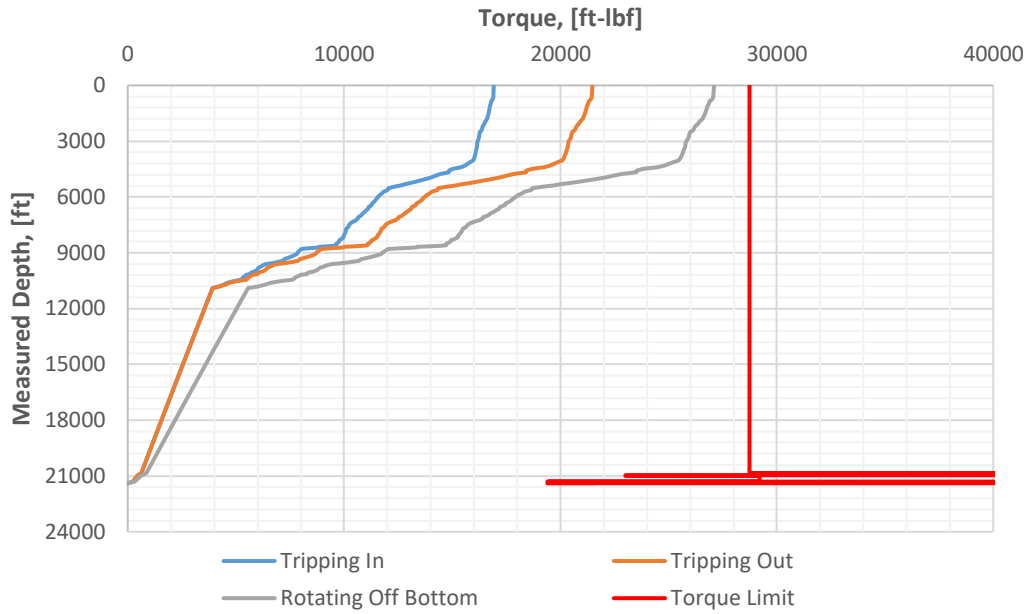


Figure G. 24: Torque plot for REF + 0.07 g Al

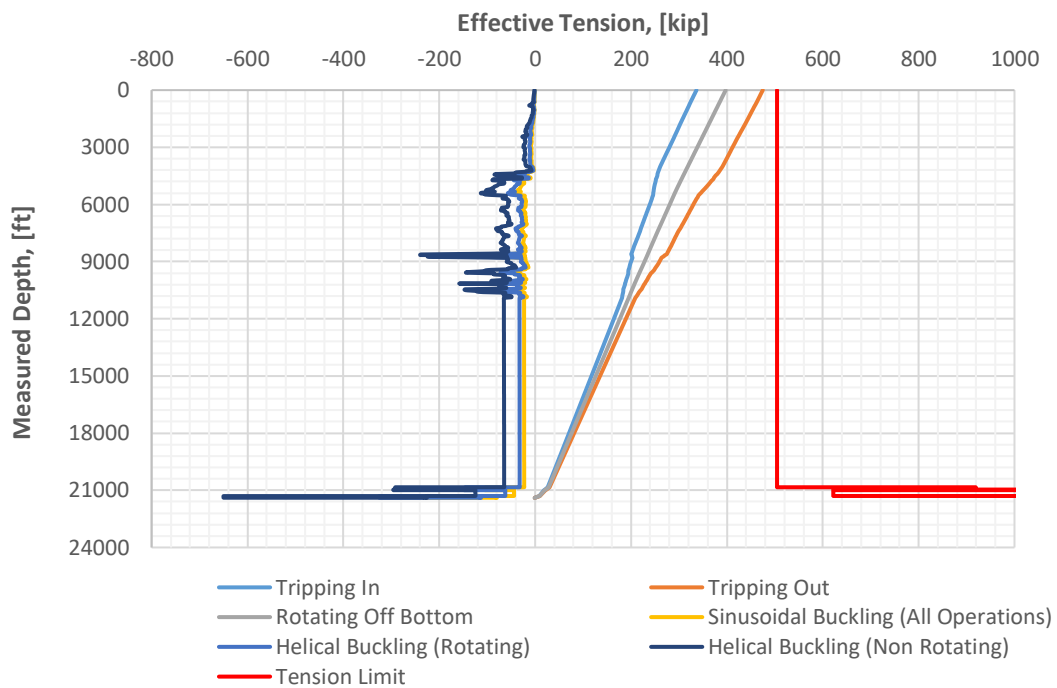


Figure G. 25: Effective tension plot for REF + 0.07 g Al

APPENDIX H – SEM PICTURES OF FILTER CAKES

In this section, all SEM pictures of the of the REF and REF + 0.07 g MWCNT-COOH filter cakes are presented. As a reminder, the best performing flat rheology system, which contains 0.08 g carbopol, is referred to as the reference fluid. The notations of short- and long-time aging indicate that the samples have been stored for a few days and ~48 days prior to generating the filter cakes at room temperature and ambient pressure. When examining SEM pictures, brighter and darker colors represent heavier and lighter elements, respectively.

Reference Fluid (Short-Time Aging)

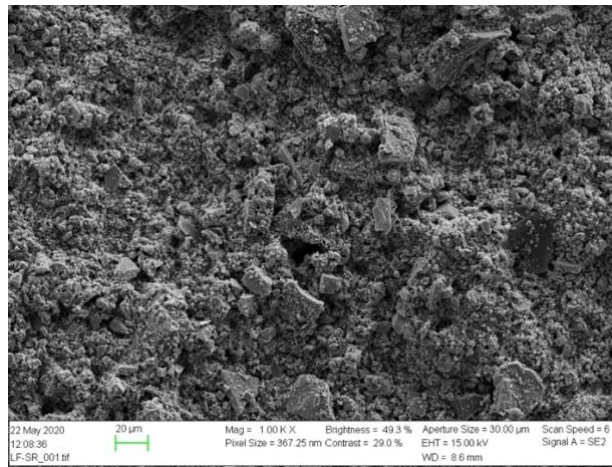


Figure H. 1: SEM picture at 20 µm magnification of filter cake (REF system, short-time)

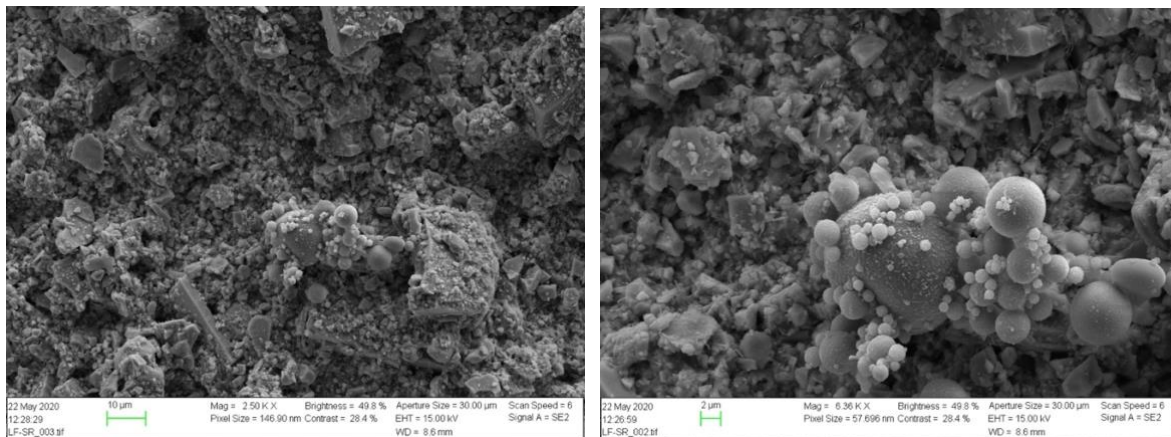


Figure H. 2: SEM picture at 10 µm (left) and 2 µm (right) magnification of location 1 (REF system, short-time)

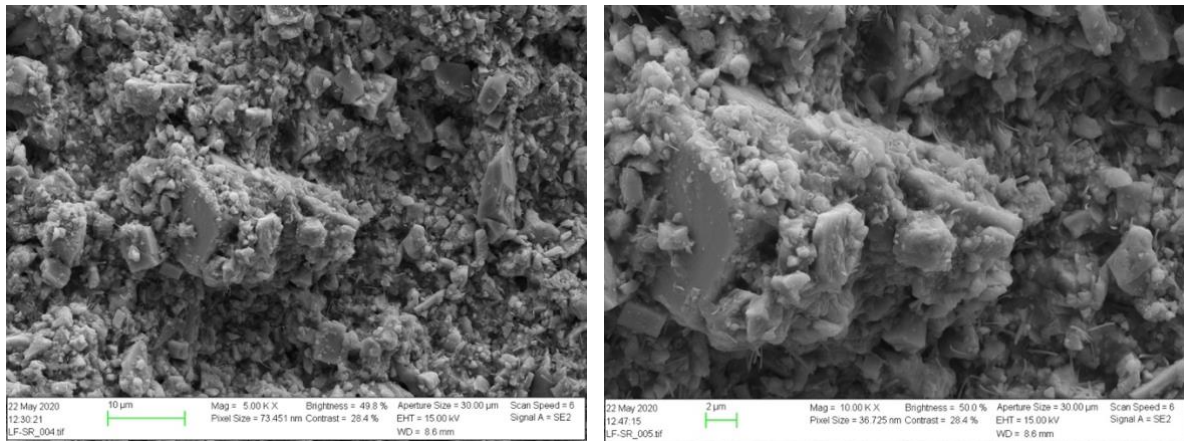


Figure H. 3: SEM picture at 10 μm (left) and 2 μm (right) magnification of location 2 (REF system, short-time)

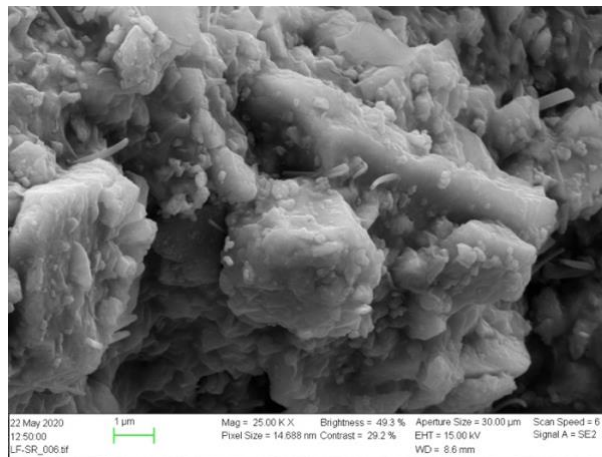


Figure H. 4: SEM picture at 1 μm magnification of location 2 (REF system, short-time)

Reference Fluid (Long-Time Aging)

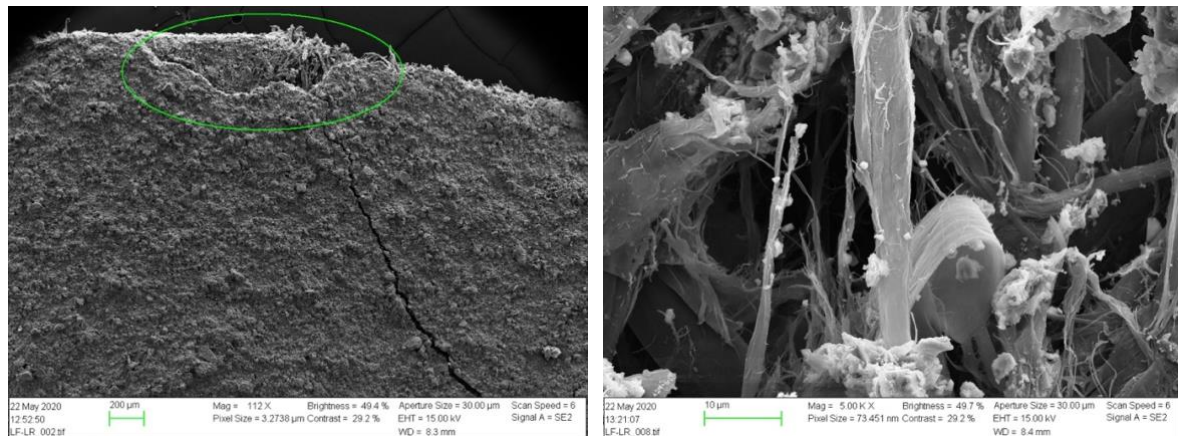


Figure H. 5: SEM picture at 200 μm (left) and 10 μm (right) magnification of the edge of the filter cake (REF system, long-time)

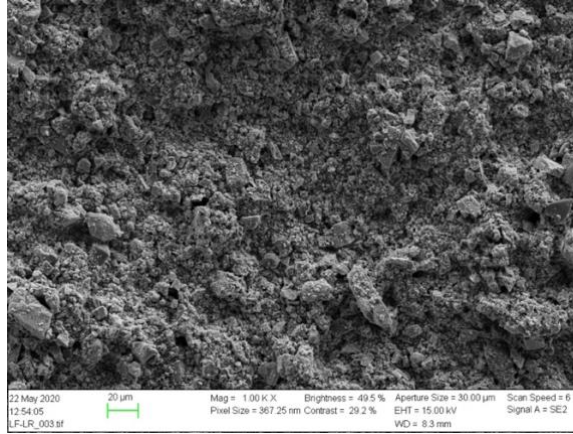


Figure J. 1: SEM picture at 20 μm magnification of filter cake (REF system, long-time)

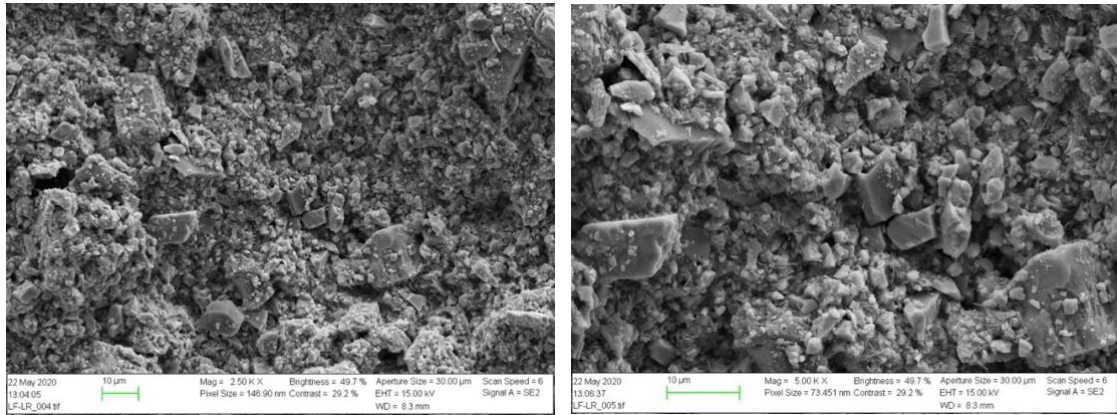


Figure H. 6: SEM picture at 10 μm magnification of location 1, Mag = 2.50 K X (left) and Mag = 5.00 K X (right) (REF system, long-time)

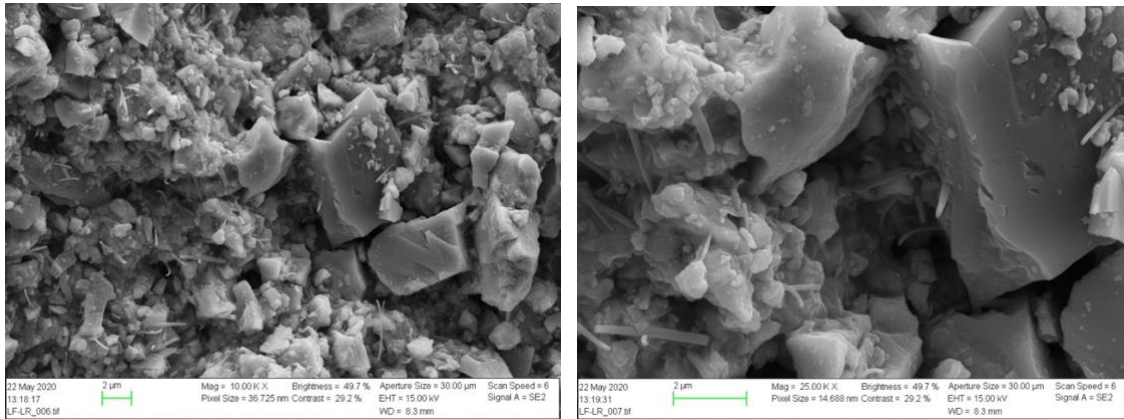


Figure H. 7: SEM picture at 2 μm magnification of location 1, Mag = 10.00 K X (left) and Mag = 25.00 K X (right), (REF system, long-time)

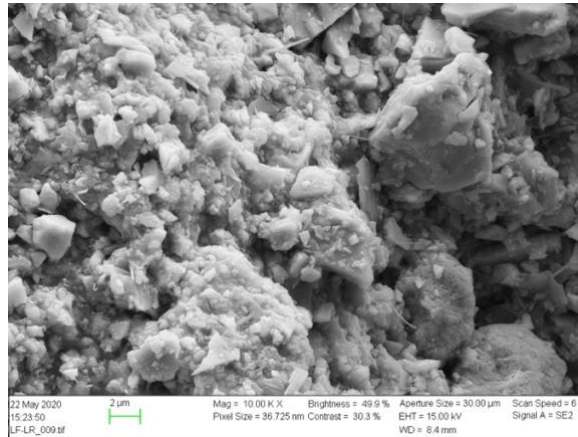


Figure H. 8: SEM picture at 2 μm magnification of location 2 (REF system, long-time)

Reference Fluid Containing 0.07 g Multi-Walled Carbon Nanotube (Short-Time Aging)

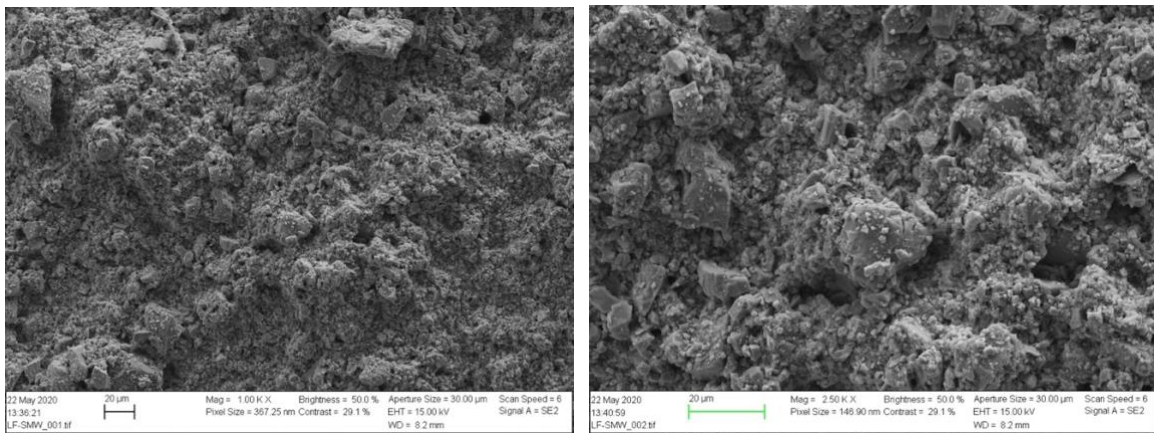


Figure H. 9: SEM picture at 20 μm magnification of filter cake, Mag = 1.00 K X (left) and Mag = 2.50 K X (right), (REF+0.07 g MW system, short-time)

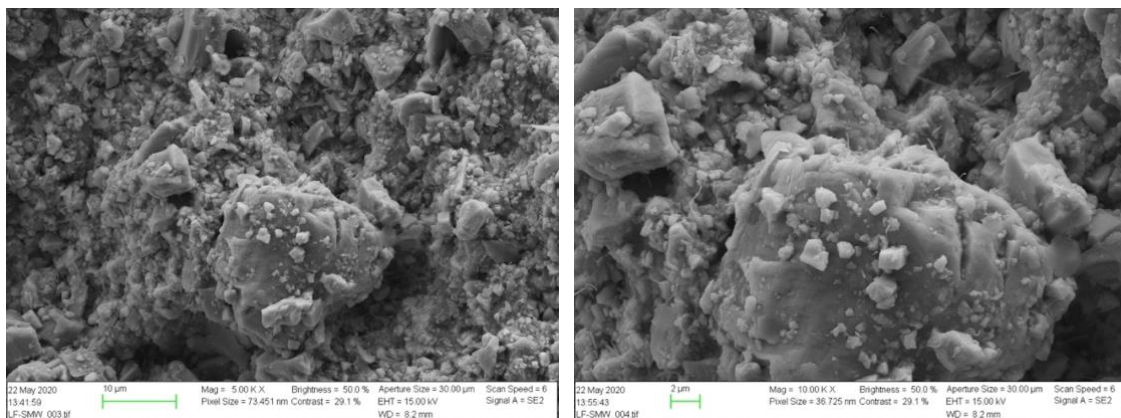


Figure H. 10: SEM picture at 10 μm (left) and 2 μm (right) magnification of location 1 (REF+0.07 g MW system, short-time)

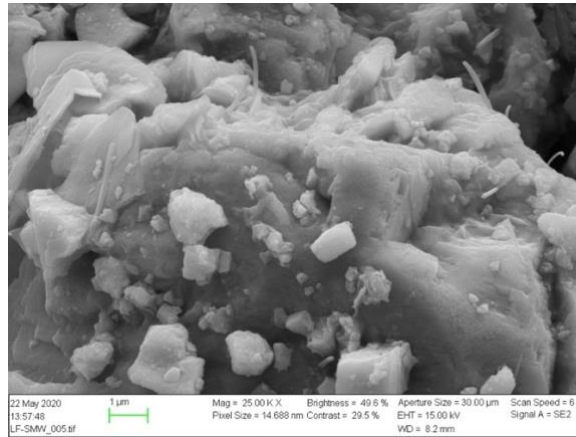


Figure H. 11: SEM picture at 1 μm magnification of location 1 (REF+0.07 g MW system, short-time)

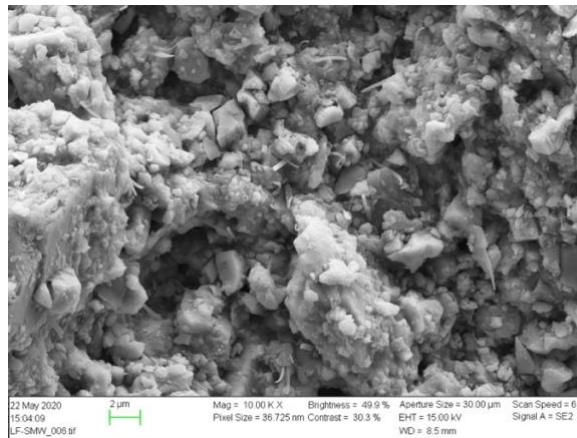


Figure H. 12: SEM picture at 2 μm magnification of location 2 (REF+0.07 g MW system, short-time)

Reference Fluid Containing 0.07 g Multi-Walled Carbon Nanotube (Long-Time Aging)

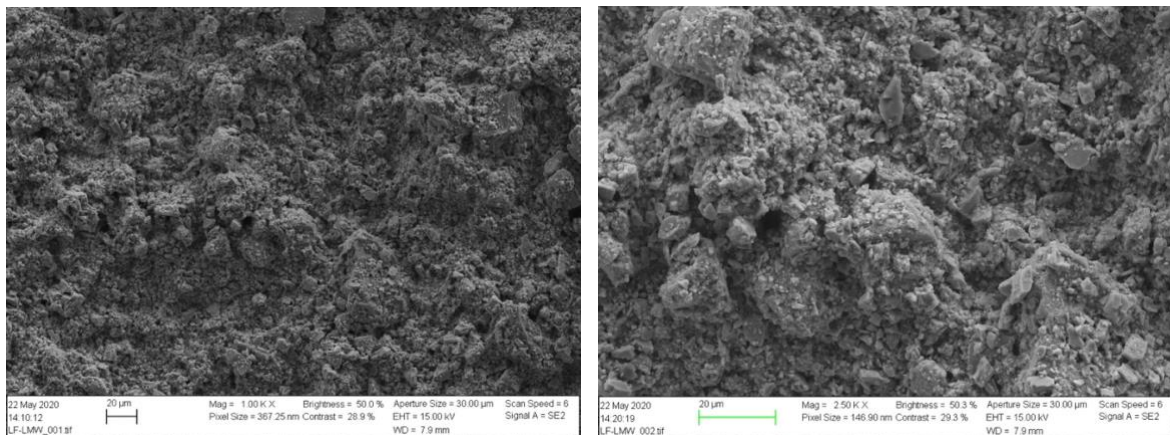


Figure H. 13: SEM picture at 20 μm magnification of filter cake, Mag = 1.00 K X (left) and Mag = 2.50 K X (right), (REF+0.07 g MW system, long-time)

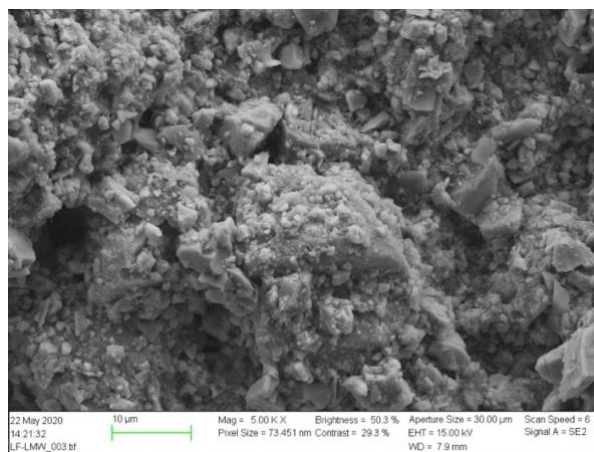


Figure H. 14: SEM picture at 10 µm magnification of location 1 (REF+0.07 g MW system, long-time)

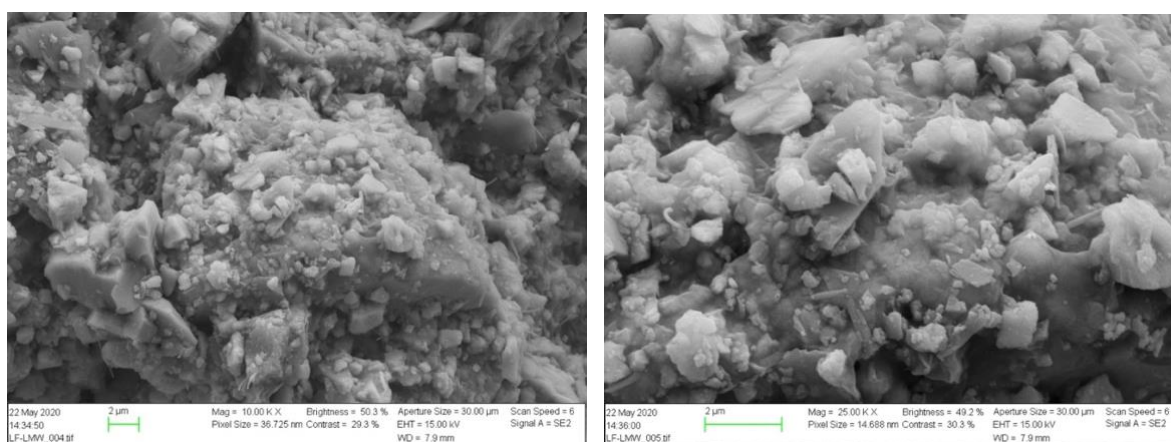


Figure H. 15: SEM picture at 2 µm magnification of location 1, Mag = 10.00 K X (left) and Mag = 10.00 K X (right), (REF+0.07 g MW system, long-time)

APPENDIX I – SEM ELEMENT ANALYSIS OF FILTER CAKE SURFACE AREA

Reference Fluid (Short-Time Aging)

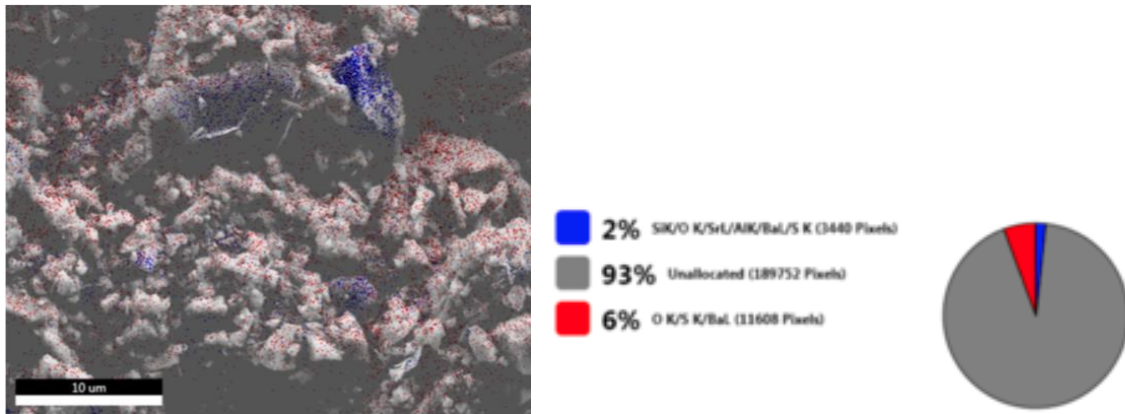
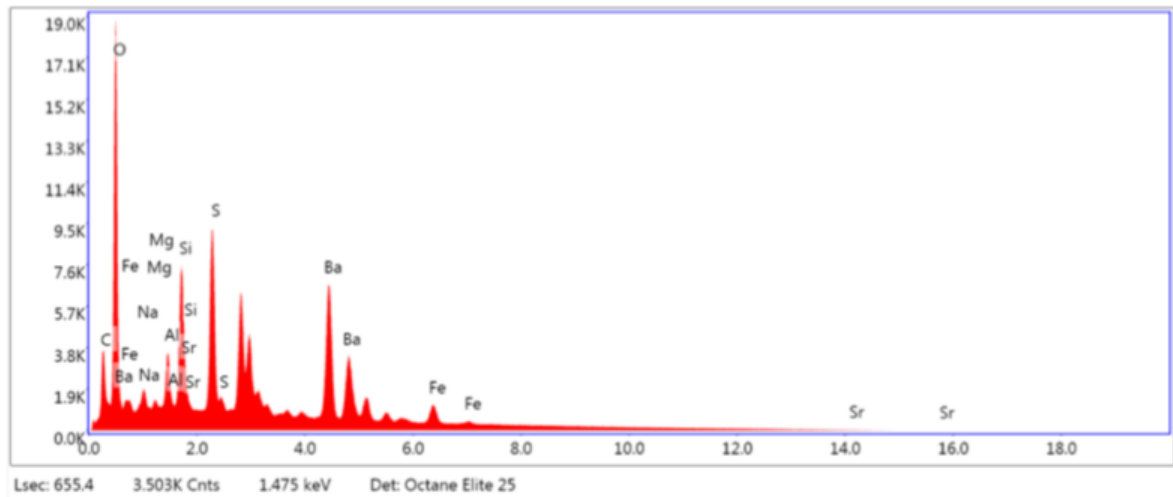


Figure I. 1: SEM picture and element analysis of surface at 10 μm magnification (REF system, short-time)

kV: 15 Mag: 5000 Takeoff: 35.2 Live Time(s): 655.4 Amp Time(μs): 7.68 Resolution:(eV) 132.4

Sum Spectrum



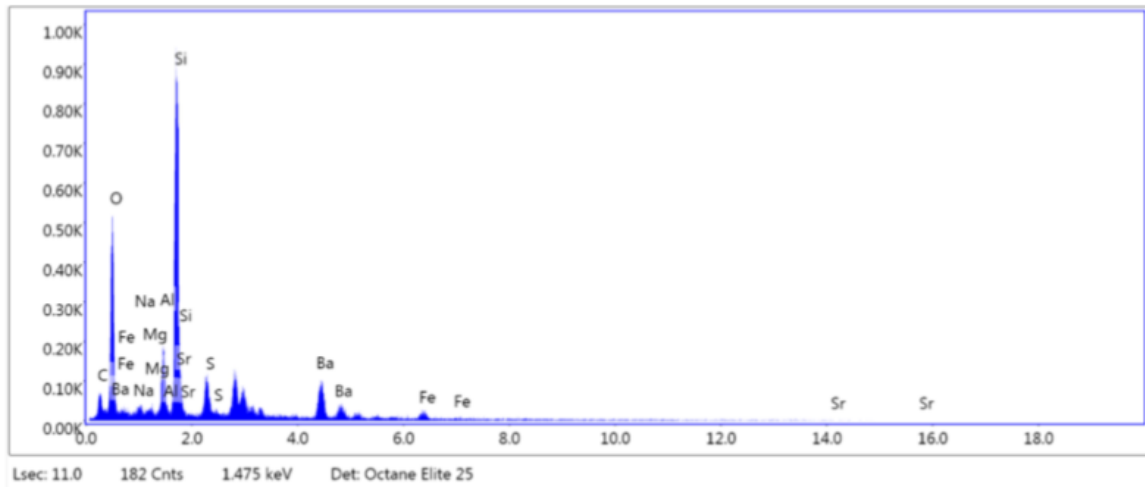
eZAF Smart Quant Results with SEC (BCNOF_2017-09-14)

Element	Weight %	Atomic %	Net Int.	Error %	Kratio	Z	A	F
CK	18.41	40.94	82.90	9.27	0.0614	1.2560	0.2657	1.0000
OK	19.87	33.17	403.60	7.82	0.0881	1.2023	0.3687	1.0000
NaK	1.47	1.71	26.80	11.61	0.0056	1.0926	0.3459	1.0011
MgK	0.60	0.66	16.40	14.12	0.0029	1.1116	0.4294	1.0021
AlK	2.28	2.26	74.40	6.99	0.0134	1.0708	0.5440	1.0038
SiK	5.07	4.83	192.80	5.48	0.0362	1.0946	0.6481	1.0059
SrL	0.36	0.11	6.70	20.72	0.0024	0.8231	0.8056	1.0011
SK	7.88	6.57	266.10	3.94	0.0682	1.0727	0.7960	1.0134
BaL	39.84	7.75	247.80	2.97	0.3010	0.7233	1.0437	1.0008
FeK	4.21	2.02	37.40	6.09	0.0376	0.9240	0.9528	1.0148

Figure I. 2: Element analysis: Sum spectrum (REF system, short-time)

kV: 15 Mag: 5000 Takeoff: 35.2 Live Time(s): 11 Amp Time(μs): 7.68 Resolution:(eV) 132.4

Phase: **SiK/O K/SrL/AIK/BaL/S K**



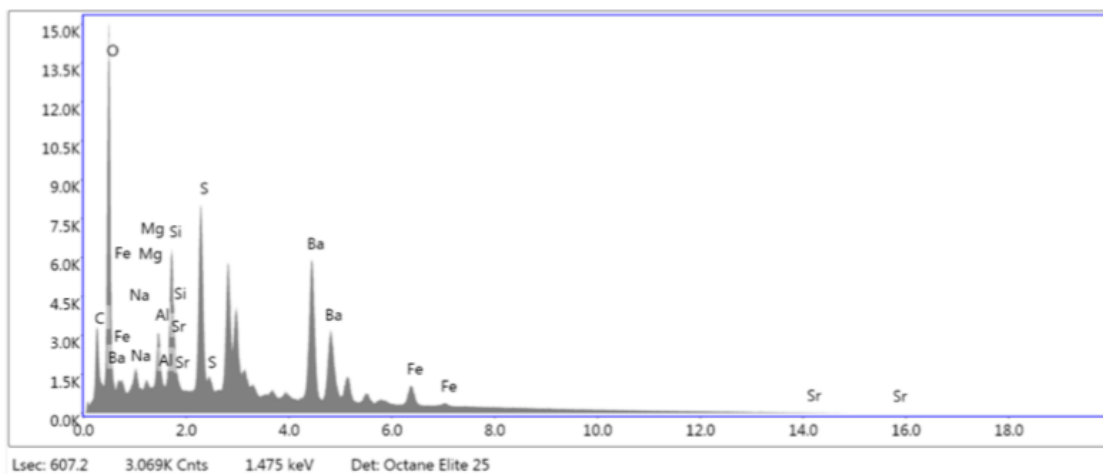
eZAF Smart Quant Results with SEC (BCNOF_2017-09-14)

Element	Weight %	Atomic %	Net Int.	Error %	Kratio	Z	A	F
CK	19.13	36.34	91.40	14.74	0.0440	1.1806	0.1948	1.0000
OK	22.84	32.57	627.40	9.43	0.0890	1.1284	0.3453	1.0000
NaK	0.97	0.96	31.50	27.47	0.0043	1.0234	0.4281	1.0013
MgK	0.60	0.56	29.40	26.92	0.0033	1.0405	0.5342	1.0025
AlK	4.53	3.83	254.40	8.14	0.0297	1.0017	0.6515	1.0042
SiK	22.02	17.89	1353.40	5.22	0.1652	1.0233	0.7304	1.0039
SrL	0.05	0.01	1.40	99.99	0.0003	0.7693	0.8614	1.0000
SK	3.60	2.56	170.70	10.91	0.0284	1.0016	0.7805	1.0096
BaL	22.52	3.74	201.50	14.69	0.1591	0.6720	1.0504	1.0008
FeK	3.72	1.52	48.50	23.62	0.0317	0.8555	0.9752	1.0204

Figure I. 3: Element analysis: SiK/O K/SrL/AIK/BaL/S K phase (REF system, short-time)

kV: 15 Mag: 5000 Takeoff: 35.2 Live Time(s): 607.2 Amp Time(μs): 7.68 Resolution:(eV) 132.4

Phase: Unallocated



eZAF Smart Quant Results with SEC (BCNOF_2017-09-14)

Element	Weight %	Atomic %	Net Int.	Error %	Kratio	Z	A	F
C K	18.92	42.36	81.50	9.36	0.0638	1.2593	0.2677	1.0000
O K	18.77	31.55	358.20	7.89	0.0826	1.2055	0.3648	1.0000
NaK	1.52	1.77	26.10	11.99	0.0057	1.0956	0.3445	1.0011
MgK	0.61	0.68	15.80	15.24	0.0029	1.1147	0.4272	1.0021
AlK	2.29	2.28	70.50	7.15	0.0134	1.0737	0.5414	1.0038
SiK	4.85	4.64	174.30	5.54	0.0346	1.0977	0.6457	1.0059
SrL	0.43	0.13	7.50	19.24	0.0029	0.8255	0.8033	1.0011
S K	7.81	6.55	250.00	4.00	0.0677	1.0757	0.7947	1.0135
BaL	40.36	7.90	238.30	2.98	0.3058	0.7255	1.0434	1.0008
FeK	4.43	2.13	37.40	6.22	0.0397	0.9269	0.9521	1.0146

Figure I. 4: Element analysis: Unallocated phase (REF system, short-time)

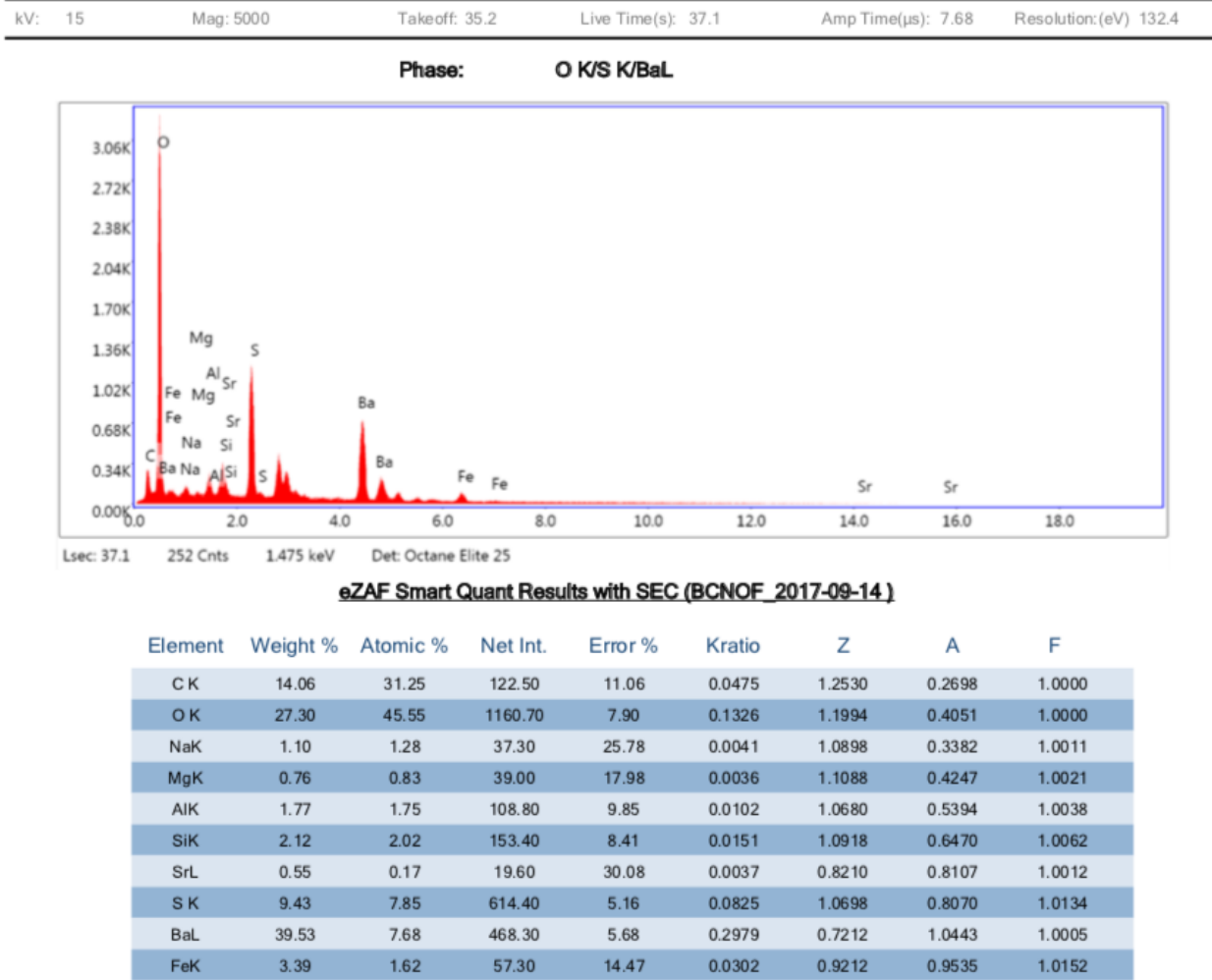


Figure I. 5: Element analysis: O K/S K/BaL phase (REF system, short-time)

Reference Fluid (Long-Time Aging)

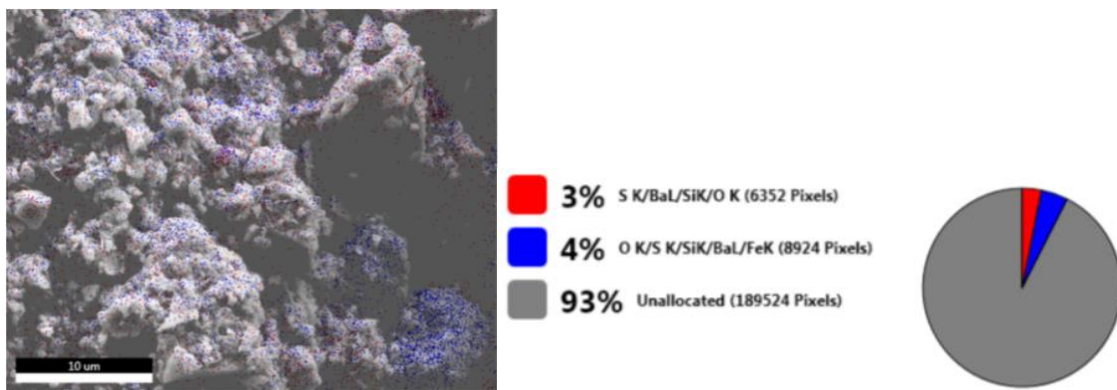
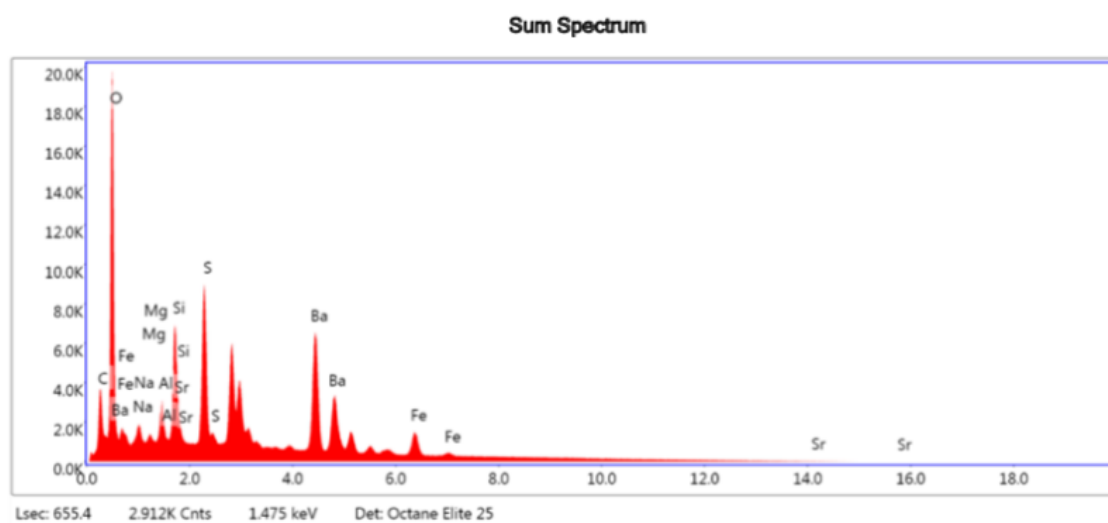


Figure I. 6: SEM picture and element analysis of surface at 10 μm (REF system, long-time)

kV: 15 Mag: 5000 Takeoff: 34.9 Live Time(s): 655.4 Amp Time(μs): 7.68 Resolution:(eV) 132.4



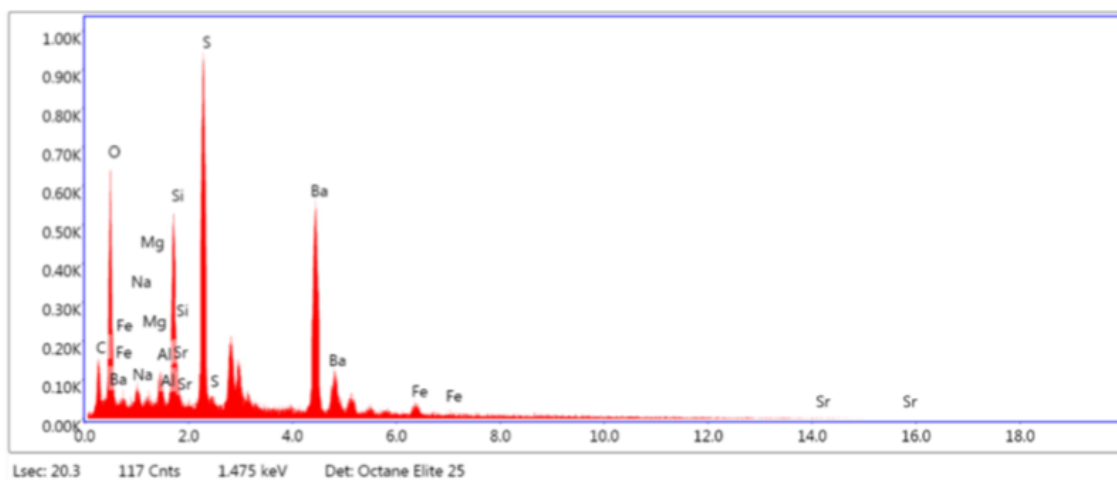
eZAF Smart Quant Results with SEC (BCNOF_2017-09-14.)

Element	Weight %	Atomic %	Net Int.	Error %	Kratio	Z	A	F
C K	18.26	40.28	86.10	9.19	0.0622	1.2524	0.2722	1.0000
O K	20.93	34.66	441.50	7.79	0.0938	1.1988	0.3739	1.0000
NaK	1.43	1.64	26.20	12.96	0.0053	1.0893	0.3404	1.0011
MgK	0.62	0.67	17.20	14.06	0.0029	1.1083	0.4259	1.0021
AlK	1.85	1.82	61.60	7.35	0.0107	1.0675	0.5411	1.0038
SiK	4.65	4.39	181.40	5.55	0.0331	1.0913	0.6480	1.0059
SrL	0.21	0.06	4.00	35.56	0.0014	0.8206	0.8074	1.0011
S K	7.57	6.25	263.10	3.99	0.0655	1.0694	0.7989	1.0135
BaL	38.69	7.47	247.40	3.04	0.2920	0.7209	1.0454	1.0013
FeK	5.80	2.75	52.90	5.17	0.0517	0.9208	0.9544	1.0145

Figure I. 7: Element analysis: Sum spectrum (REF system, long-time)

kV: 15 Mag: 5000 Takeoff: 34.9 Live Time(s): 20.3 Amp Time(μs): 7.68 Resolution:(eV) 132.4

Phase: S K/BaL/SiK/O K



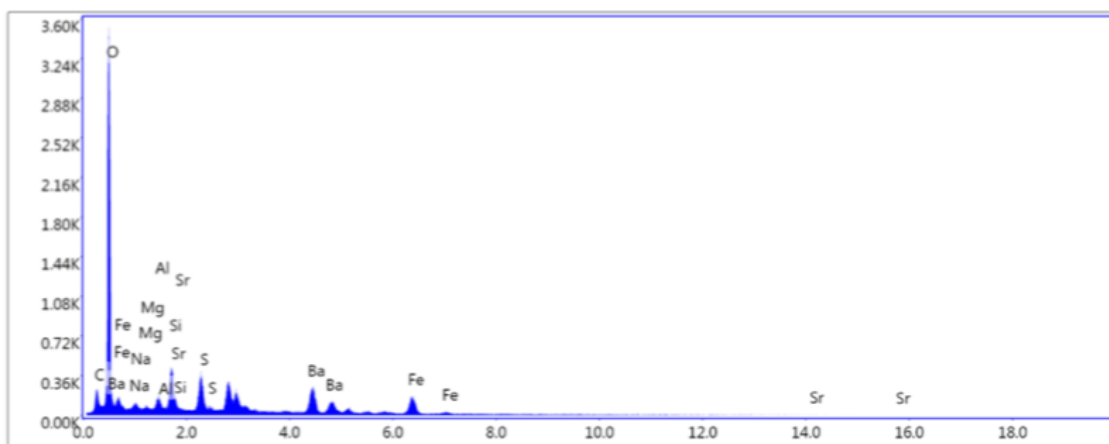
eZAF Smart Quant Results with SEC (BCNOF_2017-09-14)

Element	Weight %	Atomic %	Net Int.	Error %	Kratio	Z	A	F
C K	14.96	40.11	111.60	12.61	0.0432	1.3158	0.2195	1.0000
O K	11.42	22.98	441.40	9.35	0.0502	1.2601	0.3491	1.0000
NaK	1.33	1.86	46.50	20.86	0.0050	1.1459	0.3305	1.0011
MgK	0.68	0.90	35.10	29.10	0.0032	1.1661	0.4033	1.0022
AlK	1.46	1.75	90.50	12.16	0.0085	1.1236	0.5129	1.0040
SiK	5.67	6.50	417.00	7.17	0.0408	1.1490	0.6217	1.0062
SrL	0.40	0.15	14.20	64.82	0.0027	0.8641	0.7745	1.0013
S K	12.97	13.03	858.00	5.07	0.1144	1.1266	0.7729	1.0132
BaL	48.99	11.49	608.80	6.40	0.3848	0.7619	1.0310	0.9999
FeK	2.13	1.23	37.80	22.52	0.0197	0.9756	0.9370	1.0139

Figure I. 8: Element analysis: S K/BaL/SiK/O K phase (REF system, long-time)

kV: 15 Mag: 5000 Takeoff: 34.9 Live Time(s): 28.6 Amp Time(μs): 7.68 Resolution:(eV) 132.4

Phase: O K/S K/SiK/BaL/FeK



Lsec: 28.6 167 Cnts 1.475 keV Det: Octane Elite 25

eZAF Smart Quant Results with SEC (BCNOF_2017-09-14)

Element	Weight %	Atomic %	Net Int.	Error %	Kratio	Z	A	F
C K	14.65	26.90	121.00	11.18	0.0525	1.1761	0.3047	1.0000
O K	41.00	56.50	1642.00	7.39	0.2093	1.1241	0.4542	1.0000
NaK	0.71	0.68	20.90	66.34	0.0025	1.0195	0.3508	1.0010
MgK	0.66	0.60	31.30	22.52	0.0032	1.0366	0.4645	1.0019
AlK	1.52	1.24	85.40	11.38	0.0089	0.9979	0.5890	1.0034
SiK	4.08	3.20	266.10	7.09	0.0292	1.0195	0.6969	1.0051
SrL	0.03	0.01	0.90	99.99	0.0002	0.7665	0.8655	1.0005
S K	4.32	2.97	245.20	6.49	0.0366	0.9979	0.8394	1.0122
BaL	21.97	3.53	221.50	9.66	0.1569	0.6696	1.0615	1.0046
FeK	11.06	4.37	160.30	7.46	0.0939	0.8525	0.9793	1.0166

Figure I. 9: Element analysis: O K/S K/SiK/BaL/FeK phase (REF system, long-time)

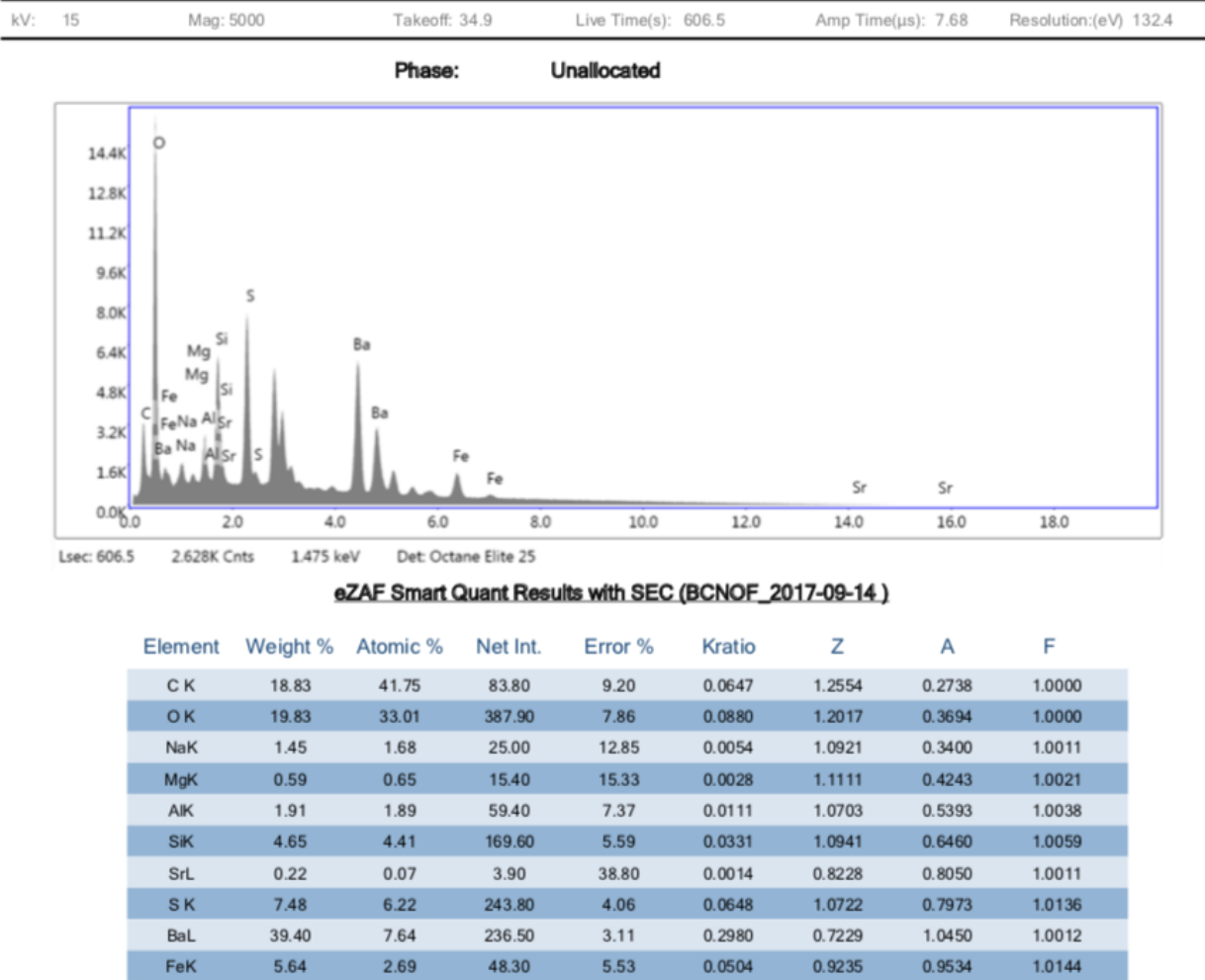


Figure I. 10: Element analysis: Unallocated phase (REF system, long-time)

Reference Fluid Containing 0.07 g Multi-Walled Carbon Nanotube (Short-Time Aging)

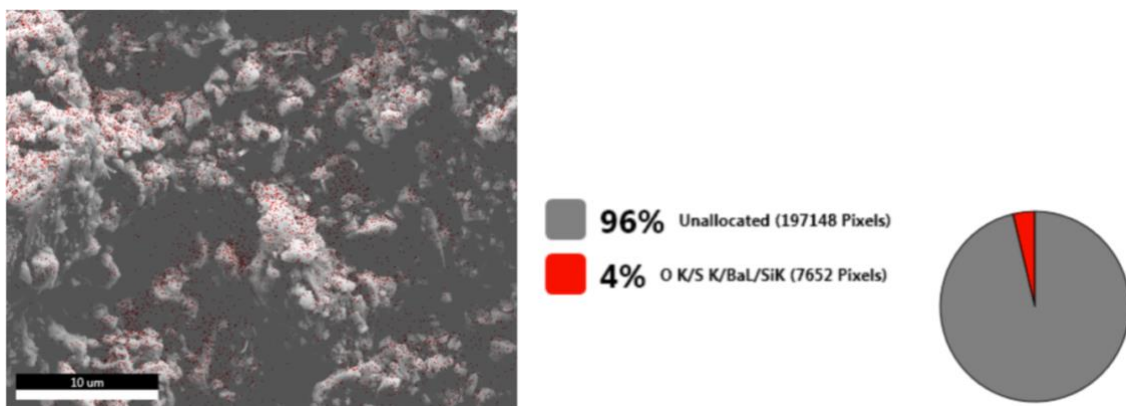
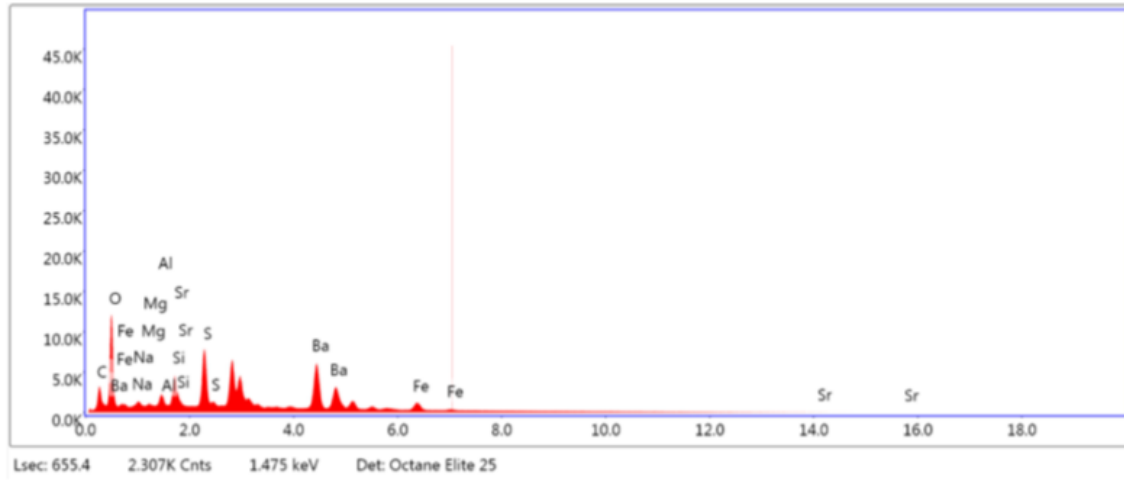


Figure I. 11: SEM picture and element analysis of surface at 10 μm (REF + 0.07 g MW system, short-time)

kV: 15 Mag: 5000 Takeoff: 35 Live Time(s): 655.4 Amp Time(μs): 7.68 Resolution:(eV) 132.4

Sum Spectrum



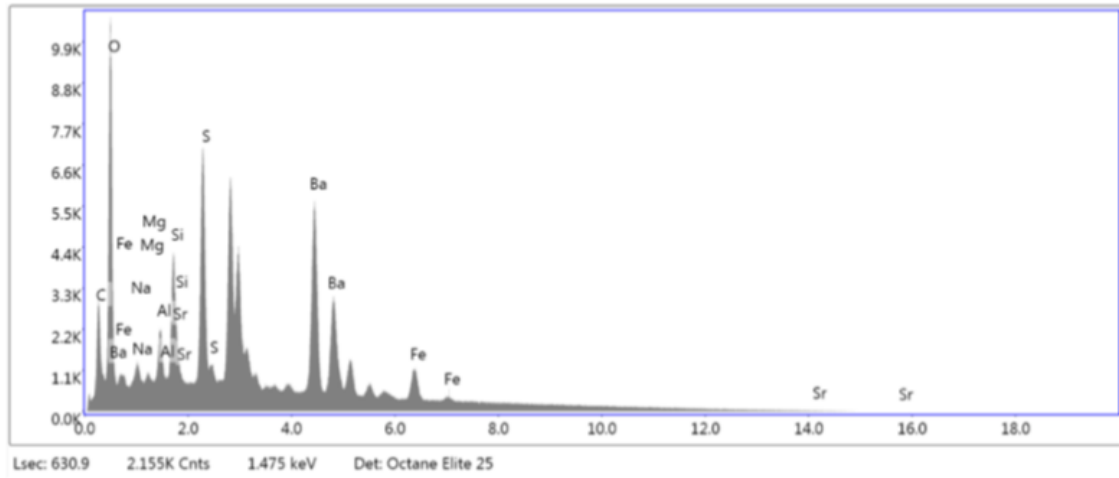
eZAF Smart Quant Results with SEC (BCNOF_2017-09-14)

Element	Weight %	Atomic %	Net Int.	Error %	Kratio	Z	A	F
C K	18.99	44.98	72.30	9.24	0.0664	1.2813	0.2728	1.0000
O K	15.58	27.71	254.50	7.99	0.0686	1.2269	0.3591	1.0000
NaK	1.39	1.71	19.90	12.30	0.0051	1.1154	0.3309	1.0011
MgK	0.67	0.78	14.50	14.66	0.0031	1.1349	0.4108	1.0021
AlK	1.87	1.97	48.40	7.57	0.0107	1.0934	0.5234	1.0038
SiK	3.47	3.52	106.30	5.88	0.0247	1.1179	0.6309	1.0061
SrL	0.87	0.28	13.00	12.07	0.0058	0.8407	0.7895	1.0012
S K	8.06	7.15	222.60	3.99	0.0704	1.0959	0.7872	1.0137
BaL	43.44	9.00	223.30	2.86	0.3349	0.7400	1.0408	1.0011
FeK	5.68	2.89	41.60	3.75	0.0516	0.9463	0.9471	1.0138

Figure I. 12: Element analysis: Sum spectrum (REF + 0.07 g MW system, short-time)

kV: 15 Mag: 5000 Takeoff: 35 Live Time(s): 630.9 Amp Time(μs): 7.68 Resolution:(eV) 132.4

Phase: Unallocated



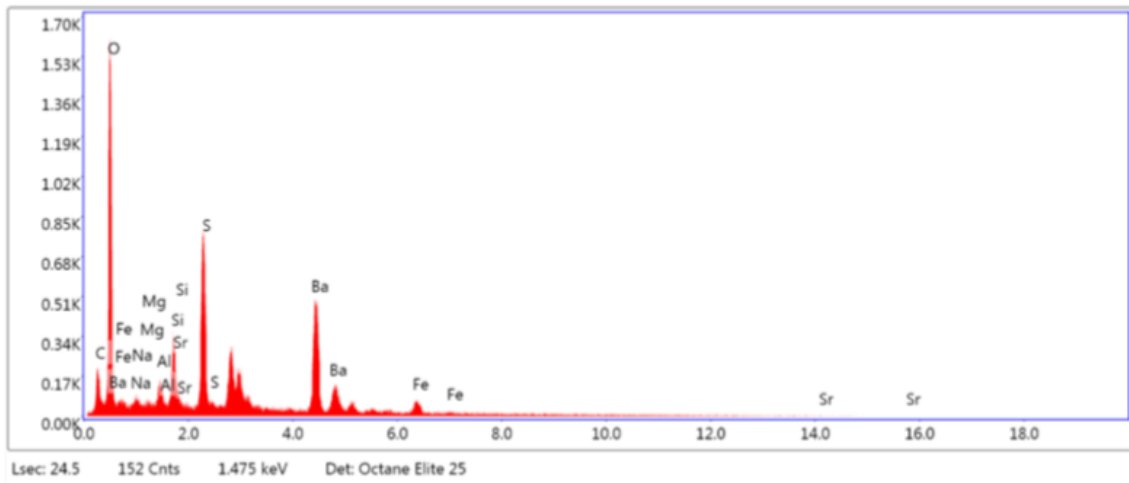
eZAF Smart Quant Results with SEC (BCNOF_2017-09-14)

Element	Weight %	Atomic %	Net Int.	Error %	Kratio	Z	A	F
C K	19.58	46.07	75.80	9.21	0.0687	1.2795	0.2743	1.0000
O K	15.12	26.71	247.70	8.08	0.0660	1.2251	0.3566	1.0000
NaK	1.39	1.71	20.30	12.34	0.0051	1.1137	0.3318	1.0011
MgK	0.71	0.82	15.50	13.69	0.0033	1.1333	0.4119	1.0021
AlK	1.92	2.01	50.30	7.58	0.0110	1.0918	0.5244	1.0038
SiK	3.58	3.61	110.80	5.88	0.0254	1.1163	0.6315	1.0061
SrL	0.72	0.23	11.00	13.79	0.0048	0.8395	0.7901	1.0012
S K	7.92	6.98	221.40	4.07	0.0692	1.0942	0.7881	1.0138
BaL	43.22	8.90	224.60	2.92	0.3328	0.7388	1.0412	1.0012
FeK	5.85	2.96	43.30	5.63	0.0531	0.9447	0.9476	1.0138

Figure I. 13: Element analysis: Unallocated phase (REF + 0.07 g MW system, short-time)

kV: 15 Mag: 5000 Takeoff: 35 Live Time(s): 24.5 Amp Time(μs): 7.68 Resolution:(eV) 132.4

Phase: O K/S K/BaL/SiK



eZAF Smart Quant Results with SEC (BCNOF_2017-09-14)

Element	Weight %	Atomic %	Net Int.	Error %	Kratio	Z	A	F
C K	15.73	36.34	130.90	11.47	0.0514	1.2675	0.2579	1.0000
O K	21.60	37.47	860.30	8.38	0.0994	1.2134	0.3791	1.0000
NaK	1.12	1.35	37.90	24.18	0.0042	1.1029	0.3367	1.0011
MgK	0.86	0.98	43.70	18.65	0.0040	1.1221	0.4201	1.0021
AlK	1.79	1.84	108.90	10.61	0.0103	1.0810	0.5330	1.0038
SiK	3.13	3.09	224.40	7.84	0.0223	1.1051	0.6405	1.0061
SrL	0.80	0.25	28.10	23.16	0.0053	0.8311	0.8014	1.0012
S K	9.70	8.40	625.60	4.88	0.0848	1.0831	0.7963	1.0133
BaL	41.42	8.37	491.10	6.70	0.3154	0.7307	1.0415	1.0006
FeK	3.85	1.91	65.30	15.23	0.0347	0.9339	0.9499	1.0147

Figure I. 14: Element analysis: O K/S K/BaL/SiK phase (REF + 0.07 g MW system, short-time)

Reference Fluid Containing 0.07 g Multi-Walled Carbon Nanotube (Long-Time Aging)

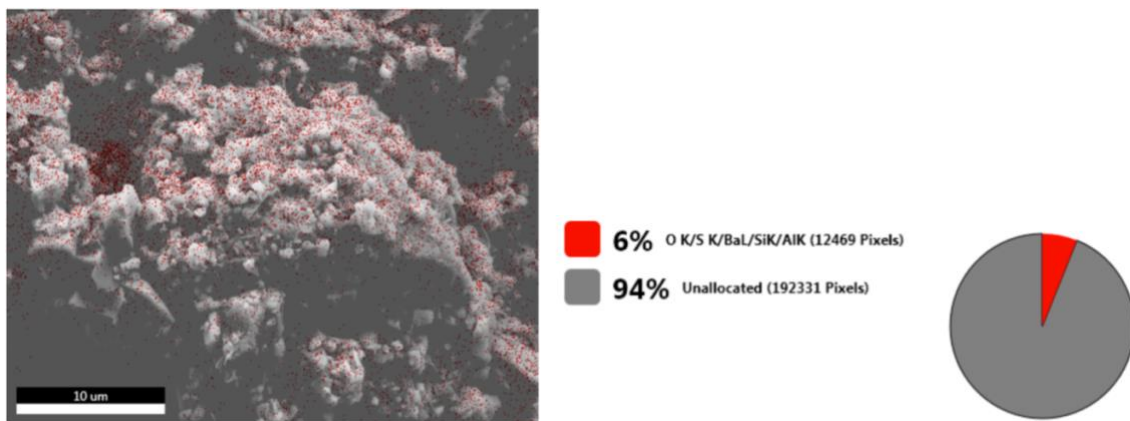
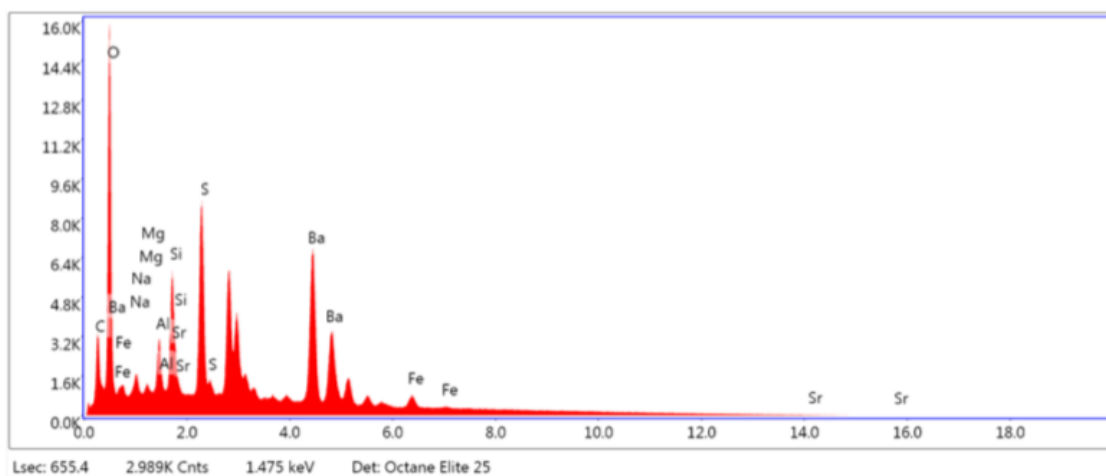


Figure I. 15: SEM picture and element analysis of surface at 10 μm (REF + 0.07 g MW system, long-time)

kV: 15 Mag: 5000 Takeoff: 34.2 Live Time(s): 655.4 Amp Time(μs): 7.68 Resolution:(eV) 132.4

Sum Spectrum



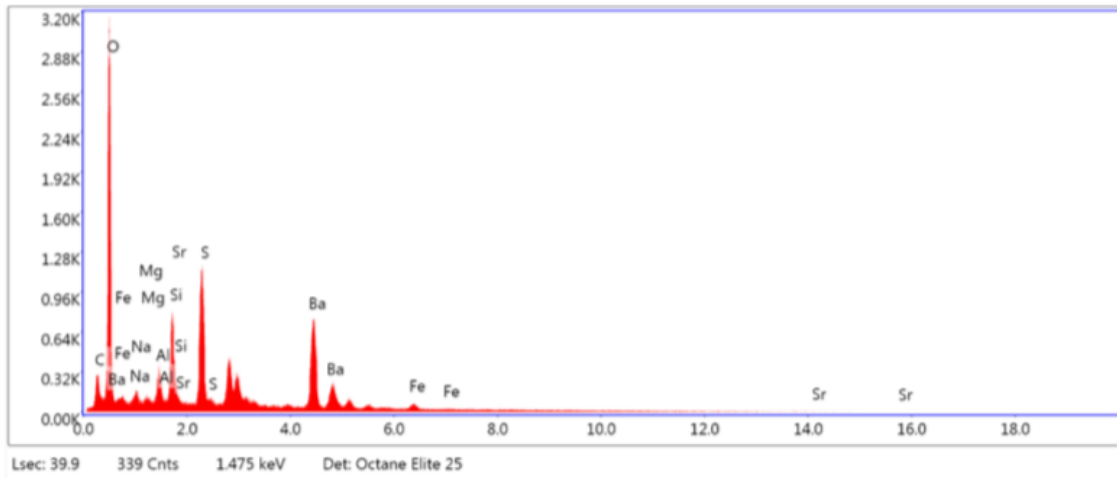
eZAF Smart Quant Results with SEC (BCNOF_2017-09-14)

Element	Weight %	Atomic %	Net Int.	Error %	Kratio	Z	A	F
C K	18.17	41.84	78.00	9.21	0.0631	1.2723	0.2731	1.0000
O K	18.78	32.46	352.80	7.89	0.0835	1.2182	0.3649	1.0000
NaK	1.39	1.67	22.80	12.59	0.0051	1.1073	0.3326	1.0011
MgK	0.62	0.71	15.30	15.50	0.0029	1.1267	0.4111	1.0022
AlK	2.17	2.22	64.00	7.43	0.0124	1.0855	0.5238	1.0039
SiK	4.06	3.99	141.00	5.80	0.0285	1.1097	0.6297	1.0061
SrL	0.36	0.11	6.10	23.17	0.0024	0.8346	0.7896	1.0012
S K	8.01	6.91	252.30	4.09	0.0695	1.0877	0.7868	1.0141
BaL	43.95	8.85	257.40	2.97	0.3364	0.7342	1.0425	1.0002
FeK	2.50	1.24	20.80	11.58	0.0225	0.9386	0.9461	1.0145

Figure I. 16: Element analysis: Sum spectrum (REF + 0.07 g MW system, long-time)

KV: 15 Mag: 5000 Takeoff: 34.2 Live Time(s): 39.9 Amp Time(μs): 7.68 Resolution:(eV) 132.4

Phase: O K/S K/BaL/SiK/AIK



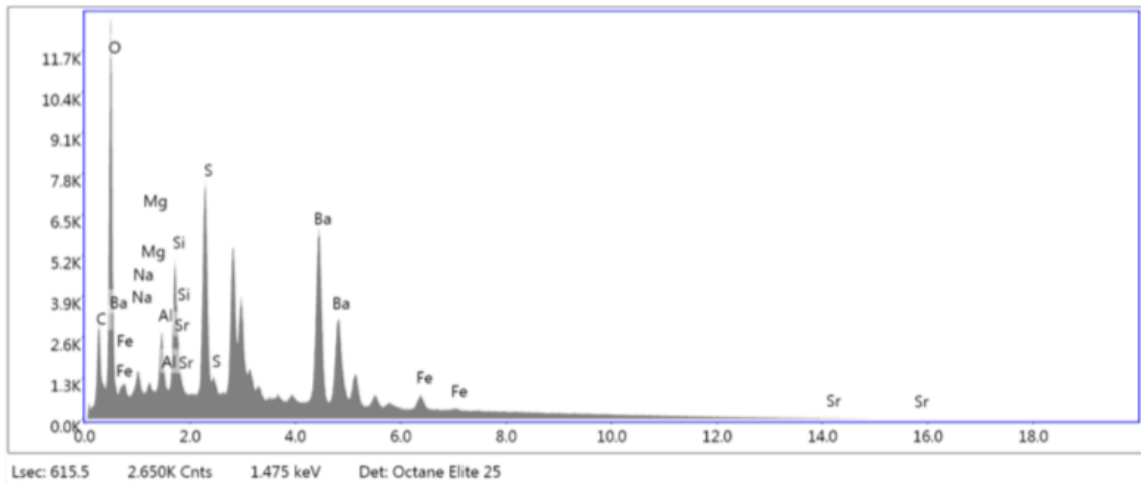
eZAF Smart Quant Results with SEC (BCNOF_2017-09-14)

Element	Weight %	Atomic %	Net Int.	Error %	Kratio	Z	A	F
C K	15.22	33.02	128.40	10.82	0.0489	1.2440	0.2581	1.0000
O K	26.31	42.83	1097.00	8.07	0.1220	1.1906	0.3894	1.0000
NaK	1.06	1.20	37.40	25.32	0.0039	1.0817	0.3439	1.0011
MgK	0.87	0.93	46.40	15.38	0.0041	1.1004	0.4302	1.0022
AlK	2.40	2.31	152.80	8.74	0.0139	1.0599	0.5443	1.0038
SiK	4.66	4.32	346.40	6.77	0.0329	1.0835	0.6483	1.0060
SrL	0.06	0.02	2.10	99.99	0.0004	0.8147	0.8100	1.0011
S K	8.78	7.13	583.30	5.29	0.0755	1.0616	0.7999	1.0133
BaL	38.75	7.35	472.10	5.62	0.2899	0.7153	1.0459	1.0001
FeK	1.90	0.89	33.20	18.90	0.0168	0.9133	0.9536	1.0157

Figure I. 17: Element analysis: O K/S K/BaL/SiK/AIK phase (REF + 0.07 g MW system, long-time)

kV: 15 Mag: 5000 Takeoff: 34.2 Live Time(s): 615.5 Amp Time(μs): 7.68 Resolution:(eV) 132.4

Phase: Unallocated



eZAF Smart Quant Results with SEC (BCNOF_2017-09-14)

Element	Weight %	Atomic %	Net Int.	Error %	Kratio	Z	A	F
C K	18.96	43.65	79.10	9.24	0.0655	1.2729	0.2712	1.0000
O K	17.41	30.08	313.50	7.99	0.0758	1.2187	0.3572	1.0000
NaK	1.63	1.96	26.50	11.28	0.0061	1.1079	0.3350	1.0011
MgK	0.85	0.97	20.50	11.31	0.0040	1.1273	0.4125	1.0021
AlK	2.32	2.38	67.10	7.29	0.0133	1.0860	0.5240	1.0039
SiK	3.92	3.86	133.30	5.85	0.0275	1.1103	0.6291	1.0061
SrL	0.73	0.23	12.10	13.86	0.0048	0.8350	0.7892	1.0012
S K	7.88	6.80	242.40	4.10	0.0683	1.0883	0.7849	1.0139
BaL	43.72	8.80	250.70	2.94	0.3348	0.7346	1.0422	1.0003
FeK	2.57	1.27	21.00	11.15	0.0232	0.9391	0.9462	1.0146

Figure I. 18: Element analysis: Unallocated phase (REF + 0.07 g MW system, long-time)

APPENDIX J – SEM ELEMENT ANALYSIS OF SELECTED AREAS OF THE FILTER CAKE

Reference Fluid (Short-Time Aging)

Area 1

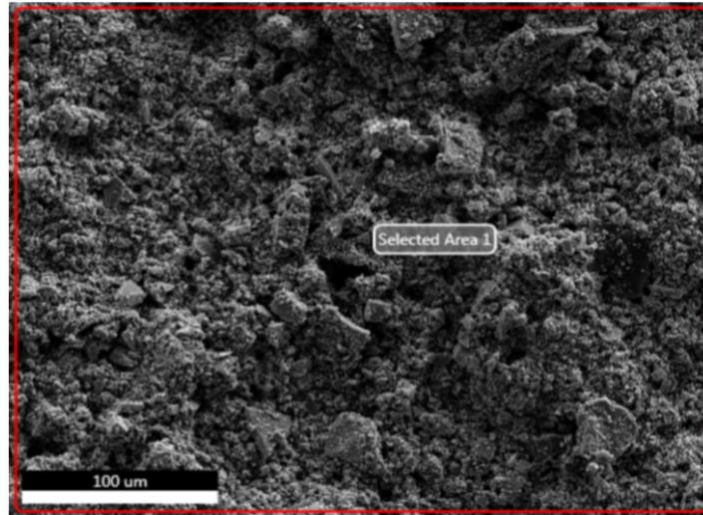
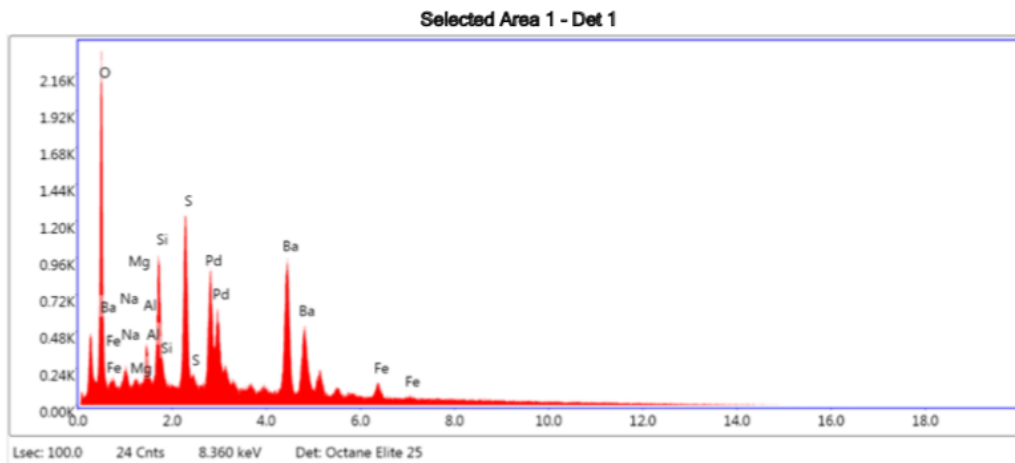


Figure J. 2: Area 1 - SEM picture and element analysis of surface at 100 μm (REF system, short-time)

kV: 15 Mag: 1000 Takeoff: 35.2 Live Time(s): 100 Amp Time(μs): 7.68 Resolution:(eV) 132.4



eZAF Smart Quant Results with SEC (BCNOF_2017-09-14)

Element	Weight %	Atomic %	Net Int.	Error %	Kratio	Z	A	F
O K	18.55	47.11	348.66	7.47	0.0951	1.3100	0.4621	1.0000
NaK	2.26	3.99	26.82	17.67	0.0070	1.1915	0.3051	1.0011
MgK	1.15	1.92	20.16	20.98	0.0044	1.2127	0.3727	1.0021
AlK	2.88	4.34	61.05	9.78	0.0137	1.1686	0.4787	1.0038
SiK	7.15	10.35	180.82	7.13	0.0424	1.1951	0.5832	1.0059
S K	10.67	13.53	248.67	5.46	0.0796	1.1721	0.7420	1.0136
BaL	53.19	15.74	241.59	4.69	0.3667	0.7939	1.0253	1.0003
FeK	4.15	3.02	26.79	15.95	0.0337	1.0182	0.9298	1.0131

Figure J. 3: Area 1 - Element analysis of selected area 1 (REF system, short-time)

Area 2

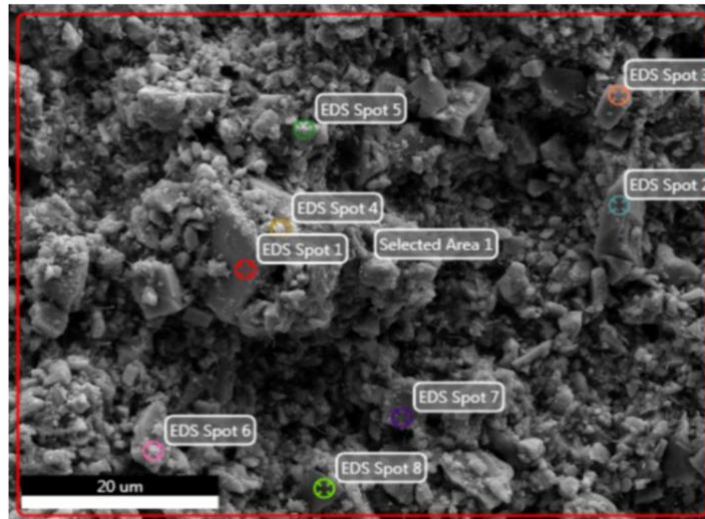
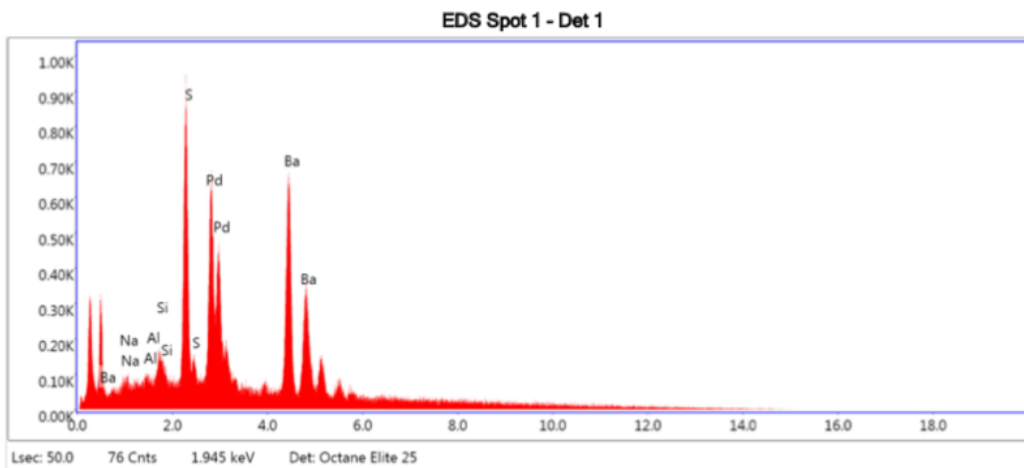


Figure J. 4: Area 2 - SEM picture and element analysis of surface at 20 µm (REF system, short-time)

kV: 15 Mag: 5000 Takeoff: 35.2 Live Time(s): 50 Amp Time(µs): 7.68 Resolution:(eV) 132.4

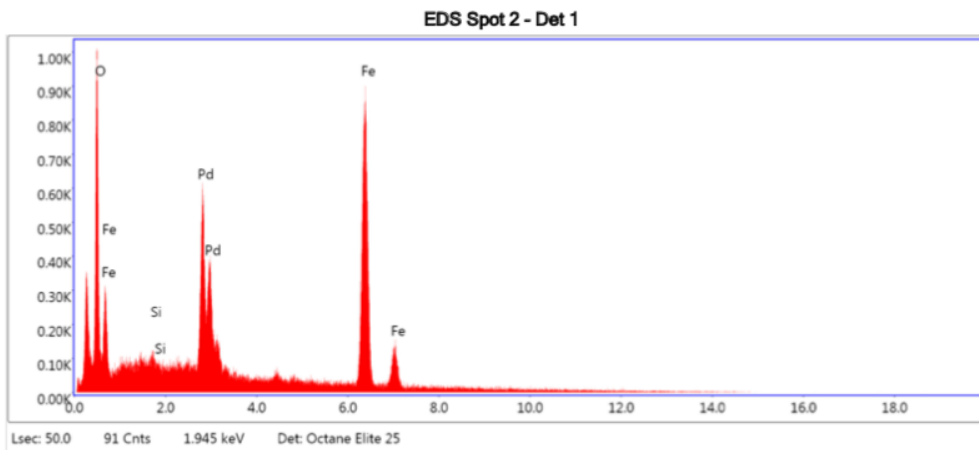


eZAF Smart Quant Results with SEC (BCNOF_2017-09-14)

Element	Weight %	Atomic %	Net Int.	Error %	Kratio	Z	A	F
NaK	2.35	7.68	22.74	21.83	0.0064	1.3361	0.2639	1.0011
AlK	1.89	5.27	32.42	17.12	0.0079	1.3111	0.4108	1.0040
SiK	2.33	6.23	49.35	10.71	0.0126	1.3413	0.5175	1.0067
S K	16.62	38.88	347.25	5.71	0.1212	1.3169	0.7048	1.0149
BaL	76.80	41.94	323.69	4.96	0.5355	0.8990	1.0023	0.9994

Figure J. 5: Area 2 - Element analysis of EDS spot 1 (REF system, short-time)

kV: 15 Mag: 5000 Takeoff: 35.2 Live Time(s): 50 Amp Time(μs): 7.68 Resolution:(eV) 132.4

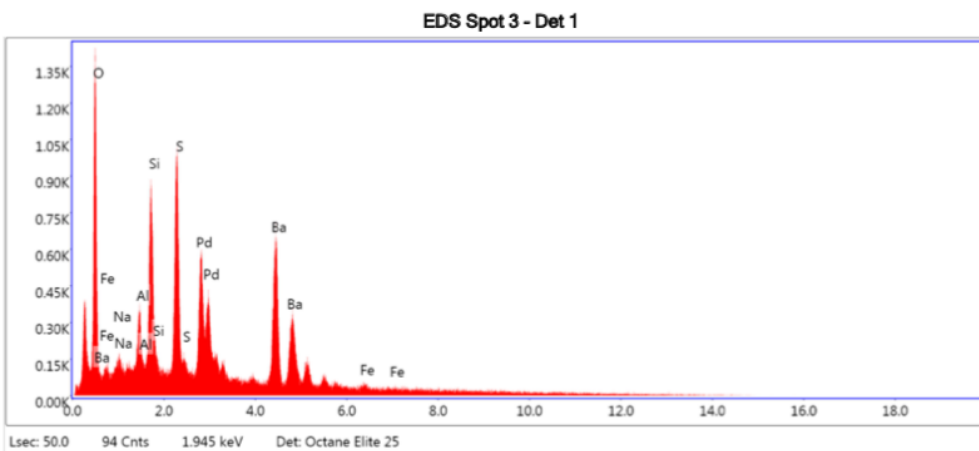


eZAF Smart Quant Results with SEC (BCNOF_2017-09-14)

Element	Weight %	Atomic %	Net Int.	Error %	Kratio	Z	A	F
O K	12.59	33.28	256.28	7.03	0.0744	1.2498	0.5787	1.0000
SiK	0.69	1.04	15.59	38.50	0.0039	1.1364	0.6039	1.0028
FeK	86.72	65.68	508.52	3.35	0.6805	0.9572	1.0018	1.0010

Figure J. 6: Area 2 - Element analysis of spot 2 (REF system, short-time)

kV: 15 Mag: 5000 Takeoff: 35.2 Live Time(s): 50 Amp Time(μs): 7.68 Resolution:(eV) 132.4

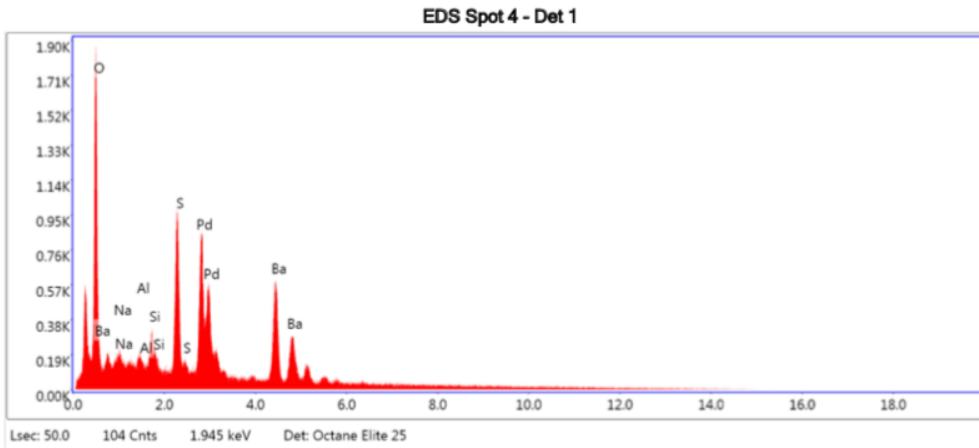


eZAF Smart Quant Results with SEC (BCNOF_2017-09-14)

Element	Weight %	Atomic %	Net Int.	Error %	Kratio	Z	A	F
O K	17.21	43.31	427.11	7.92	0.0830	1.3041	0.4363	1.0000
NaK	2.65	4.65	46.23	15.64	0.0086	1.1861	0.3201	1.0012
AlK	4.33	6.46	132.77	9.33	0.0212	1.1632	0.4958	1.0039
SiK	9.36	13.42	336.28	6.92	0.0563	1.1895	0.5926	1.0058
S K	12.81	16.09	415.87	5.44	0.0949	1.1666	0.7397	1.0129
BaL	52.79	15.48	333.93	5.53	0.3612	0.7899	1.0226	0.9994
FeK	0.84	0.60	7.56	66.01	0.0068	1.0127	0.9295	1.0139

Figure J. 7: Area 2 - Element analysis of spot 3 (REF system, short-time)

kV: 15 Mag: 5000 Takeoff: 35.2 Live Time(s): 50 Amp Time(μs): 7.68 Resolution:(eV) 132.4

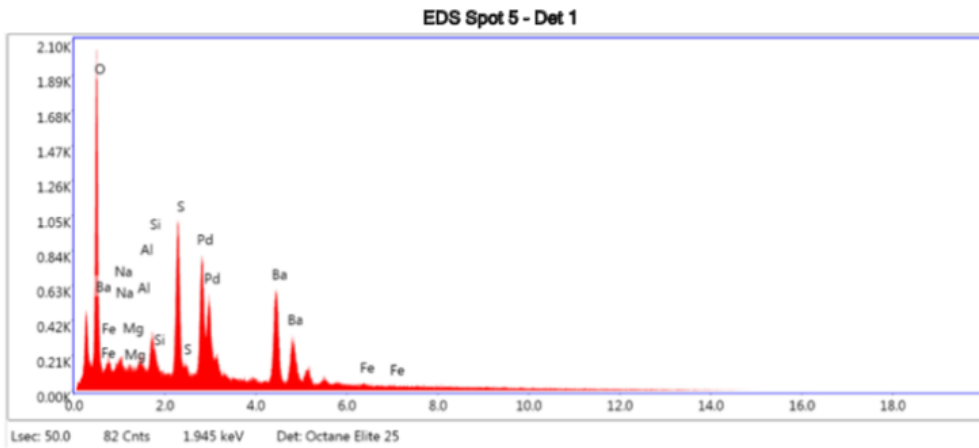


eZAF Smart Quant Results with SEC (BCNOF_2017-09-14)

Element	Weight %	Atomic %	Net Int.	Error %	Kratio	Z	A	F
O K	24.55	55.75	602.75	7.43	0.1143	1.2822	0.4742	1.0000
NaK	4.69	7.41	73.78	13.50	0.0133	1.1660	0.3178	1.0011
AlK	2.94	3.96	81.09	10.93	0.0127	1.1434	0.4902	1.0038
SiK	3.55	4.60	116.52	8.25	0.0190	1.1692	0.5943	1.0062
S K	13.00	14.72	396.84	5.41	0.0884	1.1465	0.7646	1.0135
BaL	51.27	13.56	296.40	6.21	0.3130	0.7756	1.0284	0.9993

Figure J. 8: Area 2 - Element analysis of spot 4 (REF system, short-time)

kV: 15 Mag: 5000 Takeoff: 35.2 Live Time(s): 50 Amp Time(μs): 7.68 Resolution:(eV) 132.4

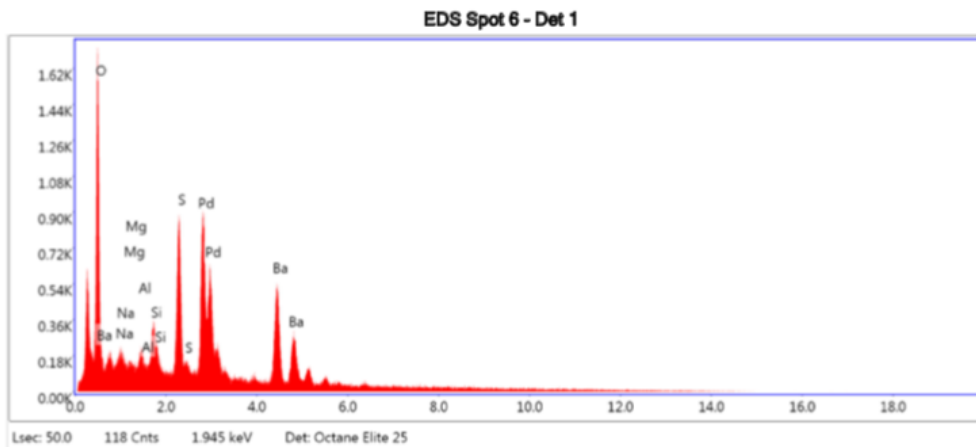


eZAF Smart Quant Results with SEC (BCNOF_2017-09-14)

Element	Weight %	Atomic %	Net Int.	Error %	Kratio	Z	A	F
O K	25.16	55.97	678.03	7.39	0.1206	1.2735	0.4752	1.0000
NaK	3.27	5.06	56.98	16.15	0.0096	1.1580	0.3212	1.0011
MgK	2.36	3.45	59.86	13.19	0.0086	1.1784	0.3882	1.0021
AlK	2.58	3.40	77.98	10.97	0.0114	1.1354	0.4909	1.0038
SiK	3.66	4.63	131.81	8.07	0.0202	1.1610	0.5968	1.0061
S K	12.86	14.27	431.03	5.31	0.0900	1.1383	0.7666	1.0132
BaL	49.52	12.83	313.69	5.60	0.3106	0.7698	1.0295	0.9995
FeK	0.60	0.38	5.44	66.87	0.0045	0.9857	0.9361	1.0144

Figure J. 9: Area 2 - Element analysis of spot 5 (REF system, short-time)

kV: 15 Mag: 5000 Takeoff: 35.2 Live Time(s): 50 Amp Time(μs): 7.68 Resolution:(eV) 132.4

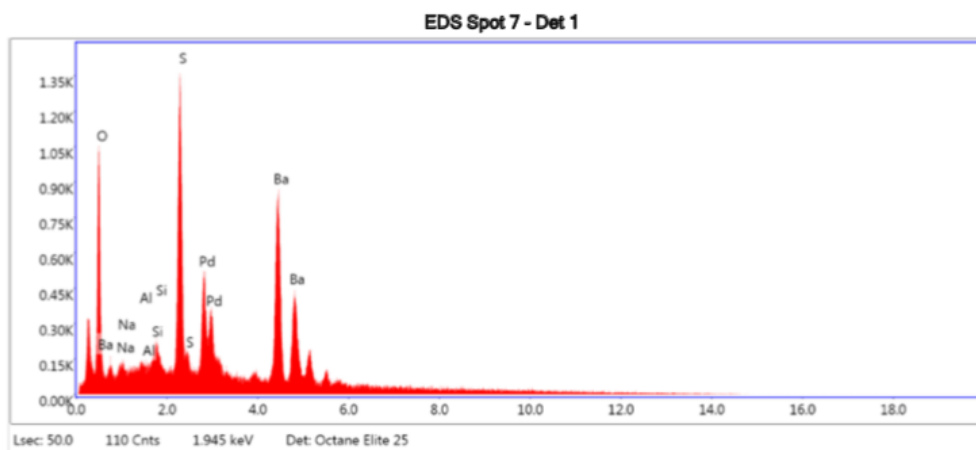


eZAF Smart Quant Results with SEC (BCNOF_2017-09-14)

Element	Weight %	Atomic %	Net Int.	Error %	Kratio	Z	A	F
O K	23.97	53.06	556.99	7.52	0.1055	1.2702	0.4698	1.0000
NaK	4.29	6.60	66.75	14.08	0.0120	1.1549	0.3293	1.0011
MgK	2.78	4.05	62.36	12.60	0.0095	1.1753	0.3926	1.0021
AlK	2.97	3.90	78.76	10.99	0.0123	1.1324	0.4934	1.0038
SiK	4.63	5.83	145.60	7.65	0.0237	1.1578	0.5974	1.0060
S K	12.69	14.01	369.06	5.39	0.0821	1.1352	0.7633	1.0130
BaL	48.68	12.55	268.69	6.02	0.2834	0.7674	1.0293	0.9993

Figure J. 10: Area 2 - Element analysis of spot 6 (REF system, short-time)

kV: 15 Mag: 5000 Takeoff: 35.2 Live Time(s): 50 Amp Time(μs): 7.68 Resolution:(eV) 132.4

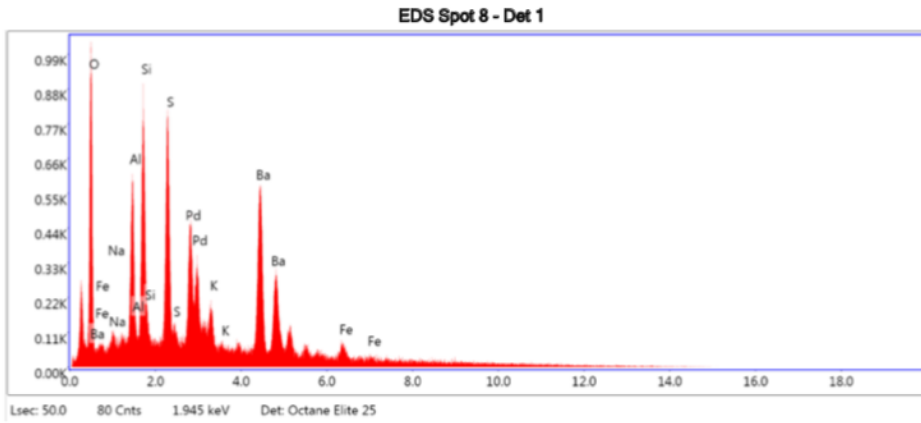


eZAF Smart Quant Results with SEC (BCNOF_2017-09-14)

Element	Weight %	Atomic %	Net Int.	Error %	Kratio	Z	A	F
O K	12.11	38.36	303.78	8.25	0.0631	1.3792	0.4299	1.0000
NaK	2.31	5.09	36.55	20.36	0.0072	1.2548	0.2837	1.0011
AlK	1.82	3.41	51.36	15.92	0.0088	1.2311	0.4449	1.0040
SiK	2.02	3.65	69.80	10.09	0.0125	1.2593	0.5533	1.0066
S K	15.93	25.19	529.92	5.14	0.1293	1.2358	0.7366	1.0144
BaL	65.81	24.29	426.07	4.63	0.4925	0.8402	1.0143	0.9994

Figure J. 11: Area 2 - Element analysis of spot 7 (REF system, short-time)

kV: 15 Mag: 5000 Takeoff: 35.2 Live Time(s): 50 Amp Time(μs): 7.68 Resolution:(eV) 132.4

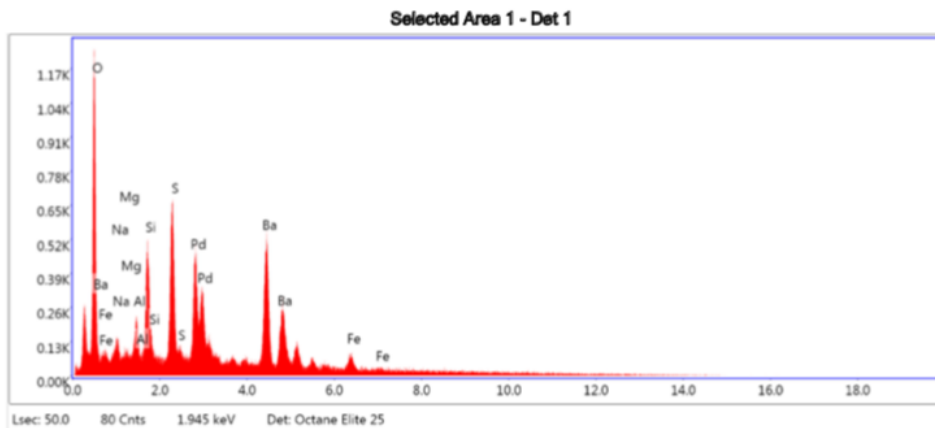


eZAF Smart Quant Results with SEC (BCNOF_2017-09-14)

Element	Weight %	Atomic %	Net Int.	Error %	Kratio	Z	A	F
O K	14.45	38.31	273.96	8.49	0.0677	1.3152	0.4112	1.0000
NaK	0.34	0.62	4.69	83.04	0.0011	1.1962	0.3165	1.0012
AlK	7.45	11.72	186.97	8.63	0.0380	1.1731	0.5002	1.0038
SiK	9.59	14.48	274.78	7.55	0.0585	1.1997	0.5832	1.0056
S K	11.21	14.83	291.62	6.69	0.0847	1.1766	0.7317	1.0128
K K	1.82	1.98	38.47	15.24	0.0161	1.1166	0.8701	1.0470
BaL	52.84	16.32	270.24	5.65	0.3718	0.7970	1.0195	0.9996
FeK	2.30	1.75	16.81	28.35	0.0191	1.0222	0.9280	1.0135

Figure J. 12: Area 2 - Element analysis of spot 8 (REF system, short-time)

kV: 15 Mag: 5000 Takeoff: 35.2 Live Time(s): 50 Amp Time(μs): 7.68 Resolution:(eV) 132.4



eZAF Smart Quant Results with SEC (BCNOF_2017-09-14)

Element	Weight %	Atomic %	Net Int.	Error %	Kratio	Z	A	F
O K	18.35	46.05	401.82	7.71	0.0939	1.3052	0.4624	1.0000
NaK	2.77	4.83	38.65	17.15	0.0086	1.1871	0.3086	1.0011
MgK	1.66	2.74	34.05	15.50	0.0064	1.2081	0.3754	1.0021
AlK	3.21	4.78	79.33	10.22	0.0153	1.1641	0.4797	1.0038
SiK	6.92	9.88	203.47	7.48	0.0409	1.1905	0.5830	1.0058
S K	10.60	13.28	287.93	5.69	0.0790	1.1675	0.7430	1.0134
BaL	51.96	15.19	274.74	5.51	0.3574	0.7906	1.0259	1.0004
FeK	4.54	3.26	34.17	17.39	0.0368	1.0137	0.9314	1.0131

Figure J. 13: Area 2 - Element analysis of selected area 1 (REF system, short-time)

Reference Fluid (Long-Time Aging)

Area 1

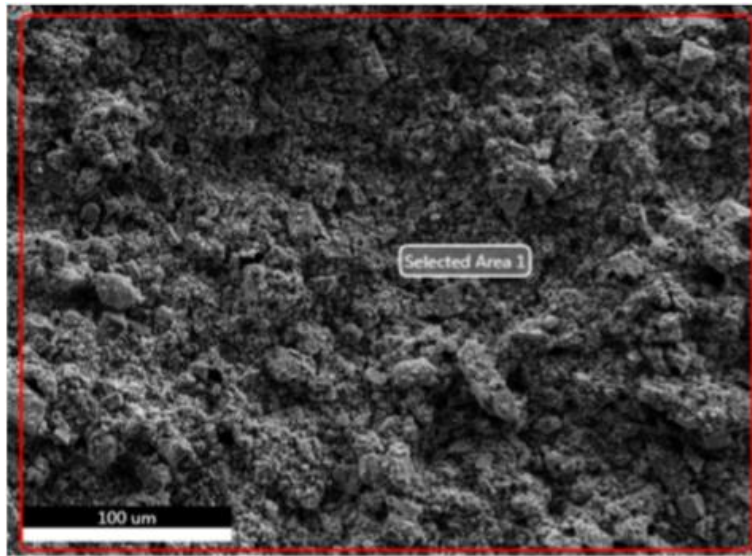
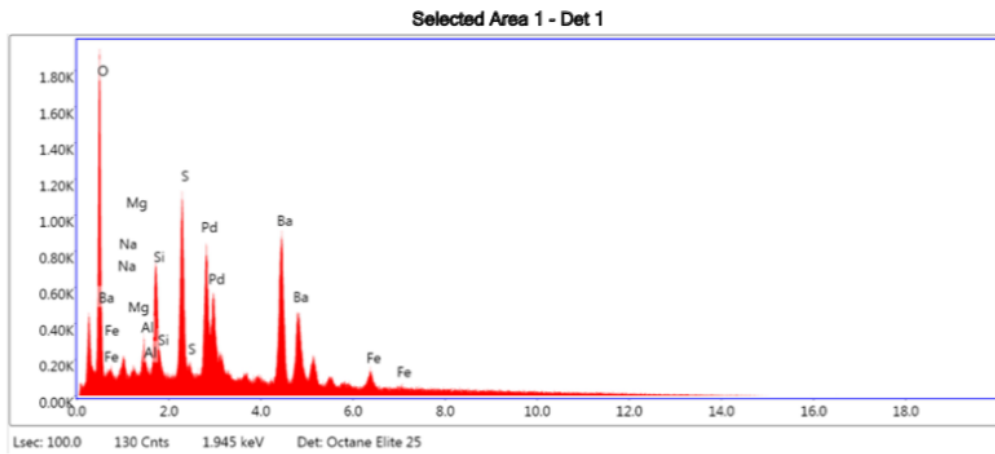


Figure J. 14: Area 1 - SEM picture and element analysis of surface at 100 μm (REF system, long-time)

kV: 15 Mag: 1000 Takeoff: 34.7 Live Time(s): 100 Amp Time(μs): 7.68 Resolution:(eV) 132.4



eZAF Smart Quant Results with SEC (BCNOF_2017-09-14)

Element	Weight %	Atomic %	Net Int.	Error %	Kratio	Z	A	F
OK	17.07	45.07	291.86	7.55	0.0870	1.3223	0.4602	1.0000
NaK	2.53	4.64	26.74	16.32	0.0076	1.2028	0.2970	1.0011
MgK	1.45	2.53	22.64	16.15	0.0054	1.2242	0.3619	1.0021
AlK	2.58	4.04	48.75	10.62	0.0119	1.1798	0.4656	1.0038
SiK	6.36	9.57	144.65	7.28	0.0370	1.2066	0.5718	1.0060
SK	10.45	13.77	221.71	5.47	0.0774	1.1835	0.7363	1.0138
BaL	54.99	16.92	229.03	4.39	0.3788	0.8022	1.0245	1.0004
FeK	4.57	3.46	27.05	15.38	0.0370	1.0293	0.9263	1.0128

Figure J. 15: Area 1 - Element analysis of selected area 1 (REF system, long-time)

Area 2

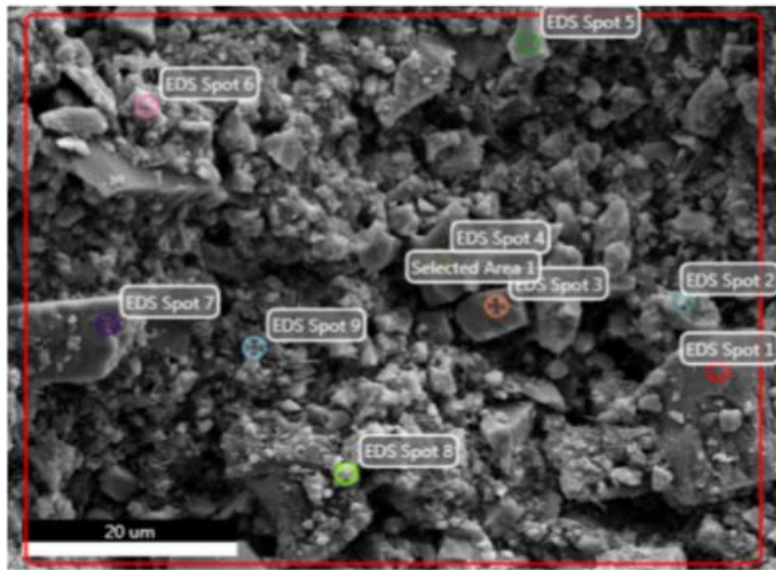
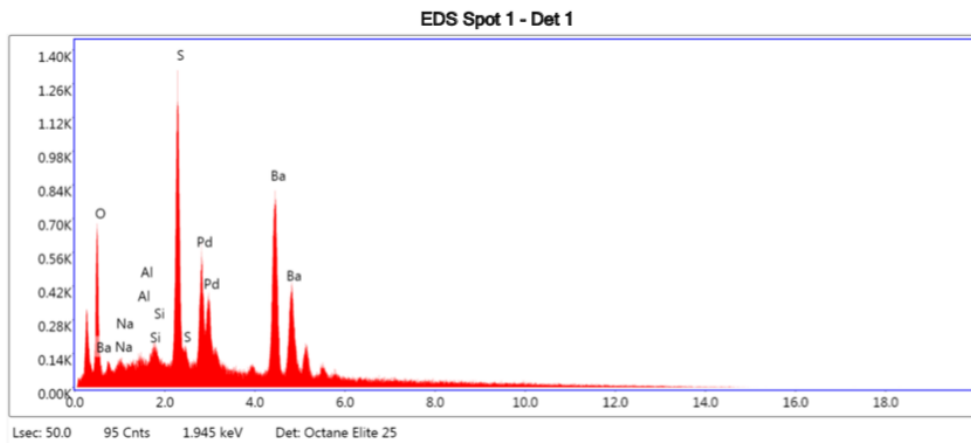


Figure J. 16: Area 2 - SEM picture and element analysis of surface at 20 μm (REF system, long-time)

kV: 15 Mag: 5000 Takeoff: 34.7 Live Time(s): 50 Amp Time(μs):7.68 Resolution:(eV) 132.4

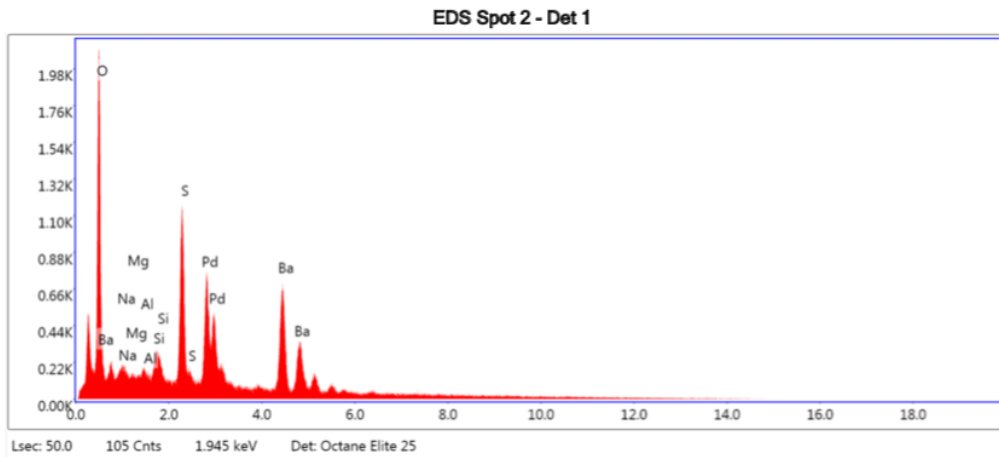


eZAF Smart Quant Results with SEC (BCNOF_2017-09-14)

Element	Weight %	Atomic %	Net Int.	Error %	Kratio	Z	A	F
O K	8.40	29.39	190.47	8.95	0.0420	1.4035	0.4144	1.0000
NaK	2.32	5.66	33.66	21.08	0.0071	1.2769	0.2760	1.0011
AlK	2.00	4.15	51.75	15.87	0.0094	1.2529	0.4326	1.0040
SiK	1.74	3.48	55.20	10.67	0.0105	1.2816	0.5400	1.0067
S K	16.76	29.27	518.03	5.24	0.1338	1.2579	0.7266	1.0145
BaL	68.78	28.05	418.28	4.22	0.5120	0.8562	1.0108	0.9993

Figure J. 17: Area 2 - Element analysis of spot 1 (REF system, long-time)

kV: 15 Mag: 5000 Takeoff: 34.7 Live Time(s): 50 Amp Time(μs): 7.68 Resolution:(eV) 132.4

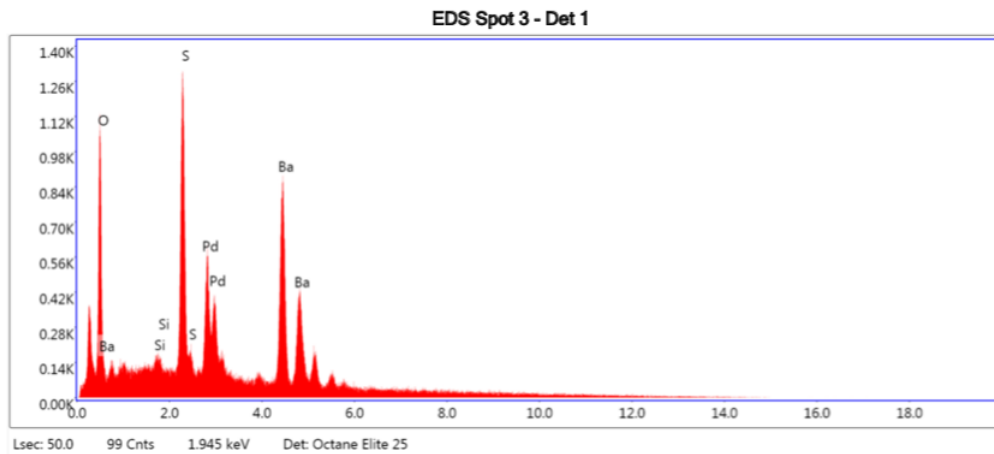


eZAF Smart Quant Results with SEC (BCNOF_2017-09-14)

Element	Weight %	Atomic %	Net Int.	Error %	Kratio	Z	A	F
O K	23.89	54.80	667.14	7.44	0.1174	1.2844	0.4688	1.0000
NaK	3.54	5.65	63.64	15.47	0.0106	1.1680	0.3146	1.0011
MgK	2.36	3.56	61.62	13.27	0.0087	1.1887	0.3784	1.0021
AlK	2.17	2.96	67.83	11.99	0.0098	1.1454	0.4801	1.0038
SiK	2.98	3.89	111.46	8.02	0.0168	1.1712	0.5880	1.0062
S K	13.40	15.34	471.38	5.14	0.0970	1.1485	0.7625	1.0135
BaL	51.65	13.80	344.84	5.42	0.3365	0.7771	1.0282	0.9993

Figure J. 18: Area 2 - Element analysis of spot 2 (REF system, long-time)

kV: 15 Mag: 5000 Takeoff: 34.7 Live Time(s): 50 Amp Time(μs): 7.68 Resolution:(eV) 132.4

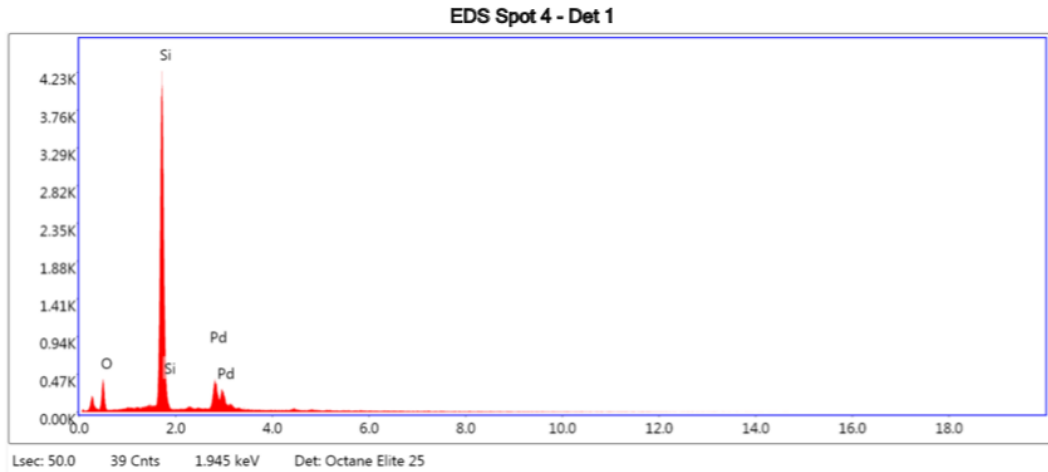


eZAF Smart Quant Results with SEC (BCNOF_2017-09-14)

Element	Weight %	Atomic %	Net Int.	Error %	Kratio	Z	A	F
O K	13.59	44.34	335.45	8.23	0.0702	1.3900	0.4300	1.0000
SiK	1.52	2.83	51.68	14.22	0.0093	1.2694	0.5508	1.0068
S K	16.48	26.83	541.43	5.19	0.1326	1.2458	0.7362	1.0148
BaL	68.41	26.00	437.49	4.73	0.5077	0.8477	1.0135	0.9994

Figure J. 19: Area 2 - Element analysis of spot 3 (REF system, long-time)

kV: 15 Mag: 5000 Takeoff: 34.7 Live Time(s): 50 Amp Time(μs): 7.68 Resolution:(eV) 132.4

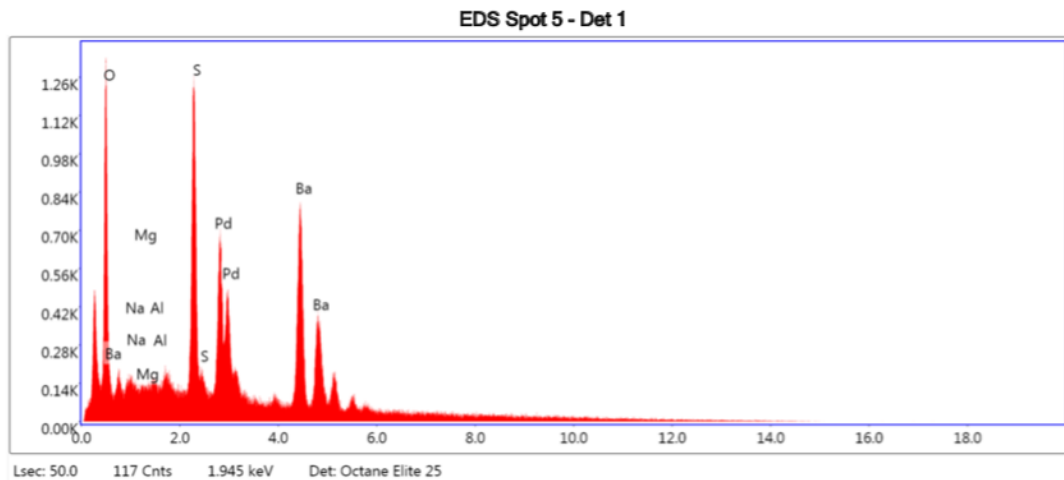


eZAF Smart Quant Results with SEC (BCNOF_2017-09-14)

Element	Weight %	Atomic %	Net Int.	Error %	Kratio	Z	A	F
OK	14.58	23.05	75.59	11.37	0.0378	1.0902	0.3062	1.0000
SiK	85.42	76.95	1475.05	2.07	0.6328	0.9838	0.9692	1.0001

Figure J. 20: Area 2 - Element analysis of spot 4 (REF system, long-time)

kV: 15 Mag: 5000 Takeoff: 34.7 Live Time(s): 50 Amp Time(μs): 7.68 Resolution:(eV) 132.4

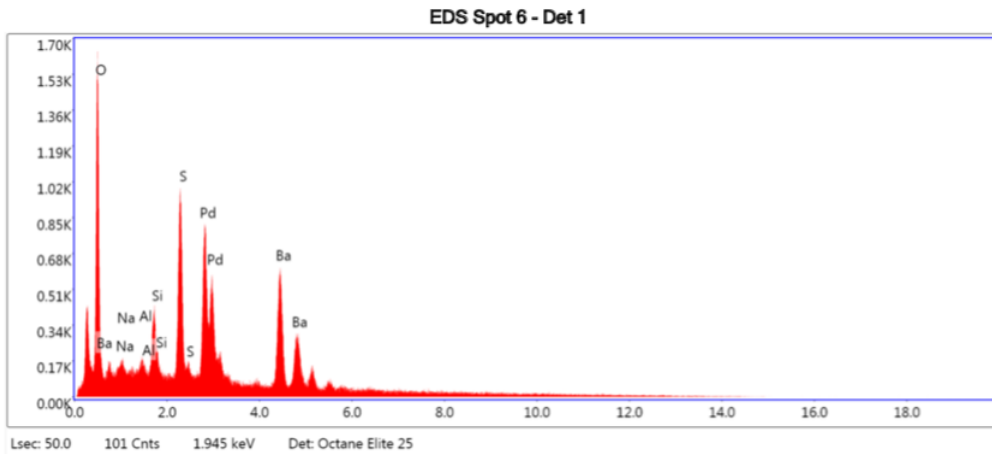


eZAF Smart Quant Results with SEC (BCNOF_2017-09-14)

Element	Weight %	Atomic %	Net Int.	Error %	Kratio	Z	A	F
OK	15.82	44.50	409.26	7.86	0.0786	1.3471	0.4443	1.0000
NaK	3.02	5.91	49.23	16.64	0.0090	1.2255	0.2919	1.0011
MgK	2.32	4.29	54.69	15.28	0.0084	1.2475	0.3495	1.0021
AlK	2.10	3.50	59.61	12.51	0.0094	1.2023	0.4473	1.0039
SK	15.48	21.72	522.87	5.06	0.1174	1.2065	0.7475	1.0142
BaL	61.26	20.07	398.26	4.90	0.4240	0.8189	1.0194	0.9994

Figure J. 21: Area 2 - Element analysis of spot 5 (REF system, long-time)

kV: 15 Mag: 5000 Takeoff: 34.7 Live Time(s): 50 Amp Time(μs): 7.68 Resolution:(eV) 132.4

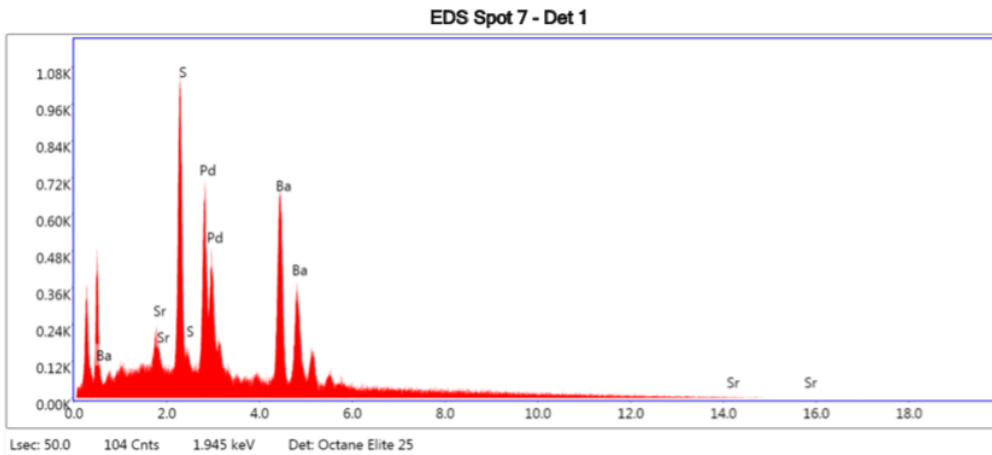


eZAF Smart Quant Results with SEC (BCNOF_2017-09-14)

Element	Weight %	Atomic %	Net Int.	Error %	Kratio	Z	A	F
O K	22.11	52.63	492.37	7.64	0.1003	1.2946	0.4563	1.0000
NaK	3.65	6.05	53.25	15.19	0.0103	1.1775	0.3118	1.0011
AlK	2.64	3.72	68.14	12.22	0.0114	1.1547	0.4849	1.0039
SiK	4.87	6.61	150.15	8.09	0.0262	1.1808	0.5901	1.0062
S K	13.72	16.30	392.09	5.32	0.0935	1.1580	0.7557	1.0134
BaL	53.01	14.70	289.55	6.16	0.3272	0.7839	1.0259	0.9993

Figure J. 22: Area 2 - Element analysis of spot 6 (REF system, long-time)

kV: 15 Mag: 5000 Takeoff: 34.7 Live Time(s): 50 Amp Time(μs): 7.68 Resolution:(eV) 132.4

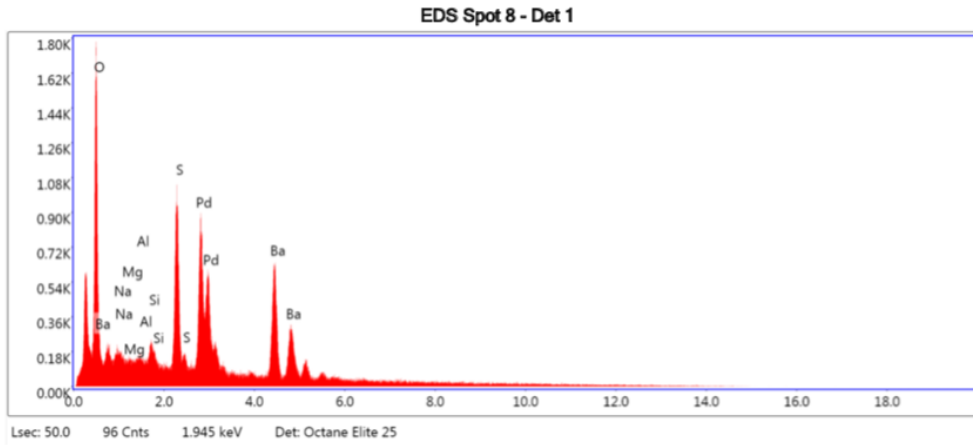


eZAF Smart Quant Results with SEC (BCNOF_2017-09-14)

Element	Weight %	Atomic %	Net Int.	Error %	Kratio	Z	A	F
SrL	6.01	5.65	71.44	9.00	0.0326	1.0197	0.6746	1.0017
S K	19.26	49.50	434.65	5.63	0.1416	1.3309	0.6923	1.0130
BaL	74.73	44.85	345.18	4.48	0.5330	0.9093	0.9962	0.9993

Figure J. 23: Area 2 - Element analysis of spot 7 (REF system, long-time)

kV: 15 Mag: 5000 Takeoff: 34.7 Live Time(s): 50 Amp Time(μs):7.68 Resolution:(eV) 132.4

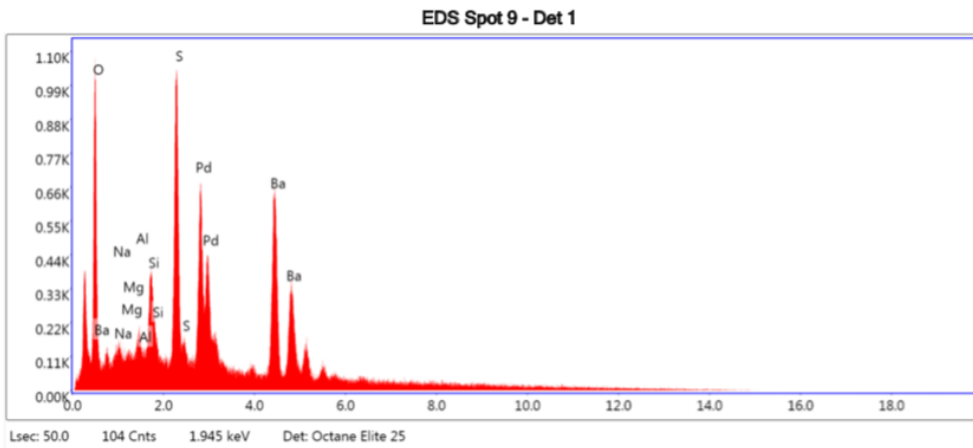


eZAF Smart Quant Results with SEC (BCNOF_2017-09-14)

Element	Weight %	Atomic %	Net Int.	Error %	Kratio	Z	A	F
O K	22.69	53.11	561.08	7.52	0.1051	1.2910	0.4676	1.0000
NaK	3.92	6.38	62.18	14.97	0.0111	1.1741	0.3132	1.0011
MgK	2.68	4.13	61.54	13.36	0.0092	1.1949	0.3747	1.0021
AlK	2.27	3.14	62.05	12.23	0.0095	1.1514	0.4746	1.0038
SiK	2.45	3.26	80.65	9.60	0.0130	1.1774	0.5823	1.0063
S K	13.37	15.62	416.45	5.28	0.0913	1.1546	0.7602	1.0136
BaL	52.64	14.35	311.96	5.83	0.3241	0.7815	1.0274	0.9993

Figure J. 24: Area 2 - Element analysis of spot 8 (REF system, long-time)

kV: 15 Mag: 5000 Takeoff: 34.7 Live Time(s): 50 Amp Time(μs):7.68 Resolution:(eV) 132.4



eZAF Smart Quant Results with SEC (BCNOF_2017-09-14)

Element	Weight %	Atomic %	Net Int.	Error %	Kratio	Z	A	F
O K	14.52	39.83	314.87	8.25	0.0679	1.3328	0.4296	1.0000
NaK	2.77	5.29	40.95	18.41	0.0084	1.2124	0.3050	1.0011
MgK	2.08	3.75	44.33	16.24	0.0077	1.2340	0.3649	1.0022
AlK	2.68	4.36	68.60	12.14	0.0121	1.1892	0.4647	1.0039
SiK	5.01	7.83	154.37	7.77	0.0285	1.2163	0.5698	1.0062
S K	14.89	20.38	430.80	5.32	0.1086	1.1931	0.7392	1.0135
BaL	58.05	18.55	326.72	5.61	0.3905	0.8092	1.0193	0.9993

Figure J. 25: Area 2 - Element analysis of spot 9 (REF system, long-time)

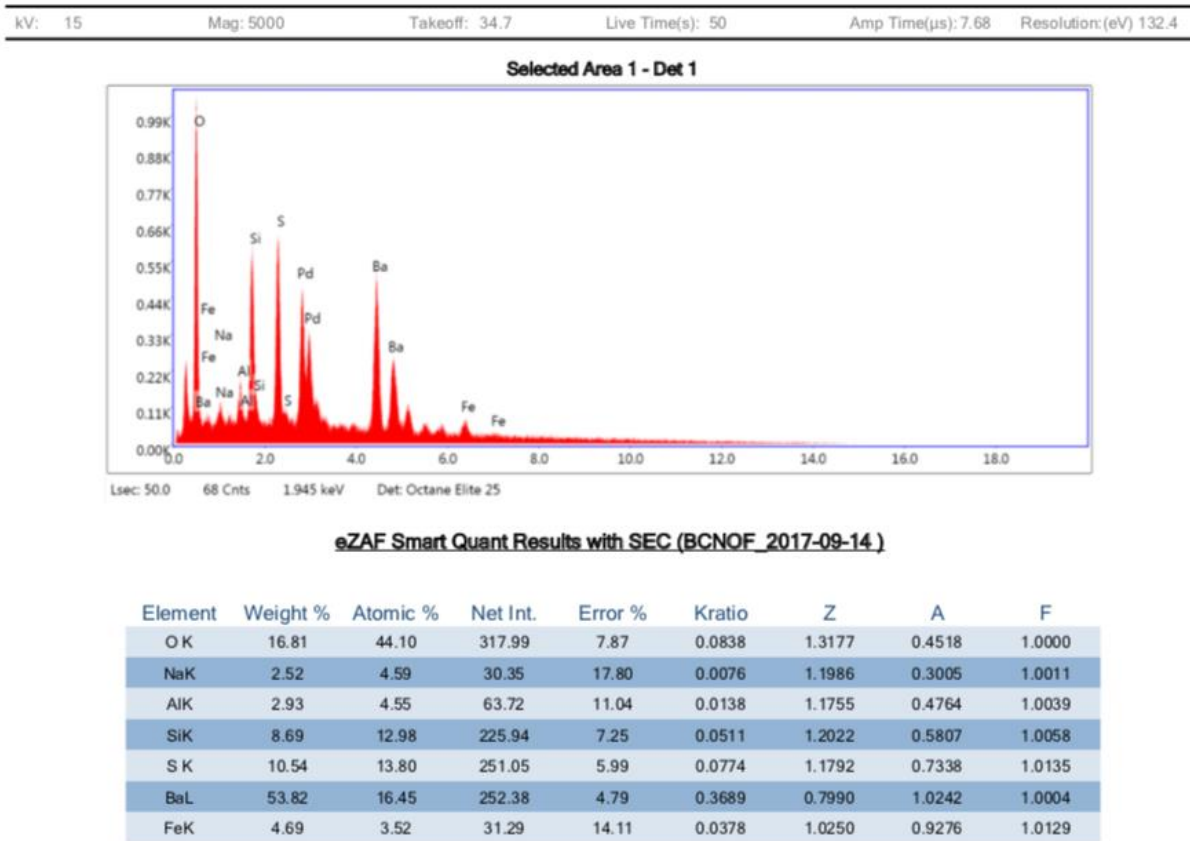


Figure J. 26: Area 2 - Element analysis of selected area 1 (REF system, long-time)

Filter paper

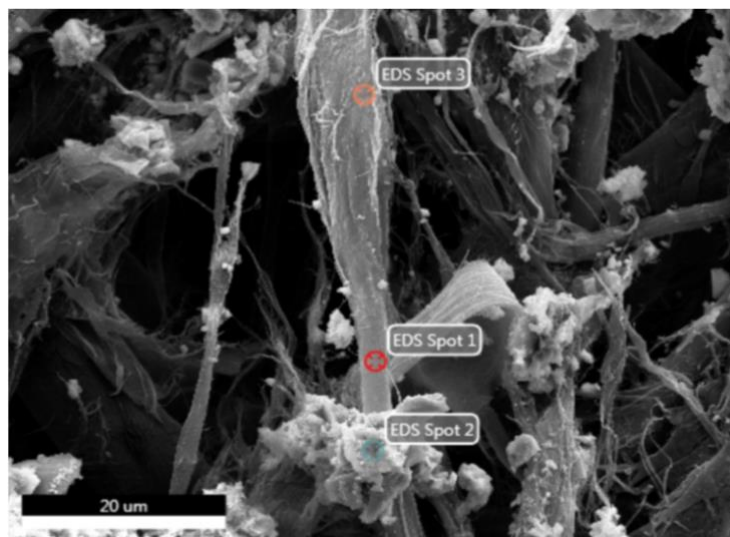
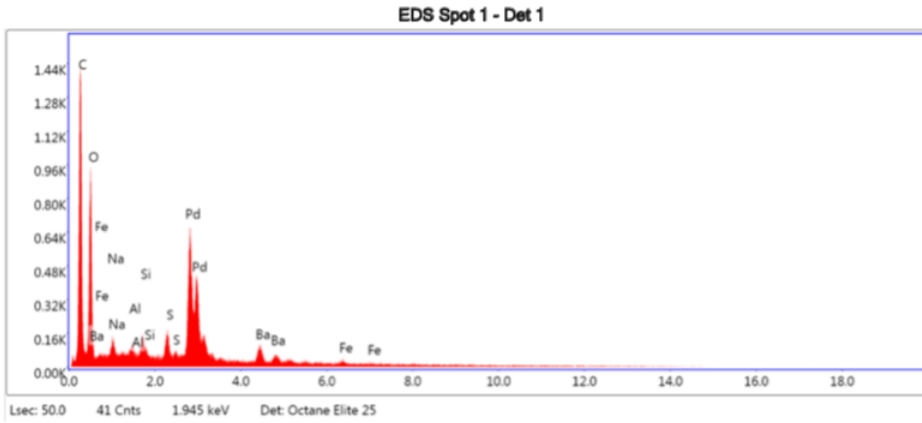


Figure J. 27: Filter paper - SEM picture and element analysis of surface at 20 μm (REF system, long-time)

kV: 15 Mag: 5000 Takeoff: 34.8 Live Time(s): 50 Amp Time(μs): 7.68 Resolution:(eV) 132.4

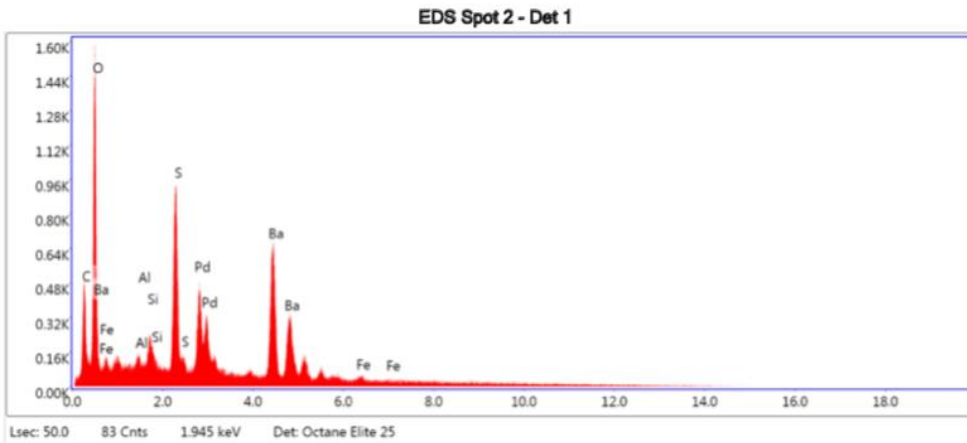


eZAF Smart Quant Results with SEC (BCNOF_2017-09-14)

Element	Weight %	Atomic %	Net Int.	Error %	Kratio	Z	A	F
C K	47.13	61.77	177.13	99.99	0.1542	1.0787	0.4810	1.0000
O K	33.70	33.16	236.84	10.46	0.0606	1.0281	0.2771	1.0000
NaK	1.68	1.15	18.40	20.70	0.0045	0.9298	0.4540	1.0011
AlK	0.46	0.27	8.98	54.75	0.0019	0.9087	0.7073	1.0037
SiK	1.32	0.74	28.50	13.50	0.0063	0.9277	0.8061	1.0058
S K	2.39	1.17	42.62	9.94	0.0128	0.9069	0.9222	1.0134
BaL	12.11	1.39	35.28	18.04	0.0501	0.6058	1.0811	1.0017
FeK	1.22	0.34	5.17	60.51	0.0061	0.7691	0.9977	1.0322

Figure J. 28: Filter paper - Element analysis of spot 1 (REF system, long-time)

kV: 15 Mag: 5000 Takeoff: 34.8 Live Time(s): 50 Amp Time(μs): 7.68 Resolution:(eV) 132.4



eZAF Smart Quant Results with SEC (BCNOF_2017-09-14)

Element	Weight %	Atomic %	Net Int.	Error %	Kratio	Z	A	F
C K	21.96	48.03	134.46	99.99	0.0747	1.2626	0.3040	1.0000
O K	20.01	32.86	464.61	8.75	0.0758	1.2089	0.3536	1.0000
AlK	0.89	0.86	33.74	18.21	0.0045	1.0773	0.5321	1.0040
SiK	1.58	1.48	71.49	9.72	0.0100	1.1014	0.6434	1.0066
S K	9.40	7.71	386.28	5.48	0.0738	1.0796	0.8085	1.0149
BaL	45.35	8.68	337.40	5.85	0.3057	0.7287	1.0438	0.9998
FeK	0.81	0.38	8.58	62.32	0.0064	0.9315	0.9462	1.0146

Figure J. 29: Filter paper - Element analysis of spot 2 (REF system, long-time)

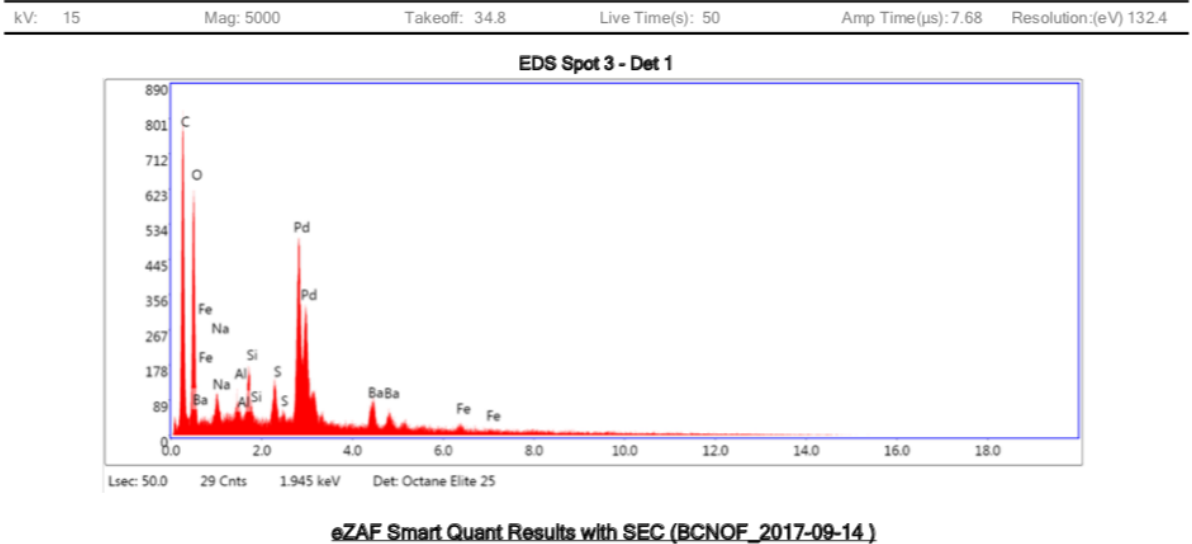


Figure J. 30: Filter paper - Element analysis of spot 3 (REF system, long-time)

Reference Fluid Containing 0.07 g Multi-Walled Carbon Nanotube (Short-Time Aging)

Area 1

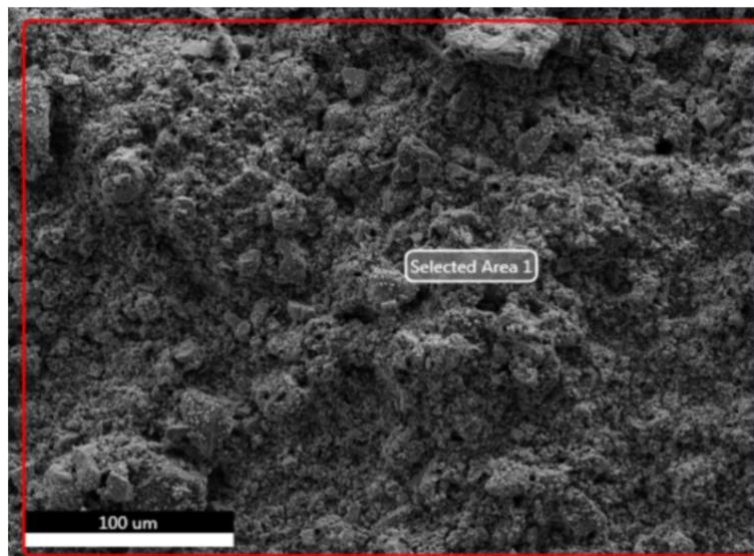
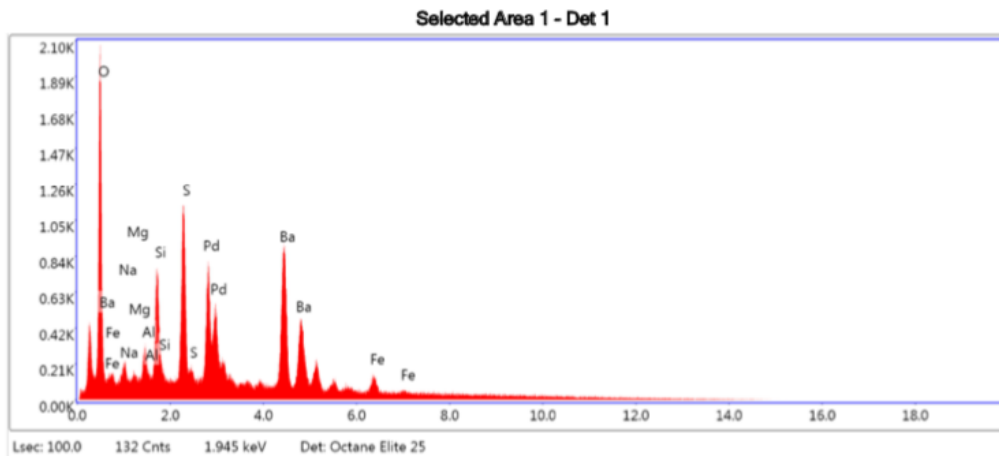


Figure J. 31: Area 1 - SEM picture and element analysis of surface at 100 μm (REF+ 0.07 g MW system, short-time)

kV: 15 Mag: 1000 Takeoff: 34.6 Live Time(s): 100 Amp Time(μs): 7.68 Resolution:(eV) 132.4



eZAF Smart Quant Results with SEC (BCNOF_2017-09-14)

Element	Weight %	Atomic %	Net Int.	Error %	Kratio	Z	A	F
O K	17.92	46.66	321.13	7.51	0.0933	1.3188	0.4623	1.0000
NaK	2.39	4.34	26.38	16.75	0.0073	1.1995	0.2964	1.0011
MgK	1.38	2.36	22.43	16.17	0.0052	1.2209	0.3621	1.0021
AlK	2.62	4.05	51.75	10.18	0.0123	1.1765	0.4663	1.0038
SiK	6.06	8.99	144.01	7.27	0.0359	1.2032	0.5725	1.0060
S K	10.48	13.62	232.71	5.44	0.0790	1.1802	0.7381	1.0138
BaL	54.55	16.55	237.38	4.36	0.3823	0.7998	1.0252	1.0004
FeK	4.60	3.43	28.45	15.06	0.0379	1.0262	0.9269	1.0128

Figure J. 32: Area 1 - Element analysis of selected area 1 (REF+ 0.07 g MW system, short-time)

Area 2

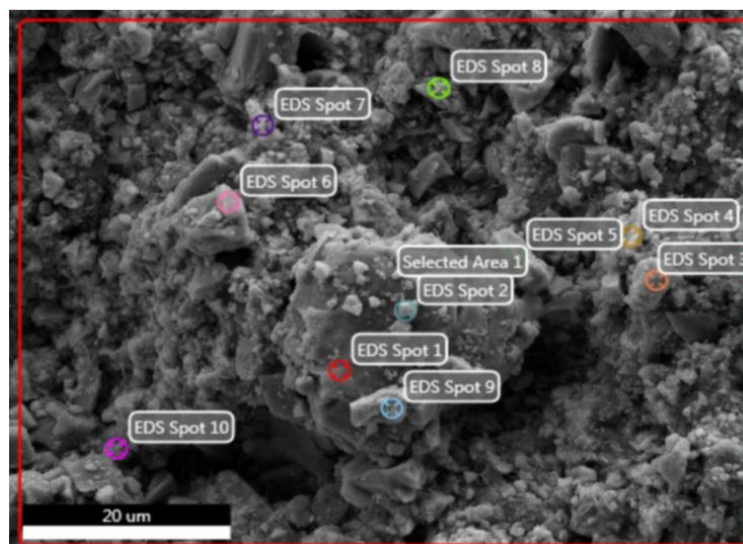
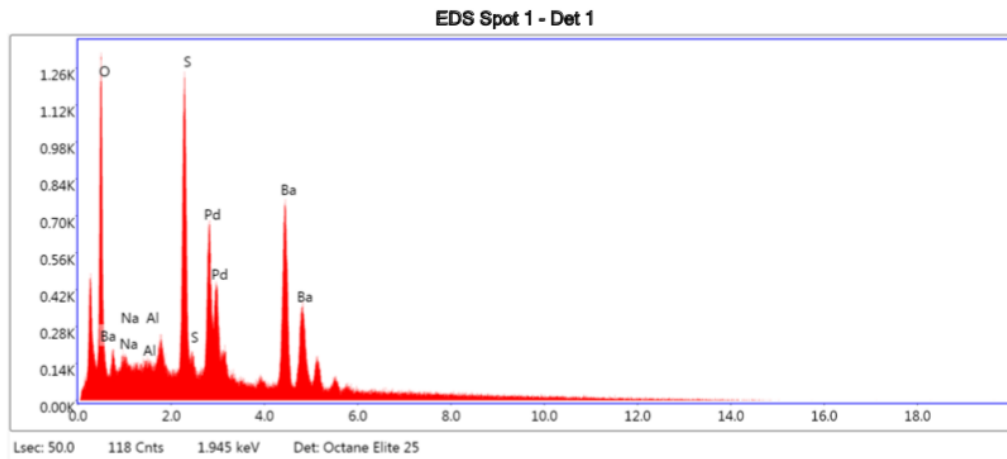


Figure J. 33: Area 2 - SEM picture and element analysis of surface at 20 μm (REF+ 0.07 g MW system, short-time)

kV: 15 Mag: 5000 Takeoff: 34.6 Live Time(s): 50 Amp Time(μs): 7.68 Resolution:(eV) 132.4

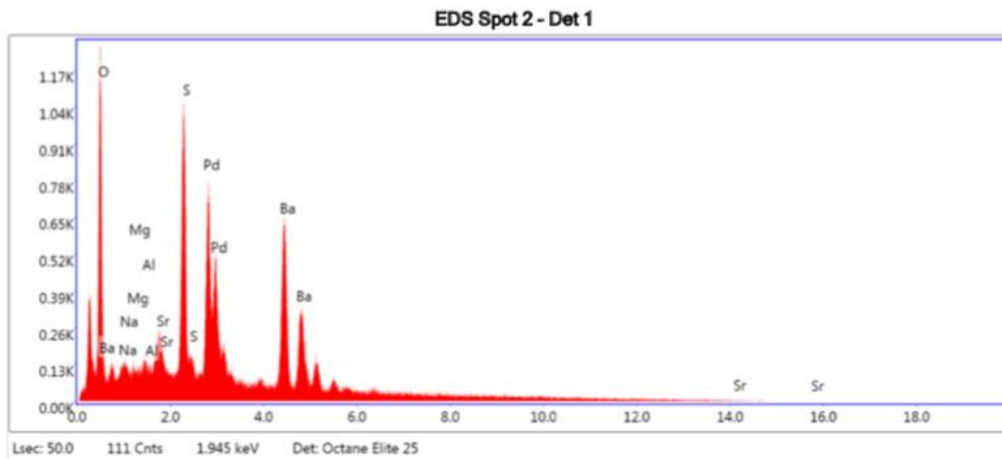


eZAF Smart Quant Results with SEC (BCNOF_2017-09-14)

Element	Weight %	Atomic %	Net Int.	Error %	Kratio	Z	A	F
O K	16.38	45.65	403.39	7.87	0.0807	1.3453	0.4433	1.0000
NaK	4.24	8.22	65.83	13.83	0.0125	1.2238	0.2912	1.0011
AlK	2.61	4.32	71.74	10.60	0.0118	1.2006	0.4521	1.0039
S K	15.86	22.04	512.87	5.05	0.1199	1.2047	0.7495	1.0142
BaL	60.90	19.77	378.11	4.99	0.4189	0.8177	1.0197	0.9993

Figure J. 34: Area 2 - Element analysis of spot 1 (REF+ 0.07 g MW system, short-time)

kV: 15 Mag: 5000 Takeoff: 34.6 Live Time(s): 50 Amp Time(μs): 7.68 Resolution:(eV) 132.4

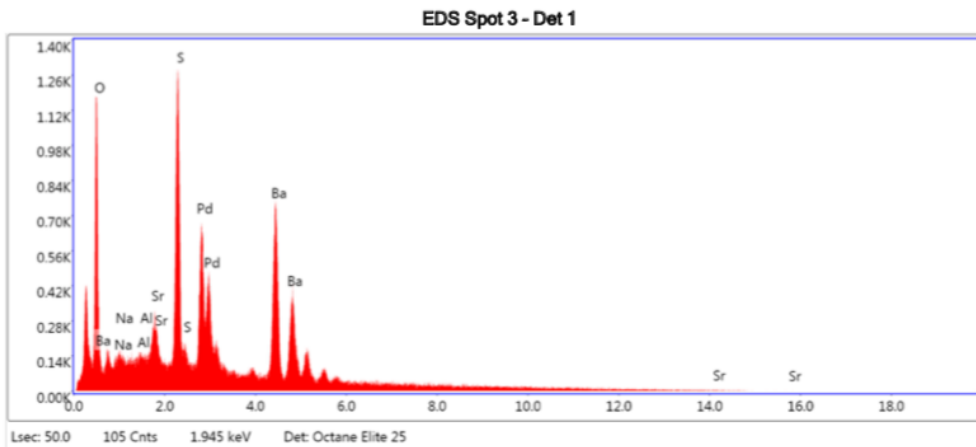


eZAF Smart Quant Results with SEC (BCNOF_2017-09-14)

Element	Weight %	Atomic %	Net Int.	Error %	Kratio	Z	A	F
O K	17.77	48.68	374.75	8.36	0.0776	1.3384	0.4134	1.0000
NaK	2.42	4.61	35.47	22.53	0.0070	1.2176	0.2998	1.0011
MgK	1.81	3.26	38.80	20.01	0.0064	1.2393	0.3629	1.0021
AlK	1.66	2.69	42.91	15.60	0.0073	1.1944	0.4643	1.0039
SrL	5.24	2.62	81.83	11.18	0.0278	0.9189	0.7301	1.0014
S K	14.75	20.16	428.67	5.41	0.1038	1.1985	0.7348	1.0122
BaL	56.35	17.98	320.67	5.72	0.3681	0.8131	1.0182	0.9993

Figure J. 35: Area 2 - Element analysis of spot 2 (REF+ 0.07 g MW system, short-time)

kV: 15 Mag: 5000 Takeoff: 34.6 Live Time(s): 50 Amp Time(μs): 7.68 Resolution:(eV) 132.4

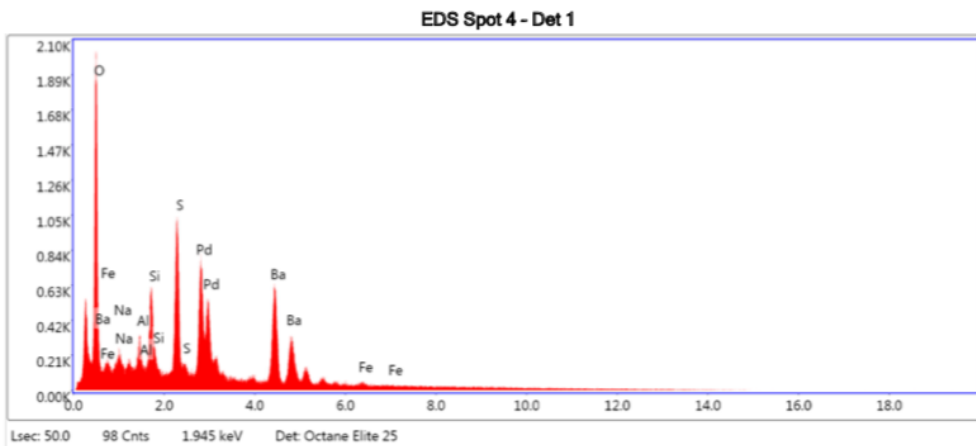


eZAF Smart Quant Results with SEC (BCNOF_2017-09-14)

Element	Weight %	Atomic %	Net Int.	Error %	Kratio	Z	A	F
O K	15.05	43.65	350.33	8.56	0.0672	1.3528	0.3965	1.0000
NaK	3.38	6.82	56.85	14.49	0.0103	1.2307	0.2985	1.0011
AlK	2.13	3.67	63.61	12.42	0.0100	1.2074	0.4652	1.0039
SrL	5.85	3.10	104.92	8.78	0.0330	0.9289	0.7280	1.0015
S K	16.13	23.35	536.07	5.22	0.1201	1.2116	0.7300	1.0119
BaL	57.46	19.42	375.49	4.87	0.3988	0.8226	1.0150	0.9993

Figure J. 36: Area 3 - Element analysis of spot 2 (REF+ 0.07 g MW system, short-time)

kV: 15 Mag: 5000 Takeoff: 34.6 Live Time(s): 50 Amp Time(μs): 7.68 Resolution:(eV) 132.4

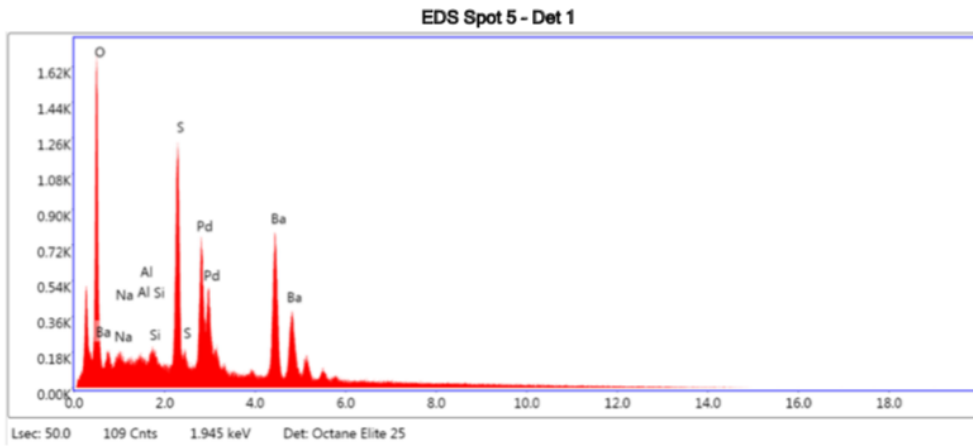


eZAF Smart Quant Results with SEC (BCNOF_2017-09-14)

Element	Weight %	Atomic %	Net Int.	Error %	Kratio	Z	A	F
O K	23.88	53.31	633.03	7.55	0.1123	1.2719	0.4613	1.0000
NaK	4.12	6.39	73.24	13.44	0.0123	1.1565	0.3228	1.0011
AlK	3.92	5.19	122.92	9.54	0.0179	1.1339	0.5000	1.0038
SiK	6.34	8.06	233.61	7.39	0.0355	1.1595	0.5992	1.0059
S K	12.49	13.92	421.13	5.41	0.0873	1.1368	0.7573	1.0129
BaL	48.42	12.59	312.14	5.98	0.3068	0.7685	1.0292	0.9995
FeK	0.84	0.54	7.73	64.82	0.0063	0.9839	0.9362	1.0145

Figure J. 37: Area 2 - Element analysis of spot 4 (REF+ 0.07 g MW system, short-time)

kV: 15 Mag: 5000 Takeoff: 34.6 Live Time(s): 50 Amp Time(μs): 7.68 Resolution:(eV) 132.4

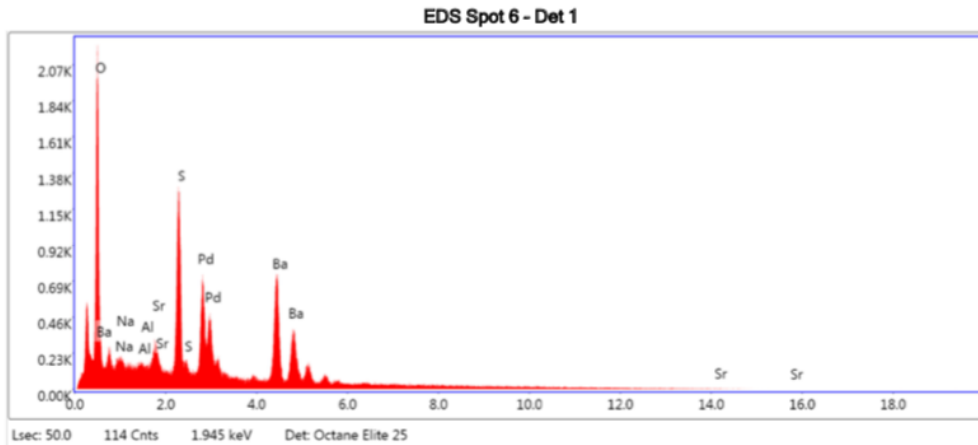


eZAF Smart Quant Results with SEC (BCNOF_2017-09-14)

Element	Weight %	Atomic %	Net Int.	Error %	Kratio	Z	A	F
O K	19.55	50.44	536.34	7.67	0.0960	1.3223	0.4524	1.0000
NaK	3.76	6.76	65.31	14.29	0.0111	1.2028	0.2981	1.0011
AlK	2.48	3.79	76.30	11.69	0.0112	1.1798	0.4649	1.0039
SiK	1.81	2.65	67.03	9.65	0.0103	1.2066	0.5713	1.0065
S K	14.77	19.03	524.08	5.06	0.1097	1.1836	0.7532	1.0139
BaL	57.64	17.33	391.38	4.99	0.3884	0.8024	1.0229	0.9993

Figure J. 38: Area 2 - Element analysis of spot 5 (REF+ 0.07 g MW system, short-time)

kV: 15 Mag: 5000 Takeoff: 34.6 Live Time(s): 50 Amp Time(μs): 7.68 Resolution:(eV) 132.4

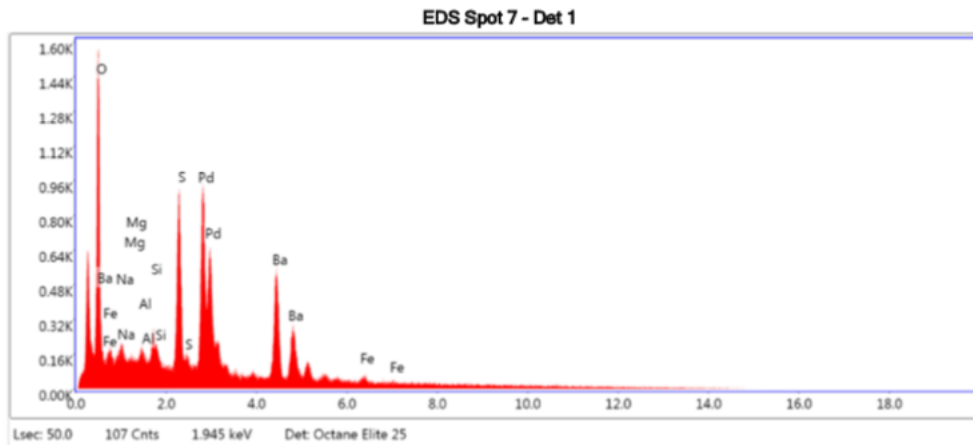


eZAF Smart Quant Results with SEC (BCNOF_2017-09-14)

Element	Weight %	Atomic %	Net Int.	Error %	Kratio	Z	A	F
O K	24.09	57.51	681.28	7.69	0.1142	1.2993	0.4348	1.0000
NaK	3.83	6.37	74.15	13.94	0.0118	1.1818	0.3100	1.0011
AlK	2.10	2.98	72.53	11.58	0.0100	1.1590	0.4851	1.0038
SrL	4.81	2.10	98.61	8.75	0.0271	0.8915	0.7526	1.0014
S K	14.15	16.86	536.10	5.14	0.1051	1.1625	0.7519	1.0120
BaL	51.01	14.19	371.43	5.10	0.3451	0.7872	1.0245	0.9993

Figure J. 39: Area 2 - Element analysis of spot 6 (REF+ 0.07 g MW system, short-time)

kV: 15 Mag: 5000 Takeoff: 34.6 Live Time(s): 50 Amp Time(μs): 7.68 Resolution:(eV) 132.4

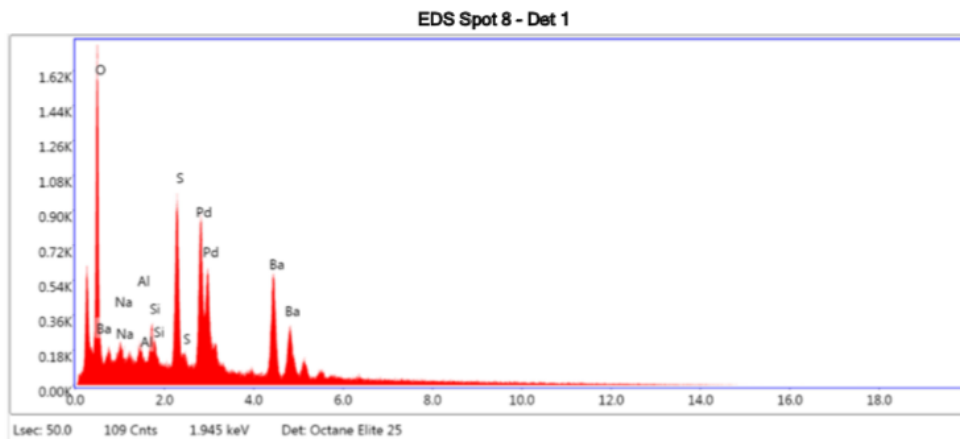


eZAF Smart Quant Results with SEC (BCNOF_2017-09-14)

Element	Weight %	Atomic %	Net Int.	Error %	Kratio	Z	A	F
O K	22.73	52.26	494.85	7.61	0.0980	1.2827	0.4659	1.0000
NaK	4.24	6.79	60.15	14.68	0.0113	1.1664	0.3162	1.0011
MgK	2.60	3.94	53.34	14.25	0.0085	1.1870	0.3787	1.0021
AlK	2.57	3.50	62.88	12.22	0.0102	1.1438	0.4797	1.0038
SiK	3.03	3.96	88.73	9.39	0.0151	1.1696	0.5861	1.0061
S K	13.25	15.21	365.44	6.35	0.0846	1.1468	0.7612	1.0132
BaL	50.26	13.47	263.62	6.39	0.2892	0.7758	1.0286	0.9996
FeK	1.32	0.87	9.87	62.06	0.0089	0.9937	0.9337	1.0141

Figure J. 40: Area 2 - Element analysis of spot 7 (REF+ 0.07 g MW system, short-time)

kV: 15 Mag: 5000 Takeoff: 34.6 Live Time(s): 50 Amp Time(μs): 7.68 Resolution:(eV) 132.4

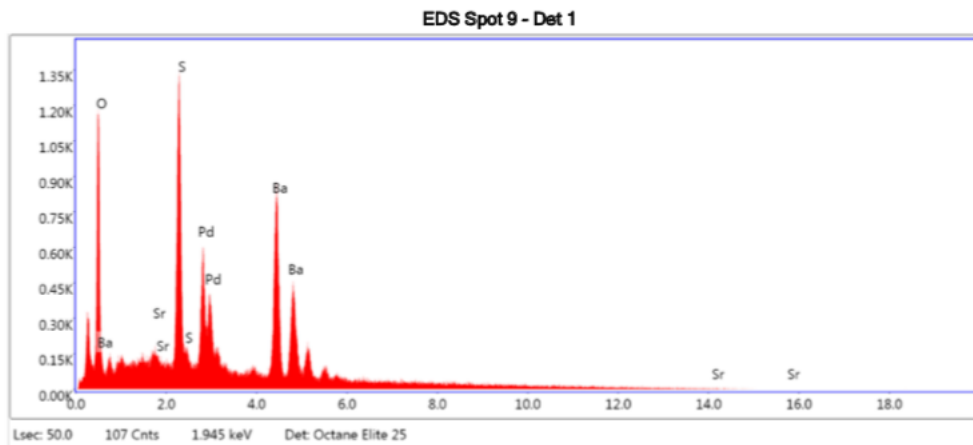


eZAF Smart Quant Results with SEC (BCNOF_2017-09-14)

Element	Weight %	Atomic %	Net Int.	Error %	Kratio	Z	A	F
O K	24.19	54.87	564.16	7.54	0.1083	1.2808	0.4668	1.0000
NaK	4.88	7.70	73.94	13.35	0.0135	1.1648	0.3164	1.0011
AlK	3.04	4.09	80.89	11.22	0.0127	1.1421	0.4880	1.0038
SiK	3.69	4.77	116.71	8.42	0.0192	1.1679	0.5918	1.0062
S K	13.38	15.15	394.98	5.35	0.0887	1.1451	0.7623	1.0133
BaL	50.82	13.43	284.82	6.42	0.3031	0.7746	1.0286	0.9993

Figure J. 41: Area 2 - Element analysis of spot 8 (REF+ 0.07 g MW system, short-time)

kV: 15 Mag: 5000 Takeoff: 34.6 Live Time(s): 50 Amp Time(μs): 7.68 Resolution:(eV) 132.4

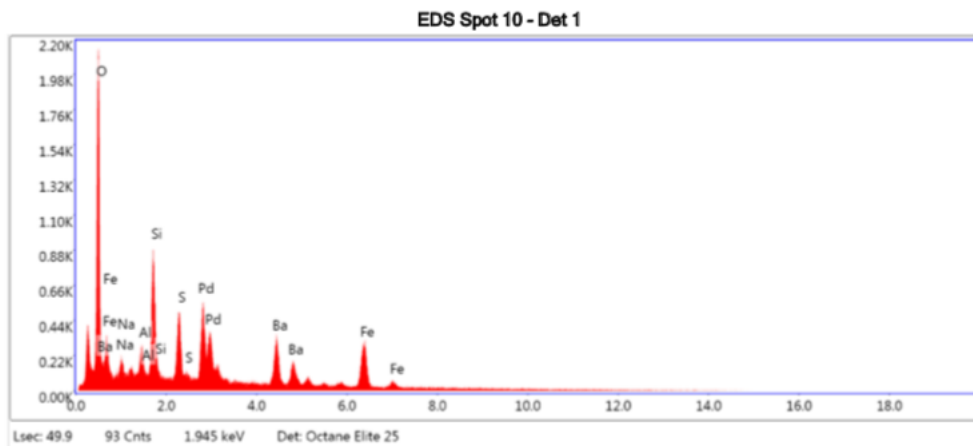


eZAF Smart Quant Results with SEC (BCNOF_2017-09-14)

Element	Weight %	Atomic %	Net Int.	Error %	Kratio	Z	A	F
O K	14.60	47.46	345.12	8.15	0.0768	1.3920	0.4347	1.0000
SrL	0.38	0.23	6.05	54.23	0.0022	0.9563	0.6987	1.0018
S K	16.17	26.24	504.63	5.99	0.1313	1.2477	0.7371	1.0149
BaL	68.85	26.07	417.71	5.12	0.5151	0.8492	1.0140	0.9994

Figure J. 42: Area 2 - Element analysis of spot 9 (REF+ 0.07 g MW system, short-time)

kV: 15 Mag: 5000 Takeoff: 34.6 Live Time(s): 49.9 Amp Time(μs): 7.68 Resolution:(eV) 132.4

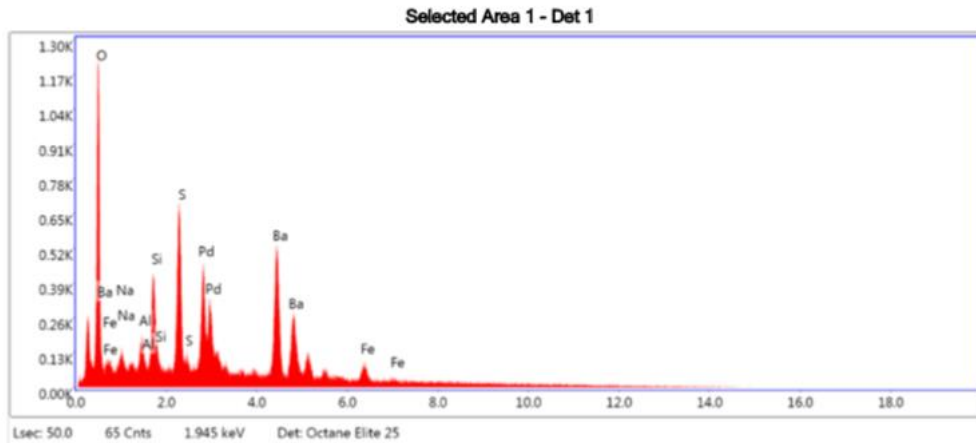


eZAF Smart Quant Results with SEC (BCNOF_2017-09-14)

Element	Weight %	Atomic %	Net Int.	Error %	Kratio	Z	A	F
O K	26.63	53.62	630.92	7.05	0.1372	1.2193	0.5041	1.0000
NaK	3.74	5.24	52.85	15.76	0.0109	1.1075	0.3136	1.0009
AlK	3.58	4.27	96.57	9.58	0.0172	1.0851	0.5273	1.0033
SiK	9.67	11.09	305.10	6.73	0.0569	1.1091	0.6295	1.0046
S K	6.44	6.47	179.57	7.53	0.0457	1.0865	0.7696	1.0108
BaL	27.82	6.53	148.69	9.18	0.1792	0.7318	1.0435	1.0061
FeK	22.13	12.77	169.91	5.66	0.1693	0.9345	0.9649	1.0119

Figure J. 43: Area 2 - Element analysis of spot 10 (REF+ 0.07 g MW system, short-time)

KV: 15 Mag: 5000 Takeoff: 34.6 Live Time(s): 50 Amp Time(μs): 7.68 Resolution:(eV) 132.4



eZAF Smart Quant Results with SEC (BCNOF_2017-09-14)

Element	Weight %	Atomic %	Net Int.	Error %	Kratio	Z	A	F
O K	18.43	47.73	382.91	7.69	0.0961	1.3174	0.4632	1.0000
NaK	2.96	5.33	37.57	16.84	0.0089	1.1983	0.2951	1.0011
AlK	2.89	4.44	66.54	11.16	0.0137	1.1753	0.4696	1.0038
SiK	5.74	8.47	158.42	7.95	0.0341	1.2020	0.5745	1.0060
S K	10.77	13.92	277.71	5.81	0.0815	1.1790	0.7408	1.0138
BaL	54.12	16.33	272.57	5.57	0.3790	0.7989	1.0256	1.0005
FeK	5.09	3.77	36.39	17.31	0.0418	1.0249	0.9275	1.0128

Figure J. 44: Area 2 - Element analysis of selected area 1 (REF+ 0.07 g MW system, short-time)

Reference Fluid Containing 0.07 g Multi-Walled Carbon Nanotube (Long-Time Aging)

Area 1

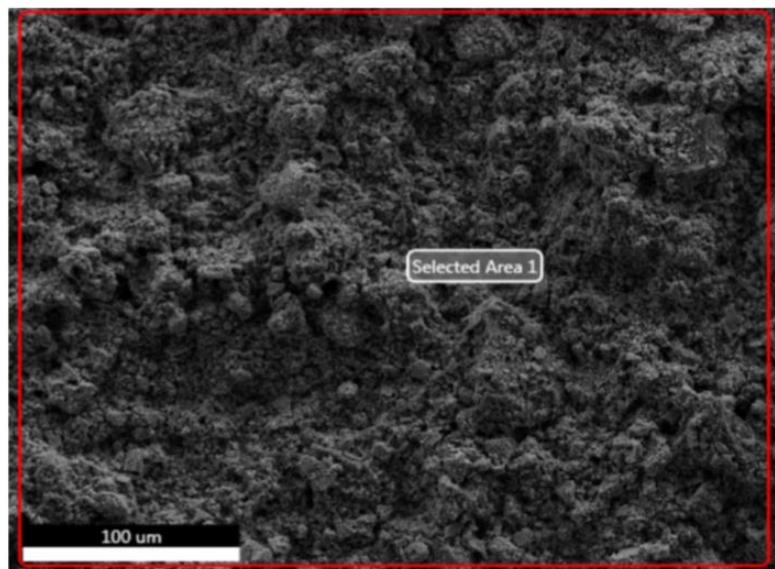


Figure J. 45: Area 1 - SEM picture and element analysis of surface at 100 μm (REF+ 0.07 g MW system, long-time)

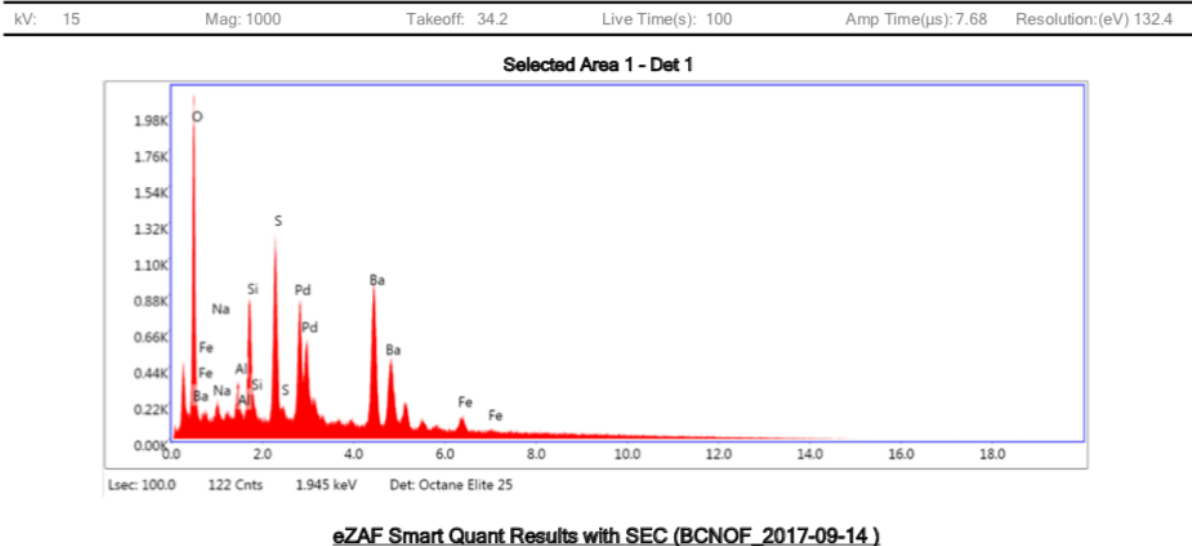


Figure J. 46: Area 1 - Element analysis of selected area 1 (REF+ 0.07 g MW system, long-time)

Area 2

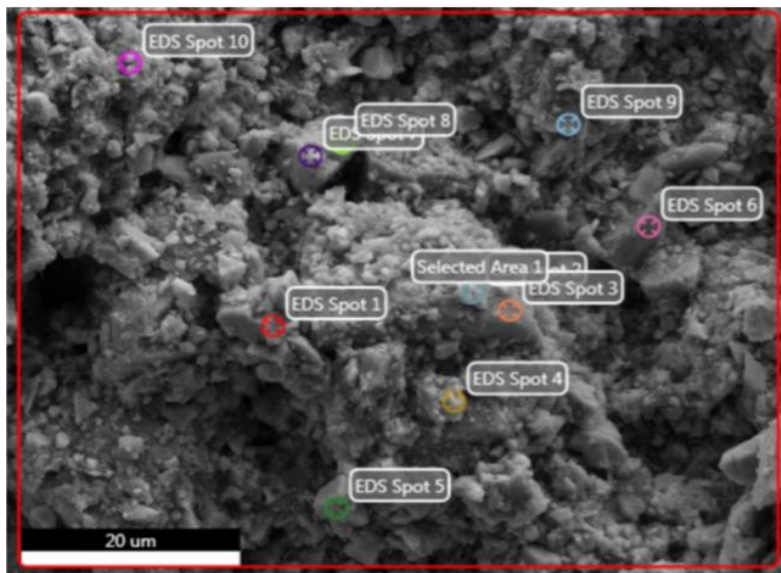
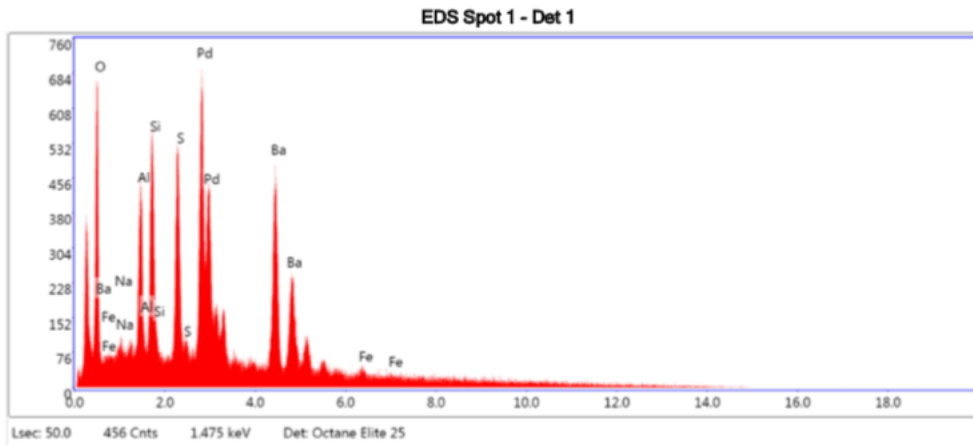


Figure J. 47: Area 2 - SEM picture and element analysis of surface at 20 μm (REF+ 0.07 g MW system, long-time)

kV: 15 Mag: 5000 Takeoff: 34.2 Live Time(s): 50 Amp Time(μs): 7.68 Resolution:(eV) 132.4

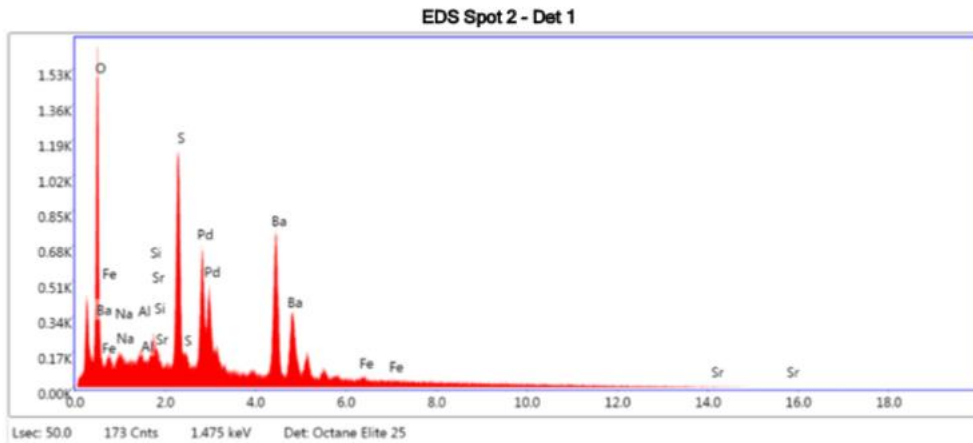


eZAF Smart Quant Results with SEC (BCNOF_2017-09-14)

Element	Weight %	Atomic %	Net Int.	Error %	Kratio	Z	A	F
O K	13.17	35.59	202.60	8.54	0.0553	1.3250	0.4276	1.0000
NaK	1.89	3.56	20.39	21.86	0.0053	1.2052	0.3117	1.0012
AlK	8.75	14.03	167.13	8.85	0.0373	1.1820	0.4847	1.0038
SiK	9.51	14.64	206.86	8.05	0.0483	1.2088	0.5632	1.0057
S K	10.36	13.97	207.94	7.87	0.0662	1.1857	0.7168	1.0132
BaL	55.28	17.41	222.79	6.13	0.3361	0.8035	1.0210	0.9995
FeK	1.03	0.80	5.92	70.34	0.0074	1.0310	0.9238	1.0136

Figure J. 48: Area 2 - Element analysis of spot 1 (REF+ 0.07 g MW system, long-time)

kV: 15 Mag: 5000 Takeoff: 34.2 Live Time(s): 50 Amp Time(μs): 7.68 Resolution:(eV) 132.4

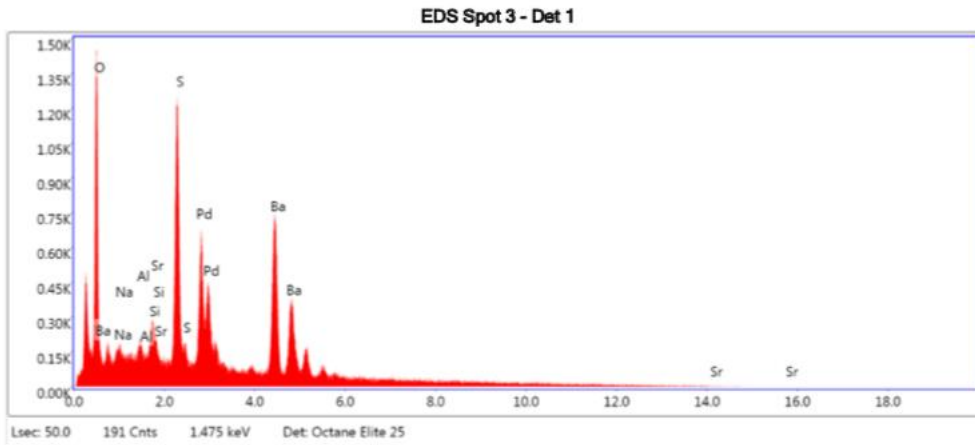


eZAF Smart Quant Results with SEC (BCNOF_2017-09-14)

Element	Weight %	Atomic %	Net Int.	Error %	Kratio	Z	A	F
O K	19.76	51.43	495.44	7.81	0.0961	1.3243	0.4398	1.0000
NaK	3.19	5.78	51.63	16.10	0.0095	1.2047	0.2954	1.0011
AlK	2.19	3.38	63.68	13.07	0.0101	1.1817	0.4652	1.0039
SiK	1.55	2.29	54.32	12.21	0.0090	1.2086	0.5728	1.0065
SrL	1.87	0.89	32.62	19.69	0.0104	0.9090	0.7277	1.0015
S K	14.29	18.57	473.09	5.30	0.1069	1.1855	0.7456	1.0133
BaL	56.40	17.10	361.03	5.56	0.3867	0.8038	1.0223	0.9995
FeK	0.75	0.56	6.82	65.01	0.0060	1.0317	0.9229	1.0136

Figure J. 49: Area 2 - Element analysis of spot 2 (REF+ 0.07 g MW system, long-time)

kV: 15 Mag: 5000 Takeoff: 34.2 Live Time(s): 50 Amp Time(μs): 7.68 Resolution:(eV) 132.4

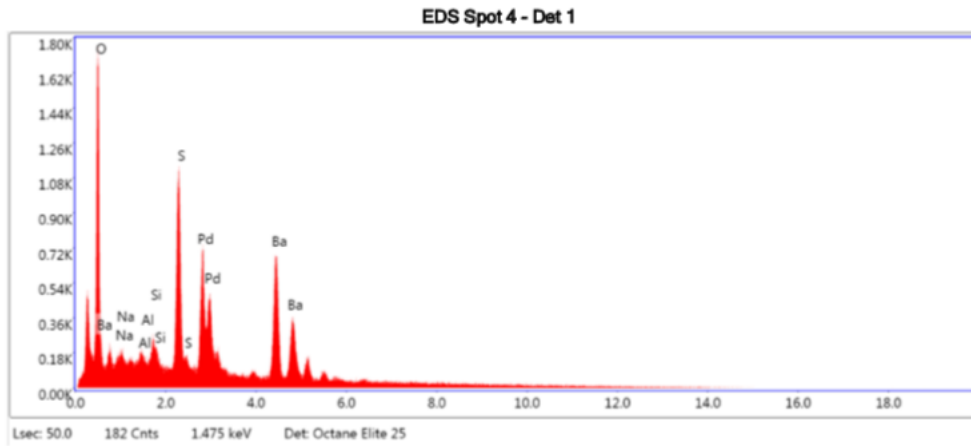


eZAF Smart Quant Results with SEC (BCNOF_2017-09-14)

Element	Weight %	Atomic %	Net Int.	Error %	Kratio	Z	A	F
O K	17.73	47.54	444.82	8.00	0.0846	1.3315	0.4250	1.0000
NaK	3.58	6.68	60.61	14.55	0.0109	1.2112	0.2984	1.0011
AlK	2.49	3.96	74.98	11.84	0.0117	1.1881	0.4655	1.0039
SiK	1.82	2.78	65.98	11.06	0.0107	1.2151	0.5716	1.0064
SrL	2.49	1.22	44.70	17.48	0.0139	0.9140	0.7256	1.0014
S K	14.99	20.05	509.53	5.20	0.1130	1.1920	0.7401	1.0129
BaL	56.91	17.77	376.30	5.04	0.3955	0.8085	1.0201	0.9993

Figure J. 50: Area 2 - Element analysis of spot 3 (REF+ 0.07 g MW system, long-time)

kV: 15 Mag: 5000 Takeoff: 34.2 Live Time(s): 50 Amp Time(μs): 7.68 Resolution:(eV) 132.4

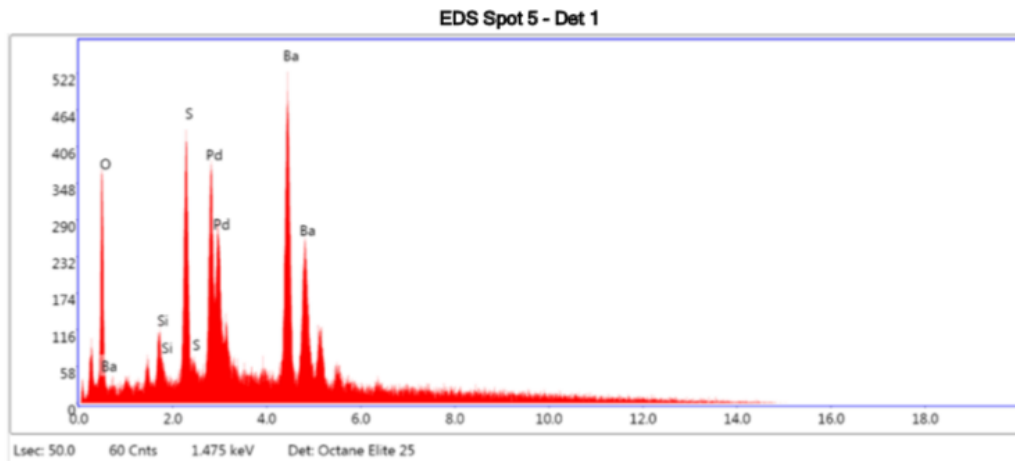


eZAF Smart Quant Results with SEC (BCNOF_2017-09-14)

Element	Weight %	Atomic %	Net Int.	Error %	Kratio	Z	A	F
O K	21.51	52.50	554.44	7.63	0.1049	1.3045	0.4556	1.0000
NaK	4.05	6.89	66.90	14.28	0.0120	1.1865	0.3034	1.0011
AlK	2.81	4.07	82.29	11.22	0.0127	1.1637	0.4725	1.0039
SiK	2.59	3.60	90.84	8.91	0.0147	1.1901	0.5775	1.0064
S K	14.27	17.38	474.79	5.24	0.1047	1.1672	0.7553	1.0137
BaL	54.76	15.57	348.25	5.24	0.3640	0.7905	1.0255	0.9993

Figure J. 51: Area 2 - Element analysis of spot 4 (REF+ 0.07 g MW system, long-time)

kV: 15 Mag: 5000 Takeoff: 34.2 Live Time(s): 50 Amp Time(μs): 7.68 Resolution:(eV) 132.4

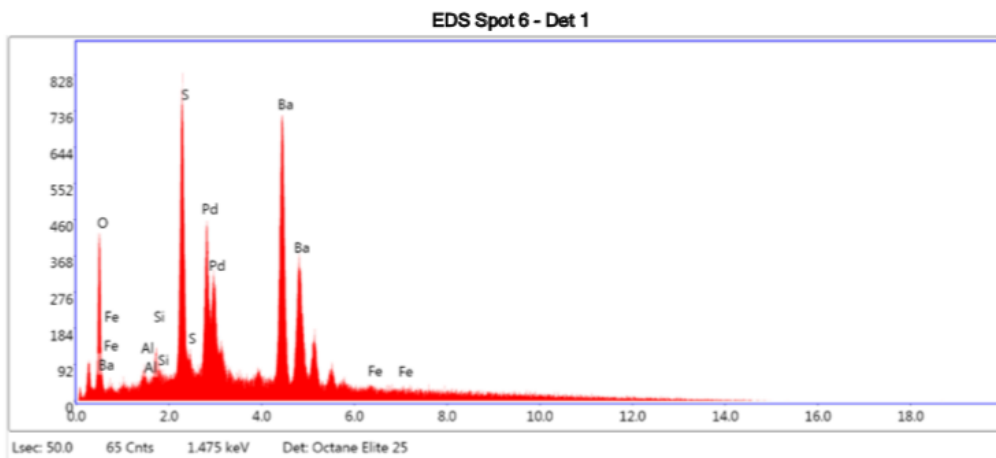


eZAF Smart Quant Results with SEC (BCNOF_2017-09-14)

Element	Weight %	Atomic %	Net Int.	Error %	Kratio	Z	A	F
O K	8.17	34.65	106.86	8.92	0.0439	1.4669	0.4477	1.0000
SiK	1.67	4.03	26.50	17.37	0.0093	1.3396	0.5061	1.0069
S K	10.34	21.89	165.03	7.43	0.0790	1.3154	0.6982	1.0166
BaL	79.82	39.44	260.70	4.92	0.5917	0.8984	1.0089	0.9996

Figure J. 52: Area 2 - Element analysis of spot 5 (REF+ 0.07 g MW system, long-time)

kV: 15 Mag: 5000 Takeoff: 34.2 Live Time(s): 50 Amp Time(μs): 7.68 Resolution:(eV) 132.4

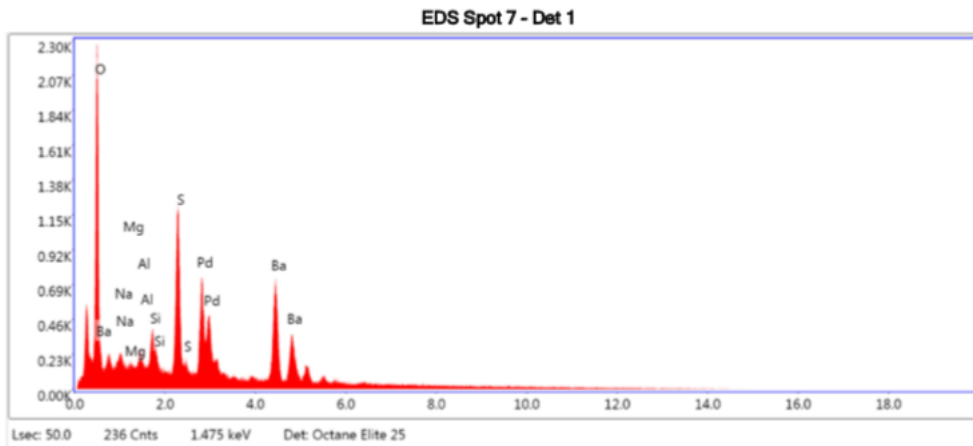


eZAF Smart Quant Results with SEC (BCNOF_2017-09-14)

Element	Weight %	Atomic %	Net Int.	Error %	Kratio	Z	A	F
O K	6.34	27.32	116.18	9.54	0.0338	1.4630	0.4252	1.0000
AlK	0.50	1.27	9.35	72.49	0.0022	1.3058	0.3989	1.0041
SiK	0.94	2.31	22.24	23.22	0.0055	1.3360	0.5106	1.0069
S K	13.63	29.31	323.54	5.88	0.1095	1.3118	0.7046	1.0159
BaL	78.14	39.23	375.60	4.41	0.6028	0.8956	1.0069	0.9996
FeK	0.46	0.57	3.09	88.38	0.0041	1.1572	0.8889	1.0114

Figure J. 53: Area 2 - Element analysis of spot 6 (REF+ 0.07 g MW system, long-time)

kV: 15 Mag: 5000 Takeoff: 34.2 Live Time(s): 50 Amp Time(μs): 7.68 Resolution:(eV) 132.4

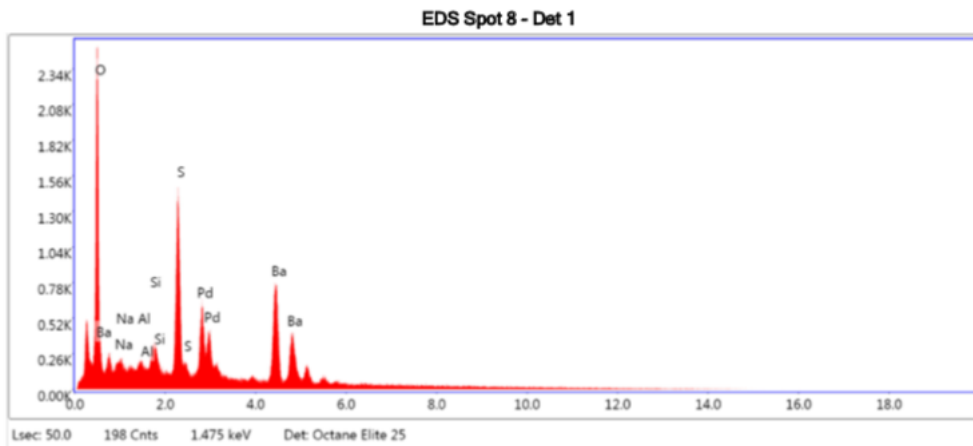


eZAF Smart Quant Results with SEC (BCNOF_2017-09-14)

Element	Weight %	Atomic %	Net Int.	Error %	Kratio	Z	A	F
O K	24.16	53.93	720.18	7.38	0.1186	1.2737	0.4636	1.0000
NaK	3.92	6.09	77.49	13.77	0.0121	1.1582	0.3197	1.0011
MgK	2.52	3.71	72.23	12.38	0.0095	1.1786	0.3834	1.0021
AlK	2.88	3.82	98.45	10.27	0.0133	1.1356	0.4849	1.0038
SiK	3.79	4.82	154.11	7.73	0.0217	1.1612	0.5897	1.0061
S K	13.27	14.78	504.72	5.09	0.0969	1.1385	0.7609	1.0131
BaL	49.45	12.86	357.84	5.45	0.3256	0.7698	1.0295	0.9993

Figure J. 54: Area 2 - Element analysis of spot 7 (REF+ 0.07 g MW system, long-time)

kV: 15 Mag: 5000 Takeoff: 34.2 Live Time(s): 50 Amp Time(μs): 7.68 Resolution:(eV) 132.4

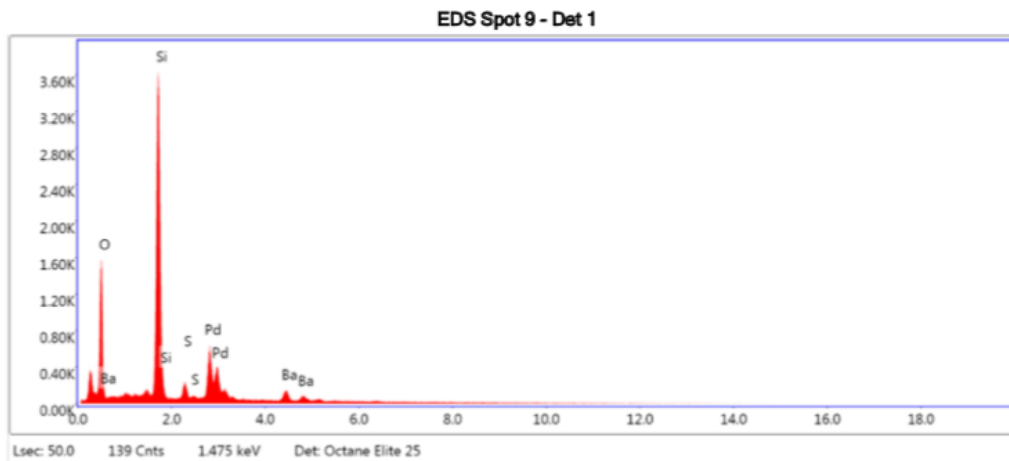


eZAF Smart Quant Results with SEC (BCNOF_2017-09-14)

Element	Weight %	Atomic %	Net Int.	Error %	Kratio	Z	A	F
O K	24.30	56.37	757.71	7.33	0.1261	1.2890	0.4628	1.0000
NaK	3.67	5.92	72.87	14.35	0.0115	1.1723	0.3068	1.0011
AlK	2.39	3.29	84.74	11.16	0.0115	1.1496	0.4806	1.0039
SiK	2.90	3.83	123.05	7.97	0.0175	1.1756	0.5874	1.0063
S K	14.16	16.39	565.59	4.95	0.1097	1.1528	0.7620	1.0135
BaL	52.58	14.21	398.61	5.07	0.3665	0.7803	1.0277	0.9993

Figure J. 55: Area 2 - Element analysis of spot 8 (REF+ 0.07 g MW system, long-time)

kV: 15 Mag: 5000 Takeoff: 34.2 Live Time(s): 50 Amp Time(μs): 7.68 Resolution:(eV) 132.4

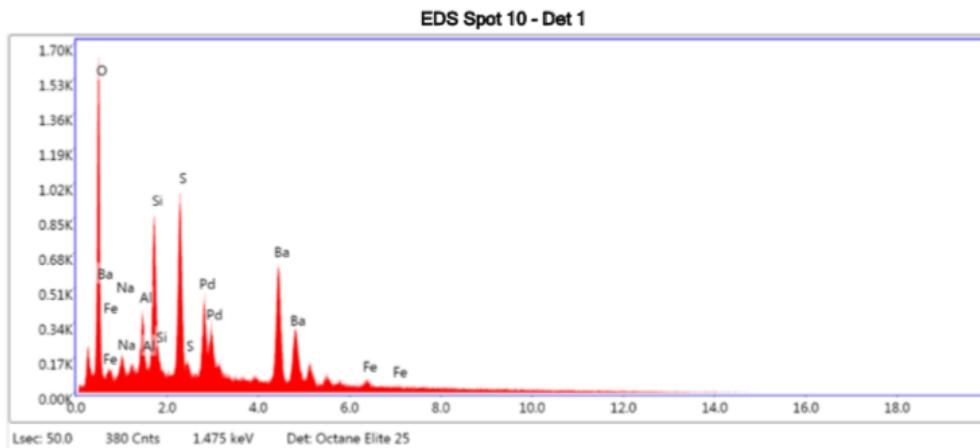


eZAF Smart Quant Results with SEC (BCNOF_2017-09-14)

Element	Weight %	Atomic %	Net Int.	Error %	Kratio	Z	A	F
O K	33.97	51.99	409.86	8.25	0.1169	1.1122	0.4040	1.0000
SiK	49.58	43.22	1297.65	3.63	0.3164	1.0064	0.8260	1.0021
S K	3.18	2.43	52.13	14.04	0.0173	0.9843	0.7191	1.0054
BaL	13.27	2.37	44.24	15.91	0.0697	0.6588	1.0430	0.9983

Figure J. 56: Area 2 - Element analysis of spot 9 (REF+ 0.07 g MW system, long-time)

kV: 15 Mag: 5000 Takeoff: 34.2 Live Time(s): 50 Amp Time(μs): 7.68 Resolution:(eV) 132.4

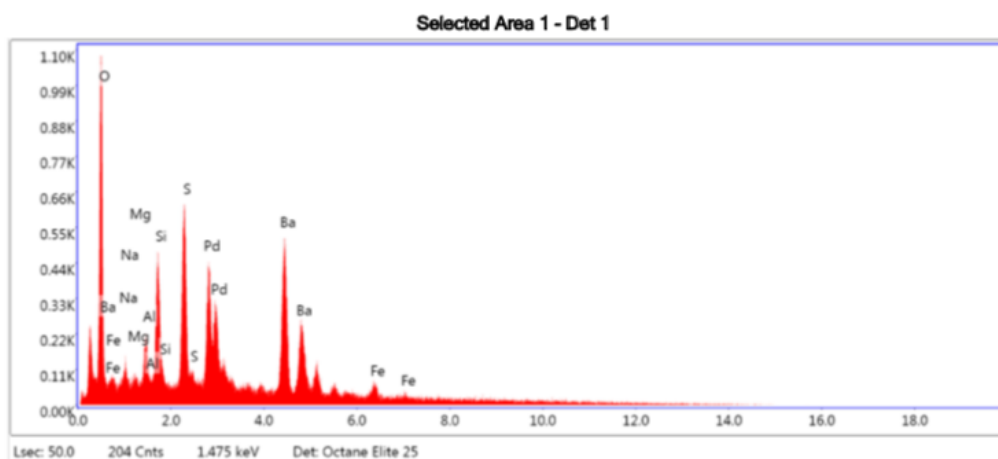


eZAF Smart Quant Results with SEC (BCNOF_2017-09-14)

Element	Weight %	Atomic %	Net Int.	Error %	Kratio	Z	A	F
O K	19.85	47.15	492.78	7.79	0.0998	1.2866	0.4409	1.0000
NaK	2.74	4.53	47.21	15.46	0.0091	1.1700	0.3186	1.0011
AlK	4.62	6.51	141.88	9.01	0.0235	1.1472	0.4980	1.0039
SiK	9.21	12.47	330.37	6.96	0.0572	1.1731	0.5937	1.0057
S K	12.16	14.41	394.34	5.40	0.0931	1.1503	0.7413	1.0127
BaL	49.67	13.75	314.11	5.56	0.3515	0.7782	1.0263	0.9996
FeK	1.74	1.19	15.75	32.04	0.0146	0.9969	0.9329	1.0141

Figure J. 57: Area 2 - Element analysis of spot 10 (REF+ 0.07 g MW system, long-time)

kV: 15 Mag: 5000 Takeoff: 34.2 Live Time(s): 50 Amp Time(μs): 7.68 Resolution:(eV) 132.4



eZAF Smart Quant Results with SEC (BCNOF_2017-09-14)

Element	Weight %	Atomic %	Net Int.	Error %	Kratio	Z	A	F
O K	17.50	45.32	340.93	7.81	0.0890	1.3167	0.4553	1.0000
NaK	2.47	4.46	30.44	18.35	0.0075	1.1977	0.2992	1.0011
MgK	1.59	2.71	28.83	16.77	0.0060	1.2190	0.3639	1.0021
AlK	3.36	5.15	73.45	10.45	0.0157	1.1747	0.4671	1.0038
SiK	6.62	9.76	173.33	7.79	0.0387	1.2013	0.5700	1.0059
S K	10.54	13.61	257.57	5.90	0.0783	1.1783	0.7340	1.0137
BaL	54.51	16.45	262.40	5.70	0.3784	0.7984	1.0249	1.0001
FeK	3.41	2.53	23.35	23.26	0.0278	1.0242	0.9262	1.0131

Figure J. 58: Area 2 - Element analysis of selected area 1 (REF+ 0.07 g MW system, long-time)